



HAL
open science

Study of dwell-effect on behaviour and fracture of the alloy Ti-6242

Konstantin Kuzmenkov

► **To cite this version:**

Konstantin Kuzmenkov. Study of dwell-effect on behaviour and fracture of the alloy Ti-6242. Other. Ecole Nationale Supérieure des Mines de Paris, 2012. English. NNT : 2012ENMP0029 . pastel-00745834

HAL Id: pastel-00745834

<https://pastel.hal.science/pastel-00745834>

Submitted on 26 Oct 2012

HAL is a multi-disciplinary open access archive for the deposit and dissemination of scientific research documents, whether they are published or not. The documents may come from teaching and research institutions in France or abroad, or from public or private research centers.

L'archive ouverte pluridisciplinaire **HAL**, est destinée au dépôt et à la diffusion de documents scientifiques de niveau recherche, publiés ou non, émanant des établissements d'enseignement et de recherche français ou étrangers, des laboratoires publics ou privés.

École doctorale n°432 : Sciences des Métiers de l'Ingénieur

Doctorat ParisTech

T H È S E

pour obtenir le grade de docteur délivré par

l'École nationale supérieure des mines de Paris

Spécialité « Mécanique »

présentée et soutenue publiquement par

Konstantin KUZMENKOV

le 08 juin 2012

**Étude de l'effet du temps de maintien sur le comportement
et la rupture de l'alliage Ti-6242**

Study of dwell-effect on behaviour and fracture of the alloy Ti-6242

Directeur de thèse : **Georges CAILLETAUD**

Maître de thèse : **Farida AZZOUC**

Jury

Mme Anne HABRAKEN, Directeur de Recherche FNRS, Université de Liège

M. Patrick VILLECHAISE, Directeur de Recherche, LMPM, ENSMA

Mme Brigitte BACROIX, Directeur de Recherche CNRS, Université Paris 13

M. Boris MELNIKOV, Professeur, Université Polytechnique de St.Pétersbourg

Mme Farida AZZOUC, Docteur, Ingénieur de Recherche, ENSMP, Mines ParisTech

M. Georges CAILLETAUD, Professeur, ENSMP, Mines ParisTech

M. Alexandre DALLOZ, Docteur, Ingénieur de Recherche, Snecma

M. Jean-Yves GUEDOU, Docteur d'Etat, Snecma

Rapporteur

Rapporteur

Examinateur

Examinateur

Examinateur

Examinateur

Examinateur

Examinateur

MINES ParisTech

Centre des Matériaux

Pierre-Marie FORT BP 87 - 91003 Evry Cedex-France

**T
H
È
S
E**

Contents

I	Acknowledgements	1
II	Introduction	3
III	Studied Alloy and Dwell Effect	7
III.1	Titanium Alloy for Some Aeronautic Applications	8
III.2	Dwell-Fatigue Effect	8
III.3	Material Microstructure: Crystallography	12
III.4	Effects of Alloying Elements	15
III.5	Forging Process and Thermal Heat Treatment	19
III.6	Microstructural Morphologies	19
III.7	General Mechanical Properties	21
III.8	Barstock and Forged Compressor Disc	21
III.9	Texture and Scatter Effects	21
III.10	Microstructure of Ti-6242 Forged in the Domain β	23
III.11	Main Causality of Dwell Effect	25
III.12	Conclusions	27
IV	Macroscopic Constitutive Equations	29
IV.1	Introduction	30
IV.2	Mechanical Behaviour of Ti-6242 at Room Temperature	30
IV.3	Mechanical Behaviour of Ti-6242 at Other Temperatures	31
IV.4	Presentation of a Phenomenological Material Model	37
IV.4.1	Constitutive Equations	37
IV.4.2	Model Calibration	38
IV.4.3	Numerical Prediction of Tensile, Cyclic and Creep Tests	39
IV.4.4	Conclusions	48
V	Residual Stress Calculation in Forged Discs	49
V.1	Introduction	50
V.2	Effects of heat treatment on the stress state	50
V.3	2D Finite Element Disc Simulations	51
V.3.1	Geometric Models	51
V.3.2	Boundary Conditions and Loading	51
V.3.3	Material Models	51
V.3.4	Heat Treatment Analysis	52
V.3.5	Disc Machining	56
V.4	2D Finite Element Simulations of the Disc in Operation	60
V.4.1	Stress and Strain Results Analysis	61
V.5	3D Finite Element Disc Simulations	64

V.5.1	Geometric Models	64
V.5.2	Boundary Conditions and Loading	64
V.5.3	Material models	65
V.5.4	Stress and Strain Analysis Results	65
V.5.5	Stress and Strain Analyses Results of the Disc with a Slit	68
V.6	General Conclusions	70
VI	Multiscale Constitutive Equations	73
VI.1	Introduction	74
VI.2	Single Crystal Model (Microscopic Model)	74
VI.2.1	Material Description	74
VI.2.2	Basic Material Data for α and β phases	75
VI.2.3	Size-effect in Crystal Plasticity	79
VI.2.4	Final Calibration and Results	81
VI.2.5	Determination of τ_{CRSS} for β Phase	81
VI.2.6	Calibration of the Material Model	82
VI.2.7	Framework and Theory for a General Multimat	84
VI.2.8	Calibration Results of Material Parameters	87
VI.2.9	Analysis of the Local Behaviour	88
VI.3	Conclusions	92
VII	Full Field Model of a Microstructure with Plumets	93
VII.1	Introduction	94
VII.2	Meshes and Calculation List	94
VII.2.1	FE Calculations of Plumets with Real Angles	97
VII.3	FE Calculations of Plumets with Virtual Angles	104
VII.3.1	Local Stress Fields	104
VII.3.2	The Most Critical and Safest Crystal Orientations	105
VII.3.3	The Most Critical and Safest Morphological Orientations	105
VII.3.4	Comparison of Configurations with Real and Virtual Crystal Orientations	106
VII.4	Influence of the Shape of the Main Plume	106
VII.5	Conclusions	106
VIII	Life Prediction under Fatigue and Dwell Loadings	117
VIII.1	Introduction	118
VIII.2	Macroscopic Damage Model	118
VIII.2.1	Fatigue damage model	118
VIII.2.2	Creep-Fatigue Interaction	120
VIII.2.3	Calibration results	120
VIII.3	A Microstructure Based Damage Model	122
VIII.4	Conclusions	126
IX	General Conclusions and Outlook	129
IX.1	Conclusions	129
IX.2	Outlook	130
X	Abbreviation	135

A	Appendix	137
A.1	Crystallographic Slip Systems	137
A.2	CC model	141
A.3	RL model (alternative model)	142
A.4	Relationship between Eigenstrain Influence Operators	145
	References	155

Chapter -I-

Acknowledgements

First, I would like to acknowledge great help, encouraging ideas and vision on our project of Georges CAILLETAUD. He is one of the best professors I have ever met. I also would like to acknowledge advice on calculations, constructive critical points and organisational tasks on reports and presentations of my supervisor Farida AZZOUZ. She has definitely improved my skills which I still have to develop to reach that kind of level which she has got.

I would like to acknowledge moral support and belief in me of my professor Boris MELNIKOV from Russia, Saint-Petersburg. I am very grateful to him. The group VAL from Centre des Mat'eriaux is acknowledged for their technical expertise, especially I would like to thank Nikolay OSIPOV for his understanding and great help at the beginning of my thesis. He taught me a lot of techniques and methods.

I acknowledge work of Immanuel FREIHERR VON THUNGEN and Patrick VILLECHAISE from ENSMA. Their provision of experimental data and strong opinions on the development of our models are also acknowledged.

Benedicte BONNET, Alexandre DALLOZ and Jean-Yves GUEDOU from Snecma Groupe SAFRAN are acknowledged for providing experimental results and their comments on work.

Arnaud LONGUET, Yannick ROBERT, Laurent BAROUMES and Pierre LEFRANC are acknowledged for their developed models and some results which were used in the present thesis.

I thank all the members of my jury for their comments and questions: Anne HABRAKEN and Brigitte BACROIX (other members are thanked above).

I acknowledge common cooperative tasks with Guillaume MARTIN. It was a great pleasure to work with him.

I greatly acknowledge work of all authors and co-authors of cited articles in the thesis. Computer support by Centre des Matériaux is also acknowledged.

If I have forgotten anyone, consider yourself thanked

Chapter -II-

Introduction

La sensibilité au temps de maintien de la durée de vie en fatigue à température ambiante des alliages de titane est un phénomène qui pose depuis longtemps des problèmes dans les applications aéronautiques. Cet “effet dwell” peut en effet être la source de ruptures prématurées. De récentes publications font état de problèmes qui persistent dans les alliages de titane α/β [Hasija et al., 2003] et [McBagonluri et al., 2005], et qui obligent les concepteurs à prendre de larges marges de sécurité en dimensionnement [Venkatramani et al., 2007]. Les micro-fissures se développent sur une longueur d’environ un grain (où le grain est défini comme une région d’orientation cristallographique uniforme), la rupture étant presque toujours associée aux plans basaux du réseau HCP. Si le grain dans lequel le phénomène se produit est grand, il y a une possibilité que le temps de propagation ultérieur soit très limité. La durée de vie du composant, dans lequel se produirait ce phénomène de développement de facettes est donc raccourcie, de façon difficilement prévisible, car la nucléation des défauts est étroitement liée aux microstructures locales – combinaison des orientations cristallographiques du grain, orientation par rapport à la direction de chargement macroscopique, systèmes de glissement actifs, morphologie granulaire [Dunne et al., 2007]. Les défauts peuvent se former tant sous conditions de chargement statiques ou cycliques. Les sites peuvent très bien être sous la surface, puisqu’ils qu’ils peuvent se développer sans aucune interaction avec l’environnement externe [Bache, 1999].

De nombreuses recherches ont été réalisées pour expliquer de façon fondamentale le “dwell effect”. Celui-ci a été identifié dans les années 1972–73 comme étant la source d’échecs répétés dans des aubes en titane dans les moteurs Rolls-Royce RB211 [Bache, 2003]. Afin de replacer cet évènement dans le champ des recherches du domaine, nous mentionnons quelques événements historiques tels que présentés dans [Bathias and Pineau, 2010] (Tab.II.1).

Les études expérimentales sur le “dwell” et la fatigue pure ont confirmé que les éprouvettes soumises à un temps de maintien présentent une réduction significative du nombre de cycles à amorçage, en comparaison avec les éprouvettes de fatigue pure. Les études attribuent la sensibilité au temps de maintien à toute une gamme de mécanismes possibles : présence de “facettes de quasi-clivage” ; effets de température ; rôle d’éléments interstitiels tels que l’hydrogène, l’azote et l’oxygène ; accumulation des déformations dépendantes du temps ; dépendance de la fréquence ; effets du rapport R de la contrainte min sur la contrainte max ; influence de la microstructure et la texture ; dépendance aux orientations cristallographiques. Si l’on écarte les processus chimiques et les effets de l’environnement (comme la formation

d'hydrures) [Evans and Bache, 1994], il reste à considérer le rôle du fluage à froid, qui continue à compromettre le design [Bache, 2003] et [Evans and Bache, 1994].

Après cette introduction (partie I) et une revue de la littérature (partie II), le travail de thèse s'effectue en suivant trois axes principaux.

1) Ayant en vue le lien entre les éprouvettes de laboratoire et les applications aux disques réels, nous avons d'abord étudié les conditions du processus industriel, afin de bien clarifier dans les observations réalisées les effets sur les structures qui proviennent des traitements thermomécaniques et ce qui doit être relié au comportement intrinsèque de l'élément de volume représentatif. Nous avons donc revisité les lois de comportement macroscopiques développées au cours d'études précédentes [Baroumes, 1998, Robert, 2007, Longuet, 2010] afin d'évaluer les champs de contrainte et de déformation dans les disques au cours de la fabrication. Plusieurs jeux de paramètres ont été considérés, en accordant une attention particulière aux effets de viscosité à haute température (partie III). Les modèles sont ensuite utilisés pour l'étude numérique d'un disque de compresseur. En partie IV.1-IV.4, nous considérons un modèle axisymétrique. Le calcul démarre à la fin de l'opération de forgeage, et comporte une simulation des traitements thermiques et de l'usinage. La partie IV.5 présente des calculs 3D, dont le but est d'évaluer les effets des contraintes résiduelles. Une coupe radiale a été pratiquée sur un disque : la fermeture de celle-ci permet de mettre en évidence l'effet du champ de contraintes résiduelles. Des éprouvettes ont été usinées dans des disques et testées sous chargement cyclique.

2) Une approche micro-macro a ensuite été développée dans le cadre de notre étude. Les équations proposées décrivent les propriétés mécaniques de l'alliage Ti6242 forgé dans le domaine β (partie V). Les données expérimentales qui ont plus particulièrement retenu notre attention sont celles qui sont obtenues à température ambiante pour des charges élevées, dans la mesure où l'effet de viscosité qui s'y manifeste est l'un des paramètres-clés à la source de l'effet dwell [Stubbington and Pearson, 1978].

3) Une étude numérique exhaustive a ensuite été effectuée. Son but est de comprendre le rôle spécifique de la plasticité cristalline (réseaux cristallins hexagonal compact et cubique centré avec des positions relatives bien définies) et de la géométrie locale (présence de grains de grande taille, ou "plumes") sur les champs de contrainte et de déformation, donc sur les mécanismes locaux d'amorçage de fissure. Des calculs par éléments finis 3D sont menés dans ce but (partie VI). Une analyse détaillée des résultats nous permet de proposer un modèle basé sur la microstructure qui permet de prévoir l'amorçage de fissure. Il est exposé en partie VII, en même temps qu'un modèle macroscopique traditionnel, ce dernier gardant un intérêt certain pour une approche "ingénieur" du problème.

La dernière partie du manuscrit (partie VIII) est consacrée à des conclusions, discussions et perspectives.

The phenomenon of room temperature (RT) dwell sensitive fatigue (in which the load cycle includes a hold period of time) in titanium alloys has been a concern for the aeronautical applications for a long period of time. Dwell fatigue has been identified to cause early failure. It is known as a deleterious failure mechanism in structural components made from α/β titanium alloys [Hasija et al., 2003] and [McBagonluri et al., 2005]. Dwell fatigue could provoke serious accidents due to a sub-surface initiation and brittle cleavage-like, faceted features [Venkatramani et al., 2007]. Facetting is a micro-crack development at a length of about the grain size (where grain is defined as an area of approximately uniform crystal orientation) in which failure is almost always associated with basal planes of HCP crystals (α phase). If the grain is large, where facetting has occurred, there is a possibility that propagation time may be limited. Lifetime, under these circumstances, is dominated by nucleation. There is also a high probability that nucleation is dependant on the following microstructural features: the local grain crystallographic orientations, the grain morphology and the active slip systems [Dunne et al., 2007]. They are formed under static and cyclic loadings and occur at subsurface sites and they can develop without the external environment [Bache, 1999].

An enormous amount of research has been carried out to investigate the fundamental reasons controlling dwell behaviour. RT dwell sensitivity was first considered in late 1972/early 1973 through failure titanium alloy fan discs in Rolls-Royce RB211 engines [Bache, 2003]. Having placed this event in the history of the research field, we mention the main historical events, as shown in [Bathias and Pineau, 2010] (Tab.II.1).

Experimental studies on pure fatigue and on dwell have demonstrated that the dwell samples show a significant reduction in the number of cycles to failure compared to the pure fatigue specimens. The earlier research on titanium alloys attributes dwell sensitivity to a range of possible mechanisms. The presence of “quasi-cleavage facets”, temperature effects, the role of interstitial elements such as hydrogen, nitrogen and oxygen, time-dependent strain accumulation, frequency dependence, stress ratio effects, microstructural and micro-texture influences, crystallographic orientation dependence. If chemical or environmental processes, such as a hydrogen, are discounted as a means of causing dwell failures [Evans and Bache, 1994], then the alternative time dependant mechanism of creep has to be considered. “Cold dwell” continues to compromise design [Bache, 2003], [Evans and Bache, 1994].

After this introduction (part I) and a review of the literature (part II), the thesis work follows three research directions.

1) Having in mind the link between laboratory specimens and application to real discs, we have first investigated the conditions of the industrial process, in order to be able to make a clear difference between possible structural effects coming from the history of the thermomechanical treatment and the intrinsic behaviour of a representative material element. We have then revisited macroscopic constitutive equations developed in previous studies [Baroumes, 1998, Robert, 2007, Longuet, 2010] to compute stress and strain fields during the fabrication of the disc. Various material parameter sets have been considered, paying special attention to the viscous effect at high temperature (part III). The models are then used for studying turbine discs. In part IV.1-IV.4, we consider a 2D axisymmetric model. The calculation starts at the end of the forging operation, and includes thermal treatments and the machining of the disc. Part IV.5 introduces 3D computations, in order to evaluate the effects of residual stresses. A radial cut has been made on a disc: the closure of the cut allows to highlight the effect of the residual stress field. Specimens have been taken from real

Year	Event
1842	Meudon railway accident
1858	First publication by Wöhler
1860-70	Wöhler experiments on smooth and notched axles. Bending and torsion tests - investigation on the mean stress effect
-1881	Study by Bauschinger which initiated low-cycle fatigue
1910	Basquin law
1913	Stress distribution within notches (Inglis)
1920	Energy balance regarding the propagation of a crack (Griffith)
1930	Stress concentration factor and endurance limit (Peterson)
1937	Neuber concept applied to notches
1939	Statistical approach Weibull law
1945	Miner concept for fatigue damage accumulation
1953-54	Low cycle fatigue. Manson–Coffin law
1954	Comet aircrafts accidents
1956	Introduction of strain energy released rate (Irwin)
1960	Servo-hydraulic machines
1961	Paris law
1968	Introduction of effective stress intensity factor (Elber)
1988	Aloha B737 accident
1989	DC 10 Sioux City accident
1996	Pensacola accident
1998	ICE. Eshede railway accident
2006	Los Angeles B767 accident

Table II.1 : A few stages and main events regarding the history of the fatigue phenomenon [Bathias and Pineau, 2010]

discs and tested in cyclic loadings.

2) Multiscale constitutive equations are then developed in the framework of our study. They describe the mechanical properties of the Ti6242 alloy forged in the β domain (part V). The data obtained in the high stress–room temperature domain do receive a special attention, since this viscous effect is one of the key parameters for the description of dwell effect [Stubbington and Pearson, 1978].

3) A comprehensive numerical study is then performed, the purpose of which is to understand the specific role of crystal plasticity (HCP and BCC networks with given relative orientations) and of the local geometry (presence large grains, called “feathers” or “plumes”) on local strain and stress fields, thus on the crack initiation mechanisms. Three dimensional Finite Element Analyses are made for that purpose (part VI). A detailed analysis of the results allows us to propose a microstructure based model for crack initiation. It is shown in part VII, together with a more traditional macroscopic approach that can be more convenient for engineers.

The last section (part VIII) is devoted to conclusions, outlook and perspectives of this study.

Chapter -III-

Studied Alloy and Dwell Effect

III.1 Titanium Alloy for Some Aeronautic Applications

One of the most abundant metals on Earth, titanium is only recently used in industry, since an efficient processing route was found only in the middle of the 20th century (Kroll). A history of the material can be found in [Lutjering and Williams, 2003]. It is now widely used in aerospace industry, due to its high strength and corrosion resistance and its low density (about 50 % less if compared to steel). Different aeronautic components of airplane engines made of titanium alloy have to operate at low to moderately elevated temperatures [Han, 1990]. Depending on the alloying elements, titanium alloys can be used up to 600 °C, a very high temperature, if compared to aluminium alloys that have also a low density [Boyer, 1996].

Figure III.1 shows two jet engines GP7200 and GE90 which are some of the most powerful in the world. They are installed on airplanes by different companies [saf, 2010], [sta, 2010].

In Fig.III.2 some of the main components of GE90 engine are represented. It consists of: 1. Composite fan 2. Low Pressure Compressor (LPC) / Booster 3. High Pressure Compressor (HPC) 4. Dual Dome Combustor 5. High Pressure Turbine (HPT) 6. Low pressure Turbine (LPT) [sta, 2010].

The studied discs made from Ti-6242 forged in the domain β are situated in the high pressure compressor (HPC).



Figure III.1 : A view of two recent aeronautical engines: GP7200 (left), manufactured by General Electric Aviation and Pratt & Whitney [saf, 2010]; GE90 (right), manufactured by General Electric Aviation and Snecma (Groupe SAFRAN) [sta, 2010]

III.2 Dwell-Fatigue Effect

Flights of the civil planes generally present a few periods with different regimes, as shown in Fig.III.3: take-off and landing correspond to the higher stress and temperature levels, meanwhile descent produces very low regimes. The cruise itself does not show particular events. As a consequence, flights can be seen as LCF loading cycles, with loading/unloading transients and a hold period. High Cycle Fatigue is superimposed to this main cycles, due to the vibrations and the engine rotation, but LCF–HCF interaction will not be considered in our approach.

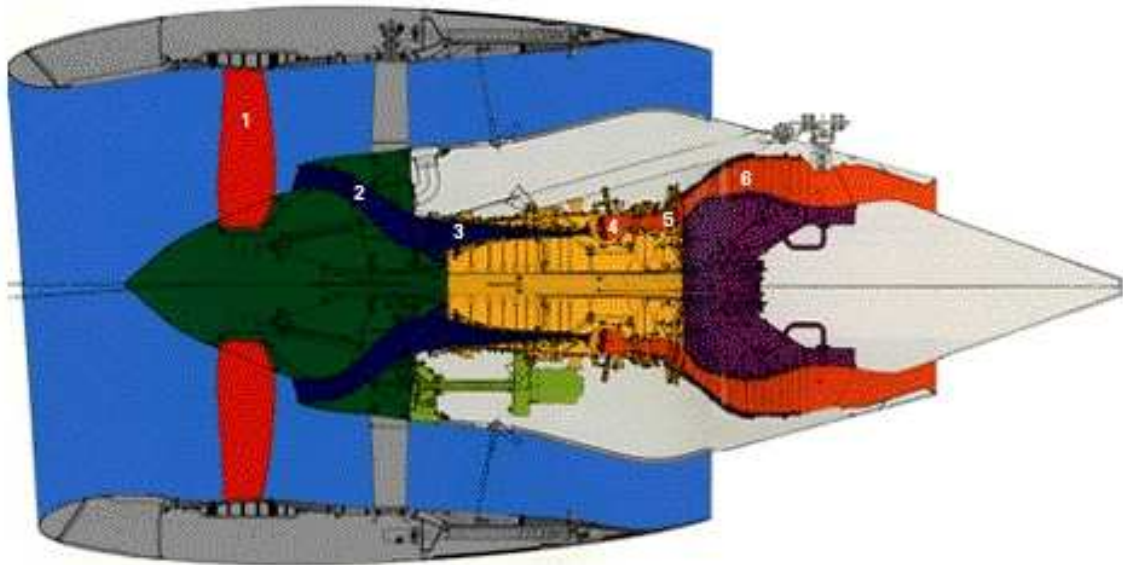


Figure III.2 : The jet engine GE90 consists of: 1. Composite fans, 2. Low Pressure Compressor (LPC) / Booster, 3. High Pressure Compressor (HPC), 4. Dual Dome Combustor, 5. High Pressure Turbine (HPT), 6. Low pressure Turbine (LPT) [sta, 2010]

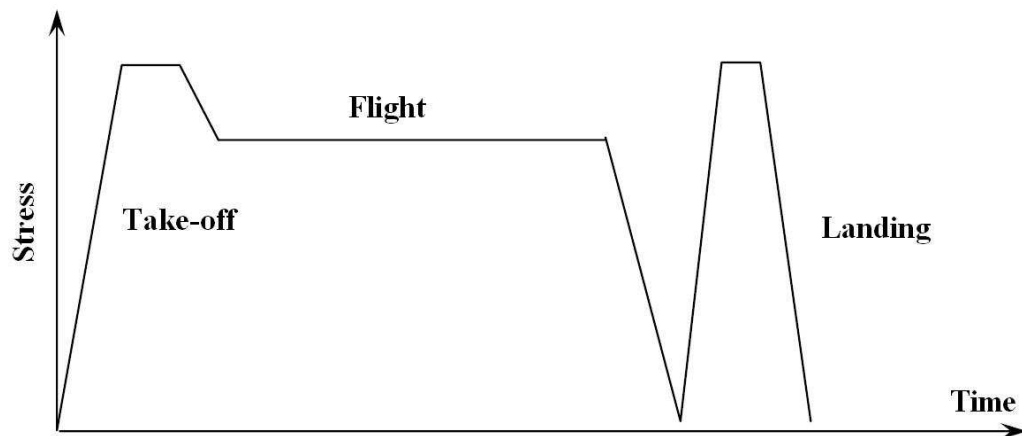


Figure III.3 : Simplified load history during a flight

1) **Influence of hold time duration.** Several sources in the literature have demonstrated that the presence of a hold time in a fatigue test has a drastical effect on the life of the specimen. Authors use cycles including a dwell period varying between two [Jousset, 2008] and five [Bache, 2003] minutes (see Fig.III.4). Cabocel's results [Cabocel, 2004] in the same alloy show that there is a life reduction for increasing hold time, with a saturation at 40 seconds (Fig.III.5 (a)). This conclusion is supported by another source [Bache et al., 1997] in Fig.III.5 (b), where the material IMI834 is considered. The saturation is obtained at around 120 seconds.

2) Influence of mean stress. Dwell effect is strongly affected by mean stress demonstrated for Timetal 834 in Fig.III.6 [Evans, 1998]. For $R = -0.5$ the number of cycles to failure is extended, even if the stress amplitude is greater than in the case of $R = 0.1$ or $R = 0.5$.

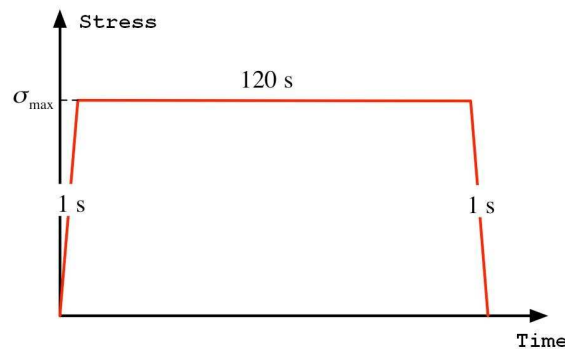


Figure III.4 : An example of dwell-fatigue test [Jousset, 2008]

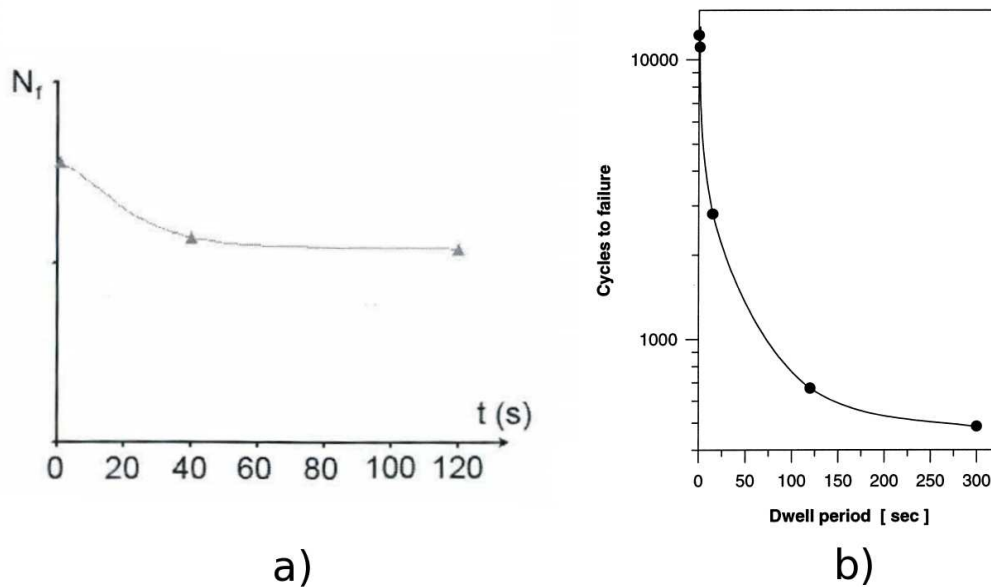


Figure III.5 : Cycles to failure in dwell tests with different hold periods of time (a) [Cabocel, 2004] and (b) [Bache et al., 1997]

3) Influence of temperature. Concerning temperature effect, Stubbington and Pearson's study shows that fatigue crack growth rate in Ti-6Al-4V is larger at 20°C than at a higher temperature and becomes negligible at about 70°C in Fig.III.7. They demonstrated that the introduction of a dwell period does not produce any increase in growth rate at 125 and 100°C . There was a small increase in rate at 75°C , a larger one at 50°C , and a substantial one at 40°C , although at this temperature the rate was still less than at 20°C [Stubbington and Pearson, 1978]. Evans and Gostelow's work on IMI685 demonstrates that the dwell effect remains up to 425 K [Evans and Gostelow, 1979]. It can then be

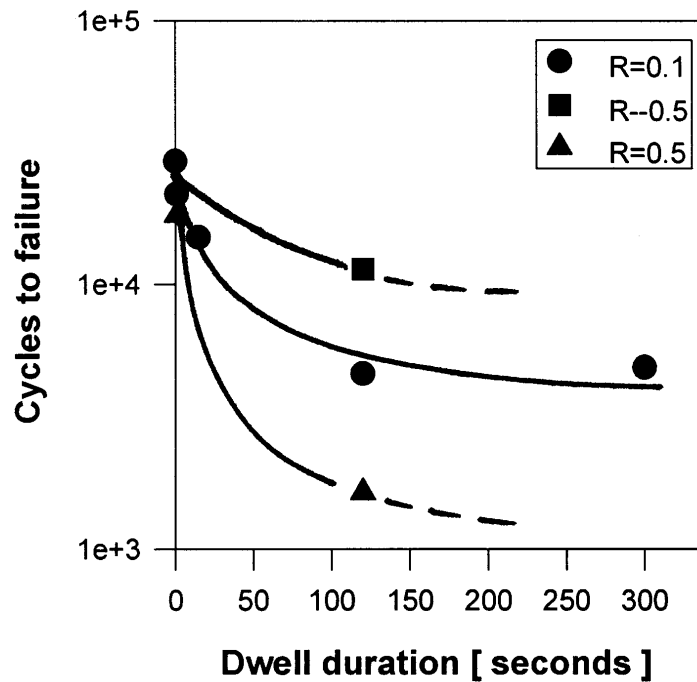


Figure III.6 : Effect of R value on dwell life Timetal 834 [Evans, 1998]

concluded that the effect is present in several alloys, and that the intensity of the effect changes from one alloy to the other.

4) Influence of environment. The review of the main articles and conclusions concerning the environmental effects can be found in [Lefranc, 2007]. Especially an influence of hydrogen level on the alloy Ti-6242 was considered in detail. In this work mechanisms of deformation, damage, crack initiation and hydrogen effect have been considered to understand the influence on dwell-fatigue, fatigue and cracking in Ti-6242. The author shows that the increase of hydrogen level in the material improves lifetime in dwell and fatigue tests due to a higher elasticity level but he also acknowledge the fact that this can not be explained by the presence of this chemical element in the alloy. In tensile tests this effect depends on strain rate and it can be similar to the previous case or opposite. In addition, it seems that the environment influences a little bit the crack resistance in dwell tests and it does not influence the behaviour in fatigue regime.

In conclusion, environmental effects, as means to influence the behaviour at RT, are discarded for Ti-6242 forged in the domain β .

5) Influence of loading mode. The reduction in lifetime for dwell-fatigue tests compared to pure fatigue ones, especially at RT is studied in [Lefranc, 2007] and [Sinha et al., 2004]. The failure modes and fractographic features under static monotonic loadings, normal fatigue and dwell fatigue tests are quite different. The comparison made for two different maximal stress levels indicates that the difference in terms of number of cycles between fatigue and dwell tests is lower for lower maximum stress [Sinha et al., 2004], [Kassner et al., 1999]. There is also a marked transition in the failure mechanism originating from cyclic-damage and from static damage, when the applied stress increases (4% of the yield strength). Moreover, a higher plastic strain to failure was observed at a higher stress for both fatigue and dwell-fatigue loadings. At a high maximum stress, the dwell-

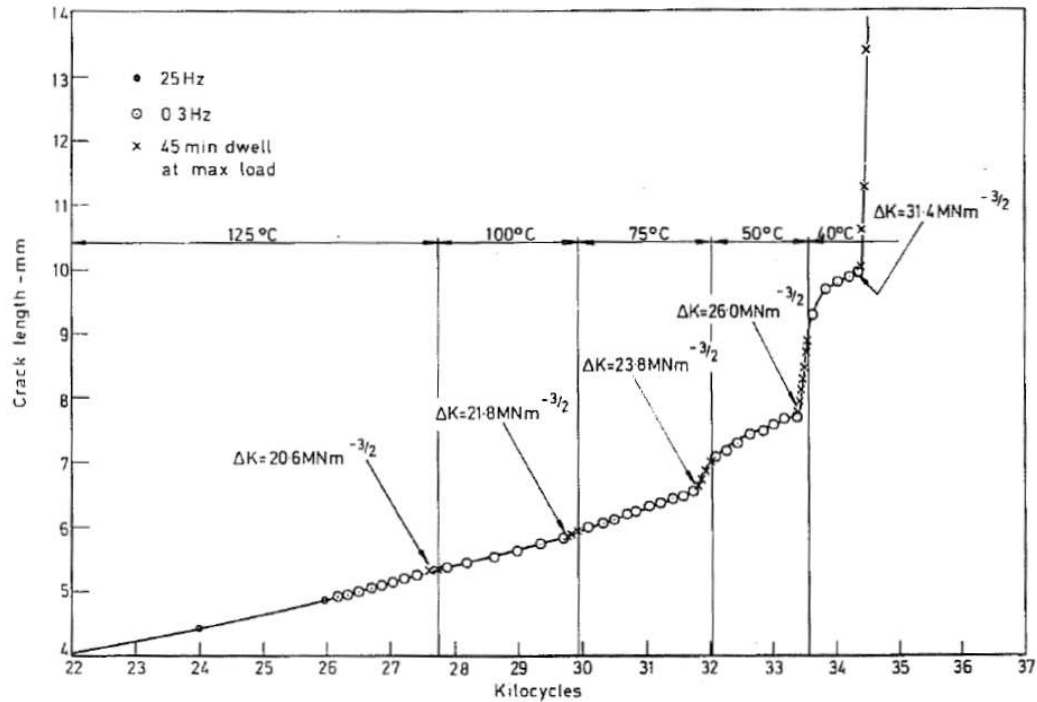


Figure III.7 : TL orientation test piece CP5A, cut from 57 mm thick annealed Ti-6Al-4V. Fatigued at 0.3 Hz and with 45 min dwell at maximum load at 125, 100, 75, 50 and 40°C. Crack growth curve. [Stubbington and Pearson, 1978]

fatigue crack initiation is faceted, with little evidence of ductility. On the other hand, the normal fatigue crack-initiation site shows evidence of local plasticity. At a lower maximum stress, the dwell-fatigue crack-initiation site is again faceted and the normal fatigue one also represents faceted features [Sinha et al., 2004]. It has been concluded that the fatigue life is governed more by the slow damage evolution than by the sudden nucleation of cracks [Toubal et al., 2009].

III.3 Material Microstructure: Crystallography

The studied titanium alloy Ti-6242 forged in the domain β is made up of two phases: α and β .

α -titanium single crystals are hexagonal close-packed crystals (HCP). The potentially active slip systems are shown in Fig. III.8 (a) [Venkataramani et al., 2008]. They consist of 1) Basal slip systems; 2) Prismatic systems; 3) Pyramidal $\langle a \rangle$ slip systems; 4) First-order pyramidal $\langle c + a \rangle$ slip systems; and 5) Second-order pyramidal $\langle c + a \rangle$ slip systems. In titanium alloys, pyramidal slip systems are observed [Feugas and Clavel, 1997], [Deka et al., 2006], [Hasija et al., 2003]. Six first-order pyramidal slip systems ($10\bar{1}1$)($\langle c + a \rangle$) and 6 second-order pyramidal slip systems ($\bar{1}2\bar{1}2$)($\langle c + a \rangle$) can also be activated, as the alloy does not have a high percentage of oxygen (0.15%) [Zaefferer, 2003] and [Bridier et al., 2005]. The less oxygen in the alloy, the less τ_{CRSS} [Naka et al., 1988].

In this work, the phase β must be taken into account, since its amount in is 20%. Due to its different behaviour (in [Feugas, 1994], it is assumed to be harder

than α phase), it will influence the global material behaviour. For instance, the susceptibility of Ti-6242 to dwell effect increases when the fraction of primary alpha becomes larger [Kassner et al., 1999]. Also, at small applied plastic strain, it seems that the plastic deformation is mostly in the soft α -phase (HCP), the hard β -phase (BCC) staying in its elastic domain [Feugas and Clavel, 1997], [Saleh and Margolin, 1979].

β -titanium single crystals are body-centered cubic (BCC). Their potentially active systems are shown in Fig. III.8 [Venkataramani et al., 2008] with the following families of active slip systems: 1) (110); 2) (112); 3) (123).

All slip systems and directions are briefly described in Appendix A.1 and in Fig.A.1 [Karthikeyan et al., 2006].

Ti-6242 forged in the domain β alloy contains a lot of colonies formed by periodically repeated HCP and BCC crystals. The $\alpha+\beta$ colonies consist of secondary α and β phases arranged in lamellar structures with twelve crystallographically admissible variants for the transformation from the β phase to the α phase [Mills et al., 1998]. The crystallographic relationship between the secondary α and β laths are defined by Burger's orientation relation (BOR) $((101)_\beta // (0001)_\alpha$ and $\langle 111 \rangle_\beta // \langle 1120 \rangle_\alpha$), as shown in Fig. III.9 [Zhang et al., 2007], [Bridier et al., 2005], Fig.III.10 [Delfosse, 2005], [Savage et al., 2004] and in Tab. III.1. Burger's relationship may be critical enough for calculations, as it was shown in [Lebensohn and Canova, 1997]. The variants which can be distinguished by means of electron diffraction are shown in [Furuhara and Maki, 2001].

Variants	Parallel slip planes	Parallel slip directions (1)	Parallel slip directions (2)
1	$(110)_\beta // (0001)_\alpha$	$[\bar{1}\bar{1}\bar{1}]_\beta // [11\bar{2}0]_\alpha$	$[\bar{1}12]_\beta // [\bar{1}100]_\alpha$
2	$(110)_\beta // (0001)_\alpha$	$[1\bar{1}\bar{1}]_\beta // [11\bar{2}0]_\alpha$	$[\bar{1}\bar{1}2]_\beta // [\bar{1}100]_\alpha$
3	$(\bar{1}\bar{1}0)_\beta // (0001)_\alpha$	$[1\bar{1}\bar{1}]_\beta // [11\bar{2}0]_\alpha$	$[112]_\beta // [\bar{1}100]_\alpha$
4	$(\bar{1}\bar{1}0)_\beta // (0001)_\alpha$	$[111]_\beta // [11\bar{2}0]_\alpha$	$[\bar{1}\bar{1}2]_\beta // [\bar{1}100]_\alpha$
5	$(011)_\beta // (0001)_\alpha$	$[1\bar{1}\bar{1}]_\beta // [11\bar{2}0]_\alpha$	$[\bar{2}1\bar{1}]_\beta // [\bar{1}100]_\alpha$
6	$(011)_\beta // (0001)_\alpha$	$[\bar{1}\bar{1}\bar{1}]_\beta // [11\bar{2}0]_\alpha$	$[21\bar{1}]_\beta // [\bar{1}100]_\alpha$
7	$(0\bar{1}\bar{1})_\beta // (0001)_\alpha$	$[\bar{1}11]_\beta // [11\bar{2}0]_\alpha$	$[211]_\beta // [\bar{1}100]_\alpha$
8	$(0\bar{1}\bar{1})_\beta // (0001)_\alpha$	$[111]_\beta // [11\bar{2}0]_\alpha$	$[\bar{2}\bar{1}\bar{1}]_\beta // [\bar{1}100]_\alpha$
9	$(101)_\beta // (0001)_\alpha$	$[\bar{1}\bar{1}1]_\beta // [11\bar{2}0]_\alpha$	$[\bar{1}\bar{2}1]_\beta // [\bar{1}100]_\alpha$
10	$(101)_\beta // (0001)_\alpha$	$[1\bar{1}\bar{1}]_\beta // [11\bar{2}0]_\alpha$	$[\bar{1}21]_\beta // [\bar{1}100]_\alpha$
11	$(\bar{1}01)_\beta // (0001)_\alpha$	$[1\bar{1}\bar{1}]_\beta // [11\bar{2}0]_\alpha$	$[121]_\beta // [\bar{1}100]_\alpha$
12	$(\bar{1}01)_\beta // (0001)_\alpha$	$[111]_\beta // [11\bar{2}0]_\alpha$	$[\bar{1}2\bar{1}]_\beta // [\bar{1}100]_\alpha$

Table III.1 : Variants of the Burgers Orientation Relationship between β (BCC) and α (HCP).

Tab.III.2 summarizes Euler's angles that define a rotation to pass from BCC crystal to HCP crystal network. In HCP crystal, the axis $[11\bar{2}0]_\alpha$ is chosen to be a_1 , $[\bar{2}110]_\alpha$ is a_2 and $[\bar{1}\bar{2}10]_\alpha$ is a_3 . These rotations are considered to find β subdomains from initial α grains which will be randomly oriented. In our case, the axis $a_1 = [\bar{1}2\bar{1}0]_\alpha$, $a_2 = [\bar{1}\bar{1}20]_\alpha$ and $a_3 = [2\bar{1}\bar{1}0]_\alpha$.

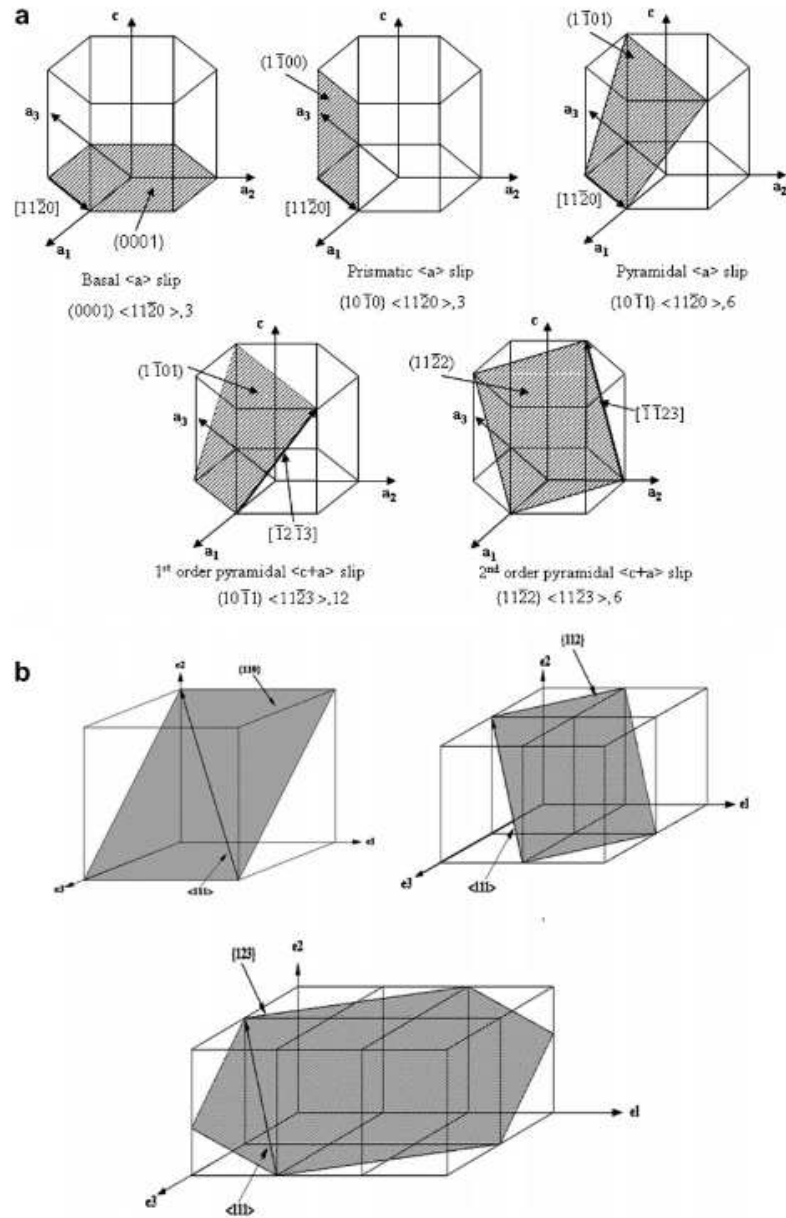


Figure III.8 : Schematic diagrams showing (a) the nonorthogonal basis and slip systems in a HCP crystal and (b) the orthogonal basis and slip systems in BCC crystals [Venkataramani et al., 2008]

A schematic illustration showing the relative orientation of the loading axis and the different slip systems is demonstrated in Fig.III.11 [Salem and Semiatin, 2009]. There is also only a slight disorientation between α and β phases (about 5.96° rotation about the c -axis and 0.78° about a -axis Fig.III.10 [Savage et al., 2004], [Mills et al., 1998]. In order to simplify the representation of angles they are assumed to be equal to -5.96° 44.22° 0° (ϕ_1 (α), Φ (β), ϕ_2 (γ)).

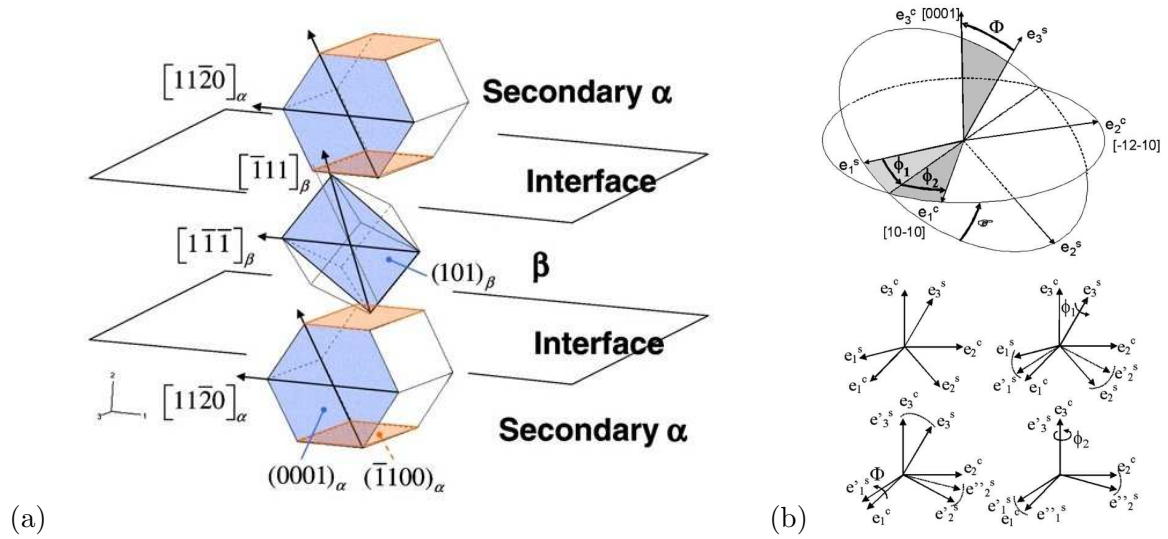


Figure III.9 : (a) Lamellar orientation relationships (variant 9 from Tab. III.1 where $[1\bar{1}\bar{1}] = [\bar{1}11]$) [Zhang et al., 2007]; (b) Euler's angles [Bridier et al., 2005].

III.4 Effects of Alloying Elements

In the following Tab.III.3 the effects of alloying elements are explained for Ti-6242 forged in the domain β :

1) **Aluminum** is a principal α stabilizer in titanium alloys that increases creep strength and Young's modulus. It can not exceed 6% of Al because above this limit, embrittlement can appear. That is why aluminum content of all titanium alloys is usually below 7 % [Han, 1990].

2) **Tin** has extensive solid solubilities in both α and β phases and this element is often used as a solid solution strengthener with aluminum in order to reach high strength without embrittlement. Tin is a less α stabilizer than aluminum, but decreases the rate of transformation in phases [Han, 1990].

3) **Zirconium** forms a continuous solid solution with titanium and increases strength at low and intermediate temperatures. This element is a weak β stabilizer. It is used below 5 to 6% to avoid a reduction in creep strength and ductility. Zirconium reduces the rate of transformation [Han, 1990].

4) **Molybdenum** is an important β stabilizer that promotes hardenability, short-time elevated-temperature strength, but reduces long-term elevated-temperature. This element can make welding more difficult [Han, 1990].

5) **Niobium** is a β stabilizer that is included to improve oxidation resistance at high temperatures [Han, 1990].

6) **Iron** is a β stabilizer that tends to decrease creep strength [Han, 1990].

7) **Carbon** is an α stabilizer that can enlarge the temperature interval between the α transus and the β transus [Han, 1990].

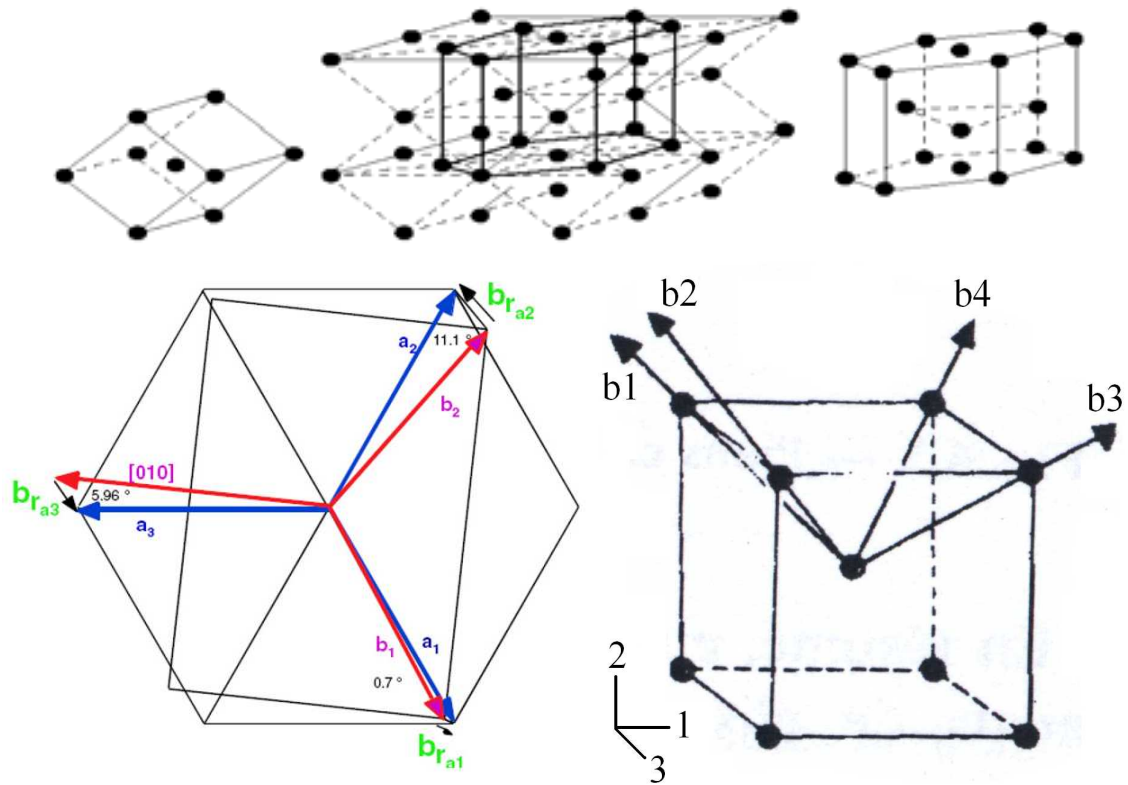


Figure III.10 : Burger's orientation relationship [Delfosse, 2005], [Savage et al., 2004]. Burger's vectors in BCC crystal [Jaoul, 2008].

There are several types of titanium alloys: 1) α alloys; 2) $\alpha + \beta$ alloys and 3) β alloys.

1) α alloys contain elements such as aluminum and tin. Due to aluminum and tin, they usually have a better creep resistance than beta alloys and are used at high temperatures. The absence of a ductile-to-brittle transition makes alpha alloys useful for a large number of applications. α alloys have very good strength, weldability, toughness, but worse forgeability than β alloys [Han, 1990], and they cannot be strengthened by heat treatment.

2) $\alpha + \beta$ alloys have compositions that allow a mixture to form between α and β phases at RT. They may include between 10 and 50 % of β phase at RT. Generally $\alpha + \beta$ alloys have a good formability [Han, 1990].

3) The last group of titanium, β alloys, usually contains transition elements such as molybdenum, niobium and vanadium which tend to decrease the transus temperature of the α to β phase change and develop large amount of the BCC β phase. They have an excellent forgeability in a wide range of temperatures. They also have excellent hardenability, and respond very well to heat treatment [Han, 1990].

In contrast to $\alpha + \beta$ alloys, β alloys do not transform martensitically during quenching process. The α phase can be precipitated from the metastable β phase as very fine particles (platelets). The main characteristic of β alloys is that they can be hardened to much higher yield stress levels than $\alpha + \beta$ alloys. Another great feature of β alloys is that they can be

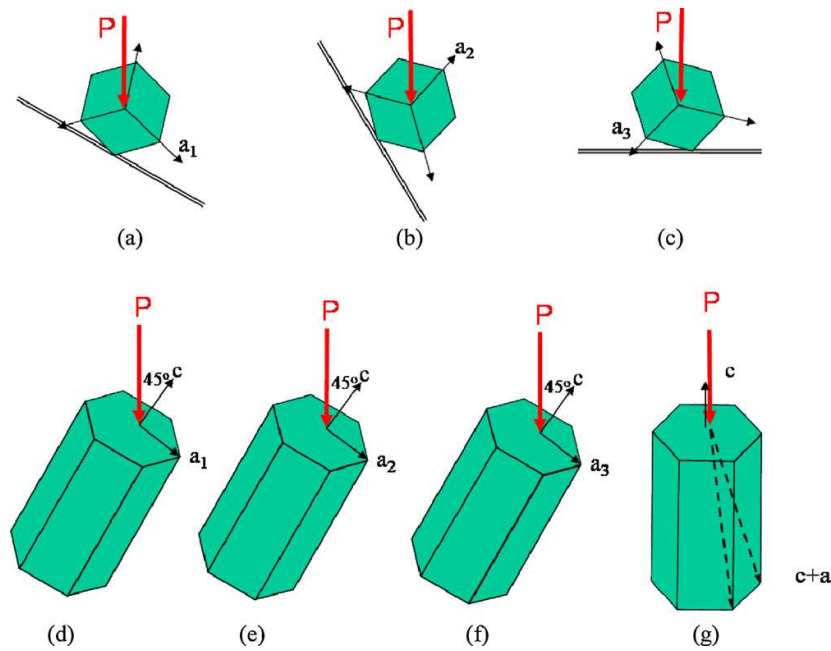


Figure III.11 : Schematic illustration showing the relative orientation of the loading axis and the different slip systems:(a-c) prism $\langle a \rangle$ slip, (d-f) basal $\langle a \rangle$ slip, and (g) pyramidal $\langle c+a \rangle$ slip. The double line in a-c represents ex-grains β [Salem and Semiatin, 2009]

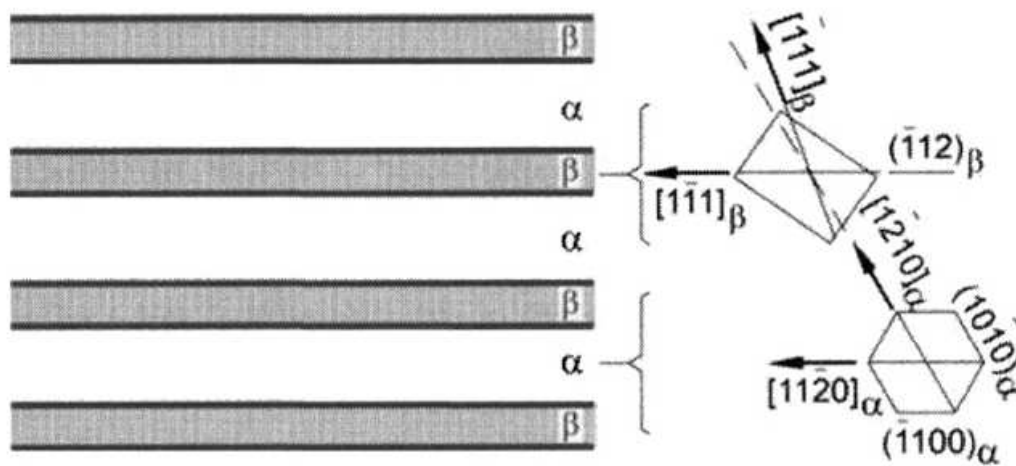


Figure III.12 : Crystallographic relationships in lamellar colonies [Lutjering and Williams, 2003]

processed at lower temperatures than $\alpha + \beta$ alloys. The corrosion resistance of β alloys is equal to or better than that of $\alpha + \beta$ alloys [Lutjering and Williams, 2003].

TI-6AL-2SN-4ZR-2MO forged in the domain β has got the chemical composition given in the following Tab. III.4 [Toubal et al., 2009] and the data from Snecma.

Adding alloying elements will result in property changes. The main effect is to affect the α - β transus transformation temperature. Some elements stabilize the α crystals and others

Variants	Slip plane	Slip direction	ϕ_1 (α) (z)	Φ (β) (x)	ϕ_2 (γ) (z)	Direction in Fig.III.10 [Jaoul, 2008]
1	(110)	$[\bar{1}\bar{1}\bar{1}]$	134.22°	-90°	-84.22°	1
2	(110)	$[\bar{1}1\bar{1}]$	134.22°	90°	84.22°	2
3	($\bar{1}$ 10)	$[1\bar{1}\bar{1}]$	45.78°	90°	95.96°	4
4	($\bar{1}$ 10)	$[11\bar{1}]$	45.78°	-90°	-95.96°	3
5	(011)	$[1\bar{1}\bar{1}]$	-5.96°	135.78°	0°	4
6	(011)	$[\bar{1}\bar{1}\bar{1}]$	5.96°	-44.22°	0°	1
7	(0 $\bar{1}$ 1)	$[\bar{1}1\bar{1}]$	0°	45.78°	5.96°	2
8	(0 $\bar{1}$ 1)	$[11\bar{1}]$	0°	-134.22°	-5.96°	3
9	(101)	$[\bar{1}\bar{1}\bar{1}]$	90°	-135.78°	-5.96°	2
10	(101)	$[1\bar{1}\bar{1}]$	90°	44.22°	5.96°	4
11	(10 $\bar{1}$)	$[1\bar{1}\bar{1}]$	90°	135.78°	-5.96°	1
12	(10 $\bar{1}$)	$[11\bar{1}]$	90°	-44.22°	5.96°	3

Table III.2 : Euler's angles for HCP crystal

Alloying element	Range (approx), wt %	Effect on structure
Aluminum	5.50 - 6.50	α stabilizer
Tin	1.80 - 2.20	α stabilizer
Zirconium	3.60 - 4.40	α and β strengthener
Molybdenum	1.80 - 2.20	β stabilizer
Vanadium	0.05	β stabilizer
Chromium	0.05	β stabilizer
Copper	0.05	β stabilizer
Silicon	0.06 - 0.10	Improves creep resistance

Table III.3 : Ranges and effects of some alloying elements used in titanium [Han, 1990]

Element	Ti(%)	Al(%)	Zr(%)	Mo(%)	Sn(%)
Base		5.50 - 6.50	3.60 - 4.40	1.80 - 2.20	1.80 - 2.20
	Si(%)	Mn(%)	Fe(%)	Cu(%)	C(%)
	0.06 - 0.10	0.05	0.5*Si	0.05	0.05
	O2(%)	N2(%)	H2(%)	Y(%) and B(%)	Other elements(%)
	0.15	0.05	0.0100	0.0050	0.20 (by 0.05)

Table III.4 : Chemical composition of Ti-6242 forged in the domain β (Sneema database)

stabilize the β crystals by decreasing the α - β transformation temperature. Aluminum is primarily an α stabilizer. Other alloying elements that support α structure include germanium, gallium, carbon, oxygen and nitrogen [Han, 1990].

III.5 Forging Process and Thermal Heat Treatment

Ti-6242 forged in the domain β can be treated in several ways. The scheme of a classical process for discs, including forging and heat treatment is shown in Fig.III.13.

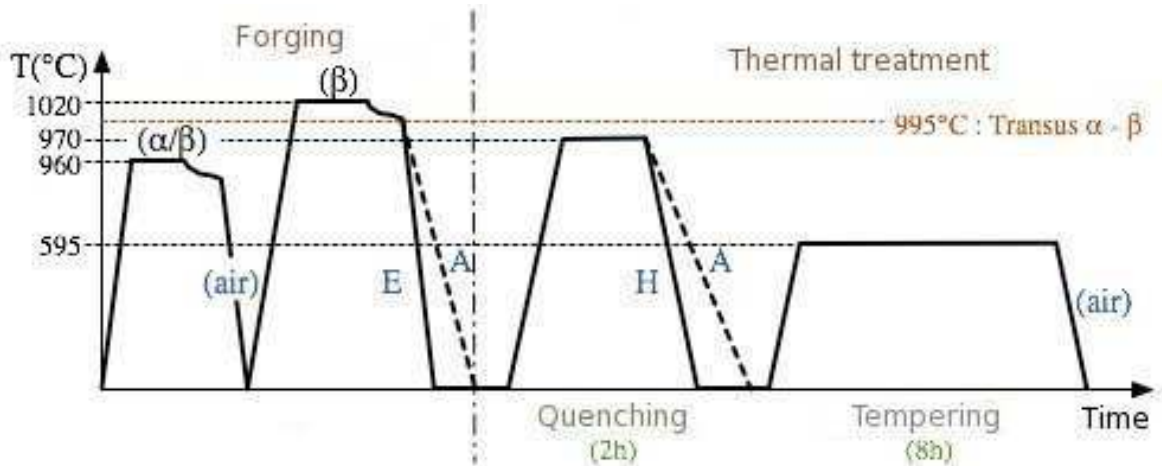


Figure III.13 : Forging and thermal heat treatment processes [Jousset, 2008]

1. Forging. The first stage of the forging process is the same for all the processes. It is conducted in the domain $\alpha - \beta$ (maximal temperature equal to 960 °C). At this temperature the alloy may start transforming. The material is then cooled down in air. The second stage of the forging process is made in the domain β at 1020 °C above the β transus temperature. After this forging process the disc can be cooled down in the air or in water.

2. Heat treatment. The disc is submitted to a solutionizing operation at 970°C for two hours. The disc, which was cooled down in air during the forging process, is also cooled down in air during quenching. Those that have been water cooled at the end of the forging process are then oil quenched. The last heat treatment governs the microstructure parameters that are critical for the present study.

Finally, thermal heat treatment ends by a tempering period of 8 hours at 595°, followed by the cooling down in air [Jousset, 2008].

III.6 Microstructural Morphologies

Three distinct microstructures, namely equiaxed, elongated and with colonies can be classically obtained. Equiaxed and elongated microstructures are related to $\alpha + \beta$ forging domain, whereas colonies are obtained in the β forging domain. They are presented in Fig.III.14 [Shen et al., 2004], [McBagonluri et al., 2005].

– Material 1 has got a near α duplex microstructure with equiaxed α grains distributed in a matrix of transformed β phase. This $\alpha + \beta$ annealed (or mill-annealed) material consists of equiaxed primary α grains (light phase) with a fine acicular α phase in a transformed β

matrix (dark phase).

– Material 2 has got a duplex α/β microstructure, consisting of elongated primary α grains in a continuous β matrix.

– Material 3 has got needles or laths of the α phase in the β phase.

In all the cases, fatigue tests produce surface and subsurface crack nucleation. Dwell-fatigue crack growth rates are faster in the equiaxed and elongated microstructures than in colony microstructures. The colony microstructure has lower peak values of acoustic emission data (counts versus time, energy versus rise time) than observed in the elongated and equiaxed microstructures [McBagonluri et al., 2005]. It can thus be concluded that a colony microstructure is the most convenient to minimize dwell effects, provided the grains are not too large.

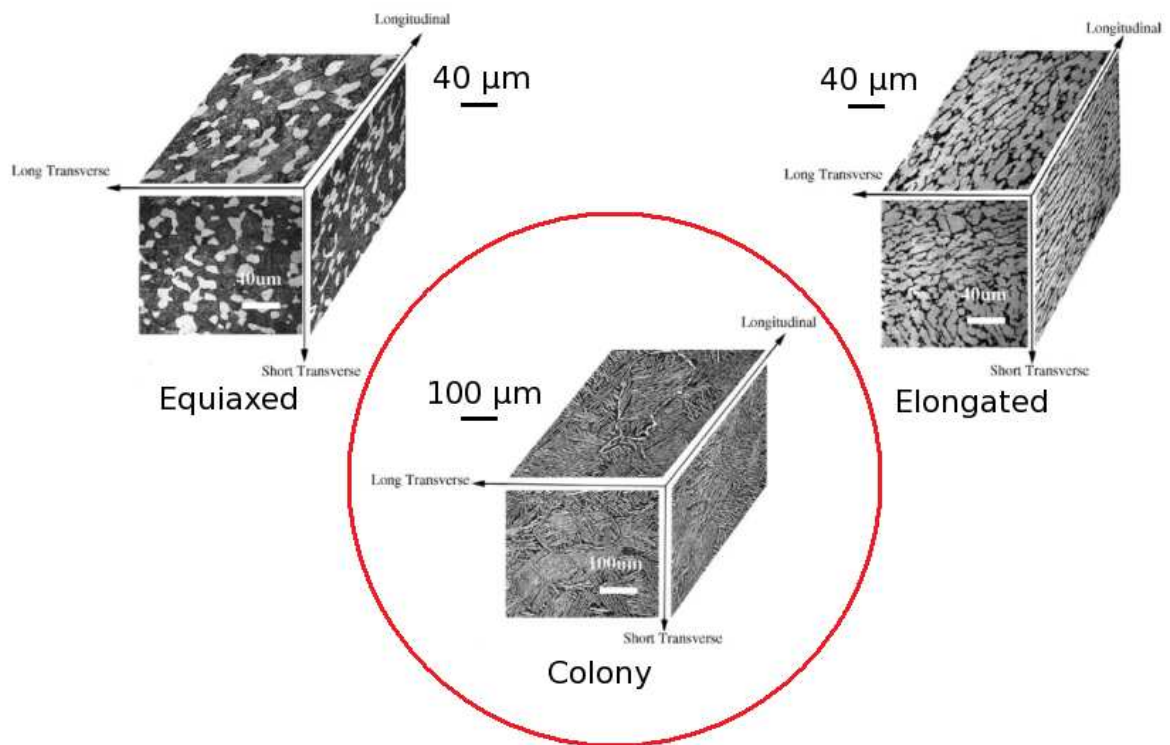


Figure III.14 : Ti-6242 microstructural morphologies: a) material 1, equiaxed microstructure, b) material 2, elongated microstructure, c) material 3, colony microstructure [McBagonluri et al., 2005], [Shen et al., 2004]

III.7 General Mechanical Properties

Mechanical properties depend on the microstructure of the alloy. Classical values of the basic properties are reported in Tab.III.5.

Temperature °C	Ultimate tensile strength, MPa	0.2 % yield strength, MPa	Elongation %	Reduction in area, %
20	1025	920	15	35
150	870	720	-	-
480	750	565	-	-
	Hardness	Modulus of elasticity, GPa	Poisson's ratio	
20	32 HRC	121	0.3	

Table III.5 : Mechanical properties of Ti-6242 forged in the domain β [Jousset, 2008] and [Han, 1990]

III.8 Barstock and Forged Compressor Disc

Facets on rupture surfaces are often found to have a near basal plane orientation. They are then the result of the separation on the slip plane [Evans and Bache, 1994], [Davidson and Eylon, 1980].

In [Bache et al., 1997] and [Bache, 1999], it is observed that rolling operation can destroy the original grain structure and that it is not the case in forged materials. Textures are then strongly dependent on the process. Thus the best solution for studying a realistic material is to cut the specimens from a forged disc. In these conditions, the role of weak zones and the related stress redistribution can be representative of the operating conditions [Evans, 1998].

In Fig.III.15 the role of weak links are considered in Timetal 834 data for barstock and forged compressor disc with the same $\alpha + \beta$ heat treatment by getting about 15% of primary α in a transformed beta matrix. It is revealed that the disc material is highly sensitive to dwell loading and the barstock is much less sensitive. That fact ensues because the redistribution process acts in a different way, if the structure remains intact or broken up [Evans, 1998].

III.9 Texture and Scatter Effects

After processing titanium alloys there is a development of crystallographic texture. It influences the behaviour of the material, its isotropy. If the crystallographic texture is altered so that its most critical directions do not match the most dangerous loading direction in components, it is possible to develop a more convenient industrial design approach [Evans et al., 2005].

In Fig.III.16 (textures of Ti-6Al-4V and Ti550) and Fig.III.17 the strain control results are primarily related to Ti-6Al-4V, as the texture measurements are based on the α phase and this alloy has rougher grains compared to Ti-550 [Evans et al., 2005]. It is evident that there is a relatively strong dependence on a crystallographic texture. In the titanium alloys

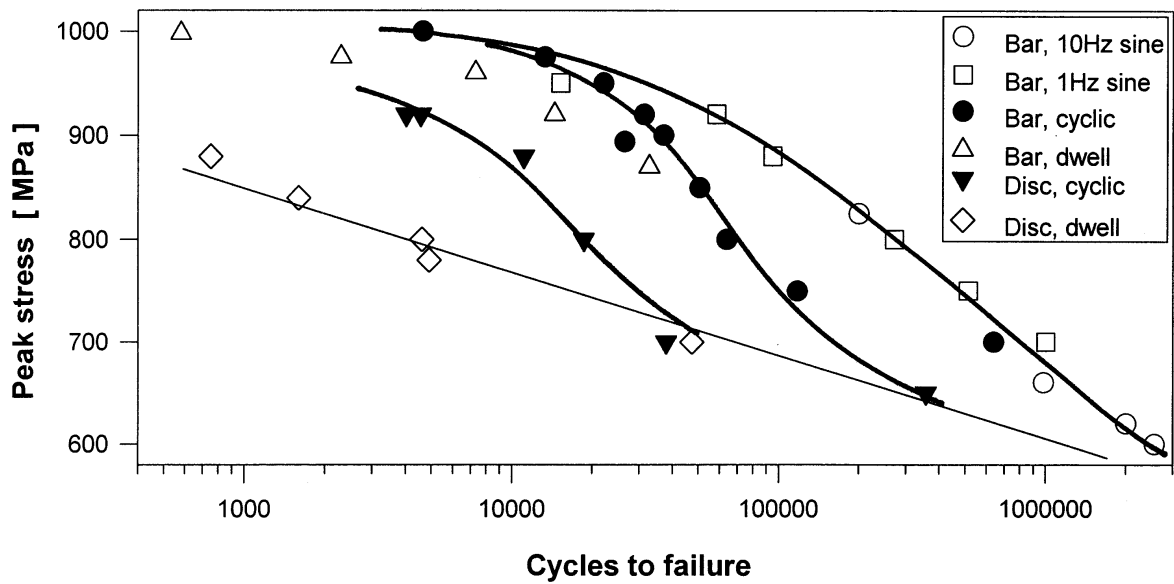


Figure III.15 : Cyclic and dwell fatigue data in Timetal 834 bar stock and disc material [Evans, 1998]

Ti-6Al-4V and Ti-550 processed in $\alpha + \beta$ domain the directions at 0° and 90° are more critical than 45° at RT. The authors in the article [Evans et al., 2005] conclude that fatigue crack initiation is controlled by the orientations of basal planes with regard to the direction of maximum shear stress.

It is important to remark in Fig.III.17 that there is a scatter effect between different crystallographic orientations and it is much less notable for the same crystal angle. This issue has been a concern regarding the aeronautical components in industry for decades, as the discrepancy is quite large to take it into account by modelling this aspect.

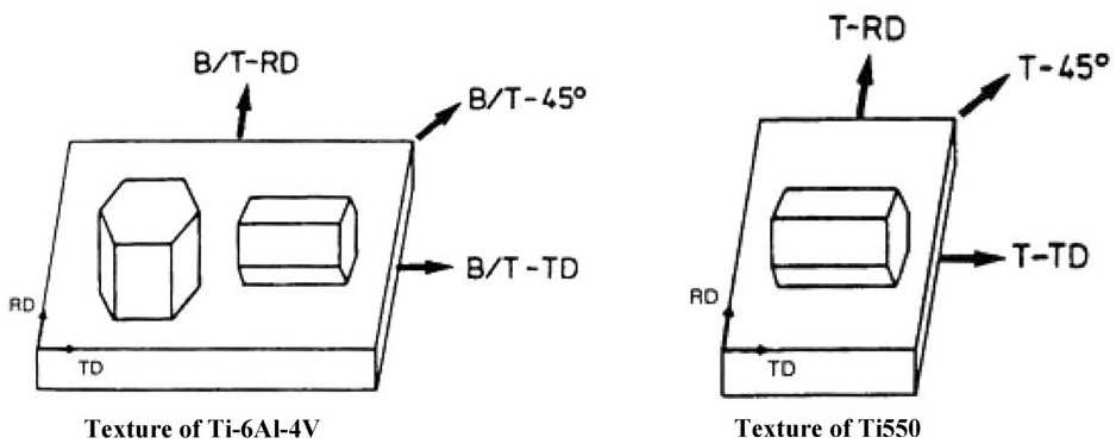


Figure III.16 : Textures of Ti-6Al-4V and Ti550 [Evans et al., 2005]

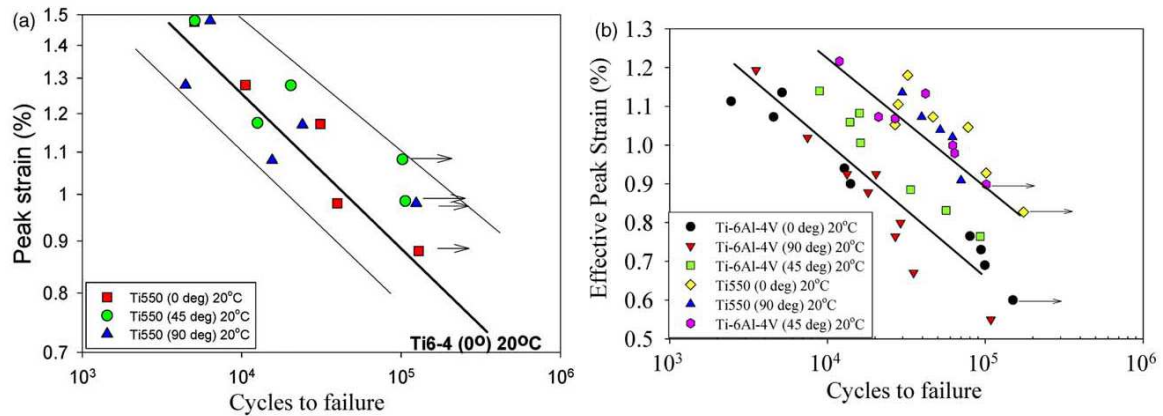


Figure III.17 : (a) Ti550 strain control results, tension. (b) Ti-6Al-4V and Ti550 strain control results, torsion [Evans et al., 2005]

III.10 Microstructure of Ti-6242 Forged in the Domain β

The microstructure of Ti-6242 forged in the domain β is highly heterogeneous (Fig.III.18 (Snecma database)), very complex and sensitive to the thermomechanical history. The specific lamellae structure is developed due to the forging velocities at different stages of heat treatment process. Texture becomes to be composed of different types of crystals, HCP (hexagonal close-packed), and BCC (body centred cubic). The relative amount of these phases is important because the increased susceptibility of Ti-6242 to load-controlled fatigue life with dwell at maximum load is attributed to larger volume fraction of primary α [Kassner et al., 1999].

According to the thermomechanical history of Ti-6242, one can obtain a distribution of grains having a relatively regular size in the material. In the same time, microstructures can exhibit very large zones with irregular crystal orientation. They have a millimetric size [Jousset, 2008], and look like “plumes”. Lamellae, situated in them, are several micrometers wide and 50–80 micrometers long. Microstructures including “plumes” seem to be more sensitive to dwell than others (Snecma and ENSMA database).

“Plumes” can have one or several domains with quasi-uniform crystal orientations. Triple domain “plumes” are also often observed in disc samples. It was noticed that sometimes there was a correlation between crystal and lamella orientations, sometimes not.

It can be seen in Fig.III.18 that α layers are still fairly continuous but have a pronounced wavy shape with only short straight segments. In other cases, α layers are broken up more into individual segments on most β grain boundaries with only a few long segments remaining on some boundaries. Despite of processing history, it is nearly impossible to completely avoid the α layers in β processed materials of high strength β alloys [Lutjering and Williams, 2003].

The arrangement of lamellas seem to be one of the most important features of the material. Their size depends mostly on the forging and heat treatment processes. The cooling velocities can vary if the alloy is cooled down in the air, water or oil. Lamellas can be without particular geometrical orientation, or with a preferred geometrical orientation – parallel or piercing each other. They may be in piles surrounded by β phase, they may present organised or disorganised patterns.

All these features contribute to the macroscopic behaviour of Ti-6242 forged in the domain β , as it is claimed that cracks develop in α colonies and that the crystallographic orientation of the colonies is a dominant factor for controlling fatigue life [Bache et al., 1998]. Fatigue crack propagation will occur along a path either traversing α lamellas or parallel to their long direction [Li et al., 2008].

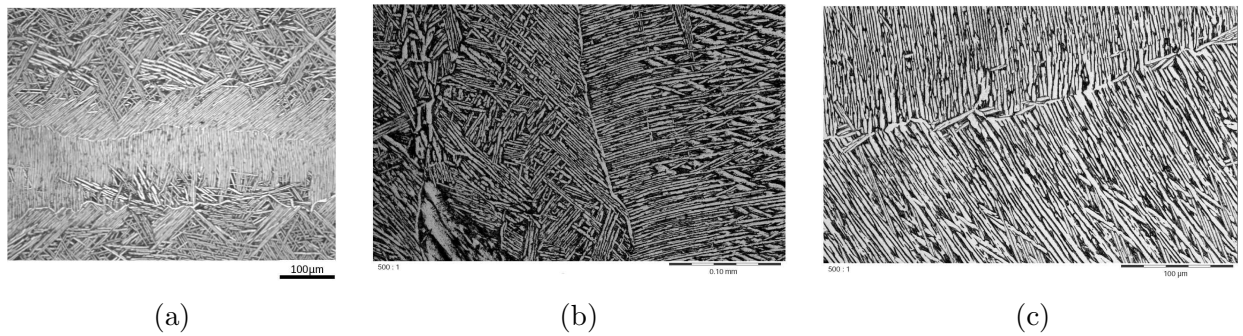


Figure III.18 : Microstructure with plume shaped grains (ENSMA-Snecma database)

In Fig.III.19 two locations, the bore and the web, are indicated from which specimens are cut out. In this thesis a special attention is paid to the web position, as the microstructure is rougher and more heterogeneous (a lot of “plumes”) compared to the bore location. The previously illustrated microstructures in this subsection are related to this spot. More information concerning the bore location is brought about in the thesis of [Baroumes, 1998].

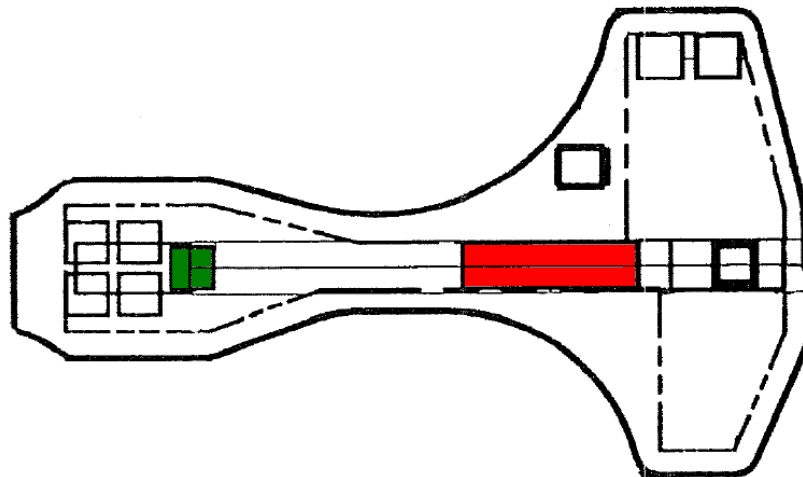


Figure III.19 : Two main locations of the microstructure in the non-manufactured disc, a green specimen on the left is in bore position and a red specimen on the right is in web one (Snecma database)

III.11 Main Causality of Dwell Effect

For a long period of time researchers try to define the main causes which are responsible for dwell effect. Until present time it is not clear, if there is a single set of parameters capable of describing it or several ones. At the present time some researchers are inclined to think that the microstructure plays the primary role in this phenomenon. In the article [Bache, 2003] the authors exemplify the titanium alloy Ti-6246 which is relatively insensitive to the dwell effect across the temperature range from -60° up to 150° . They attribute this quality to the excessive amount the β phase in the matrix of the alloy, as BCC crystals are more homogeneous compared to HCP and even HCP crystals in Ti-6246 are completely disorientated that means basal planes are distributed more randomly than in other titanium alloys. The hypothesis that the microstructure can be the most important factor in essence of the dwell effect is largely supported through this thesis.

Below some main conclusions concerning our studied titanium alloy in general are brought about from the following theses: [Feugas, 1994], [Lefranc, 2007] and [Jousset, 2008].

1) Feugas did not study the dwell effect directly but there are some important points which can be helpful for our work. He mentions that in the material, having α and β crystals, a percentage of each phase, a microstructure and internal stress are quite important factors and they have to be taken into account by modelling the behaviour of the titanium alloy. He also observes that α phase is more significant than β one and the modelling of it can explain the most part of effects but the interaction between them is important. He remarks that the heterogeneous nature of titanium alloys is essential to understand the behaviour of this kind of material.

These concise fragments from [Feugas, 1994] indicate the essential actions to be performed to model the behaviour of the titanium alloy: 1) both phases α and β have to be modelled by estimating the percentage of each phase; 2) basic coefficients must be quite precise for α crystals, as they are the most significant in the study; 3) microstructure has to be modelled in detail to much better understand heterogeneous nuances of our material.

2) Jousset studied the behaviour of Ti-6242-Si. She concentrates in her thesis on experimental data at high temperatures and microstructural analysis, especially dislocations. She observes that kinematic hardening is more important than isotropic one for this alloy, due to stress concentration and plastic flow. She notes that kinetics is slower at RT compared to high temperatures and there is an activation of all slip systems simultaneously.

Jousset mentions the presence of localized plasticity and even a complete arrest of the plastic flow in time and space on a mesoscopic scale at low temperatures. This effect induces static strain ageing. It may worsen dwell effect. This is the reason why our research is done at RT.

3) Lefranc studied an influence of different parameters, as microstructure, period of hold time in dwell tests, stress level, temperature, crack initiation and level of hydrogen on the behaviour of the alloy Ti-6242. This thesis is mainly an experimental one and Lefranc conducted a lot of different tests which are used in the present work.

Lefranc has found out that α phase and its percentage in the material is quite important and the longer the hold period of time, the shorter the lifetime. MET analysis demonstrates

that all slip systems are activated (basal, prismatic and pyramidal) and that pyramidal activation is the most important one, as slip bands are associated with this type of crystal planes. Prismatic slip activity remains low as basal and pyramidal one. Quasi-cleavage facets, surface initiating and surface-subsurface damage are observed simultaneously.

Lefranc states that damage intensity is more important in dwell tests than that in fatigue and the damage process appears to be in large misorientated colonies of lamellas. Internal cracks can reach several tens of micrometers. In the thesis the reason of cracking is associated to anisotropy of HCP and BCC crystals and Burger's vectors. Some cavities are also observed and they are attributed to the fact that the deformation mechanisms in two phases are quite different. Appearing cavities in the β phase are due to basal system slips in the α phase. It is important to note that the decrease of the number of cycles to failure is considered not to be so significant in this material compared to other alloys [Bache, 2003].

Lefranc remarks that the ratio between fatigue and dwell tests reaches 2 - 5 below the elasticity limit and 30 above it. In conclusion, tests on specimens demonstrate that the dwell effect is a combination of an early crack initiation and cracking which is faster than in fatigue experiments.

In his thesis Lefranc tried to simulate the cyclic behaviour of the titanium alloy and he identified the large difference in plastic zone between fatigue and dwell-fatigue tests. In our study a larger number of cycles in tests based on experimental data has been modelled and the accuracy is very good. It allows to make more correct conclusions about the causes of dwell effect.

III.12 Conclusions

The studied Ti-6242 forged in the domain β having the colony morphology is very heterogeneous material which is strongly affected by the dwell effect. In our work this titanium alloy is considered at RT, as this phenomenon is supposed to be worsened. Influence of environment is not taken into account because it can be discarded due to the fact that this factor does not appear to be the dominant in this occurrence.

Both phases α and β have to be modelled, as they are quite different in nature. One of them is constituted from hexagonal close-packed crystals and another is from body-centered cubic crystals. All main crystal slip systems ought to be incorporated into our model, as basal, prismatic and pyramidal for HCP and (101), (112) and (123) for BCC, because it is not known beforehand which slip system contributes to the behaviour of Ti-6242.

The microstructural features are quite important and it has to be modelled properly by simulating “plumes” and texture, where they can be responsible for scatter effect and stress/strain concentration.

Before calculating the microstructure of Ti-6242 forged in the domain β , residual stress in the forged disc must be calculated, as they can be the main cause of premature crack initiation (structural effect).

In the next chapters phenomenological models are presented to simulate the behaviour of titanium alloys.

L'alliage étudié Ti-6242 forgé dans le domaine β ayant la morphologie de colonie est la matière très hétérogène qui est fortement affectée par l'effet dwell. Dans notre travail cet alliage de titane est considéré à RT, puisque ce phénomène est censé être aggravé. L'influence d'environnement n'est pas pris en compte parce qu'elle peut être abandonnée en raison du fait que ce facteur n'a pas l'air d'être la dominante dans cet occurrence.

Les deux phases α et β doivent être modélisées, puisqu'elles sont tout à fait différentes. L'une est constituée des cristaux de la maille hexagonale et une autre est des cristaux de la maille cubique centrée. Tous les principaux systèmes doivent être incorporés dans notre modèle, comme basaux, prismatiques et pyramidaux pour HCP et (101), (112) et (123) pour BCC, parce qu'il n'est pas connu à l'avance quel système contribue le plus au comportement de Ti-6242.

Les caractéristiques microscopiques sont tout à fait importantes et elles doivent être modélisées correctement en simulant “des plumes” et une texture, où ils peuvent être responsables de l'effet de la dispersion et la concentration de la contrainte/déformation.

Dans les chapitres suivants les modèles phénoménologiques sont présentés pour simuler le comportement d'alliages de titane.

Chapter -IV-

Macroscopic Constitutive Equations

Contents

IV.1	Introduction	30
IV.2	Mechanical Behaviour of Ti-6242 at Room Temperature	30
IV.3	Mechanical Behaviour of Ti-6242 at Other Temperatures	31
IV.4	Presentation of a Phenomenological Material Model	37
IV.4.1	Constitutive Equations	37
IV.4.2	Model Calibration	38
IV.4.3	Numerical Prediction of Tensile, Cyclic and Creep Tests	39
IV.4.4	Conclusions	48

This chapter presents phenomenological constitutive equations that can be used to model the macroscopic behaviour of Ti-6242 from RT to high temperatures.

The experimental database provided by Snecma and ENSMA is carefully analysed.

A new approach is described.

The calibration strategy is used to get the material parameters where the approach is focused upon strain rates and temperature conditions.

A comparison with previously obtained results in the literature is made.

IV.1 Introduction

In this part results of tensile tests, LCF and cyclic creep tests for different applied stress amplitudes are given, a macroscopic mechanical model and its parameters calibration are proposed.

Results of LCF tests with a hold time, even of short duration at RT show drastical changes for both the stress-strain behaviour and number of cycles to initiation in Ti-6242 forged in the domain β . This is linked to a cyclic creep regime, leading to a gradual deformation on the one hand, and to a strong fatigue-hold time interaction that produces a reduction of the number of cycles to initiation on the other hand.

The lack of analysis of these phenomenon imply to use margins securely for the design of Ti-6242 components.

The fatigue behaviour of Ti-6242 has been studied across a large temperature range by [Baroumes, 1998] and [Lefranc, 2007]. In [Baroumes, 1998], the viscous effect has been taken into account, nevertheless the influence of this effect at RT (cyclic “cold creep”) has never been modelled. This is why we will perform this investigation and validate it describes the behaviour of Ti-6242 rightly.

IV.2 Mechanical Behaviour of Ti-6242 at Room Temperature

Two experimental databases are available at RT. The first one provided by Snecma and the second one by ENSMA. Snecma database is composed of tensile tests performed at a strain rate of $7.0 \cdot 10^{-4} s^{-1}$ and relaxation tests at different maximal stress level as shown in Tab.IV.1. In ENSMA database (see Tab.IV.2), tensile tests have been performed at a strain rate between $3.0 \cdot 10^{-5} s^{-1}$ and $2.0 \cdot 10^{-2} s^{-1}$. Some stress controlled fatigue tests with and without hold time have been performed by ENSMA for three stress levels A+70 MPa, A+40 MPa and A MPa under a stress ratio $R_\sigma = 0$. Note that these tests have been conducted until failure in order to obtain the number of cycles to failure at RT.

The stress/strain curves for both Snecma and ENSMA tensile tests for various strain rates are plotted in Fig.IV.1. A viscous effect appears due to the strain rate sensitivity.

A significant creep occurs at RT under stress controlled pure fatigue tests and under stress fatigue tests with the hold time of 120 s at maximal stress. The curves showing the maximal strain *versus* time resulting from cyclic tests are plotted in Fig.IV.2 for pure fatigue tests and in Fig.IV.3 for fatigue with hold time (dwell) tests.

Test (Sample)	$\dot{\epsilon}$ (s^{-1})
Tension (8/1)	$7.00 \cdot 10^{-4}$
Relaxation (19-1)	$\dot{\epsilon}_{650} = 1.50 \cdot 10^{-3}$
	$\dot{\epsilon}_{700} = 1.51 \cdot 10^{-3}$
	$\dot{\epsilon}_{750} = 1.56 \cdot 10^{-3}$

Table IV.1 : Snecma database at RT

Test (Sample)	$\dot{\epsilon}$ (s^{-1})	σ_{max} (MPa)
Tension (D2)	$8.0 \cdot 10^{-4}$	
Tension (D5)	$2.0 \cdot 10^{-4}$	
Tension (D8)	$2.0 \cdot 10^{-2}$	
Tension (D9)	$8.0 \cdot 10^{-3}$	
Tension (D11)	$3.0 \cdot 10^{-5}$	
Fatigue (D6)		A
Fatigue (D13)		A+40
Fatigue (D7)		A+70
Dwell (D15)		A
Dwell (D1)		A+40
Dwell (D4)		A+70

Table IV.2 : ENSMA database at RT

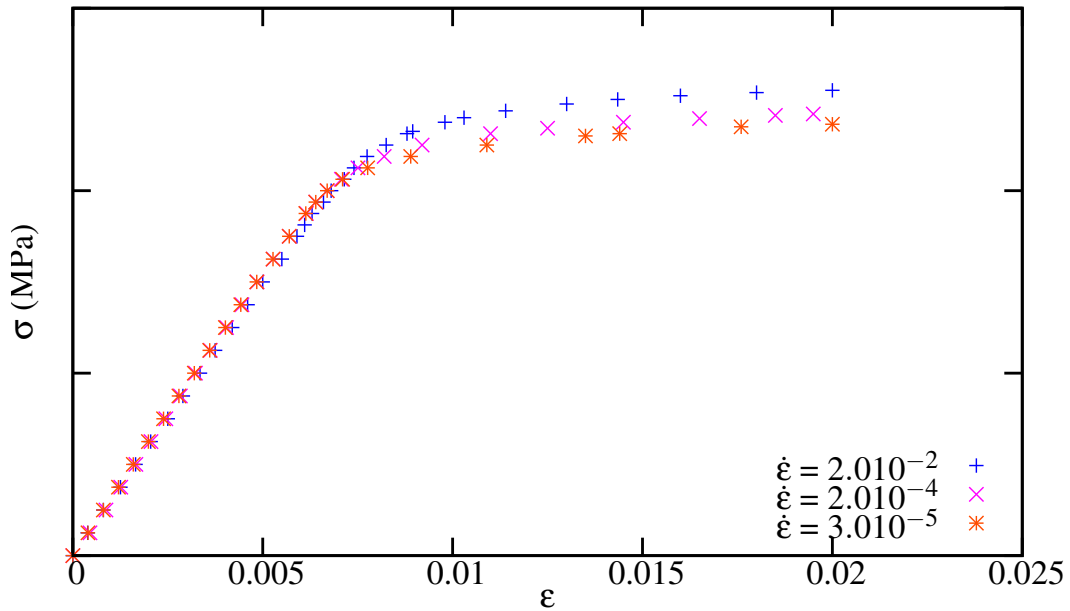


Figure IV.1 : Monotonic tensile tests for Ti-6242 at RT under various strain rates

IV.3 Mechanical Behaviour of Ti-6242 at Other Temperatures

The experimental database provided by Snecma is composed of tensile, LCF strain controlled tests, relaxation and creep tests. The database has been classified into two groups. The first group contains results at temperatures from 50°C to 200°C and consists of tensile tests performed at a strain rate of $7.0 \cdot 10^{-4} s^{-1}$ and of relaxation tests as shown in Tab.IV.4. The second group gathers tests from 450°C to 650°C, provided within the framework of the study on the Ti-6242, including tensile and cyclic tests as shown in Tab.IV.3 and Tab.IV.5, and creep tests as shown in Tab.IV.6.

- Tensile tests are performed under strain control, at a strain rate of $8.33 \cdot 10^{-5} s^{-1}$. The

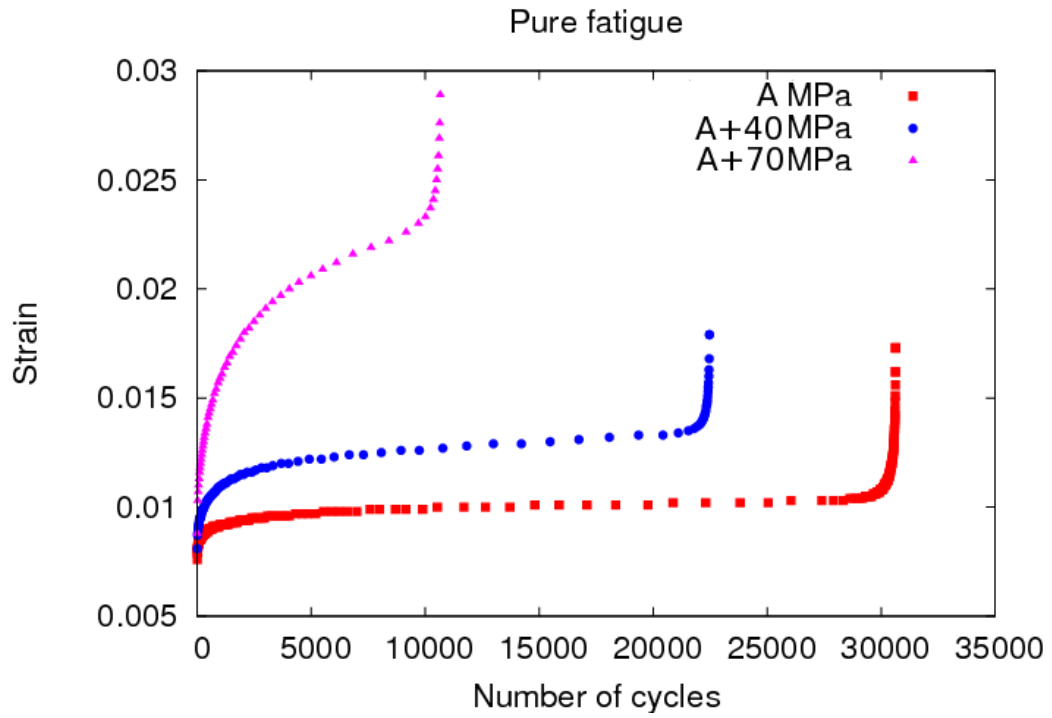


Figure IV.2 : Maximal strain evolution *versus* time in cyclic pure fatigue tests at RT, stress ratio $R_\sigma = 0$

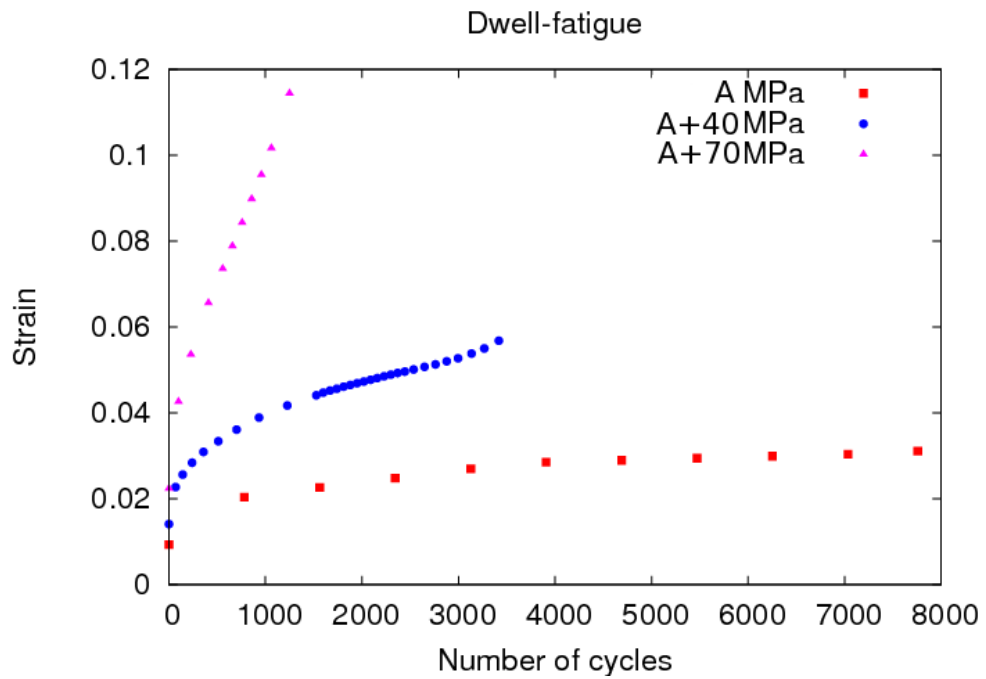


Figure IV.3 : Maximal strain evolution *versus* time in dwell tests at RT, stress ratio $R_\sigma = 0$ and hold time of 120 s

stress/strain curves for various temperatures are plotted in Fig.IV.4. The maximum stress decreases significantly when the temperature increases, especially at 600°C .

- The cyclic tests are performed under strain control under a symmetrical loading ($R_\epsilon = -1$). They are composed of three phases:
 1. loading till 0.6 % of strain: 64 cycles at 10^{-3} sec^{-1} , 32 cycles at 10^{-4} sec^{-1} , 16 cycles at 10^{-5} sec^{-1} ;
 2. loading till 0.8 % of strain: 64 cycles at 10^{-3} , 32 cycles at 10^{-4} sec^{-1} , 16 cycles at 10^{-5} sec^{-1} ;
 3. loading till 1 % of strain: 64 cycles at 10^{-3} , 32 cycles at 10^{-4} sec^{-1} , 16 cycles at 10^{-5} sec^{-1} .
- The material presents no cyclic hardening, as shown in Fig.IV.5 at 450°C .
- An important viscosity effect is present at 600°C as shown in Fig.IV.6.

Temperature (°C)	Specimens (orientation in the disc)
450	T6, T8, T9 (axial) TT2, TT5, TT8 (tangential)
500	
550	T10, T11, T12 (axial) TT3, TT6, TT9 (tangential)
600	TA-101, TA-103, TA-105 (axial)
650	TA-102, TA-104, TA-106 (axial)

Table IV.3 : Summary of the tensile tests

T (°C)	Test (Sample)	$\dot{\epsilon}$ (s^{-1})
50	Tension (9/1)	6.6710^{-4}
	Relaxation (20-1)	$\dot{\epsilon}_{650} = 1.46 \cdot 10^{-3}$ $\dot{\epsilon}_{700} = 1.46 \cdot 10^{-3}$ $\dot{\epsilon}_{725} = 1.55 \cdot 10^{-3}$ $\dot{\epsilon}_{750} = 1.60 \cdot 10^{-3}$ $\dot{\epsilon}_{800} = 1.65 \cdot 10^{-3}$
100	Tension (10/1)	$6.67 \cdot 10^{-4}$
	Tension (10/2)	$6.67 \cdot 10^{-4}$
100	Relaxation (20-2)	$\dot{\epsilon}_{500} = 1.52 \cdot 10^{-3}$ $\dot{\epsilon}_{650} = 1.47 \cdot 10^{-3}$ $\dot{\epsilon}_{700} = 1.69 \cdot 10^{-3}$
	Tension (12/1)	$6.67 \cdot 10^{-4}$
150	Tension (12/2)	$6.67 \cdot 10^{-4}$
	Relaxation (22-2)	$\dot{\epsilon}_{500} = 1.53 \cdot 10^{-3}$ $\dot{\epsilon}_{550} = 1.38 \cdot 10^{-3}$ $\dot{\epsilon}_{600} = 1.51 \cdot 10^{-3}$ $\dot{\epsilon}_{650} = 1.74 \cdot 10^{-3}$ $\dot{\epsilon}_{700} = 1.82 \cdot 10^{-3}$
200	Tension (14/1)	6.6710^{-4}
	Tension (14/2)	6.6710^{-4}
200	Relaxation (17-2)	$\dot{\epsilon}_{500} = 1.47 \cdot 10^{-3}$ $\dot{\epsilon}_{650} = 1.54 \cdot 10^{-3}$ $\dot{\epsilon}_{750} = 1.52 \cdot 10^{-3}$

Table IV.4 : Snecma database at various temperatures

Temperature (°C)	Specimens
450	FT22
500	FT23
550	FT25, FT27
600	FT24

Table IV.5 : Summary of LCF strain controlled tests

Temperature (°C)	Specimens
450	77TV4, FLT10, FLT12, FLT13
500	FLT20, FLT21, FLT22, TV3, TV7
550	TV1, FLT26, FLT29, FLT2, FLT3, FLT1, FLT9
600	FLA103, FLA104

Table IV.6 : Summary of the creep tests

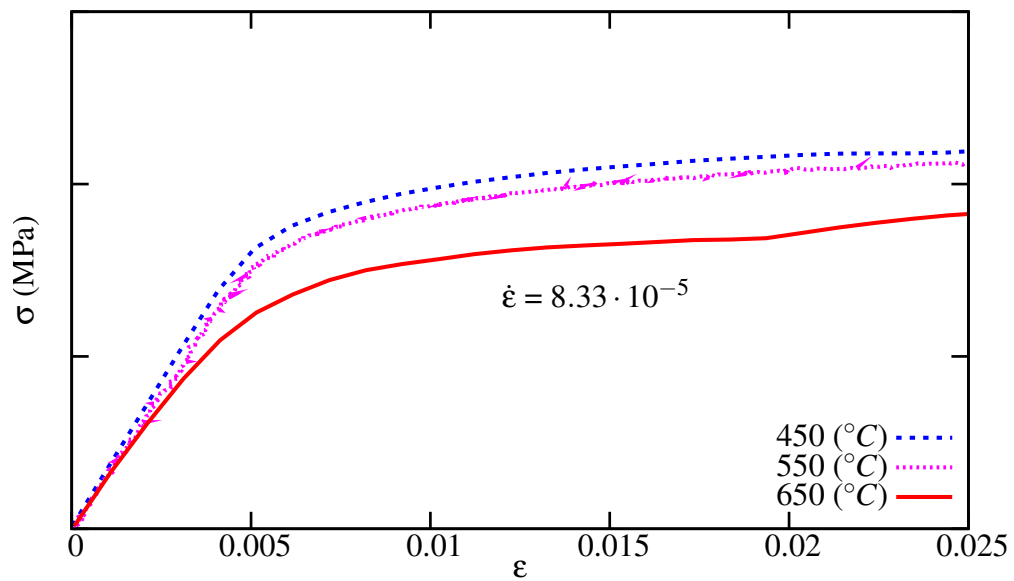


Figure IV.4 : Tensile tests at various temperatures

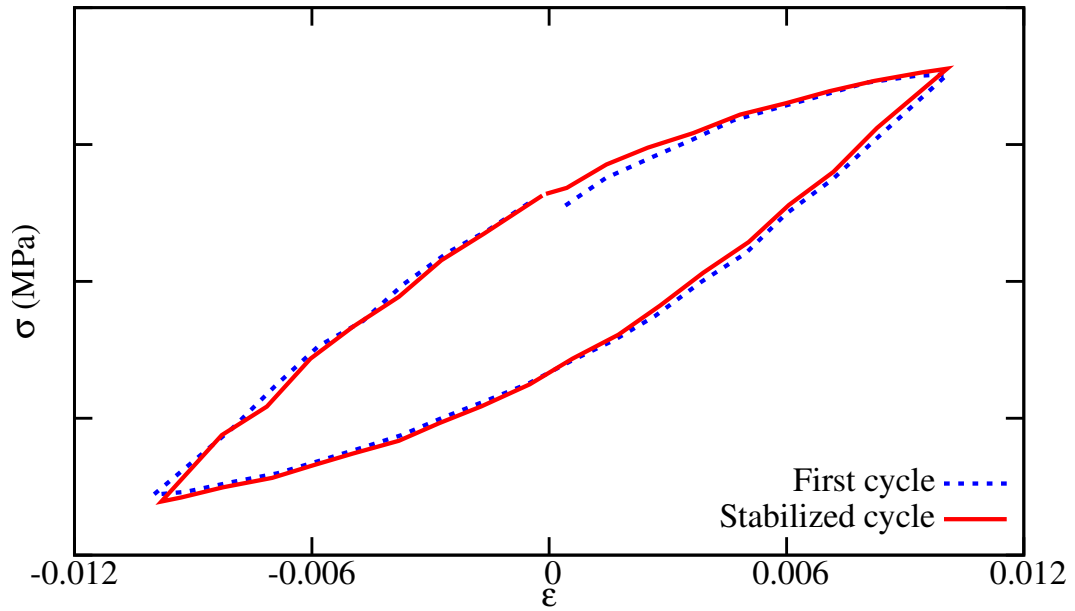


Figure IV.5 : Comparison between the first cycle and the stabilized response of Ti-6242 at 450°C

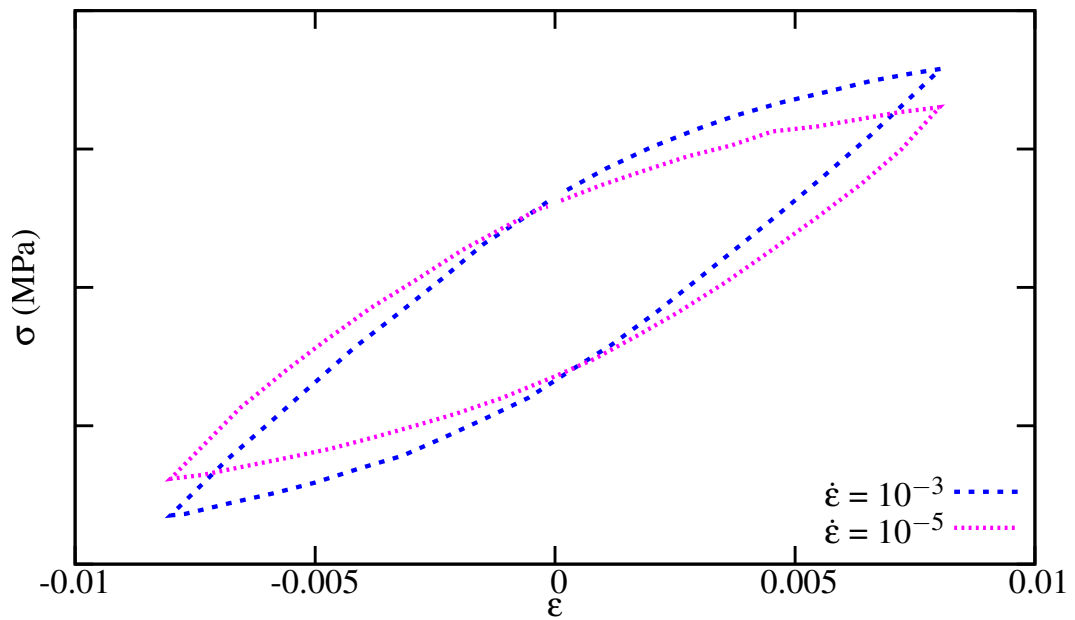


Figure IV.6 : Viscosity effect at 600°C

IV.4 Presentation of a Phenomenological Material Model

IV.4.1 Constitutive Equations

The classical viscoplastic Chaboche model with the use of one viscoplastic flow rule as used in [Baroumes, 1998] leads to an underestimation of creep at RT. In order to solve this problem, a new multi-potential model (three Norton-like flows) with isotropic and kinematic hardening has been applied. This model is an extension of the phenomenological model [Chaboche, 1989] based on thermodynamical principles and the state variable approach. Note that this modification of the basic Chaboche model was made possible easy thanks to the modularity of Z-MaT, the Object Oriented of Z-SeT code.

The constitutive equations are formulated in the small strain framework. The additional potentials allows to cover a large range of strain rates, then to model tensile, relaxation, fatigue and dwell tests. The viscoplastic strain rate tensor $\dot{\varepsilon}_v$ is split into three contributions, as two ones are not sufficient to simulate the whole range of tests. The first viscoplastic strain component (ε_{vr}) represents rapid variations with an isotropic and a kinematic hardening. The second component (ε_{vi}) corresponds to medium strain rate regime and the third one (ε_{vl}) the low strain rate regime. The second strain will be only attached a linear kinematic variable with a very high plastic modulus that will produce a limited amount of viscoplastic strain. The third viscoplastic strain component is associated with creep effects [Cailletaud and Sai, 1995]. The evolution of each viscoplastic component is given by the associated yield function.

- Partition of the strain tensor

$$\dot{\xi} = \dot{\xi}_e + \dot{\xi}_{th} + \dot{\xi}_{vr} + \dot{\xi}_{vi} + \dot{\xi}_{vl} \quad (\text{IV.1})$$

ξ_e , ξ_{th} , ξ_{vr} , ξ_{vi} , ξ_{vl} are elastic strain, thermal strain and the three components of the viscoplastic strain tensors respectively.

- Criterion: a von Mises distance is used to express the yield surfaces

$$f^r(\sigma, \mathbf{X}_r, R) = J(\sigma - \mathbf{X}_r) - R \quad (\text{IV.2})$$

$$f^i(\sigma, \mathbf{X}_i) = J(\sigma - \mathbf{X}_i) \quad (\text{IV.3})$$

$$f^l(\sigma) = J(\sigma) \quad (\text{IV.4})$$

where σ is the stress tensor, \mathbf{X}_r and \mathbf{X}_i the back-stress tensors associated with different kinematic hardening mechanisms, R the yield radius, and J the second invariant of the deviatoric part of σ .

- Normality rule

$$\dot{\varepsilon}_{vr} = \dot{p}_r \mathbf{n}_r \quad \text{with} \quad \dot{p}_r = \left(\frac{\langle f^r \rangle}{K_r} \right)^{n_r} \quad \text{and} \quad \mathbf{n}_r = \frac{3}{2} \frac{\mathbf{s} - \mathbf{X}_r}{J(\sigma - \mathbf{X}_r)} \quad (\text{IV.5})$$

$$\dot{\varepsilon}_{vi} = \dot{p}_i \mathbf{n}_i \quad \text{with} \quad \dot{p}_i = \left(\frac{\langle f^i \rangle}{K_i} \right)^{n_i} \quad \text{and} \quad \mathbf{n}_i = \frac{3}{2} \frac{\mathbf{s} - \mathbf{X}_i}{J(\sigma - \mathbf{X}_i)} \quad (\text{IV.6})$$

$$\dot{\xi}_{vl} = \dot{p}_l \tilde{\mathbf{n}}_l \quad \text{with} \quad \dot{p}_l = \left(\frac{\langle f^l \rangle}{K_l} \right)^{n_l} \quad \text{and} \quad \tilde{\mathbf{n}}_l = \frac{3}{2} \frac{\tilde{\mathbf{s}}}{J(\underline{\sigma})} \quad (\text{IV.7})$$

where:

- $\tilde{\mathbf{n}}_m$ is the normal to the flow surface f^m in the stress space ($m=r, i, l$) and $\tilde{\mathbf{s}}$ is the stress deviator tensor.
- Nonlinear isotropic hardening

$$R = R_{0r} + Q (1 - e^{-bv}) \quad (\text{IV.8})$$

- Nonlinear kinematic hardening

$$\tilde{\mathbf{X}}_r = \frac{2}{3} C_r \tilde{\alpha}_r \quad \text{with} \quad \dot{\tilde{\alpha}}_r = \left[\tilde{\mathbf{n}}_r - \frac{3 D_r}{2 C_r} \tilde{\mathbf{X}}_r \right] \dot{p}_r \quad (\text{IV.9})$$

- Linear kinematic hardening

$$\tilde{\mathbf{X}}_i = C_i \tilde{\alpha}_i \quad \text{with} \quad \dot{\tilde{\alpha}}_i = \tilde{\mathbf{n}}_i \dot{p}_r \quad (\text{IV.10})$$

The material parameters for the rapid evolution are: K_r , n_r (viscous part), R_{0r} (initial yield), C_r , D_r (nonlinear kinematic hardening), meanwhile the material parameters for the medium rate part of the model are: K_i , n_i (viscous part), C_i (linear kinematic hardening) and those of the slow part: K_l , n_l (viscous part). All these parameters are temperature dependent.

IV.4.2 Model Calibration

This section presents the methodology applied to determine the set of material constants in the phenomenological developed model (equations from III.1 to III.9).

The calibration procedure has been divided into several stages:

- Calibration of the material parameters for the first potential: initial yield stress and viscosity parameters R_{0r} , K_r and n_r have been obtained from various tensile tests performed for different applied strain rates. Kinematic hardening parameters C_r and D_r have been obtained from fatigue tests. Stabilized cycles of fatigue tests are only used and the highest priority of the modelling is given to them, as the typical loading in the critical part of the discs in operation is cyclic. Basically, this step uses data from 450°C to 600°C.
- Viscosity K_i and n_i and hardening C_i parameters for the second potential (intermediate regime) have been obtained from tensile and relaxation tests performed at the temperature from 20°C to 200°C.
- The calibration of the coefficients for the third potential K_l and n_l have been obtained from the creep tests performed between 450°C and 600°C.

The parameters presented in Tab.IV.7 are the final set of coefficients obtained at different temperatures. In order to identify the material parameters independently for the high strain rate (tensile and cyclic tests) and the low strain rate regime (creep tests), the constants K_i , n_i , C_i from 450°C to 600°C and K_l , n_l of the third potential from 20°C to 200°C vanish at these temperatures.

Temperature (°C)	20	50	100	150	200	450	500	550	600
R_0r , MPa	699	665	600	571	512	378	285	215	106
K_r , MPa·s ^{1/n_r}	50	50	50	50	50	50	149	332	825
n_r	15	15	15	15	15	14	13	10	5.56
C_r (MPa)	98090	96360	94300	93690	91890	90260	87490	83260	79160
D_r	350	350	350	350	350	350	350	350	350
K_i (MPa·s ^{1/n_i})	1200	1200	1200	1200	1200	1e09	1e09	1e09	1e09
n_i	12	12	12	12	12	12	12	12	12
C_i (MPa)	1e07	2.6e08	5.1e08	8e08	1e09	1e09	1e09	1e09	1e09
K_l (MPa·s ^{1/n_l})	100000	50000	30000	15000	8000	7810	10050	20000	27940
n_l	10	10	10	10	8.26	6.36	5.06	5.04	5.72

Table IV.7 : Final set of calibrated material parameters for Ti-6242 at different temperatures

IV.4.3 Numerical Prediction of Tensile, Cyclic and Creep Tests

The model response obtained with the optimal set of coefficients is compared to the experimental tensile data in Fig. IV.7 to IV.10. Fig. IV.7 shows the comparison at 20°C for three strain rates. The prediction at 100°C is given in Fig.IV.8. Fig. IV.9 and IV.10 shows the comparison at 450°C and 600°C respectively. In general, good agreement is observed between experimental and simulated stress/strain tensile curves.

For the case of cyclic stress controlled tests (pure fatigue and dwell tests performed at RT), the model response is in good agreement with the corresponding data as shown in Fig.IV.11 and IV.12. However, an overestimation of the maximal total strain during cycles by the model is observed.

The prediction of the stabilized cyclic response in the strain controlled fatigue tests at 450°C, 500°C, 550°C and 600°C are shown in Fig.IV.13 and Fig.IV.14. It is worth mentioning that the hysteresis loops are well described.

The relaxation tests are also simulated and compared to the experimental data. These comparisons are shown in Fig.IV.15 and Fig.IV.16. In general, the model underestimates the amount of stress relaxation.

The final set of parameters is also used to predict the material behaviour under creep. Figures IV.17 and IV.18 show the creep predictions at 450°C, 550°C and 600°C. The predicted response at 450°C overestimates the magnitude of the primary creep strain, but the rate of the secondary creep is acceptable. In general, the simulated creep curves are in good agreement with the corresponding experimental data.

To validate the model, some phenomenological aspects have been checked. In Fig.IV.20 the evolution of the yield stress $R_{0.2}$ (i.e the stress level corresponding to 0.2% of plastic strain) *versus* temperature is given. Globally, a good agreement between the model and the corresponding data is observed.

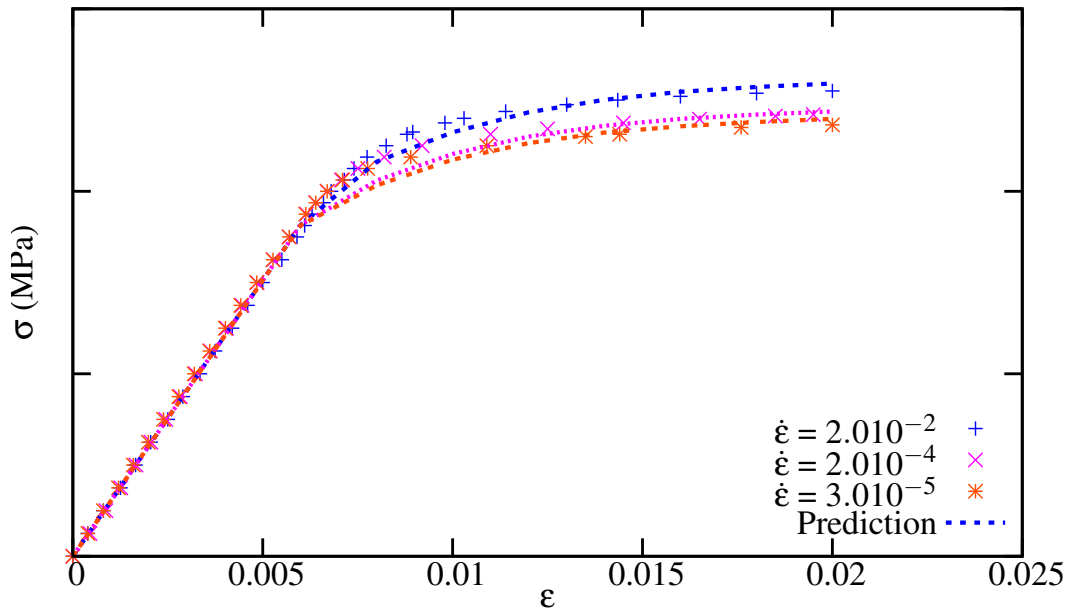


Figure IV.7 : Predicted tensile response at 20°C

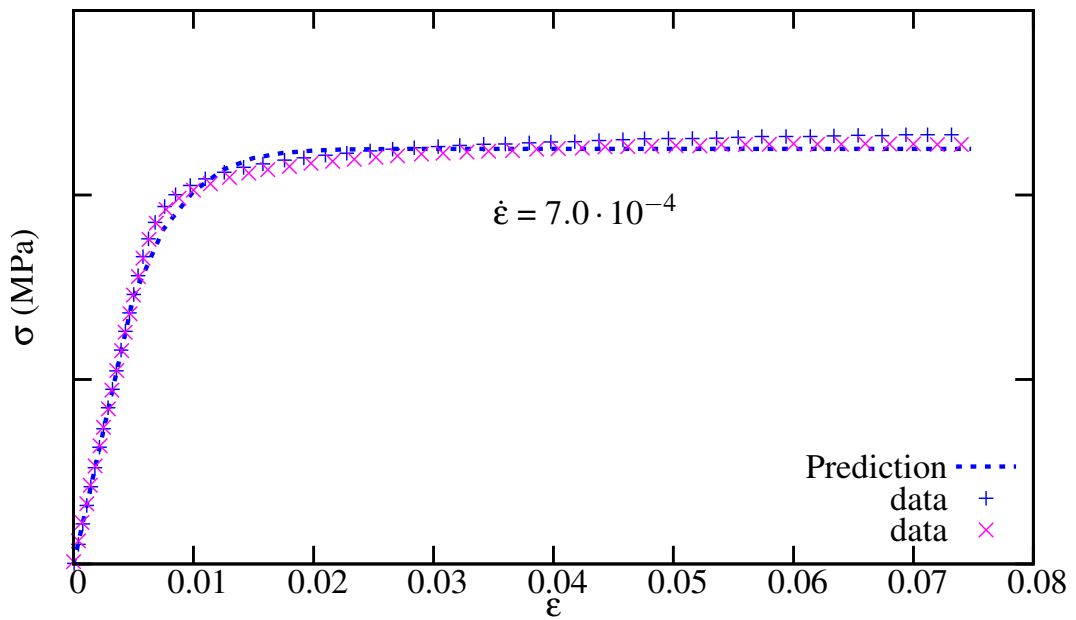


Figure IV.8 : Predicted tensile response at 100°C

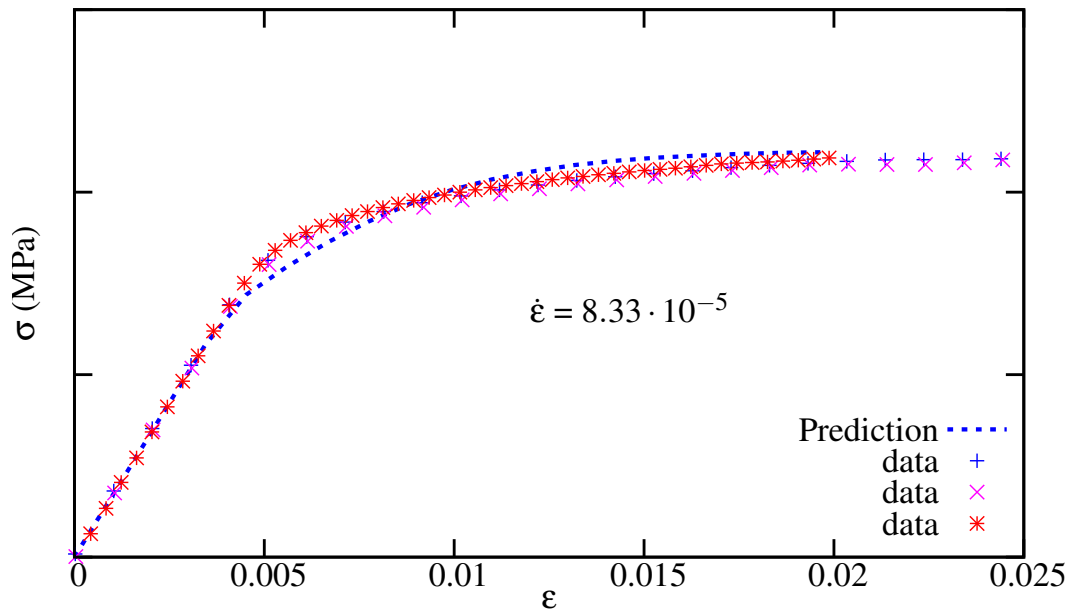


Figure IV.9 : Predicted tensile response at 450°C

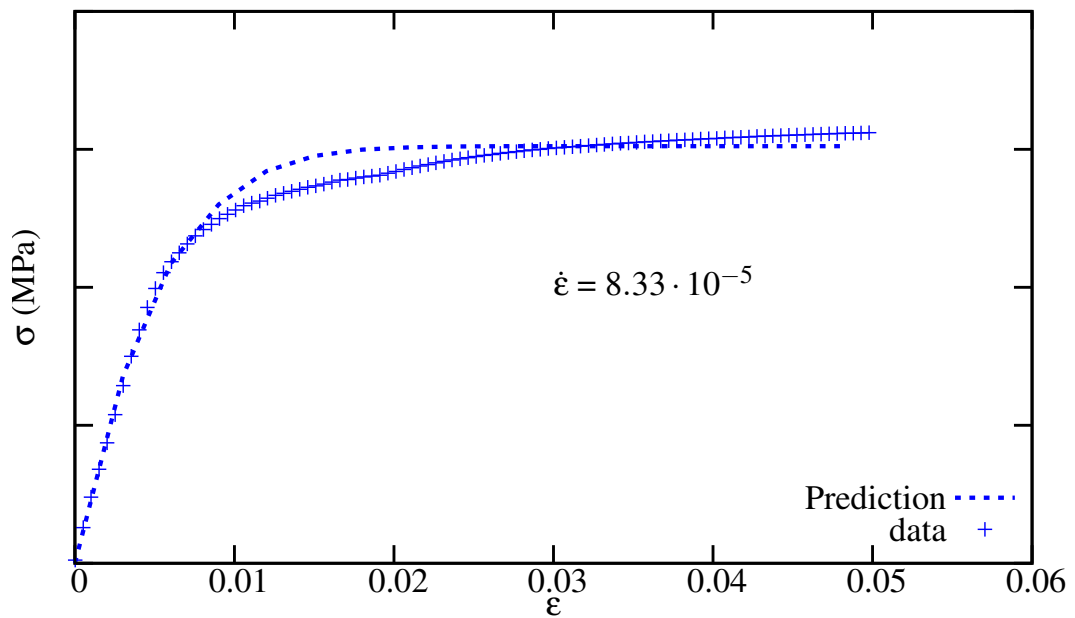


Figure IV.10 : Predicted tensile response at 600°C

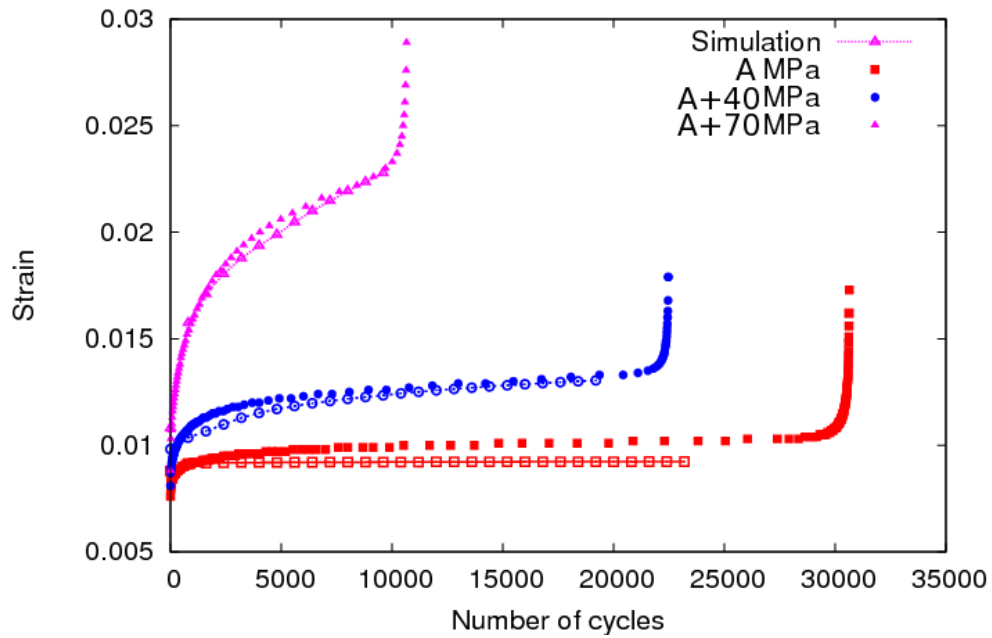


Figure IV.11 : Predicted maximal strain evolution *versus* time in pure fatigue at RT, for a stress ratio $R_\sigma = 0$

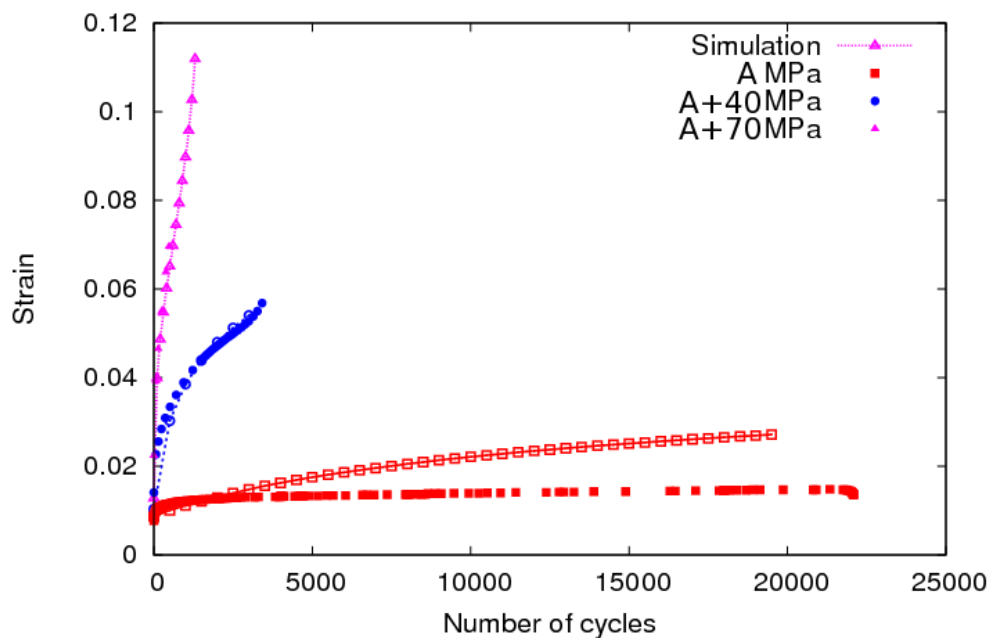


Figure IV.12 : Predicted maximal strain evolution *versus* time in dwell at RT, for a stress ratio $R_\sigma = 0$ and hold time of 120s

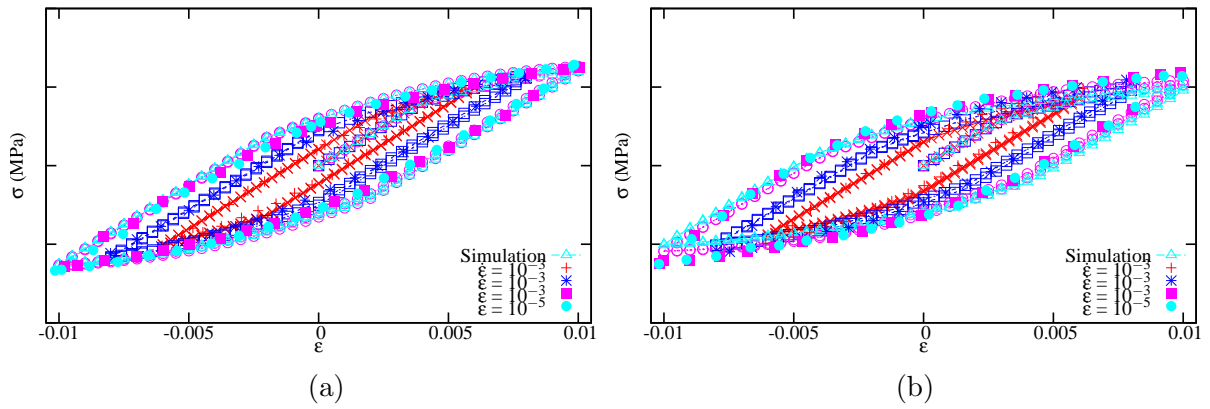


Figure IV.13 : Predicted stabilized cyclic response under symmetric strain control at a) 450°C; b) 500°C

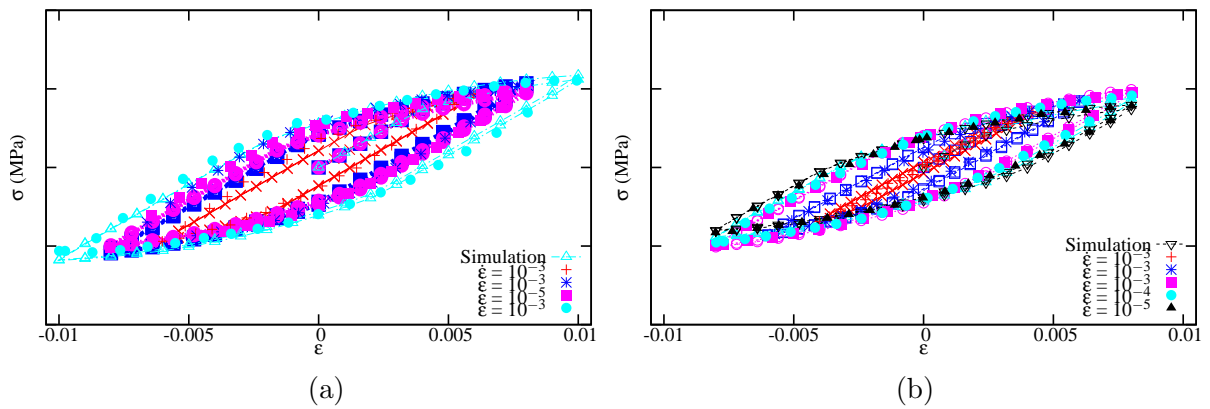


Figure IV.14 : Predicted stabilized cyclic response under symmetric strain control at a) 550°C; b) 600°C

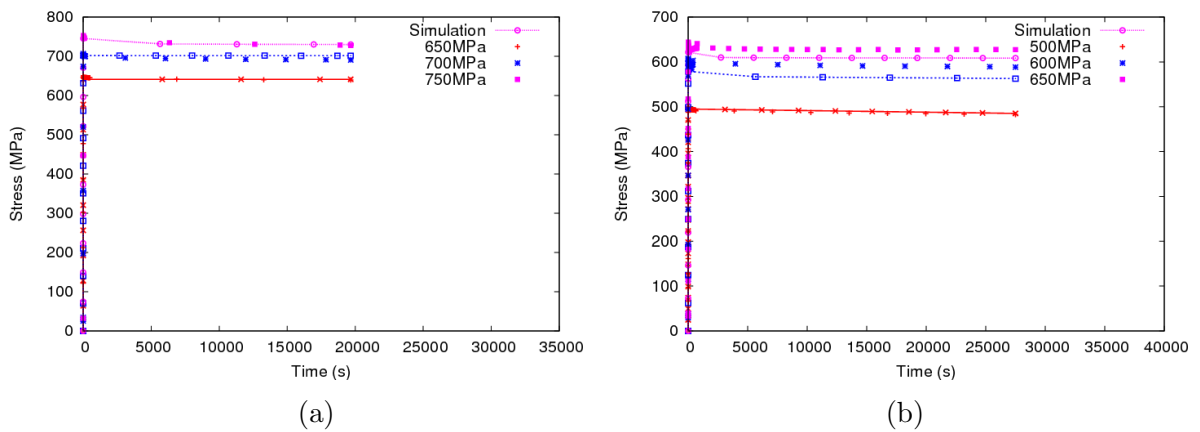


Figure IV.15 : Predicted relaxation response at a) 20°C; b) 200°C

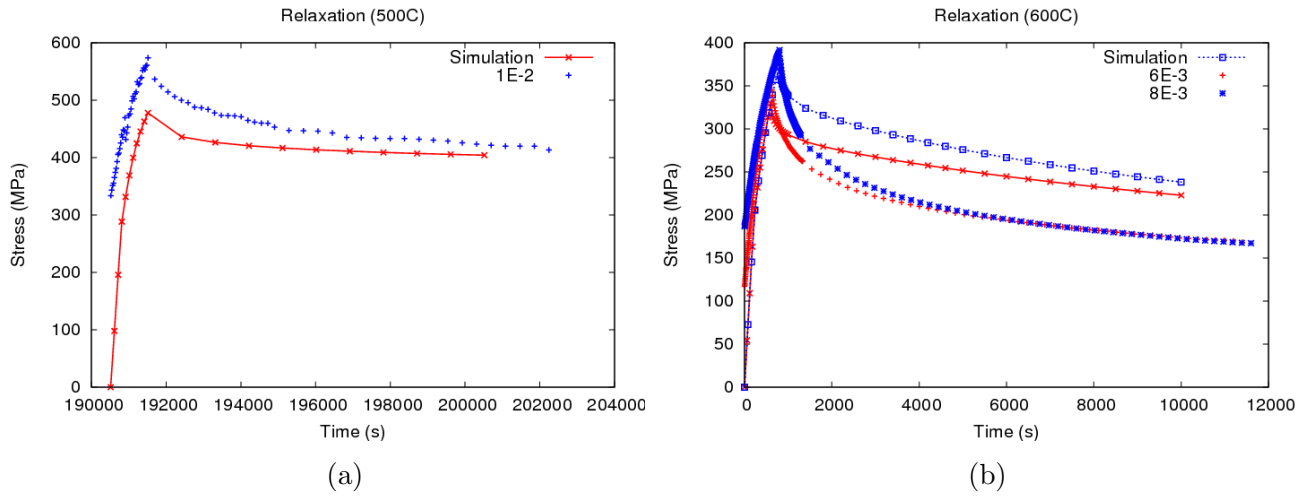


Figure IV.16 : Predicted relaxation response at a) 500°C ; b) 600°C

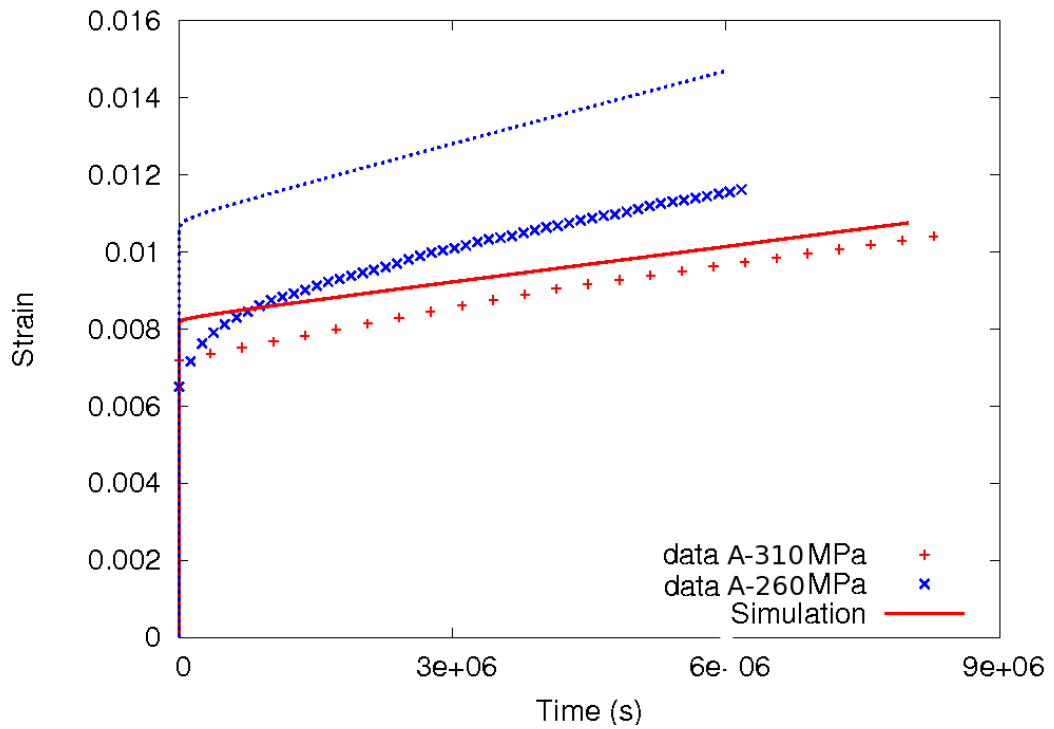


Figure IV.17 : Predicted creep response at 450°C

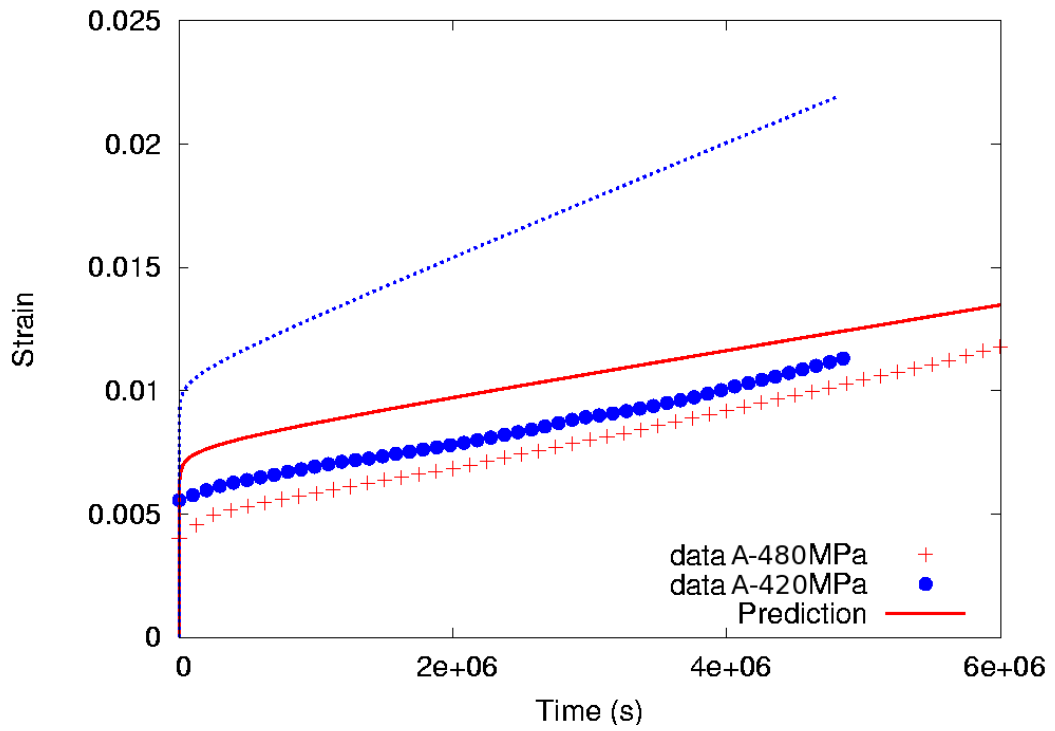


Figure IV.18 : Predicted creep response at 500°C

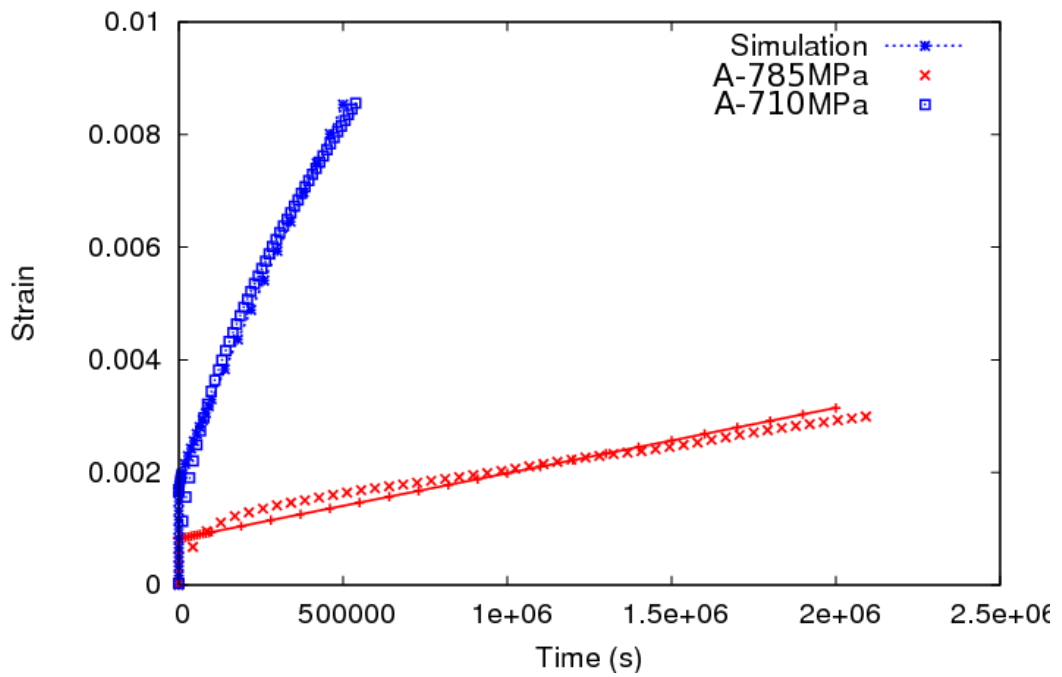


Figure IV.19 : Predicted creep response at 600°C

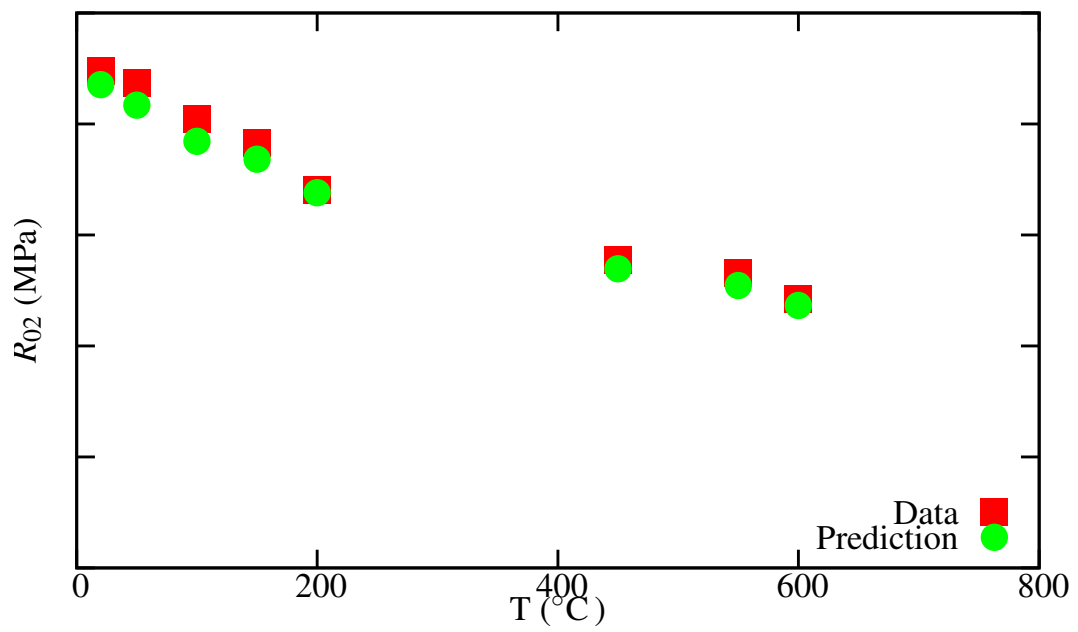


Figure IV.20 : Evolution of the yield stress $R_{0.2}$ versus temperature

IV.4.4 Conclusions

The results obtained in this chapter demonstrate the capabilities of the Z-MaT/Z-SeT tools to model the mechanical behaviour of the Ti-6242 material :

- A multi-potential viscoplastic constitutive model is proposed to represent the basic effects found in the experimental database.
- A whole set of tests has been simulated, including tensile, relaxation, creep, cyclic fatigue and dwell experiments at different temperatures from 20°C up to 600°C (Snecma and ENSMA databases).
- The simulations are in good agreement with experiments for different types of tests with various conditions (strain rates, stress and strain controlled tests).

Les résultats obtenus dans ce chapitre démontrent les capacités des outils Z-MaT/Z-SeT pour modéliser le comportement mécanique de l'alliage Ti-6242 :

- *Un modèle de comportement viscoplastique à plusieurs potentiels est proposé pour représenter les effets fondamentaux observés dans la base de données.*
- *Un grand nombre d'essais ont été simulés, incluant traction, relaxation, fluage, fatigue sans et avec temps de maintien (dwell) à différentes températures de 20°C jusqu'à 600°C (bases de données de la Snecma et l'ENSMA).*
- *Les simulations correspondent bien aux expériences pour les différents types des tests avec les différentes conditions (vitesses de déformation, contrainte ou déformation imposée).*

Chapter -V-

**Residual Stress Calculation in
Forged Discs**

Contents

V.1	Introduction	50
V.2	Effects of heat treatment on the stress state	50
V.3	2D Finite Element Disc Simulations	51
	V.3.1 Geometric Models	51
	V.3.2 Boundary Conditions and Loading	51
	V.3.3 Material Models	51
	V.3.4 Heat Treatment Analysis	52
	V.3.5 Disc Machining	56
V.4	2D Finite Element Simulations of the Disc in Operation	60
	V.4.1 Stress and Strain Results Analysis	61
V.5	3D Finite Element Disc Simulations	64
	V.5.1 Geometric Models	64
	V.5.2 Boundary Conditions and Loading	64
	V.5.3 Material models	65
	V.5.4 Stress and Strain Analysis Results	65
	V.5.5 Stress and Strain Analyses Results of the Disc with a Slit	68
V.6	General Conclusions	70

V.1 Introduction

We can not speak about forged workpieces without evoking the residual stress induced by forming process and heat treatment. Residual stress can cause the premature crack initiation and this factor must be investigated. It is important to know for the dwell loading, just as for the fatigue one, if there are possible structural effects coming from the history of the thermomechanical treatment or the dwell effect is due to the intrinsic behaviour of a representative material element, as it was mentioned in the introduction of the thesis.

The manufacturing of forged workpieces includes stages of shaping, heat treatment and machining. All these stages are very complex, since they involve thermal, mechanical and metallurgical phenomena, so that sophisticated numerical tools are requested for the modelling.

In this chapter we will focus on the residual stress induced by heat treatment and machining. Our purpose is to quantify them *via* 2D and 3D finite element simulations and to draw conclusions about their effects on the global mechanical properties (stress field and distortion). The residual stress which will be quantified are the macroscopic (first order) residual stress.

Two mechanical approaches are considered: the first approach is macroscopic and the second one is at the mesoscopic scale.

The first section is splitted into two subsections: (i) heat thermal calculation of the quenching process, (ii) FE analysis of the machining process, followed by a FE analysis of disc operation. Two cases are treated. In the first one, residual stress estimated in the first section are introduced as the initial state, meanwhile the second case assumes stress free initial conditions.

V.2 Effects of heat treatment on the stress state

As illustrated in Fig.V.1, the forging and heat treatment process involves several stages: heating, hold period at the maximum temperature and a cooling phase that is more or less rapid, depending on the cooling technique (water, oil or air).

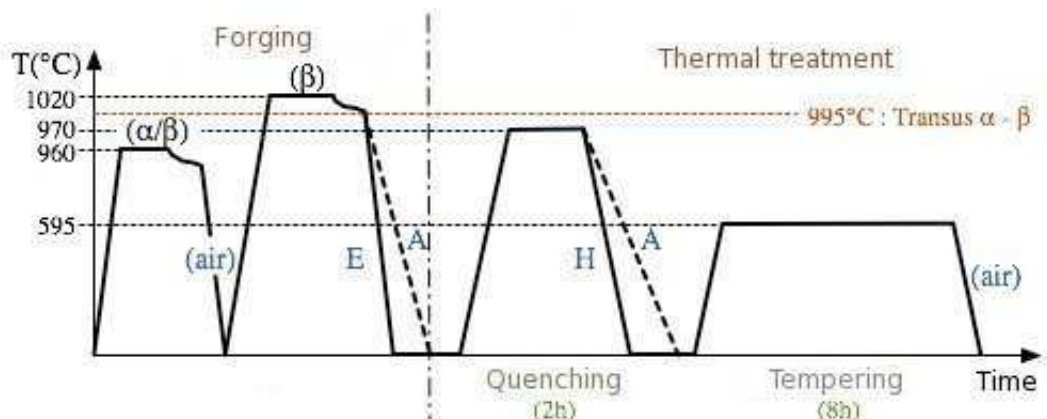


Figure V.1 : Forging and thermal heat treatment processes [Jousset, 2008]

The rapid cooling associated to the quenching operation induces temperature gradients between the surface and the bulk of the forged workpieces. This is the source of internal stress that may distort the forged parts. So, the aim of the following sections is to answer question: is there any relation between the residual stress and the dwell effect ? Simulations have been performed first on a 2D axisymmetric disc. Then simulations have been done on a simplified 3D disc.

V.3 2D Finite Element Disc Simulations

V.3.1 Geometric Models

Four geometries of the axisymmetric disc are considered in this section. The first one is the geometry of the raw disc. The others are geometries after machining. The geometries have been provided by Snecma (IGES files). They are imported in Z-SeT environment through a specific plugin [Besson and Foerch, 1997]. In each case, the mesh is made of 6-node axisymmetric elements with a full integration. A summary of the number of nodes and elements is given in table V.1, and the meshes are shown in Fig.V.2 to V.5.

V.3.2 Boundary Conditions and Loading

The only prescribed boundary condition for the raw disc consists in blocking the node `bloz` (see Fig.V.2) in y -direction. There are no external mechanical loadings. The only effect is due to thermal gradients. The successive calculations allow to represent the different stages of the machining. For each new mesh, the internal variables and the displacement fields are inherited from the previous stage, by means of the mapping operation. That allows us to recalculate the stress field on the new shape by computing the new balance of loadings.

In the final disc calculated in operation there is a constraint in the direction y on its right upper part, then MPC1 (MPC = multi-point constraint) is applied on its left side and on its right lower part.

Disc	Nb of nodes	Elements
Raw disc	8772	4185
First machining	5272	2503
Second machining	3520	1583
Final disc	8428	3869

Table V.1 : Characteristics of the successive meshes

V.3.3 Material Models

Two types of material models have been used for TA6V: (i) a classical phenomenological macroscopic model, involving viscous flow, kinematic and isotropic hardening, (ii) a multiscale model using uniform field approach proposed in [Longuet, 2010]. In fact, we have in hand the material parameters for both models for TA6V alloy, this is why the investigation is made for this alloy instead of Ti-6242 in the first place. The idea behind this section is that the conclusions obtained for TA6V will be at least qualitatively valid for our material.

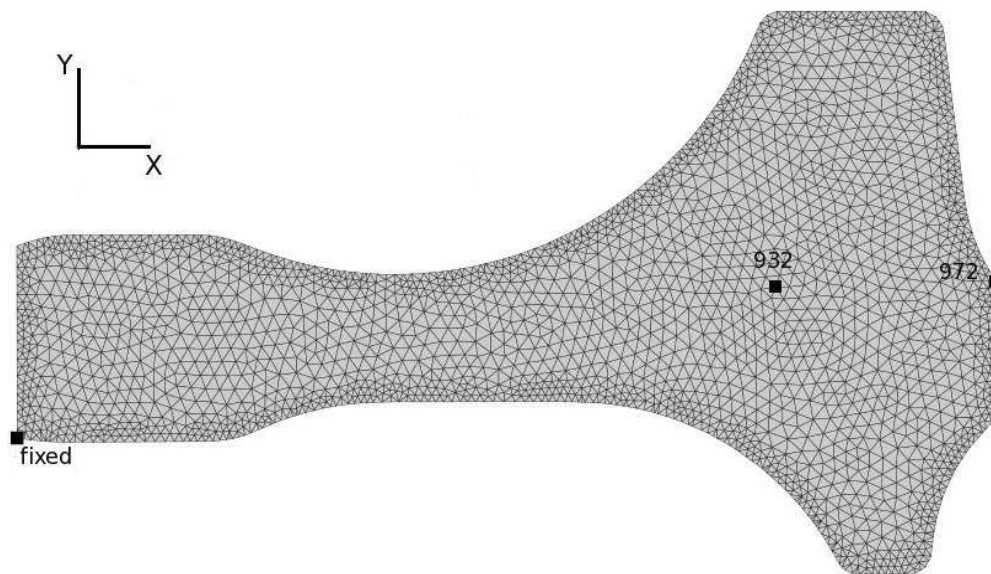


Figure V.2 : The mesh of a raw disc

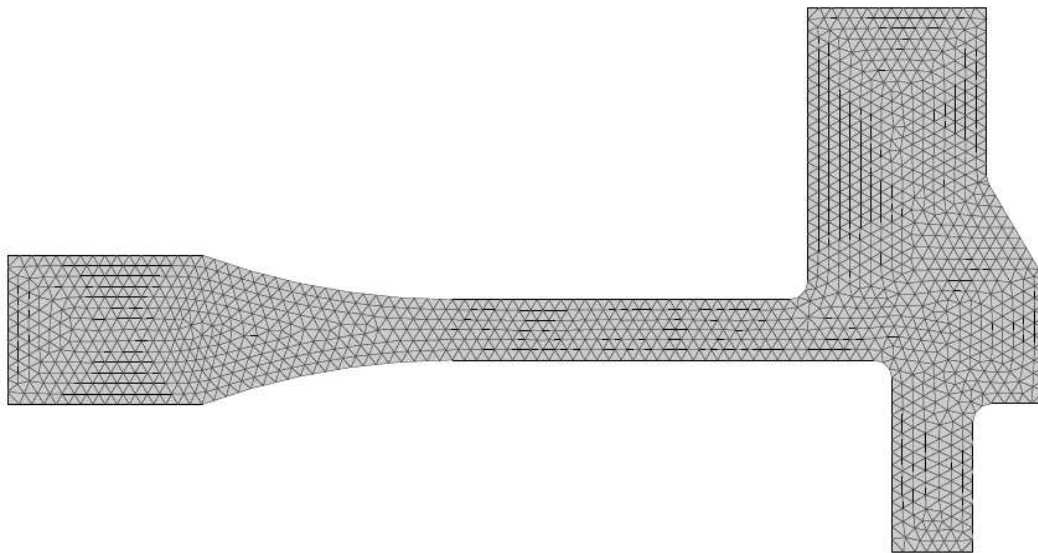


Figure V.3 : The FE mesh after the first stage of machining

V.3.4 Heat Treatment Analysis

Only the operation of oil quenching is modeled. An initial constant temperature of 970°C is imposed in the disc. The heat exchange is modeled by using convective condition with a constant heat transfer coefficient h . The heat transfer analysis has been performed with the following parameters:

- convection heat flux: $h = 800\text{W}/(\text{m}^2 \cdot \text{s})$;
- conductivity: $k = 22\text{W}/(\text{m} \cdot \text{s})$;
- density: $\rho = 4450\text{kg}/\text{m}^3$;
- capacity: $4.5428 \cdot 10^6 \text{J}/(\text{K} \cdot \text{m}^3)$.

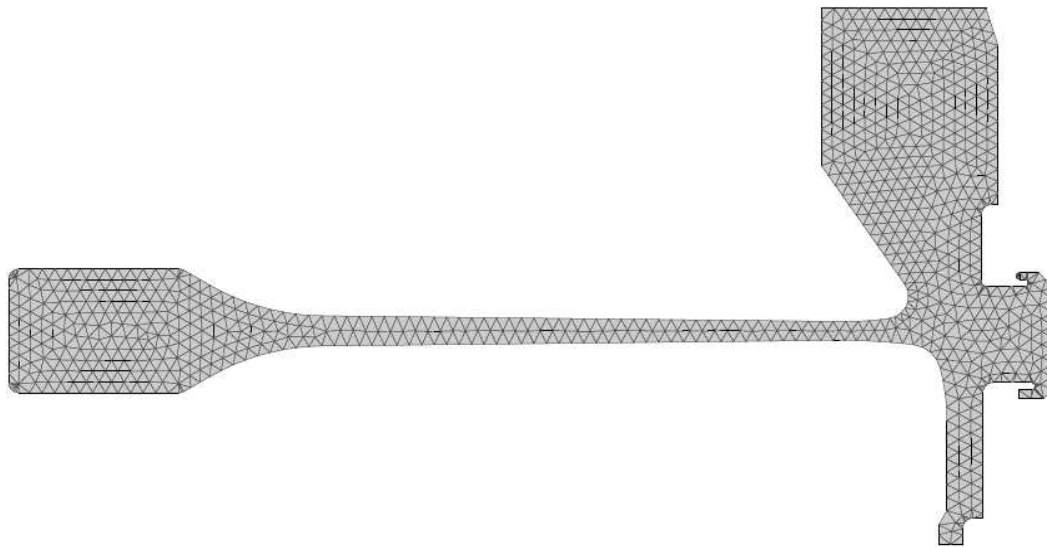


Figure V.4 : The FE mesh after the second stage of machining

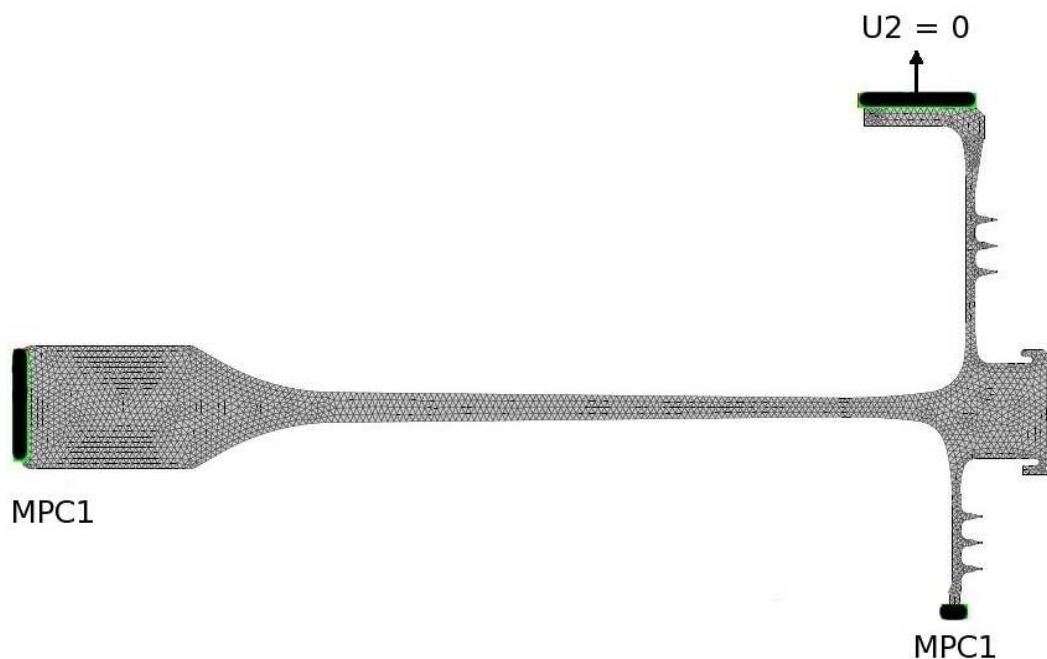


Figure V.5 : The FE mesh of the final disc and locations of the boundary condition sets

The quenching conditions are applied for the 1000 s period. The resulting temperature field is then interpolated to reach 20°C everywhere in the disc after 500 s, as after this period of time the temperature change is quite small. Maps of the temperature fields are shown in Fig.V.6 at 100 s and 1000 s after the beginning of the quenching process. After 100 s the average temperature of the disc is still very high, and the gradients are important. Behind 1000 s the whole disc is not far from RT, as shown in (b).

The convective heat transfer coefficient h has been calibrated in order to obtain cooling rates compatible with the velocities measured in [Gautier et al.,]. The velocity of quenching has been calculated in two disc locations. At node 972 located on the surface and at node 932

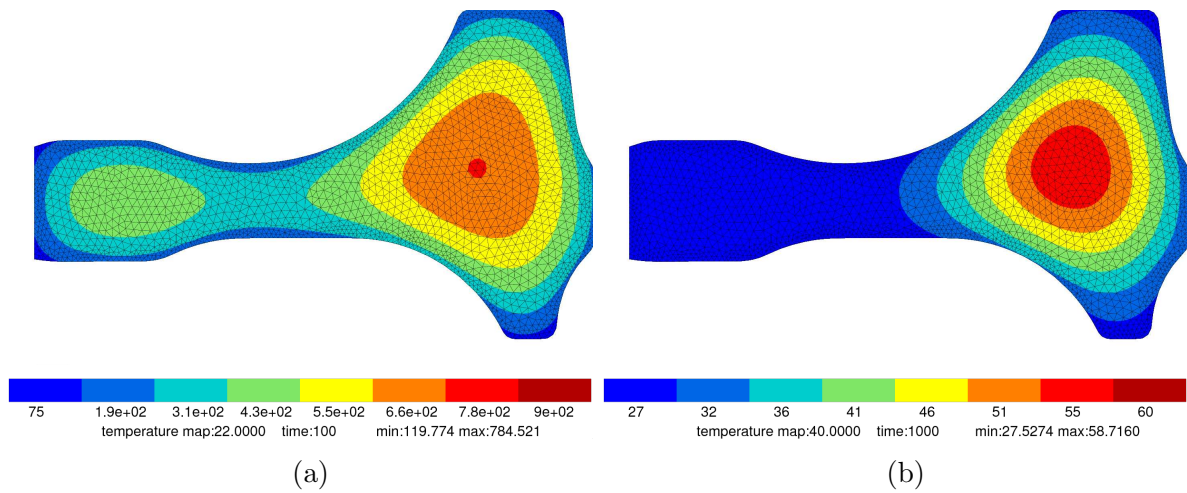


Figure V.6 : Temperature fields in the raw disc at: a) $t=100$ s; b) $t=1000$ s

located inside the disc (as shown in Fig.V.2). Temperature evolution versus time in these locations are illustrated in Fig.V.7 and V.8. These results are very close to the experimental velocity given by [Gautier et al.,].

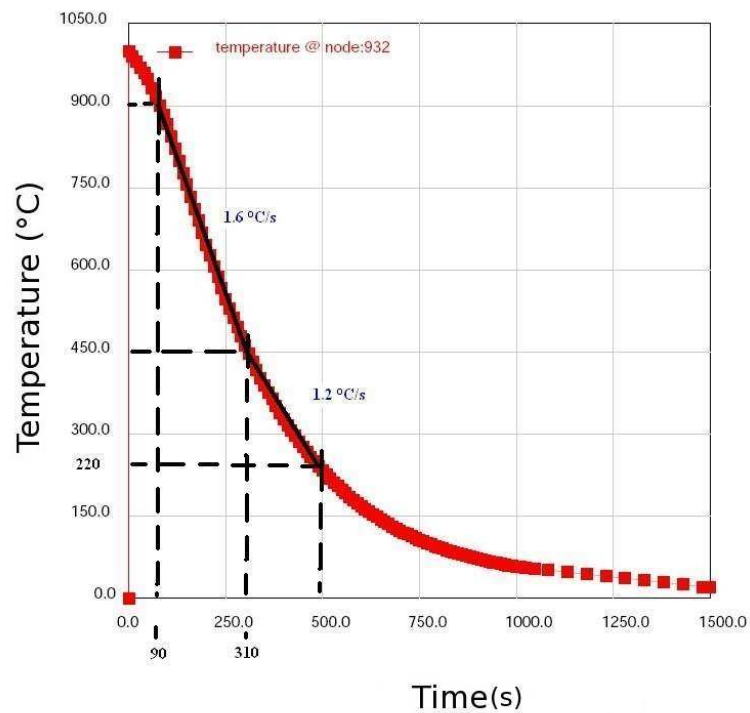


Figure V.7 : Quenching velocity at node 932 located inside the disc

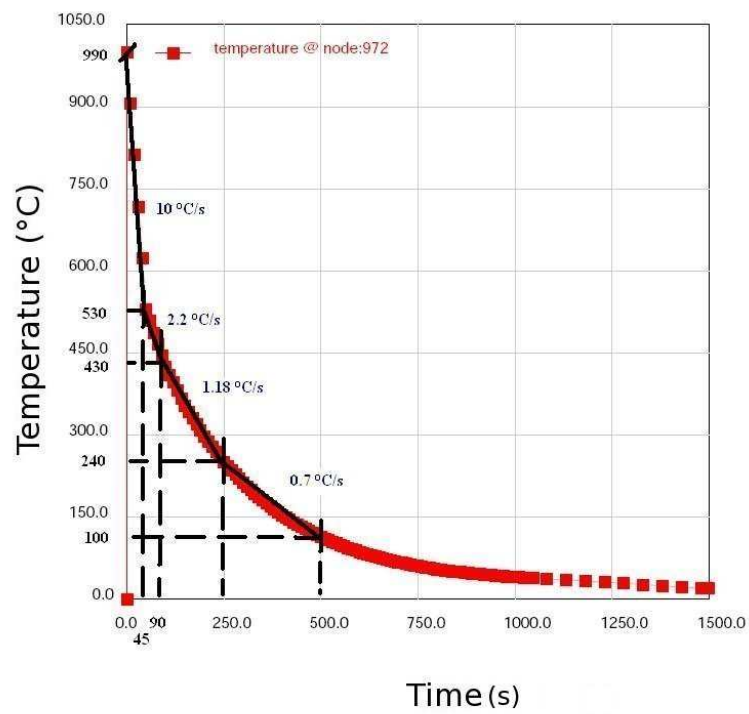


Figure V.8 : Quenching velocity at node 972 located at the surface of the disc

V.3.5 Disc Machining

The temperature field obtained after heat treatment has been used as the initial condition of the mechanical analysis of the various stages of machining. The machining of the disc consists in:

- Pre-machining, to obtain the shape shown in Fig.V.2;
- Intermediate machining, to obtain the shape shown in Fig.V.3 and Fig.V.4;
- Finished machining to reach the final shape of the disc, as shown in Fig.V.5.

The field transfer method built in Z-SeT's environment is used between the different stages.

V.3.5.1 Stress Analysis Results for the TA6V Disc

Two mechanical analyses have been done. The material parameters used in the macroscopical phenomenological model are taken from [Robert, 2007]. More details on this model are given in Appendix A.4. This model will be noted as “CC model”. The mesoscopic scale model of [Longuet, 2010] allows to account for phase volume fraction and provides an estimation of the average fields in each phase (α and β). The corresponding constitutive equations are given in Appendix A.4. The model will be called “RL”. The material parameters are taken from [Longuet, 2010].

Results obtained after the analysis of the whole residual stress evaluation procedure are presented from Fig.V.9 to V.12. All maps are defined from values at integration points.

- In the “RL model”, at the beginning of the quenching process, the fraction of β phase has been set to 1, and, accordingly, there is no α phase. The evolution of the two main phases of Ti6Al4V at 100 s is shown in Fig.V.9. The phase fields complement each other, since the sum of both volume fraction is equal to 1.
- Iso-contour of σ_{33} at the end of the heat treatment process are quite close to each other in CC and RL models as shown in Fig.V.10. On the one hand, there is a noticeable 20% difference between both models, with higher values in CC model. This large difference is observed in the bulk of the disc. The macroscopic model is more critical than the mesoscopic one. This is then a cross validation for the models, and makes us confident regarding the quality of the solution for our material.
- After the field transfer on the following machined discs, it becomes evident that the residual stress values are lower than at the previous stages. Finally, the difference between the results obtained by simulations with both models (CC and RL) at the end of machining are shown in Fig.V.11 and V.12 for “CC” and “RL” models respectively. The maximum value of the von Mises stress (σ_{Mises}) at the end of the process is equal to 142 MPa with CC model, and 100 MPa for RL model. For both cases, the stress level is significant. The way the stress field evolves in operation must then be investigated.

V.3.5.2 Conclusions

Two important questions have been answered in this section:

(a) The results given by the macroscopic approach (CC model) are relatively consistent with those given by the multiscale model (RL model). Despite the fact that the stress values are higher in CC model, this is an encouraging point for both models, and allows to conclude that a macroscopic approach may be sufficient for estimating the residual stress, as the more critical state in this case

(b) The maximum stress values remain significant at the end of the machining, according to both models. So, it seems important to consider their effect for the FE analysis of the disc in operation.

On a répondu à deux importantes questions dans cette section :

(a) Les résultats donnés par l'approche de macroscopie (CC modèle) sont relativement cohérents avec les données par le modèle multi-échelle (RL modèle). Malgré le fait que les valeurs de la traction sont plus hautes dans CC modèle, c'est un point encourageant pour les deux modèles et permet de conclure qu'une approche macroscopique peut être suffisante pour estimer les contraintes résiduelles, comme l'état plus critique dans ce cas-là

(b) Les valeurs des contraintes restent significatives à la fin d'usinage, selon les deux modèles. Donc il semble important de considérer leur effet pour l'analyse FE du disque en fonctionnement.

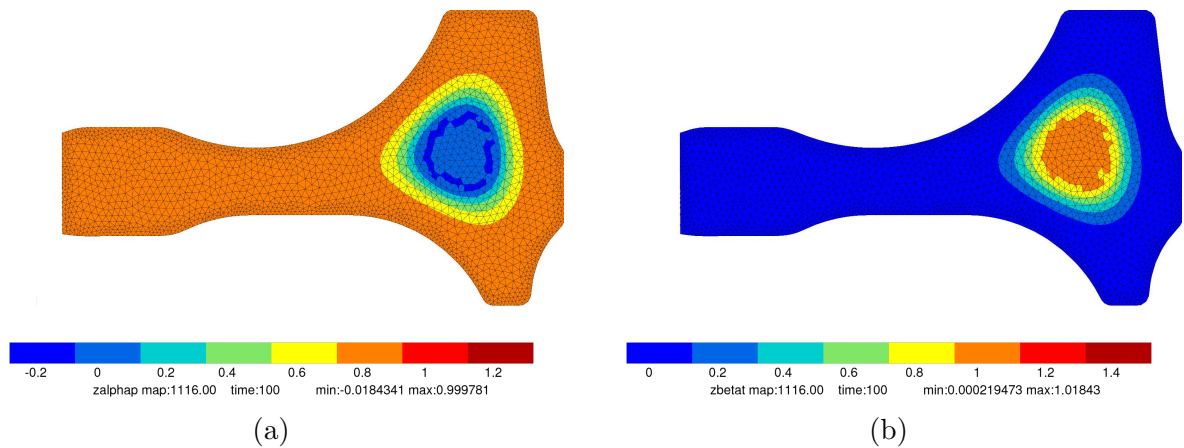


Figure V.9 : Spatial phase distribution in the disc (RL model) at 100 s for a) α phase; b) β phase

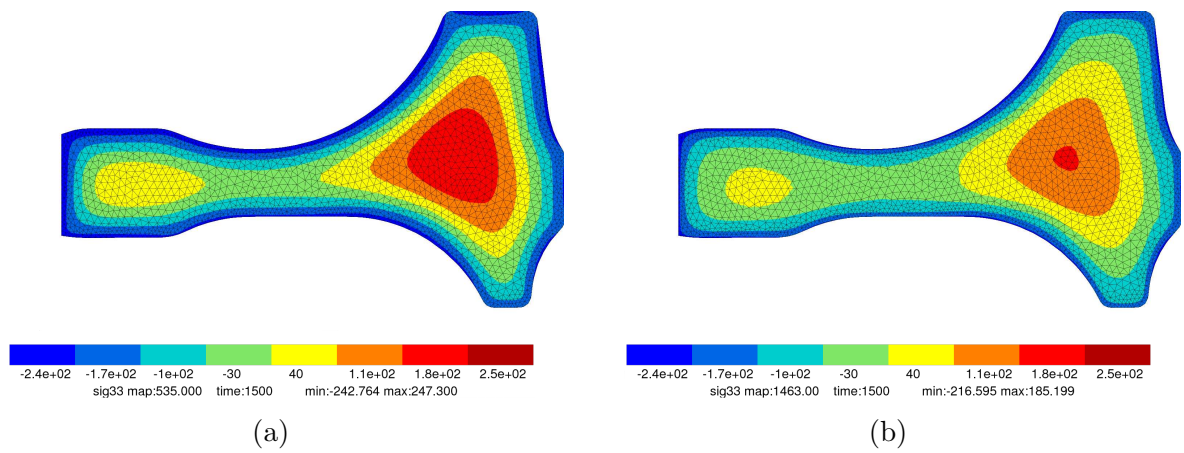


Figure V.10 : σ_{33} stress fields after quenching, as computed by a) CC model; b) RL model

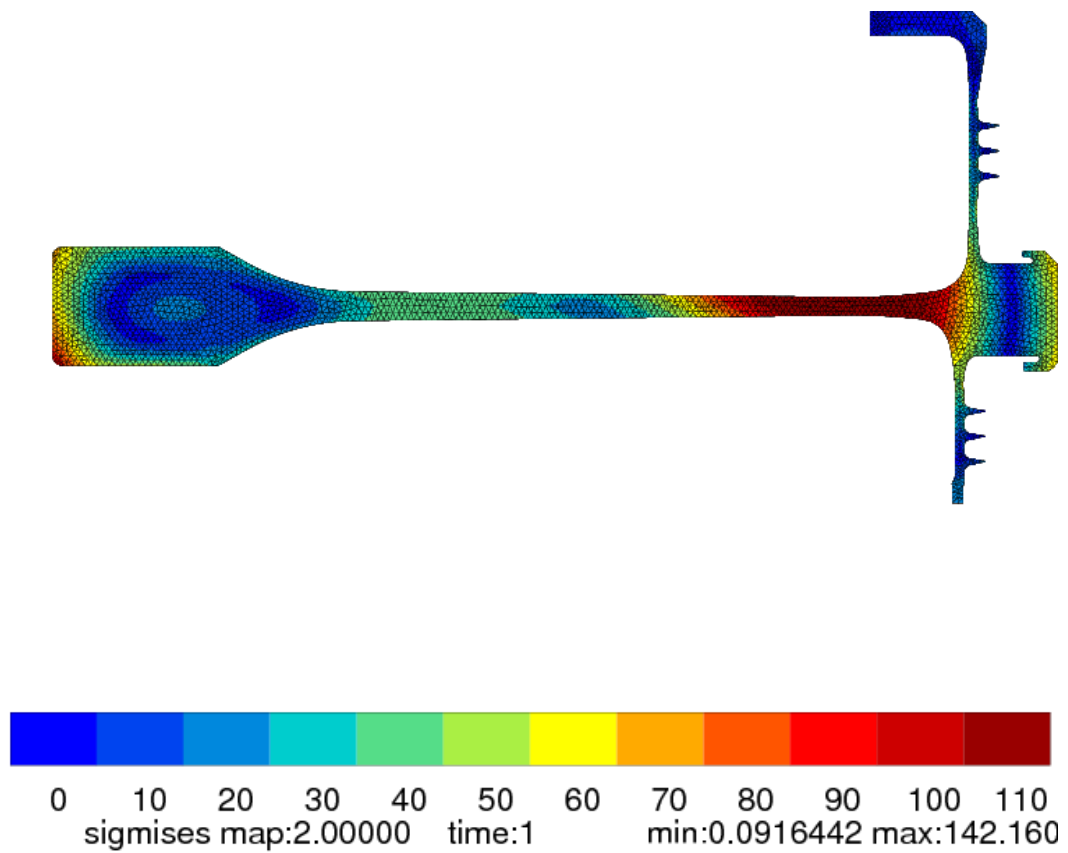


Figure V.11 : Contour map of the equivalent von Mises stress at the end of machining, CC model

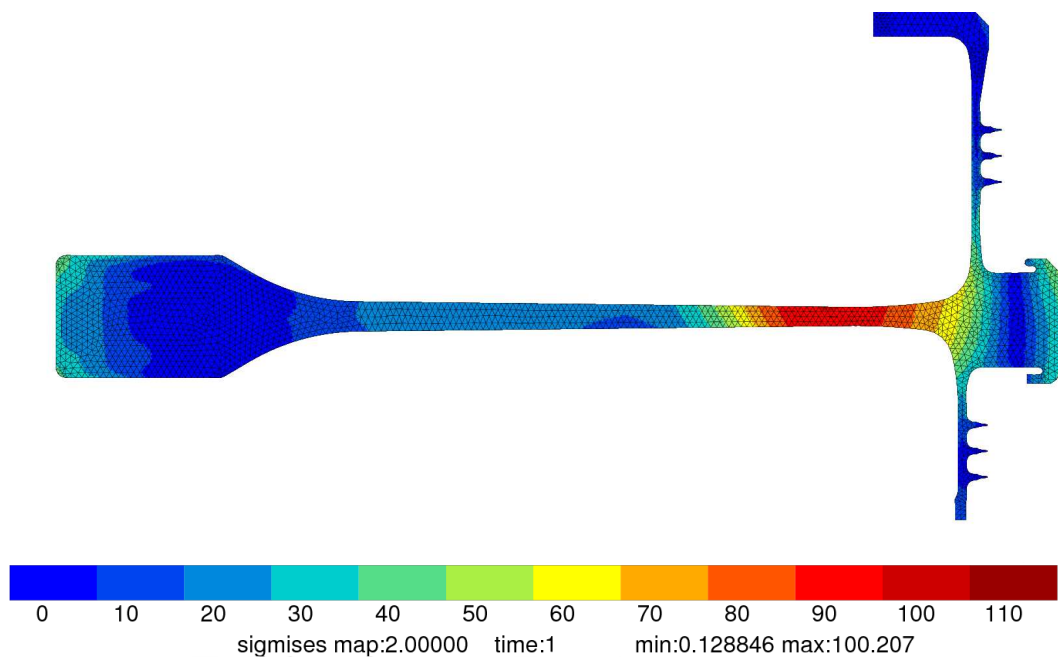


Figure V.12 : Contour map of the equivalent von Mises stress at the end of machining, RL model $\delta_{\alpha \rightarrow \beta} = -0.0014$

V.4 2D Finite Element Simulations of the Disc in Operation

A macroscopic model proposed by [Baroumes, 1998] for Ti-6242 is used in this section, as the macroscopic model “CC” is more critical for TA6V than “RL” because it has been proved in the previous section. This macroscopic model for the studied alloy Ti-6242 will be called as “CB” below.

A thermomechanical Z-set calculations of the disc in operation have been performed. The mesh represented in Fig.V.5 contains a total of 8428 nodes and 3869 of elements.

The aim of this section is to answer the following question: is there an important effect on the final state of stress field in the disc calculated with or without taking into account the residual stress due to heat treatment and machining process.

For operating conditions, the disc is submitted to cyclic temperature and centrifugal loadings. The history of prescribed rotation speed is shown in Fig.V.13 and the temperature cycle is shown in Fig.V.14.

Simulations have been performed with and without residual stress in order to answer the previous question.

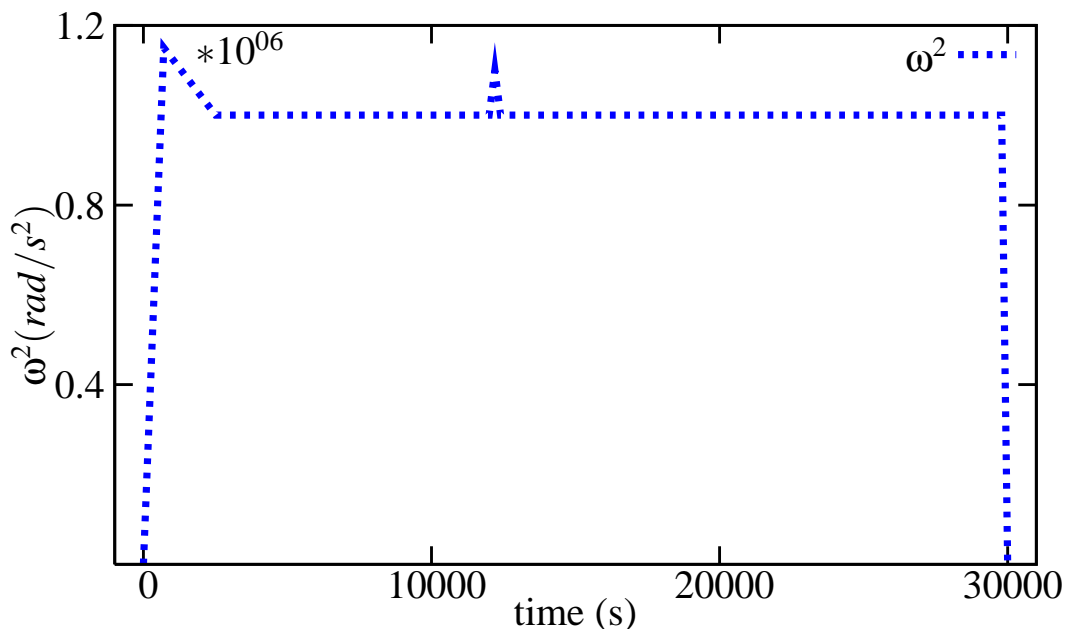


Figure V.13 : Applied rotating rate cycle

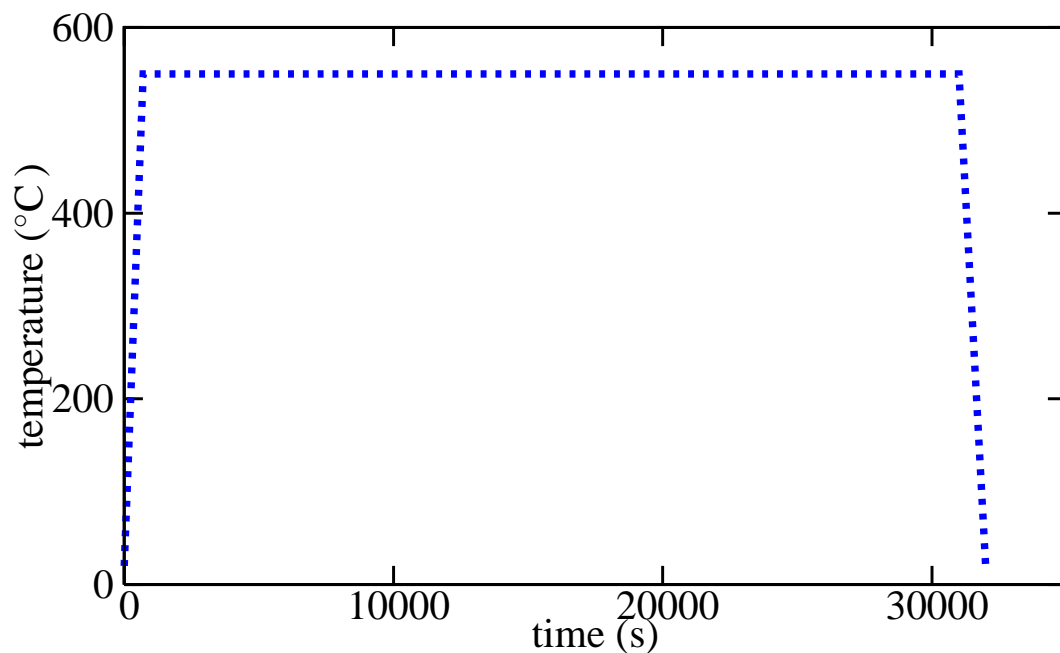


Figure V.14 : Temperature applied cycle

V.4.1 Stress and Strain Results Analysis

- Results of the simulations of the disc in operation with and without residual stress are plotted in Fig.V.15 and V.16. In the case of computations without residual stress, we can check that the equivalent von Mises stress at maximum loading reaches its maximum value of about 538 MPa in the “Upperweb” of the disc (Fig.V.15). If residual stress are taken as the initial state, the maximum value of the equivalent von Mises stress is equal to 552 MPa at the same loading map (Fig.V.16). These results demonstrate that the large initial difference between both calculations vanishes during operation, and that it is not needed to introduce the initial residual stress field in the calculation.
- Finally, Fig.V.17 shows the history of the cumulated plastic strain for the most critical Gauss point (number 6 in element 1697). A significant local plastic flow occurs in the calculation with residual stress, leading to a stress redistribution in the structure. This effect explains why the final states are not far from each other in both calculations.

V.4.1.1 Conclusions

After evaluating the residual stress field in the forged disc, a noticeable residual state was found according to the used constitutive equations. Nevertheless, it was also shown that the influence of the initial stress field vanishes during the operation, due to the large initial plastic accommodation. As a consequence, the results with and without initial stress are very similar.

Après avoir évalué le champ des contraintes dans le disque forgé, un état visible a été trouvé selon les équations essentielles utilisées. Néanmoins, on a aussi montré que l'influence des champs de la traction initial disparaît pendant le fonctionnement, en raison de la grande plastique accommodation initiale. En conséquence, les résultats avec et sans contrainte initiale sont très semblables.

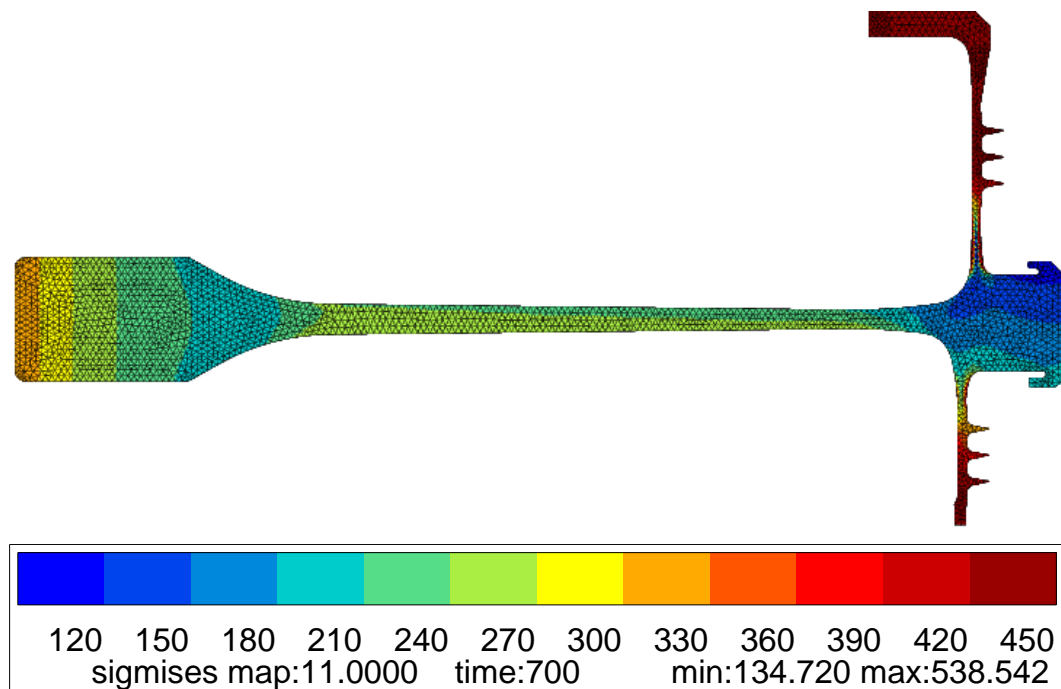


Figure V.15 : Mises stress field at maximum load, disc in operation computed without residual stress – CB model

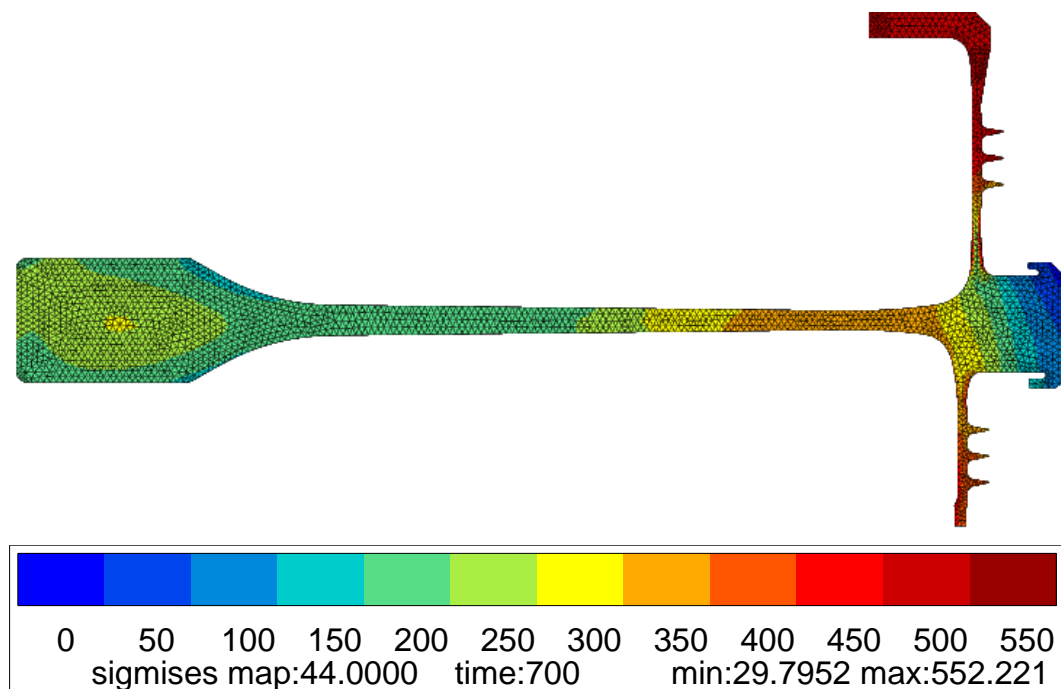


Figure V.16 : Mises stress field at maximum load, disc in operation computed with residual stress – CB model

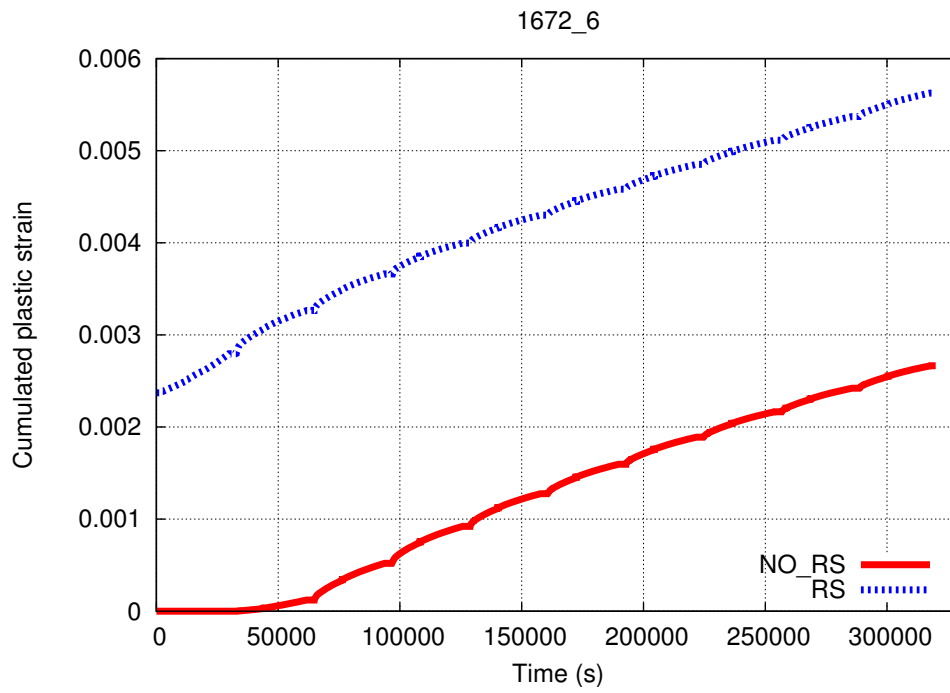


Figure V.17 : History of cumulated plastic strain at the point that shows the largest plastic flow

V.5 3D Finite Element Disc Simulations

The residual stress field that has been characterized in the previous section can introduce artefacts in the specimens that are taken from non-manufactured discs. The aim of the present section is to estimate the distortion that is present after machining of the specimens, and to check if the remaining residual stress may play a role on the subsequent behaviour, and influence the response of the specimens. These calculations are made on a sector of the disc. After calculation of the disc, the mechanical fields are transferred on two samples, the size of which are 12 mm in diameter and 56 mm in length, placed in the disc according to Fig.V.18 (Snecma data).

Using the same type of 3D mesh, another type of calculation is also performed: a slit is made in the disc, in order to see how strong is a closure due to the residual stress field. The simulated results are then qualitatively compared with experiments.

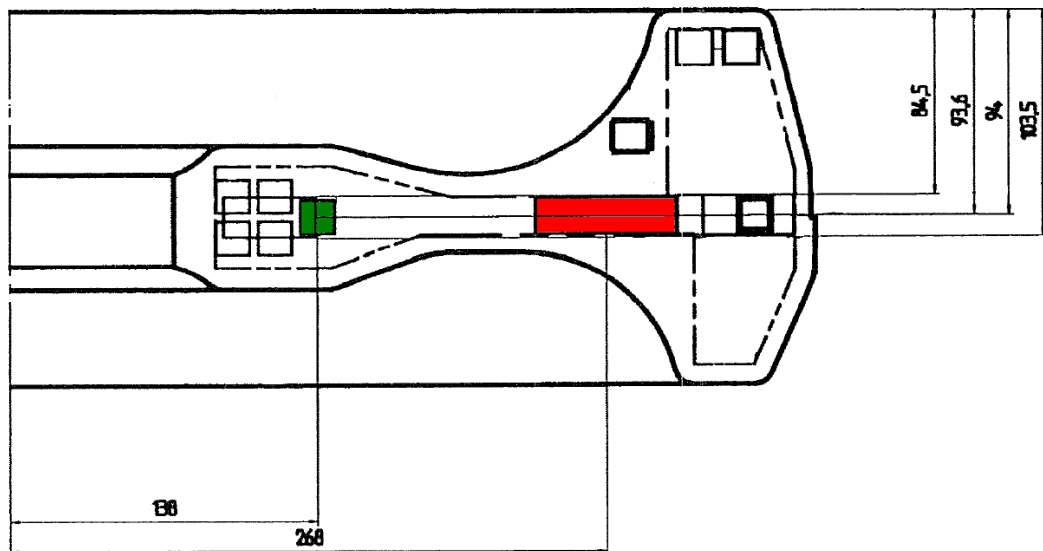


Figure V.18 : Positions of two samples in the non-manufactured disc, a green specimen on the left is in bore position, a red specimen on the right is in web one (Snecma database)

V.5.1 Geometric Models

A mesh of the entire raw disc is shown in Fig.V.19 (a). Due to the cyclic symmetry, only one 50° sector has been considered, as shown in Fig.V.19 (b). Using such an angle allows to have space for placing two specimens (respectively radial and tangential) in the mesh. The same mesh is then used to model a slit effect. The maximum number of degrees of freedom (DOF) for these simulations is 135500. The 4-node full integration finite element meshes are prepared by using Z-set and INRIA remeshing tools. All the calculations are done in the numerical package Z-set.

V.5.2 Boundary Conditions and Loading

Boundary conditions are imposed on the orthoradial faces of the disc sector. A multi-point constraint condition is used to enforce the cyclic symmetry. The oil quenching stage is simulated, with the conditions and the material properties of the 2D case described in the

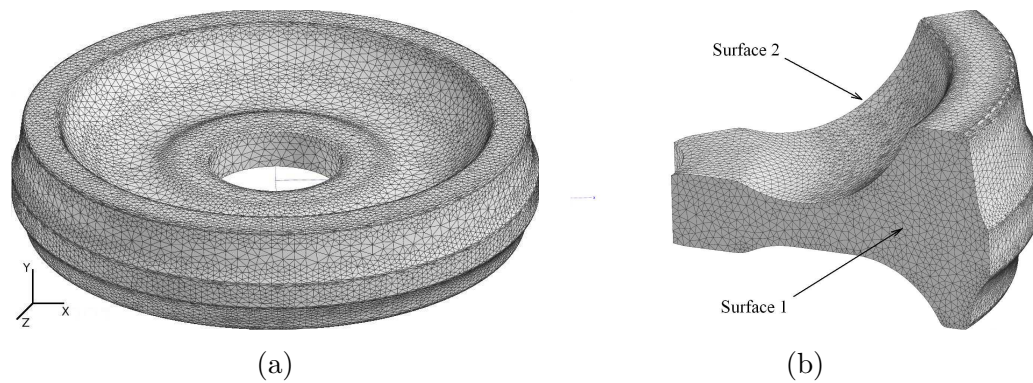


Figure V.19 : a) Mesh of the entire disc without a slit; b) A 50° disc sector

previous section. There is no external mechanical loading. The nodal temperature history is taken from a 3D heat treatment problem, that is solved in the first place.

V.5.3 Material models

One of our goals with the present calculation is to compare our estimations of the residual stress field with the results obtained by Snecma. This is one of the reasons that a classical Chaboche's model "CB" is chosen (another one is described in the previous section). The identification has been performed across a large temperature range (from RT to 1000°C) by using the parameters from [Baroumes, 1998].

V.5.4 Stress and Strain Analysis Results

The final σ_{33} stress field at the end of the quenching operation is shown in Fig.V.20, where the results computed at Centre des Matériaux are compared to those done by Snecma. The stress fields are quite similar and a discrepancy equal to 14% has been caused by some assumptions of simplification by using theoretical thermal and rotating rate cycles.

Fig.V.20 shows the contour map of the orthoradial stress component σ_{33} at the end of machining disc (final disc). A good agreement is observed between our result and Snecma computation. A relatively small difference exists in the maximum value of $\sigma_{33} = 200$ MPa in the case of Snecma evaluation and CdM one where the maximum value is equal to 283 MPa. The reason is due to the several assumptions we made, especially, for doing thermal calculation, as only the last stage of quenching was modelled and the last stage of tempering, reducing the stress level, was not modelled.

The virtual machining of specimens in the disc involves two stages:

- The transfer of the internal variable fields on specimens, without taking into account the boundary conditions.
- One stage FE calculation in order to enforce the new boundary condition (free external surface).

The specimens are pieces of cylinders, as shown in Fig.V.22. An important bending effect can be observed on the final deformed shape, once the new equilibrium is reached (Fig.V.23). The deformation is larger for the specimen in the web (right side) than in the bore (left side).

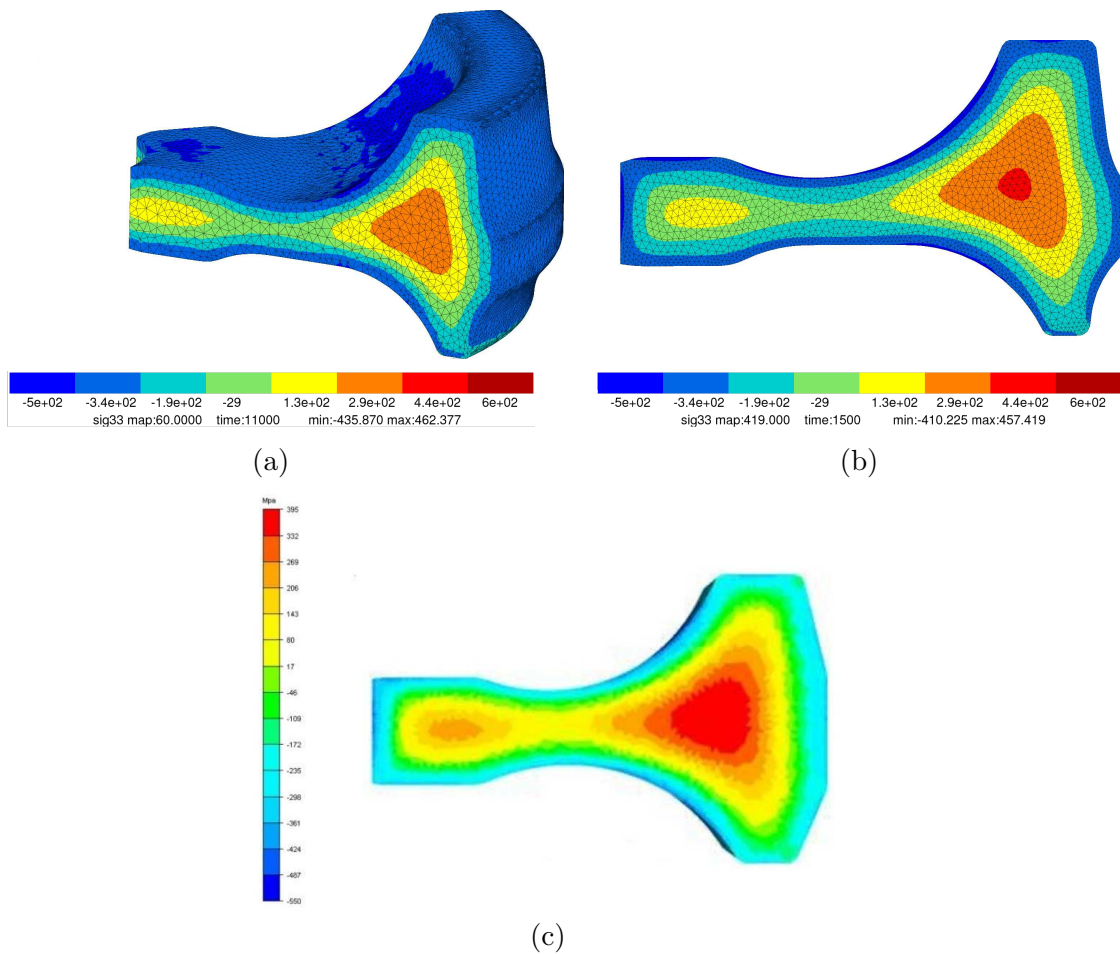


Figure V.20 : σ_{33} stress fields at the end of quenching process (a) 3D present work; (b) 2D present work; (c) Snecma

The final state of von Mises stress fields is given in Fig.V.24 (a) for the specimens located inside the disc and in Fig.V.24 (b) for the cut specimens from the disc. The maximum value of von Mises stress in the web specimen situated in the disc is equal to 321 MPa at the end of the quenching process and after cutting, the maximum value is lowered to 49 MPa. The largest strain and stress are at the end of the quenching process. In the most critical Gauss point an evolution of von Mises equivalent stress is demonstrated in Fig.V.25 (a) (element 29766 point 4) and of ε_{22} is shown in Fig.V.25 (b) (element 35562 point 1). The largest strain is located in the web specimen, as in this section the displacements are the largest. After cutting specimens from the disc the largest strain is situated in the same web specimen after stress redistribution. The strain field of ε_{11} (along the cylinder axis) in the cut specimens is shown in Fig.V.26. The largest strain is also in the web specimen. The maximum values of the strain and stress components in the cut specimen are summarized in Tab.V.2. The largest value of the cumulated strain is equal to $7.4 \cdot 10^{-3}$ (less than 1%) and the largest von Mises equivalent stress is equal to 49 MPa (less than 10% of the maximum applied stress in tests).

Test specimens have smaller size than cut pieces of cylinders, so compared to transfer procedure for machined disc, residual stress state would be even lower.

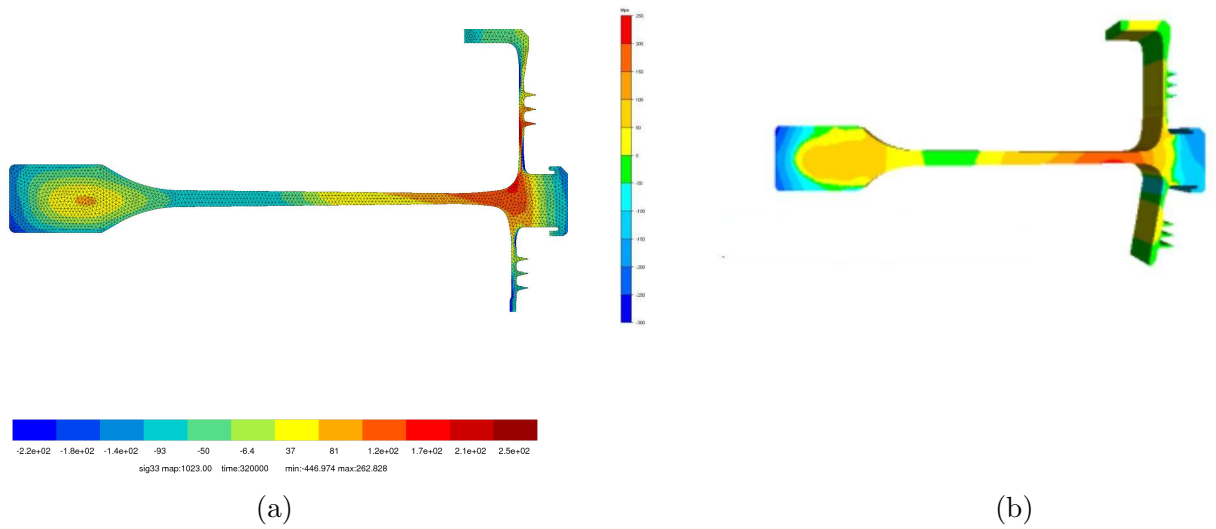


Figure V.21 : σ_{33} stress fields at the end of machining a) present work; b) Snecma



Figure V.22 : Mesh of the specimens



Figure V.23 : Mesh of the deformed specimens (displacement magnification factor = 100)

ϵ_{max}	ϵ_{min}	σ_{max}	σ_{min}
0.74%	0.03%	49.4 MPa	0.8 MPa

Table V.2 : Maximal values of strain and stress components

After the above analyses, by taking into account the possible calculated tempering process and transfer procedure, it seems that residual state conditions can be neglected for the further calculations. In the next section some results concerning computations of the disc with a slit are verified to confirm this statement.

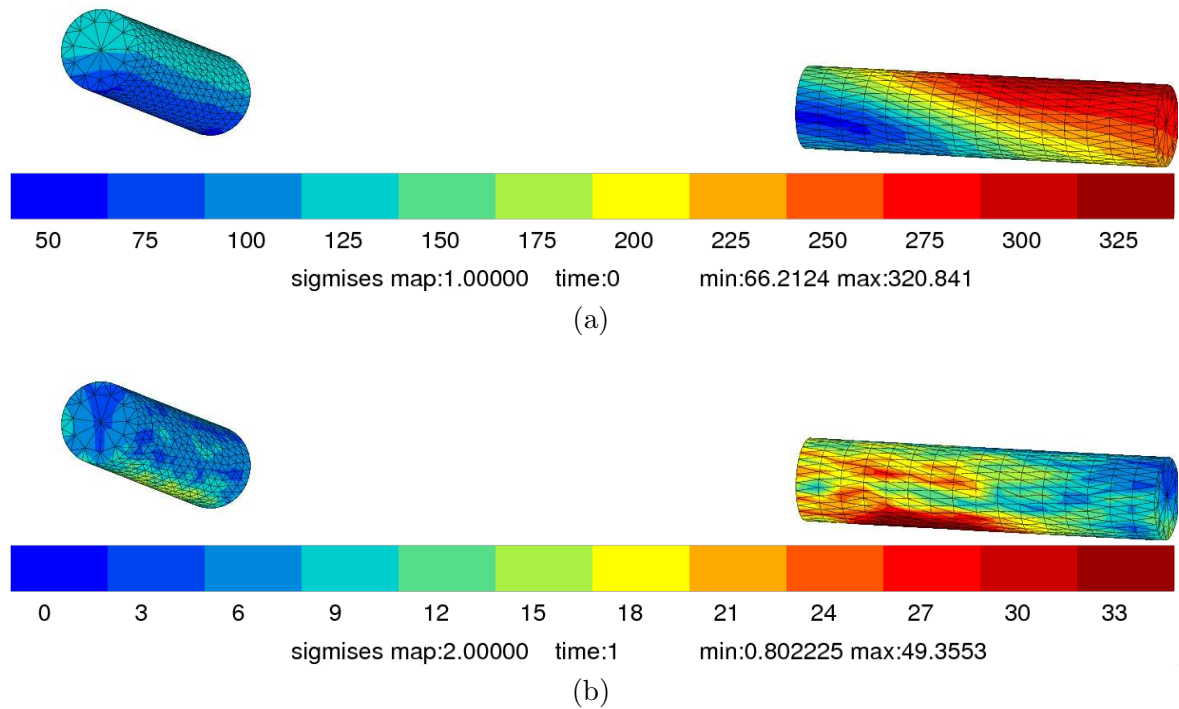


Figure V.24 : (a) von Mises stress fields in the specimens before; (b) von Mises stress fields in the specimens after virtual machining from the disc

V.5.5 Stress and Strain Analyses Results of the Disc with a Slit

When a radial cut is made in a disc after treatment, the gap between the two faces of the slit close, as observed in ENSMA's test [Freiherr von Thungen and Villechaise, 2011]. A FE calculation made in the following aims at verifying this effect.

The mesh of the disc with a slit is drawn in Fig.V.27 (a). As in the previous calculation, a 50° sector is used (Fig.V.27 (b)). In order to model the slit, one side of a surface is considered to be free of constraints.

The numerical procedure is the same as for the previous case. The maps of $U1$ and $U3$ displacements at the end of the simulation are shown in Fig.V.28 (magnification = 100). The displacement normal to the section of the disc has been computed ($U3 \cos(25^\circ) - U1 \cos(65^\circ)$). Its maximum value is equal to -0.1 mm. Due to the symmetry of the problem, and the negative sign, the final result is nothing more than a closure of the slit, with a total displacement of -0.2 mm.

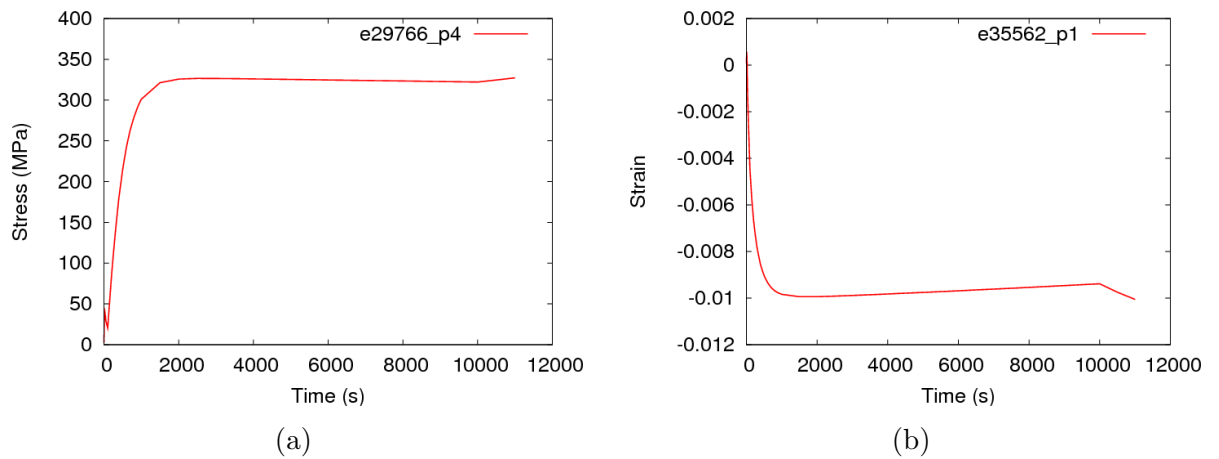


Figure V.25 : (a) Evolution of von Mises equivalent stress in the web specimen in the most critical Gauss point; (b) Evolution of ε_{22} in the web specimen in the most critical Gauss point

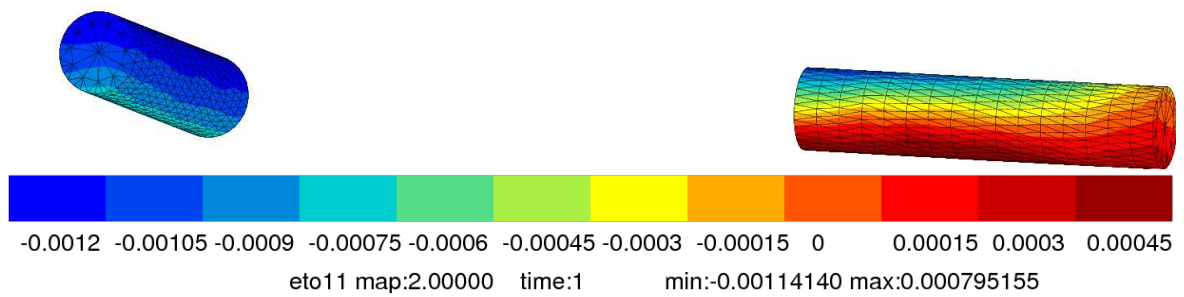


Figure V.26 : Strain field ε_{11} in the web specimen

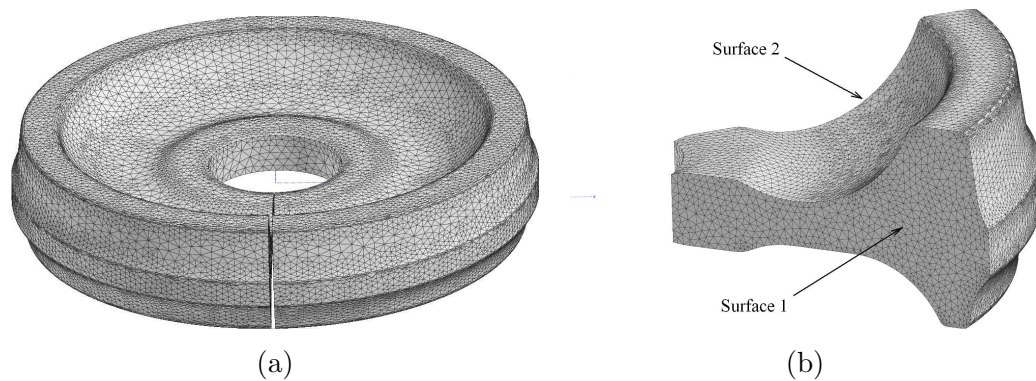


Figure V.27 : a) The mesh of the entire disc with a slit; b) The mesh of a section

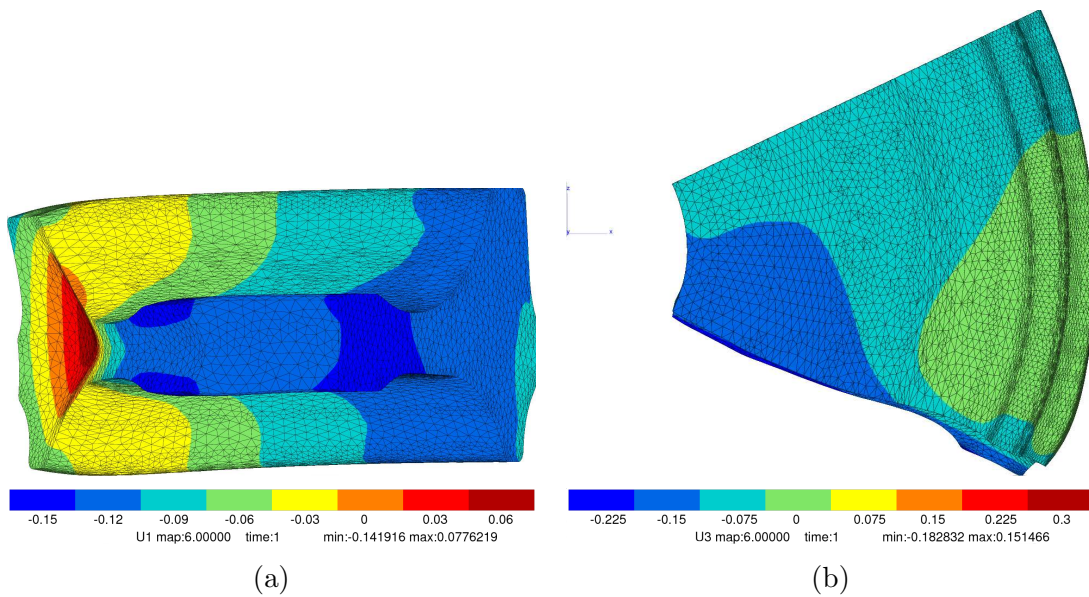


Figure V.28 : Displacement in the disc with a slit: (a) U1, (b) U3

V.6 General Conclusions

The results obtained in this chapter demonstrate the capabilities of **Z-set** code to evaluate the residual stress in a forged disc made of titanium alloy. Two similar titanium alloys have been investigated to make the final decision, if the residual stress state has to be considered or not.

- TA6V alloy:
 - A uniform field model “RL” [Longuet, 2010] which allows to determine the phase composition and the average local stress fields in each phase of the material has been used. The residual stress obtained by using this model are close to those given by a phenomenological Chaboche model “CC” [Robert, 2007], even if the nature of the two models are very different. It allows us to use only the macroscopic model “CB” [Baroumes, 1998] for Ti-6242 forged in the domain β .
- Ti-6242 forged in the domain β :
 - Snecma and CdM evaluation done on the discs are quite similar and this fact reassures that the calculations demonstrate the compatibility.
 - Taking into account residual stress in the FEA of the disc in operation does not significantly affect the final state of stress components.
 - The specimens cut out of a disc are distorted. In the web location a specimen is more deformed than in the bore due to higher displacements. The maximal value of the cumulated strain reaches a value of 1%, that might perturb the subsequent testing, even if the stress level remains low (less than 10% of the maximal applied stress in the pilot-testing). At the end of the quenching process the largest stress and strain values in the specimens are situated inside the disc.
 - Simulations also demonstrate that a slit in the disc tends to close according to experimental observations at ENSMA [Freiherr von Thungen and Villechaise, 2011].

Les résultats obtenus dans ce chapitre montrent les capacités de Z-set code pour évaluer la contrainte résiduelle dans un disque forgé en alliage de titane. Deux alliages de titane voisins ont été examinés afin d'examiner l'état de la contrainte résiduelle.

- *alliage TA6V :*
 - *Un modèle à champs moyens “RL” [Longuet, 2010] qui permet de déterminer la composition des phases et les champs de contraintes locales dans chaque phase a été utilisé. La contrainte résiduelle obtenue en utilisant ce modèle est proche de celle qui est obtenues en utilisant un modèle de Chaboche classique “CC” [Robert, 2007], même si la nature des deux modèles est très différente. Cette similitude justifie l'utilisation du modèle macroscopique “CB” [Baroumes, 1998] dans un environnement industriel.*
- *Ti-6242 forgé dans le domaine β :*
 - *Les simulations numériques des disques que nous avons effectuées confirment les résultats obtenus classiquement par Snecma.*
 - *La prise en compte de la contrainte résiduelle dans le calcul du disque en fonctionnement n'affecte pas de façon significative l'état final des composantes de la contrainte, en raison de la redistribution progressive qui s'opère.*
 - *Les échantillons prélevés dans un disque sont déformé. C'est au niveau de la toile que la déformation est la plus importante. La valeur maximale de la déformation cumulée atteint une valeur de 1 %, qui pourrait perturber l'essai ultérieur, même si le niveau de contrainte reste bas (moins de 10 %) de la traction maximale appliquée dans le test. Á la fin de la trempe, les valeurs de déformation et de contrainte les plus importantes sont situés á l'intérieur du disque.*
 - *Les simulations montrent aussi qu'une fente dans le disque a tendance á se fermer, ce qui est confirmé par les observations expérimentales effectuées à ENSMA [Freiherr von Thungen and Villechaise, 2011].*

Chapter -VI-

Multiscale Constitutive Equations

VI.1 Introduction

The aim of this chapter is to calibrate a crystal plasticity model that will be used in the rest of the document for performing a full field analysis of the stress and strain state of a microstructure with “plumes” which are described in the ”Biography”. The material parameters are obtained by fitting the model response with macroscopic curves obtained in tensile tests. The model involves 1000 grains. The behavior of the model itself is analysed, paying a special attention to the stress and strain distributions.

VI.2 Single Crystal Model (Microscopic Model)

VI.2.1 Material Description

The material behaviour of individual phases of the Ti-6242 microstructure is simulated by using an isothermal, rate-dependent, crystal plasticity model. The state of microscale stress in a polycrystalline aggregate depends on the grain orientations with respect to the loading direction and on the orientations of their neighbours. The model uses classical crystal plasticity constitutive equations, as described in [Méric et al., 1991]. In a small strain framework, the resolved shear stress (CRSS) τ^s for a slip system \mathbf{s} is the product of the stress tensor by the orientation tensor $\underline{\mathbf{m}}^s$:

$$\tau^s = \underline{\boldsymbol{\sigma}} : \underline{\mathbf{m}}^s = \underline{\boldsymbol{\sigma}} : \frac{1}{2} \cdot (\underline{\mathbf{l}}^s \otimes \underline{\mathbf{n}}^s + \underline{\mathbf{n}}^s \otimes \underline{\mathbf{l}}^s) \quad (\text{VI.1})$$

with $\underline{\mathbf{n}}^s$ the normal to the slip plane and $\underline{\mathbf{l}}^s$ the slip direction. The interaction between slip systems is taken into account by using the interaction matrix first described in [Kocks and Brown, 1966]. The components h_{rs} of this matrix define respectively selfhardening (diagonal terms) and latent hardening. Only selfhardening is considered, that is $h_{rs} = \delta_{rs}$, as in previous papers dealing with titanium alloy [Dick, 2006]. Two material parameters, \mathbf{c} , \mathbf{d} , are related to nonlinear kinematic hardening and \mathbf{c}_l to linear kinematic hardening. Isotropic hardening introduces \mathbf{Q} , \mathbf{b} and h_{rs} parameters. The viscous effect is kept small due to the choice of \mathbf{K} and \mathbf{n} .

The activation of the slip system \mathbf{s} is determined by a scalar yield function f^s :

$$f^s = |\tau^s - x^s| - r^s \quad (\text{VI.2})$$

where r^s and x^s are the hardening variable accounting respectively for isotropic and kinematic hardening, with:

$$r^s = r_0 + bQ \sum_{r \in S} h_{rs} \rho^r \quad (\text{VI.3})$$

$$x^s = c\alpha^s \quad (\text{VI.4})$$

and:

$$\dot{\rho}^s = (1 - b\rho^s) \cdot \dot{\nu}^s \quad \text{isotropic hardening} \quad (\text{VI.5})$$

$$\dot{\alpha}^s = (\text{sign}(\tau^s - x^s) - d\alpha^s) \cdot \dot{\nu}^s \quad \text{non linear kinematic hardening} \quad (\text{VI.6})$$

$$\dot{\alpha}^s = \text{sign}(\tau^s - x^s) \cdot \dot{\nu}^s \quad \text{linear kinematic hardening} \quad (\text{VI.7})$$

$$(\text{VI.8})$$

so that:

$$r^s = r_0 + Q \sum_{r \in S} h_{rs} \{1 - \exp(-b \cdot v^r)\} \quad (\text{VI.9})$$

The viscoplastic strain rate is obtained from the slip rates according to:

$$\dot{\underline{\xi}}^D = \sum_{s \in S} \dot{\gamma}^s \underline{\mathbf{m}}^s \quad (\text{VI.10})$$

The slip rate $\dot{\gamma}^s$ on the slip system s is given by :

$$\dot{\gamma}^s = \left\langle \frac{|\tau^s - x^s| - r^s}{K} \right\rangle^n \text{sign}(\tau^s - x^s) \quad (\text{VI.11})$$

A system will be active when its critical resolved shear stress τ^s (CRSS) is larger than $x^s + r^s$ or smaller than $x^s - r^s$ (slip is allowed to be positive or negative on a given direction). Isotropic hardening r^s describes an expansion, meanwhile kinematic hardening x^s figures a translation of the elastic domain.

In contrast to the macroscopic model having three partitions of strain, the present microscopic model has two partitions, as the model is only used at RT:

- Partition of the strain tensor

$$\dot{\underline{\xi}} = \dot{\underline{\xi}}_e + \dot{\underline{\xi}}_{vr} + \dot{\underline{\xi}}_{vl} \quad (\text{VI.12})$$

$\dot{\underline{\xi}}_e$, $\dot{\underline{\xi}}_{vr}$, $\dot{\underline{\xi}}_{vl}$ are elastic strain and the two components of the viscoplastic strain tensors respectively.

- Criteria in this case are expressed as the yield surfaces in the way

$$f_r^s(\underline{\sigma}, \underline{\mathbf{x}}_r^s, r^s) = |\tau^s - x_r^s| - r^s \quad (\text{VI.13})$$

$$f_l^s(\underline{\sigma}, \underline{\mathbf{x}}_l^s) = |\tau^s - x_l^s| \quad (\text{VI.14})$$

where $\underline{\sigma}$ is the stress tensor, $\underline{\mathbf{x}}_r$ and $\underline{\mathbf{x}}_l$ are the hardening variables associated with different kinematic hardening mechanisms and r^s is the yield radius in isotropic hardening mechanism.

The material parameters for the rapid evolution are: K_r , n_r (viscous part), r_{0r} (initial yield), c_r , d_r (nonlinear kinematic hardening), meanwhile the material parameters for the low rate part of the model are: K_l , n_l (viscous part) and c_l (linear kinematic hardening). All these parameters are not temperature dependent and they are associated to RT.

VI.2.2 Basic Material Data for α and β phases

The intrinsically anisotropic character of the hexagonal crystal structure of the α phase has important consequences for the elastic properties of titanium and its alloys. The variation of the modulus of elasticity E of pure α titanium single crystals at RT as a function of the angle γ between the c-axis of the unit cell and the stress axis is shown in Fig.VI.1 (a) [Lutjering and Williams, 2003].

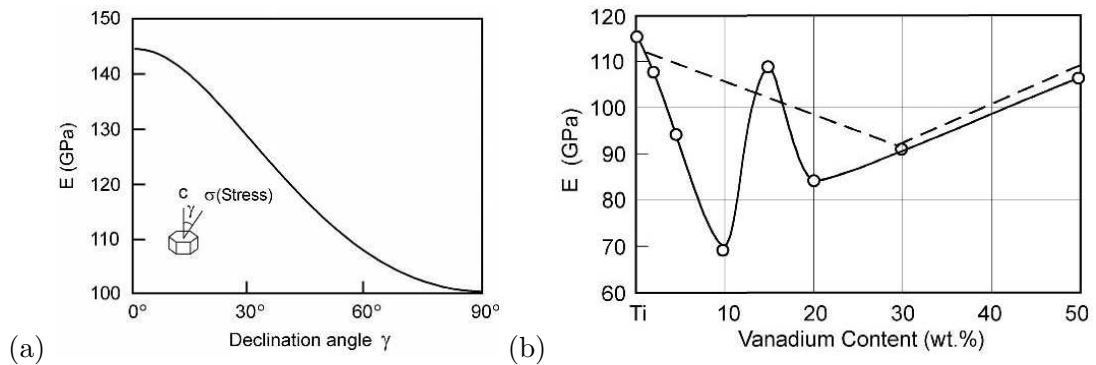


Figure VI.1 : (a) Modulus of elasticity E of α titanium single crystals as a function of declination angle γ [Lutjering and Williams, 2003]; (b) Modulus of elasticity E of Ti-V alloys, solid line: 24h, 900°C/WQ, dashed line:annealed at 600°C [Lutjering and Williams, 2003]

Modulus data for Ti-V alloys in the water quenched condition are shown in Fig.VI.1 (b). This shows that the β phase in general has a lower modulus of elasticity than the α phase, as vanadium content increases the amount of β phase and its modulus of elasticity is generally lower than the metal's E [Lutjering and Williams, 2003].

Twinning is a phenomenon that is mentioned by several authors [Lapczuk et al., 2000], [Hsiung et al., 2000]. The most critical twinning systems are described in [Chun et al., 2005], [Xiaoli et al., 1995]. The occurrence of twinning is limited by the amount of aluminium. A limited amount of twinning of the type $(10\bar{1}2)$ is observed in Fig.VI.2 by [Paton et al., 1973], who indicates a suppression of the effect after 3.5% Al. The twinning effect is neglected for Ti-6242, as it has got about 6% of aluminium. It is worth remarking that the twinning activity depends on β phase grain size [Ankem and Greene, 1999].

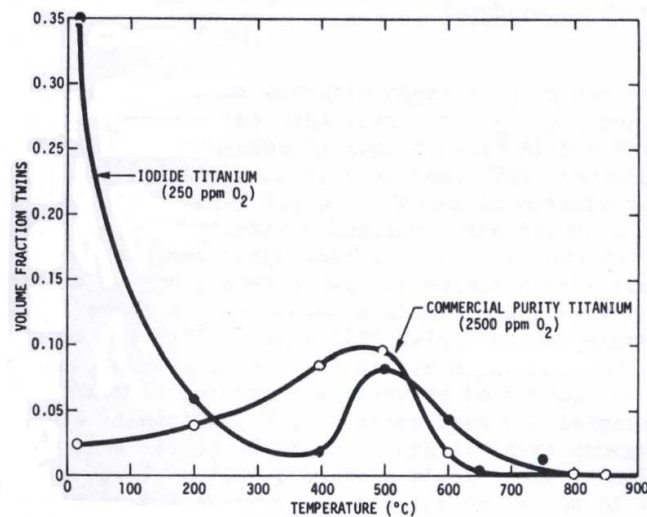


Figure VI.2 : Influence of deformation temperature on the volume fraction of twins after 5% strain in Ti of two different purities (Oxygen concentration in wt. ppm.) [Paton et al., 1973]

The anisotropic elastic components have been taken from [Simmons and Wang, 1971] for

HCP crystals and from [Stapleton et al., 2008] for BCC ones (see Tab. VI.1). It can be easily seen that these parameters are quite anisotropic in both α and β phases.

Phase	$C_{11}=C_{22}$ (GPa)	C_{33} (GPa)	C_{12} (GPa)	$C_{13}=C_{23}$ (GPa)	C_{44} (GPa)	$C_{55}=C_{66}$ (GPa)
α	162.4	180.7	92.0	69.0	46.7	46.7
β	130.0	130.0	110.0	110.0	55.0	55.0

Table VI.1 : Components of elasticity matrix in the material coordinates for HCP phase and BCC phase in the Ti-6242 microstructure

In addition to the normal anisotropy coming from crystal plasticity, two factors affect the local behaviour: 1) Burger's relationship between the two phases; 2) The difference in the length of the Burgers' vectors in both phases $|b_\alpha|/|b_\beta| = 1.04$. That will introduce CRSS differences inside each family, at RT [Savage et al., 2001], [Savage et al., 2004], [Deka et al., 2006] or at high temperatures [Salem and Semiatin, 2009] (Ti-6Al-4V at 815°C). In our case, the CRSS for every slip system is chosen from [Savage et al., 2001], [Deka et al., 2006], [Venkatramani et al., 2007] and some details on experiments are described in them. Dogbone single colony samples ([Savage et al., 2001]) have been tested and they have very small sizes, about 300 μm by 1700 μm containing both the desired Burger's vector to be activated were cut from the single colony rod using a SiC abrasive saw, so the results can be reliable enough. The lath sizes and the values of the basal and prismatic CRSS are presented in Tab.VI.2 [Venkatramani et al., 2007]. Comparable values are given elsewhere [Savage et al., 2001], [Savage et al., 2004], what makes us confident in the present estimation (these values are quite close to CRSS). l_β is much thinner than l_α and this fact is quite important to know because the colony's widths influence the behaviour of the material. They are taken into account by using the Hall-Petch relationship described below. Due to Burger's relationship, the three slip directions in HCP crystal (Fig.III.8 [Venkataramani et al., 2008]) are quite different and the values of CRSS as well.

Pyramidal slip systems are very important in Ti-6242, as they are active in this alloy and their impact is significant [Lefranc, 2007], [Freiherr von Thungen et al., 2011]. The estimation of CRSS for pyramidal systems is not a simple task. In the solution proposed below, the CRSS for the pyramidal systems have been calculated by using the results illustrated in Fig.VI.3 [Paton et al., 1973] (relative CRSS and their ratios between main slip systems are quite different and a summary table is in the article [Zhang et al., 2007]). First-order pyramidal slip systems $\langle c + a \rangle$ and second-order pyramidal slip systems $\langle c + a \rangle$ are supposed to have the same value of τ_{CRSS} . In our case (Tab.VI.2) the ratio $\tau_{CRSS}^{bas}/\tau_{CRSS}^{prism}$ is the same as in this article (the average values have been taken), so it has been assumed that the ratio $\tau_{CRSS}^{bas}/\tau_{CRSS}^{pyr\langle c+a \rangle}$ is the same for our study too. In the article [Medina Perilla and Gil Sevillano, 1995] the ratios $\tau_{CRSS}^{prism}/\tau_{CRSS}^{bas}$ and $\tau_{CRSS}^{pyr\langle c+a \rangle}/\tau_{CRSS}^{pyr\langle a \rangle}$ are the same, so for our model $\tau_{CRSS}^{pyr\langle a \rangle}$ has been calculated according to: $\tau_{CRSS}^{bas}/\tau_{CRSS}^{prism} = \tau_{CRSS}^{pyr\langle c+a \rangle}/\tau_{CRSS}^{pyr\langle a \rangle}$ (only the positions for τ_{CRSS}^{bas} and τ_{CRSS}^{prism} have been changed because $\tau_{CRSS}^{bas} > \tau_{CRSS}^{prism}$ which is contrary to our problem and it is right to do so). The final values are represented in Tab.VI.3 [Paton et al., 1973].

τ_{CRSS} for β phase were found in [Deka et al., 2006], [Venkatramani et al., 2007] and they were calculated by simulating experimental tests. Their exact values are brought about below.

Basal system	$\tau_{CRSS}^{bas\langle a1 \rangle}$ (MPa)	$\tau_{CRSS}^{bas\langle a2 \rangle}$ (MPa)	$\tau_{CRSS}^{bas\langle a3 \rangle}$ (MPa)
	284.0	315.0	243.0
Prismatic system	$\tau_{CRSS}^{prism\langle a1 \rangle}$ (MPa)	$\tau_{CRSS}^{prism\langle a2 \rangle}$ (MPa)	$\tau_{CRSS}^{prism\langle a3 \rangle}$ (MPa)
	240.0	245.0	255.0
Characteristic lath thickness of single colony	l_α (μm)	l_β (μm)	
	10.0	2.0	

Table VI.2 : τ_{CRSS} and lath characteristic size of single colonies for every basal and prismatic slip system [Deka et al., 2006], [Venkatramani et al., 2007]

Pyramidal system	$\tau_{CRSS}^{pyr\langle a \rangle}$ (MPa)	$\tau_{CRSS}^{pyr\langle a+c \rangle}$ (MPa)
	510.5	582.0

Table VI.3 : CRSS for every pyramidal slip system [Paton et al., 1973].

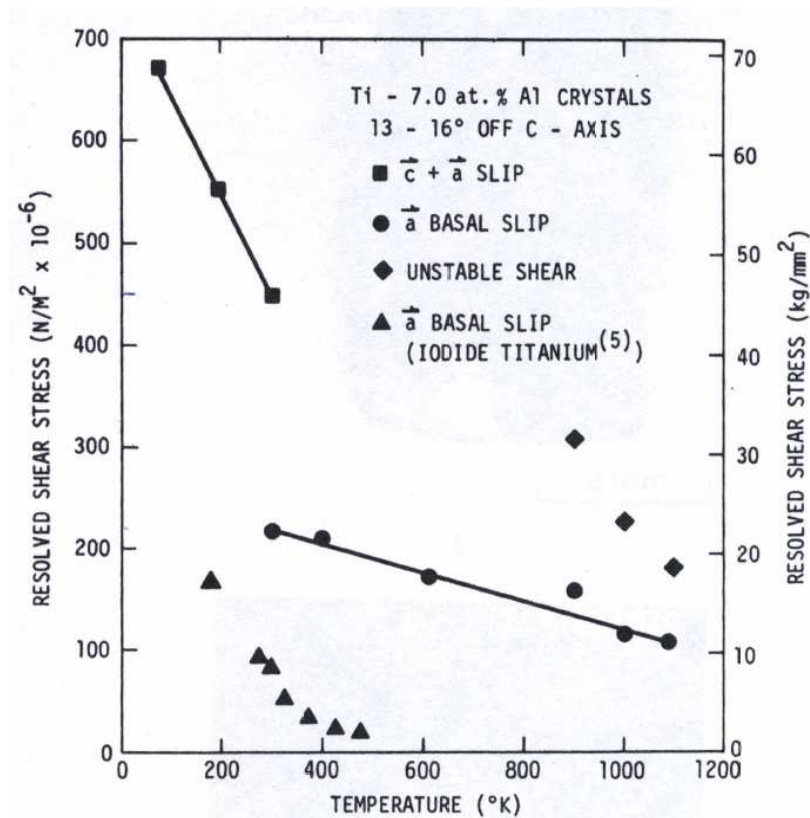


Figure VI.3 : Resolved shear stress *vs* temperature of iodide Ti and Ti-7.0% Al single crystals for the deformation modes indicated in the legend [Paton et al., 1973]

VI.2.3 Size-effect in Crystal Plasticity

VI.2.3.1 General Expression

The final mechanical properties, especially the fatigue resistance, are strongly influenced by characteristics of the microstructure like grain morphology, phase volume fraction, grain orientation and grain size. One of the most important microstructural parameters determining the mechanical properties is the width of the α and β lamellae, since this factor controls the effective slip length of the activated system. As in Ti-6242 there are a lot of lamellae which are thin enough to produce a size-effect. Following theoretical issues [Venkatramani et al., 2007] and for experiments [Maruyama et al., 2001] the Hall-Petch relationship [Hall, 1951], [Petch, 1953] is chosen to model this phenomenon. The CRSS is then written:

$$\tau_{CRSS} = \tau_{CRSS_0} + \frac{A}{\sqrt{D}}$$

where A and D refer to slope and to the characteristic length scale ruling the size effect. The length scale D represents lath thickness in the colonies respectively l_α and l_β in α and β phases. As seen previously in Fig. III.9 [Zhang et al., 2007], [Bridier et al., 2005], Fig.III.10 [Delfosse, 2005], [Savage et al., 2004] and in Tab. III.1, the respective crystal orientations of α and β phases promote an anisotropic behaviour of the material with two types of slip modes [Suri et al., 1997], [Savage et al., 2001], [Savage et al., 2004]. Tab.VI.4 recalls that directions a_1 of HCP and b_1 of BCC coincide (it is worth noting that the axis c is not always parallel to the interface α/β). This direction corresponds to easy slip. All the other will generate a hard deformation mode due to the non coherent interface.

Type of crystal	Slip system	Characteristic thickness	Deformation mode
HCP	a_1 basal	l_α	Soft
	a_2 basal		Hard
	a_3 basal		Hard
	a_1 prismatic		Soft
	a_2 prismatic		Hard
	a_3 prismatic		Hard
	pyramidal $\langle a \rangle$		Hard
	pyramidal $\langle a + c \rangle$		Hard
BCC	b_1 for (101), (112), (123)	l_β	Soft
	Other directions		Hard
	b_2, b_3, b_4 for (101), (112), (123)		

Table VI.4 : Modes in every slip system

VI.2.3.2 Determination of A for the Soft Slip Mode

The expression for the Hall-Petch slope for soft slip mode is given as [Li and Chou, 1970]:

$$A_{soft} = \sqrt{\frac{G \cdot b \cdot (2 - \nu) \cdot \tau^*}{2 \cdot \pi \cdot (1 - \nu)}}$$

where G is the shear modulus, b is the Burger's vector, ν is the Poisson's ratio and $\tau^* = 0.026 \cdot G$ is the barrier strength for the grain boundary [Dimiduk et al., 1998], [James and Gaines, 1967]. This expression is related to the original Eshelby-Frank-Nabarro problem, and has been applied by [Rao and Hazzledine, 1999].

VI.2.3.3 Determination of A for the Hard Slip Mode

The expression for the Hall-Petch slope corresponding to the hard slip mode, developed by [Eshelby, 1963] and [Semiatin and Bieler, 2001] is given by:

$$A_{hard} = \sqrt{\frac{4 \cdot G \cdot b \cdot \tau^*}{\gamma \cdot \pi}}$$

where $\gamma = (1 - \nu)$ for edge dislocations and $\gamma = 1$ for screw dislocations. An average value $(1 + (1 - \nu))$ will be used in the following. The barrier strength τ^* for the hard slip mode is calculated from calibrated values for the corresponding slip systems or $\tau^* = 0.015 \cdot G$ [Dimiduk et al., 1998] in order to compute K_{hard} for pyramidal $\langle a \rangle$ and pyramidal $\langle c + a \rangle$ slip systems.

VI.2.3.4 Critical Lamellae Spacing λ^*

The effect of lamellae spacing on mechanical properties has been shown in [Maruyama et al., 2001] and [Cao et al., 2000]. The critical lamellae spacing λ^* , below which there is no strengthening, is given:

$$\lambda^* = \frac{G \cdot b}{(1 - \nu) \cdot \tau^*}$$

In our case, there are no smaller sizes of lamellae, so this effect does not take place.

VI.2.3.5 Determination of A_{soft} and A_{hard}

The values of the lattice parameters and of the Burger's vectors for α and β phases are taken from [Suri et al., 1999]. They are collected in Tab.VI.5, together with G , ν_α , ν_β and $|b_\alpha|$ (HCP $\langle c + a \rangle$) that have been calculated by using the following formulas for:

Inplane shear modulus: $G = C_{66}$;

Poisson's ratio for loading: $\nu_{LT} = C_{13}/(C_{11} + C_{12})$;

Burger's vector $|b_\alpha|$ (HCP $\langle c + a \rangle$) = $\sqrt{|b_\alpha|(HCP \langle a \rangle)^2 + |b_\alpha|(HCP \langle c \rangle)^2}$

The ratio $c/a = 1.586$ is very close to 1.587 for a pure Ti- α [Jousset, 2008]. This value is smaller than 1.633, so the prismatic planes glide easier than the basal ones [Feaugas, 1994]. It is worth noting that the difference in the lengths of the Burger's vectors in the two phases ($|b_\alpha|/|b_\beta|$) possibly contributes to the final anisotropy of the alloy [Suri et al., 1999]. This fact is included in the expressions of the coefficients A_{soft} and A_{hard} .

Phase	Constant	Value
α	G (transformed β HCP)	46.7 GPa
β	G (transformed β BCC)	55.0 GPa
	ν_α	0.271
	ν_β	0.458
	a_α	0.295 nm
	c_α	0.468 nm
α	$ b_\alpha $ (HCP $\langle a \rangle$)	0.295 nm
	$ b_\alpha $ (HCP $\langle c + a \rangle$)	0.553 nm
	c/a	1.586
β	a_β	0.327 nm
	$ b_\beta $ (BCC)	0.284 nm

Table VI.5 : Values of constants used to calculate A_{soft} and A_{hard} [Suri et al., 1999] (lattice parameters, lengths of Burger's vectors for α and β phases). G , ν_α , ν_β and $|b_\alpha|$ (HCP $\langle c + a \rangle$) have been calculated.

VI.2.4 Final Calibration and Results

VI.2.4.1 Determination of τ_{CRSS} for α Phase

In our calibration process, the tension-compression asymmetry has not been taken into account, as this effect is not observed on macroscopic experimental curves described in the previous sections. The values in Tab.VI.2 are for the single colony samples. As seen in this table, the values related to the hard slip mode are greater than for soft slip mode, except for a_3 basal system. This observation is not currently explained by the Burger's relationship [Savage et al., 2001], but there are some hypotheses concerning dislocation movements which could contribute to the development of this effect (more details in [Savage et al., 2004]).

Tab.VI.6 (initial CRSS) shows the values obtained for τ_{CRSS_0} and A for basal and prismatic slip systems in α phase (in parenthesis a reserve number is indicated). The direction a_1 is the soft one, meanwhile a_2 is the hard direction. For the a_3 basal direction, A is found by using the inequality A_{soft} (for a_1 basal) $<$ A_{hard} (for a_3 basal) $<$ A_{hard} (for a_2 basal) and the equation:

$$A_{hard} (for a_3 basal) = [A_{soft} (for a_1 basal) + A_{hard} (for a_2 basal)]/2 \quad (VI.15)$$

τ_{CRSS_0} is supposed to be the same for every crystal direction and it is assumed to be equal to 243.0 for a_3 basal, as 258.9 (a_1) $>$ 243.0 that may not be true. The value of A_{hard} for pyramidal systems $\langle a \rangle$ and $\langle c + a \rangle$ is calculated by using the same formula as before (Tab.VI.7).

VI.2.5 Determination of τ_{CRSS} for β Phase

As previously made for α phase, b_1 is supposed to be the soft direction and $A = A_{soft}$. The value $A = A_{hard}$ is used for the other directions, as shown in

Constant	a_1 basal	a_2 basal	a_3 basal	a_1 prism	a_2 prism	a_3 prism
Single colony/ τ_{CRSS} (MPa)	284.0	315.0	243.0	240.0	245.0	255.0
A (MPa $\sqrt{\mu m}$)	79.4(7)	177.5(1)	128.4(8)	79.4(7)	95.2(8)	126.9(0)
τ_{CRSS_0} (MPa)	258.8(7)	258.8(7)	243.0	214.8(7)	214.8(7)	214.8(7)

Table VI.6 : Constants A and τ_{CRSS_0} for basal and prismatic slip systems of α phase [Deka et al., 2006], [Venkatramani et al., 2007].

Constant	a pyr $\langle a \rangle$	a pyr $\langle c + a \rangle$
Single colony/ τ_{CRSS} (MPa)	510.5	582.0
A (MPa $\sqrt{\mu m}$)	119.2(3)	163.2(4)
τ_{CRSS_0} (MPa)	472.8(0)	530.3(8)

Table VI.7 : Constants A and τ_{CRSS_0} for pyramidal slip system of α phase [Deka et al., 2006].

Tab.VI.8 [Deka et al., 2006], [Venkatramani et al., 2007]. As it was mentioned above, the initial τ_{CRSS_0} were calculated and their values for every crystal direction is not so much different compared to the case of α phase. It means that β phase (BCC crystals) is less anisotropic than α one (HCP crystals).

Constant	b_1 (101)	b (101)	b_1 (112)	b (112)	b_1 (123)	b (123)
Single colony/ τ_{CRSS} (MPa)	250.0		209.6		200.7	
A (MPa $\sqrt{\mu m}$)	100.5(9)	145.8(9)	100.5(9)	145.8(9)	100.5(9)	145.8(9)
τ_{CRSS_0} (MPa)	178.8(7)	178.8(7)	138.4(7)	138.4(7)	100.5(9)	100.5(9)

Table VI.8 : Constants A , τ_{CRSS_0} and τ_{CRSS} for different slip systems of β phase [Deka et al., 2006], [Venkatramani et al., 2007].

VI.2.6 Calibration of the Material Model

Numerical simulations are carried out by means of a 3D Finite Element model (Fig.VI.4). The model is calibrated by comparing the average response of the FE model with the macroscopic curves obtained in tensile and dwell-fatigue tests on cylindrical standard specimens. The material representative volume element (RVE) is a material piece which must include a “sufficient” number of grains, in terms of crystallographic orientation, shape and size [Barbe et al., 2001]. As far as the requested information is just the average response, the FE model can be very crude. In this case, a finite element mesh consisting of 1000 quadratic 3D elements with reduced integration ($10 \times 10 \times 10$) has been used. This number of elements is sufficient, according to the research done by ENSMA [Freiherr von Thungen and Villechaise, 2011] to represent the material

Each Gauss point is affected by a grain, with a random orientation, figuring a non-textured material. Lamellae are not explicitly represented. Such a geometric description would lead to huge meshes and are out of reach in a reasonable CPU

time. Voigt's model is chosen instead, to account for two phases in the same grain. This is a strongly constrained model, that represents a particular material state. Nevertheless, this similar simple transition rule has been successfully used in recent similar works [Deka et al., 2006], [Venkatramani et al., 2007], [Venkataramani et al., 2008].

It is supposed that all parameters but τ_{CRSS} are the same for the different slip systems, for the phases α and β : that still makes a huge number, since we have to introduce a set of (K, n, Q, b, C, D) for every slip system: 77 parameters for α phase (3 basal slip directions (in the direction a_1 there are 5 parameters for rapid and slow evolutions, for other directions there are 9 parameters), 3 prismatic slip directions (9 parameters for every direction), 1 pyramidal $\langle A \rangle$ (9 parameters) and 2 pyramidal $\langle c + a \rangle$ (first and second order, 9 parameters for each case)) and 108 parameters for β (9 parameters for every four Burger's vectors and there are 3 slip systems in this phase).

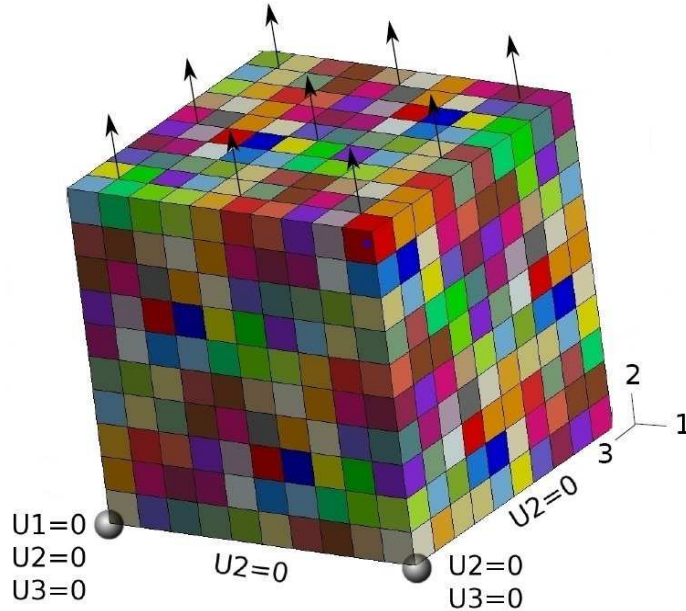


Figure VI.4 : The FE microstructure used for calibrating coefficients of Ti-6242

The standard boundary conditions are illustrated in Fig.VI.4.

Since no kinematic hardening is present in the direction a_1 for basal and prismatic slip planes in Fig.VI.5 (for a sample OA) [Suri et al., 1999] and [Deka et al., 2006], it is not simulated in our model either.

The calibration process concerns tensile tests performed at different strain rates, relaxation, pure fatigue and dwell fatigue tests.

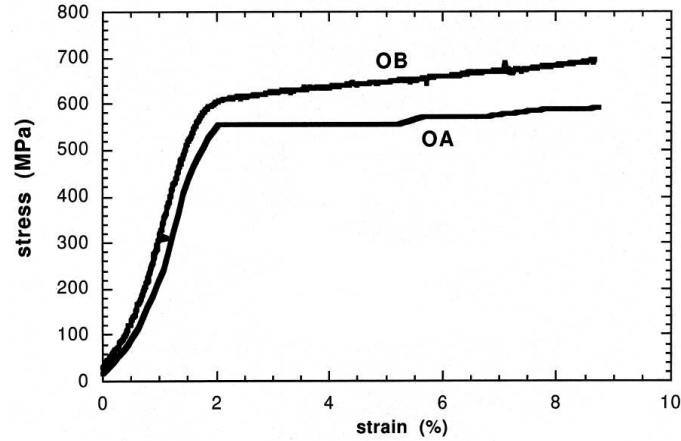


Figure VI.5 : Tensile tests at RT [Suri et al., 1999]

VI.2.7 Framework and Theory for a General Multimat

Voigt's model allows us to deliver for each Gauss point a non linear behaviour that takes into account the two phases, introducing their respecting behaviour and the individual volume fraction.

The framework and the theory very recently summarized in [Mueller, 2000]. The localization rules follow the spirit of the "Transformation Field Analysis" (TFA) of [Dvorak, 1993]. The transition rule is described by the following equation:

$$\sigma_s = \mathbf{L}_s(T)\varepsilon_s^e = L_s(T_0)(\varepsilon_s - \gamma_s)$$

where σ_s is the stress, ε_s is the total strain, ε_s^e is the elastic strain, \mathbf{L}_s is the thermally dependent and/or damaged elastic tensor, L_s is the undamaged elastic tensor. $\gamma_s = \varepsilon_s - L_s^{-1}\mathbf{L}_s\varepsilon_s^e$ is the eigenstrain, that can be expressed as $\gamma_s = \varepsilon_s - \varepsilon_s^e$, when the $\mathbf{L}_s = L_s$. In the text to follow, γ_s will be described as the formal eigenstrain.

Table VI.9 shows two equivalent means for describing a localization law. The subscript s identifies a local volume. The subscript on the stress and strain should be interpreted as averages over this local volume. Therefore, the local material laws give the relationship between the local averages of stress and strain. In general, each local volume s may be associated a different material type. For some cases the local volumes may be linked to a common material type.

The tensors A_s and B_s are strain and stress localization tensors and D_{sr} and F_{sr} are the eigenstrain and eigenstress influence tensors. All of them depend on the local geometry and the elastic modulus L_s . These tensors, in general, can be considered as functions of the temperature, i.e. $T_0 = T(t)$. However, in the developments to follow, the tensors are considered constants. Here the eigenstrain β_r has to be considered as an internal variable which must be assigned an evolution law. In the text to follow, β_r will be referred to as the constitutive eigenstrain. Normally in the literature $\beta_r = \gamma_r$ and, in this case, the stress localization and the strain localization are identical statements, i.e., one can be derived from the other.

$\varepsilon_s = A_s E + \sum_r D_{sr} \beta_r$
$\sigma_s = L_s (\varepsilon_s - \gamma_s)$
$\Sigma = \sum_s c_s \sigma_s = L (E - \Gamma)$
$\Gamma = \sum_r c_r B_r^T \beta_r + L^{-1} \sum_r c_r L_r (\gamma_r - \beta_r)$
$\sigma_s = B_s \Gamma - \sum_r F_{sr} L_r \beta_r$ $- L_s (\gamma_s - \beta_s) + B_s \sum_r c_r L_r (\gamma_r - \beta_r)$

Table VI.9 : Strain localization law

There are many good arguments to assume that constitutive eigenstrain β_r can be different from the formal eigenstrain γ_s , including:

- The local material laws are written for a homogeneous material which may not adequately consider the effects of the interface on dislocation movement. Another way of saying this is that the local plastic material models may not consider the scale of the heterogeneity.
- The eigenstrain transformations themselves assume that the displacement across material boundaries is continuous. This assumption can be rejected when cracks develop at the interface and then, depending on the load, may further open and extend or can close.
- The local material model may be suitable but the averaging over the local volume might introduce errors.

To compensate for these deficiencies, the constitutive eigenstrain is defined by an evolution law which can be tuned to fit the available data. This evolution law is associated with a stress localization or a strain localization law but not both. The last line in this Tab.VI.9 is the dual localization law when the constitutive eigenstrain β_r is defined in terms of a particular localization (See Appendix A.4). This dual form becomes important to the solution strategy to be proposed. However, it is more natural, in the context of a finite element code to localize the strain, compute the local stress, and then find the volume average for the macroscopic stress.

If the constitutive eigenstrain is expressed in the context of a stress localization law, then we must use the stress localization's dual strain localization. The derivation of this dual localization model assumes that the localization tensors and the eigenstrain influence functions satisfy constraints described by [Dvorak, 1993] and listed in equations.

- The average elastic stiffness tensor in terms of the local elastic stiffness tensor and the strain localization tensor is

$$L = \sum_s c_s L_s A_s, \quad L^{-1} = \sum_s c_s L_s^{-1} B_s$$

- and the relations between stress localization and strain localization tensors:

$$B_s = L_s A_s L^{-1}, \quad A_s = L_s^{-1} B_s L$$

- These localization tensors satisfy the relationship

$$\sum_s c_s A_s = I, \quad \sum_s c_s B_s = I$$

- In addition the eigenstrain influence tensors satisfy

$$\sum_s c_s D_{sr} = 0, \quad \sum_s c_s F_{sr} = 0 \quad \forall r$$

$$\sum_r D_{sr} L_r^{-1} = 0, \quad \sum_r F_{sr} L_r = 0 \quad \forall s$$

$$\sum_r D_{sr} = I - A_s, \quad \sum_r F_{sr} = I - B_s \quad \forall s$$

$$c_s D_{sr} L_r^{-1} = c_r L_s^{-1} D_{rs}^T, \quad c_s F_{sr} L_r = c_r L_s F_{rs}^T \quad \forall r, s$$

- There is a relationship between D_{sr} and F_{sr}

$$F_{sr} = \delta_{rs} I - L_s D_{sr} L^{-1} - c_r B_s A_r^T, \quad D_{sr} = \delta_{rs} I - L_s^{-1} F_{sr} L_r - c_r A_s B_r^T$$

To complete the description, the localization and the eigenstrain influence tensors have to be prescribed, as well as an evolution rule for the constitutive eigenstrain β_s . Note that the formal eigenstrain is set by prescribing L_s , \mathbf{L}_s , ε_s , and ε_s^e , independently of the constitutive eigenstrain.

Voigt's Homogenisation Model. It introduces the specific uniform strain assumption $\varepsilon_s = E$, then

$$A_s = I, \quad B_s = L_s L^{-1}, \quad D_{sr} = 0, \quad F_{sr} = \delta_{rs} I - c_r L_s L^{-1} \quad \forall r, s$$

and the dual stress localization expression is

$$\sigma_s = B_s \Sigma - \sum_r F_{sr} L_r \beta_r - L_s (\gamma_s - \beta_s) + B_s \sum_r c_r L_s (\gamma_r - \beta_r)$$

This rule is acceptable for highly mixed phases, and has been recently used for the same problem type in a recent study [Ankem et al., 2006].

VI.2.8 Calibration Results of Material Parameters

A specific strategy related to the use of the present model has been developed in order to calibrate the material parameters. This strategy consists in activating one part of the model for each class of tests (either nonlinear kinematic hardening plays more important role or linear kinematic hardening does it). The first category is related to rapid tests as tension, fatigue. The second category is related to slow rate tests as relaxation, creep. Dwell is associated with both categories.

The simulated values are obtained by averaging the relevant Cauchy stress and total strain components on the whole mesh. Fig.VI.6 shows a comparison between simulated and experimental curves, on tensile tests (Fig.VI.6 (a)) and on relaxation tests (Fig.VI.6 (b)). For tensile tests, the model is able to reproduce the moderate strain rate effect. The agreement is also very good for relaxation tests, where the stress levels have been simulated for three cases (650, 700 and 750 MPa). Figure VI.7 also demonstrates the good agreement for fatigue and dwell tests: in both cases, a cyclic creep phenomenon is observed. It is much larger for the case of dwell.

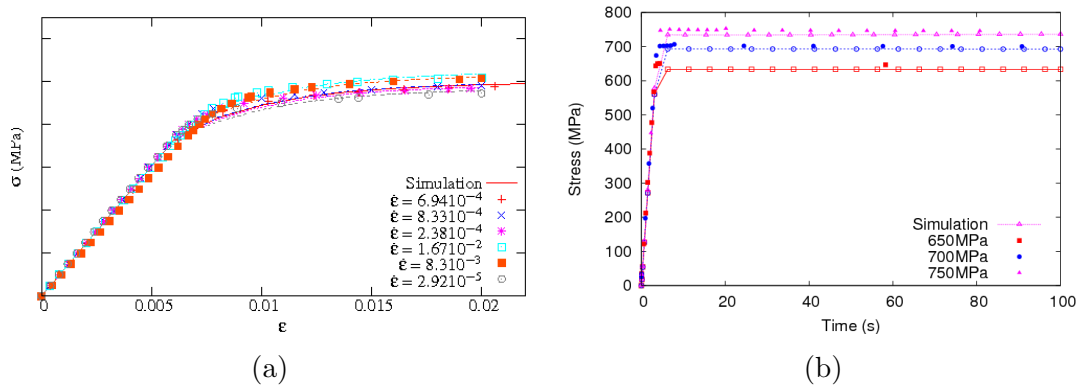


Figure VI.6 : (a) Tensile tests; (b) Relaxation tests

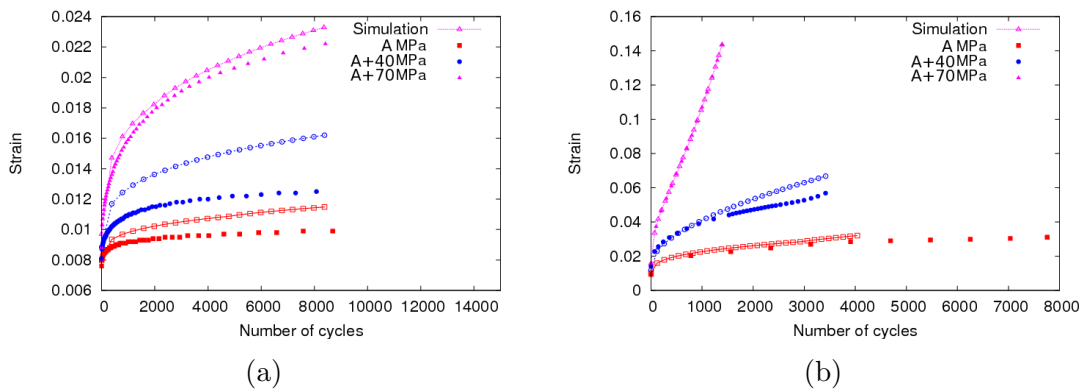


Figure VI.7 : Comparison between simulated and experimental results at various maximum stress ($R = \sigma_{min}/\sigma_{max} = 0$) for (a) Fatigue tests; (b) Dwell tests

The final set of coefficients for tests (tensile, fatigue and dwell experiments) are represented in Tab.VI.10.

Type of Tests	Tensile, Relaxation, Creep Dwell and Fatigue
K_r , MPa $\cdot s^{1/n_r}$	80
n_r	23
C_r , MPa	1000
D_r	70
Q_r , MPa	150
b_r	20
K_l , MPa $\cdot s^{1/n_l}$	615
n_l	40
C_l , MPa	600

Table VI.10 : Material parameters of Ti-6242 forged in the domain β at RT

VI.2.9 Analysis of the Local Behaviour

The main factors promoting dwell effect and crack propagation in titanium alloys have been studied for a long time [Bache, 2003]. The present section attempts to investigate the local behaviour, in order to exhibit microstructure based mechanisms explaining the macroscopic effects.

A series of plots have been done for cycle 1000, at maximal stress for pure fatigue tests, and at maximum stress at the end of the hold time for dwell tests. The main local stress components and all slip systems are checked, for α phase and β phase. Probability density function, known as the Gaussian function is used to create these plots represented below.

The plot of the local stress components 11, 22 and 33 (Fig.VI.8) do not show any remarkable effect. This is due to the fact that local stress have reached a saturation level, so that the stress state does not change during the deformation process. In Fig.VI.9 there is a big difference between dwell and fatigue tests and biggest values are in fatigue tests. It means that the stress components 12, 23 and 31 cannot play the major role in the scatter effect between dwell and fatigue tests, as the lifetime is shorter in the first case. The opposite is true for strain and accumulated slip, that can develop, following a local cyclic creep regime.

In Fig.VI.10 (dwell and fatigue loadings) the sum of plastic slips and their probability density (a percentage of slip planes on which local strain or stress occur in dwell and fatigue tests) are shown for basal, prismatic, pyramidal slip systems of HCP crystals and 101, 112, 123 slip systems of BCC crystals. There is a large difference between them. The highest value is in pyramidal slip systems of α phase and in 123 slip system of β phase. One of the reason is that the 12 pyramidal slip systems have been summed up in the same number. Anyway, this demonstrates also that pyramidal slip is significant in our model.

This difference is in good agreement with the difference between fatigue and dwell tests, where an average ratio between the number of cycles to crack initiation is around 7.6 [Sinha et al., 2004]. This result can justify the use of accumulated slip to explain the difference between fatigue and dwell at the macroscale.

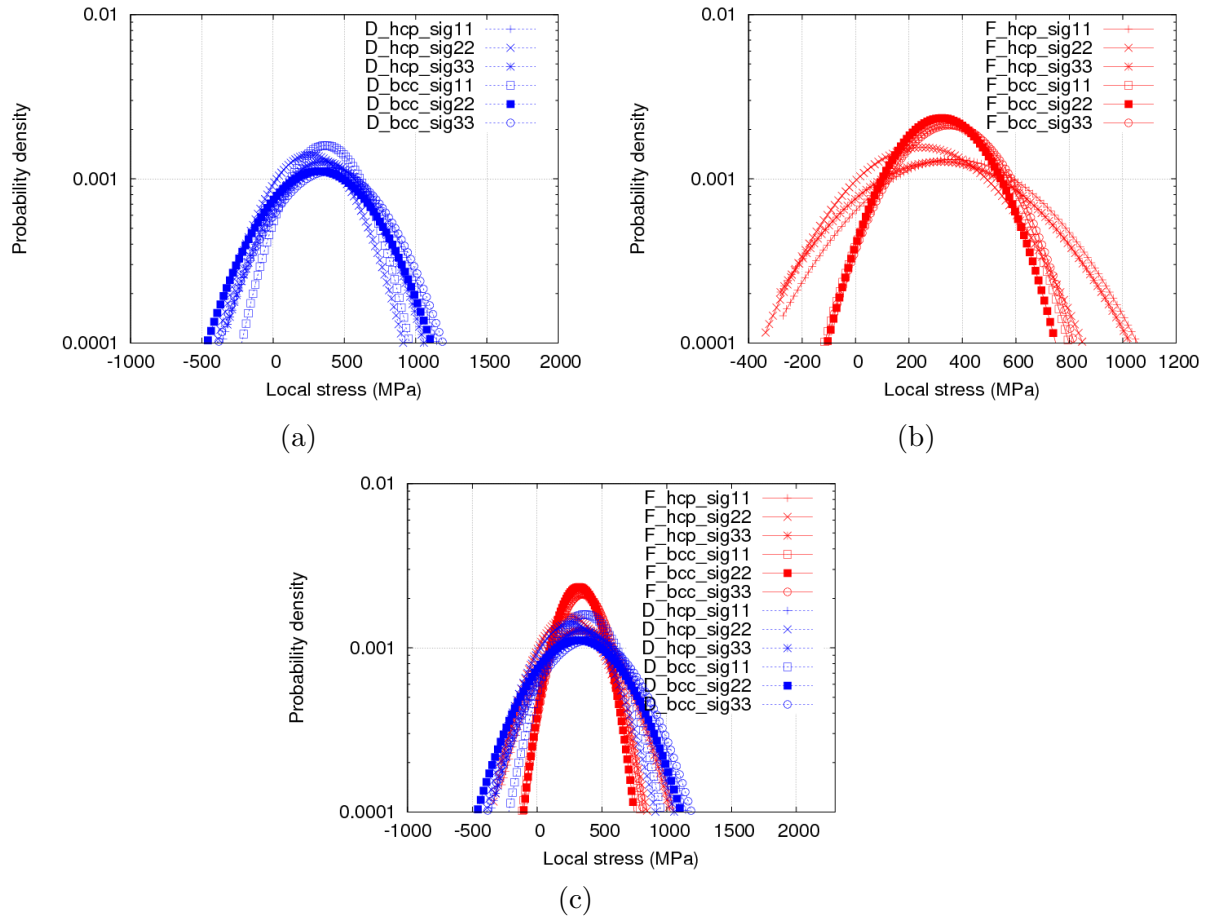


Figure VI.8 : The stress in directions 11, 22, 33 of HCP and BCC crystals for the 1000th cycle in (a) Dwell tests; (b) Fatigue tests; (c) Dwell and fatigue tests

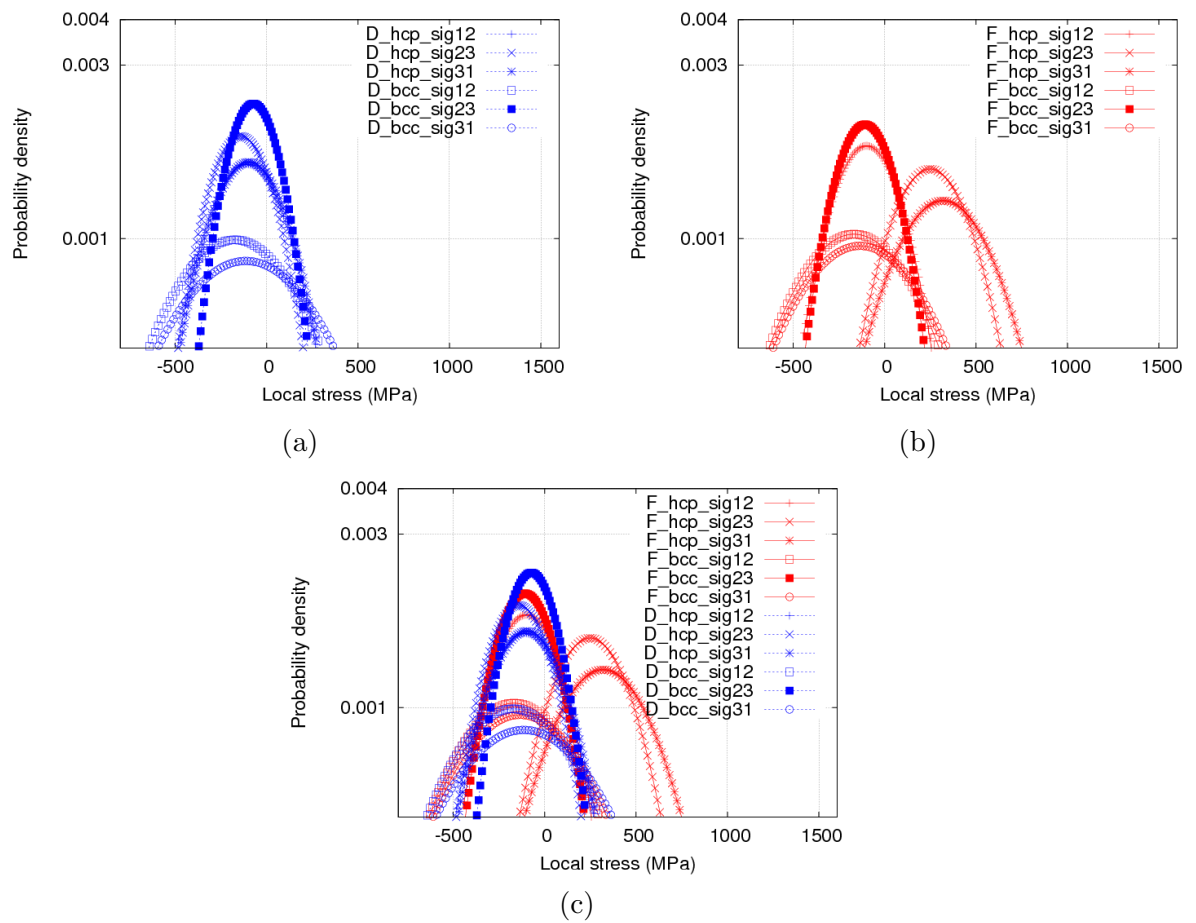


Figure VI.9 : The stress in directions 12, 23, 31 of HCP and BCC crystals for the 1000th cycle in (a) Dwell tests; (b) Fatigue tests; (c) Dwell and fatigue tests

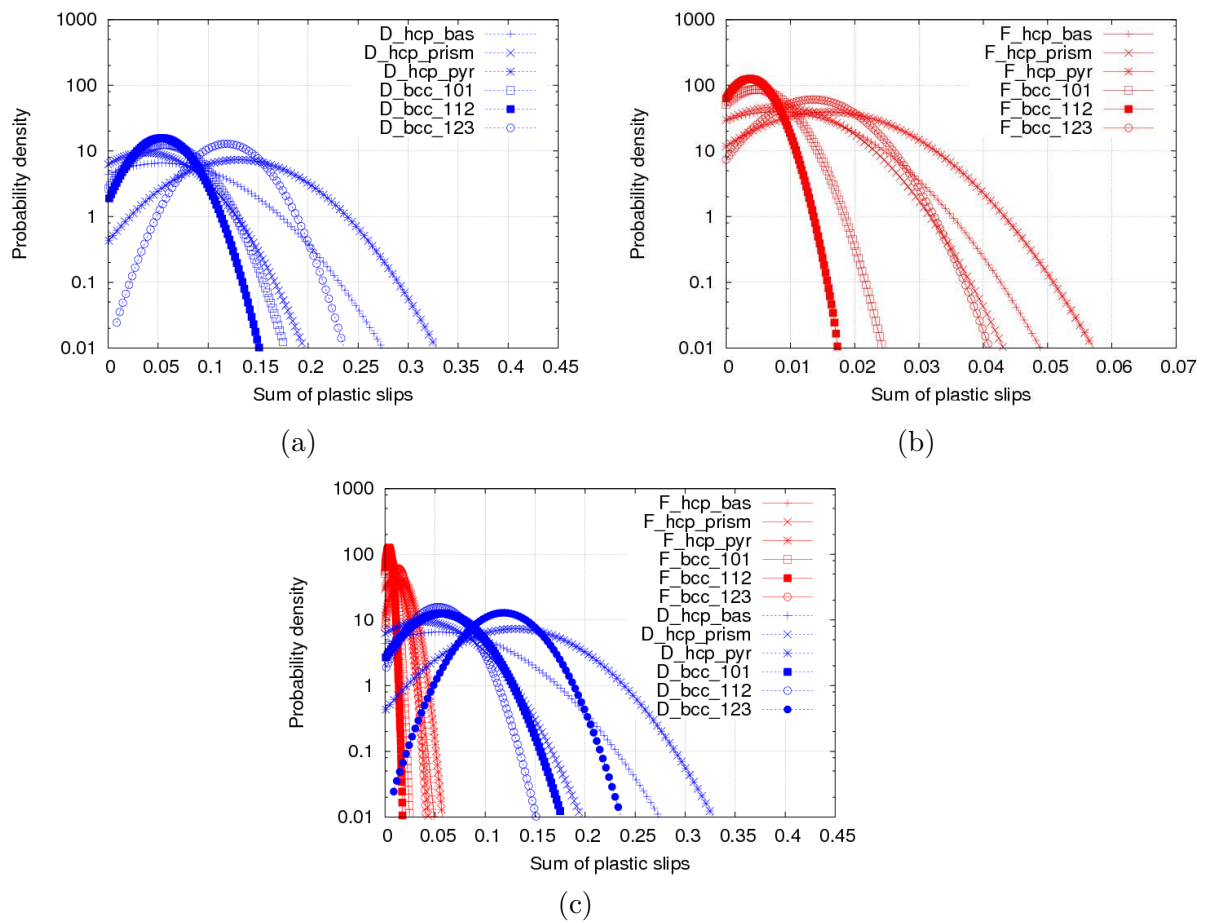


Figure VI.10 : The sum of plastic slips in different slip systems (basal, prismatic and pyramidal) of HCP crystals and 101, 112, 123 of BCC crystals for the 1000th cycle in (a) Dwell tests; (b) Fatigue tests; (c) Dwell and fatigue tests

VI.3 Conclusions

- In BCC crystals the stress components 11, 22 and 33 are higher for dwell tests and in HCP ones they are higher in fatigue simulations (1000th cycle).
- There is a little difference between stress components 11, 22 and 33 for each phase, so that they cannot be used as indicators. The stress components 12, 23 and 31 can not be used either, as the biggest values is in fatigue tests but the lifetime is shorter in dwell ones.
- The accumulated plastic slip reaches its maximum for pyramidal slip systems of HCP crystals (due to the sum on 12 slip systems) and 123 slip systems of BCC crystals.
- The values for slip in dwell simulations are 3–7 times larger than in fatigue, that is in agreement with the difference in lifetime of 7.6 reported in [Sinha et al., 2004].

A relevant criterion for the estimation of the fatigue life will be associated to the sum of plastic slips rather than to local stress, since plastic slip – and not stress – appears as a discriminant parameter.

-
- *Dans les cristaux BCC, les composantes de la contrainte 11, 22 et 33 sont plus grandes en fatigue avec temps de maintien et dans HCP elles sont plus hautes dans les simulations de fatigue continue (le 1000ème cycle).*
 - *Il y a un peu de différence entre les composantes de la contrainte 11, 22 et 33 pour chaque phase, elles ne peuvent donc pas être utilisées comme les indicateurs. Les composantes de la contrainte 12, 23 et 31 ne peuvent être utilisées non plus, car leurs valeurs sont plus grandes en fatigue alors que la durée de vie est plus courte en fatigue avec temps de maintien (dwell).*
 - *Le glissement plastique accumulée atteint sa valeur maximale pour les systèmes pyramidaux de cristaux HCP (en raison de la somme sur 12 systèmes de glissement) et sur les systèmes de glissement 123 des cristaux BCC.*
 - *Les valeurs de glissement dans les simulations de la fatigue avec temps de maintien sont 3 à 7 fois plus grandes qu'en fatigue, ce qui est en accord avec la différence de durée de vie de 7,6 indiquée dans [Sinha et al., 2004].*

Chapter -VII-

**Full Field Model of a
Microstructure with Plumes**

Contents

VII.1	Introduction	94
VII.2	Meshes and Calculation List	94
	VII.2.1 FE Calculations of Plumes with Real Angles	97
VII.3	FE Calculations of Plumes with Virtual Angles	104
	VII.3.1 Local Stress Fields	104
	VII.3.2 The Most Critical and Safest Crystal Orientations	105
	VII.3.3 The Most Critical and Safest Morphological Orientations	105
	VII.3.4 Comparison of Configurations with Real and Virtual Crystal Orientations	106
VII.4	Influence of the Shape of the Main Plume	106
VII.5	Conclusions	106

VII.1 Introduction

In “normal” microstructures of Ti6242, the grain size is equal to around 20–30 μm . Depending on the thermomechanical history during the material processing and the component fabrication, millimetric grains may appear in the material. According to recent studies [Freiherr von Thungen and Villechaise, 2011], they are the source of premature crack initiation, The purpose of this section is to exhibit a microstructural parameter that would be able to explain the differences observed at the macroscale. This is made by means of full field Crystal Plasticity Finite Element computations, where the local geometry is explicitly represented. That will allow us to characterize the possible local overstress and the enhanced plastic zones. Both fatigue and dwell loadings are considered.

This is a two part numerical study, that is first based on EBSD data obtained by Freiherr von Tungen, from Pprime Institute, Poitiers (Fig.VII.1 [Freiherr von Thungen and Villechaise, 2011]): for a series of surfaces, both grain shape and grain orientations are available. They are used here to generate a material model with so called “real angle” crystallographical orientations. This allows us to have realistic surroundings of a given plume, and to check the effect of possible interactions. Studying just one geometrical and crystallographical configuration is not enough to have a clear view of the microstructure effect. This is why we have also built a long list of calculations on “virtual” configurations, to study the combined effect of the geometrical and crystallographical orientations of the plume with respect to the loading axis.

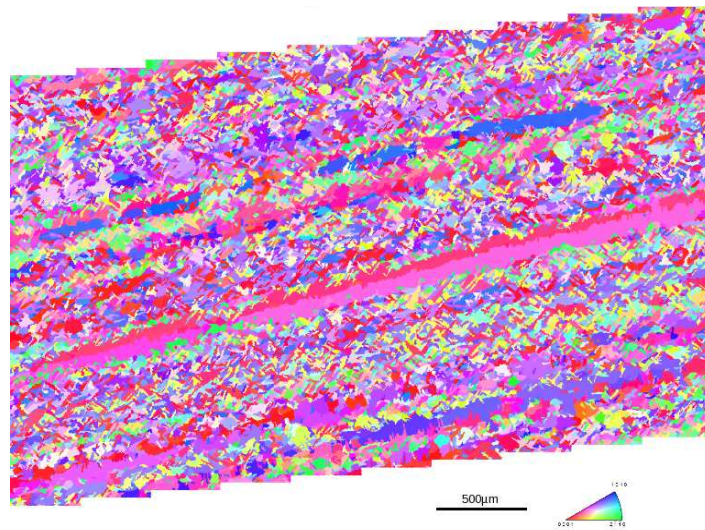


Figure VII.1 : EBSD of crystal orientations in plumes [Freiherr von Thungen and Villechaise, 2011]

VII.2 Meshes and Calculation List

EBSD results have been used to create the microstructure with proper plume’s sizes and their positions. The area inside the red square shown in Fig.VII.2 has been selected. All plumes in this zone will be considered. A special attention will be payed to the plume 11; a parametric study including various crystal orientations and different surroundings will be performed. The corresponding mesh is given in Fig.VII.3. It has been extended in one direction perpendicular

Morphological orientations β (g)	Real crystal orientations	Virtual crystal orientations (d)
0 10 30 45 60 90	According to EBSD data (Tab.VII.4)	0, 10, 30, 45, 60, 90
The number of calculations	6 + 6 = 12 fatigue + dwell fatigue	36 + 36 = 72 fatigue + dwell fatigue

Table VII.1 : Morphological and real - virtual crystallographical orientations of HCP crystals (α phase) in the central layers of the main plume

to the sheet of paper, so the mesh is in 3D.

In the FE model, the following standard boundary conditions have been applied: displacement fixed to zero at the right node for all directions and in the left one for two directions except one which is parallel to the bottom edge of the structure (Fig.A.2). MPC1 (MPC = multi-point constraint) conditions have been applied for two sides of the model so that they move in the same way (Fig.A.3). The bottom side of the model is fixed in the direction of an applied loading on the top side (Fig.A.4).

The summary of all calculations is shown in Tab.VII.1, where the letter “g” (global) is related to morphological angles and “d” is to crystal orientations. Both real crystal angles and virtual crystal angles are reported here. In all the computations, the load direction is y axis. Plumes are defined as specific elliptic shaped domains at the surface of the mesh, that are extruded in the bulk, forming a 3D mesh. The schema of a plume is illustrated in Fig.VII.4. The main axis is a line separating two long symmetrical domains. The angle ϕ between $X1$ axis and the main axis of the plume defines plume’s orientation. The axis c (Fig.III.8) is related to the crystal HCP (α phase), which is orientated according to three Euler’s angles $\phi_1 \Phi \phi_2$. The crystal angles are connected to the global coordinate system.

As shown in Fig.VII.4, the global geometry is characterized by a “morphological angle” ϕ , which value is equal to 10° in the present case. Other values of this angle will be considered, as summarized in Tab.VII.2. The corresponding meshes are shown in Fig.VII.5. There are only 6 configurations, as it is supposed to be that this number is sufficient enough to analyse possible variants and plumes are considered to be relatively symmetrical with respect to the main principal plume. Another important point of the study is the description of the main plume’s surroundings and its crystal orientations.

In Fig.VII.6 the attached models are indicated: (a) the macroscopic model used in the zone in red and (b) the microscopic model incorporated in the zones in colour. As macroscopic and microscopic physical laws are used for the same mesh at the same time, some features must be included to represent the microstructure more precisely. Around the main plume, smaller grains are modelled. We do not need to model grain boundaries, since the probability

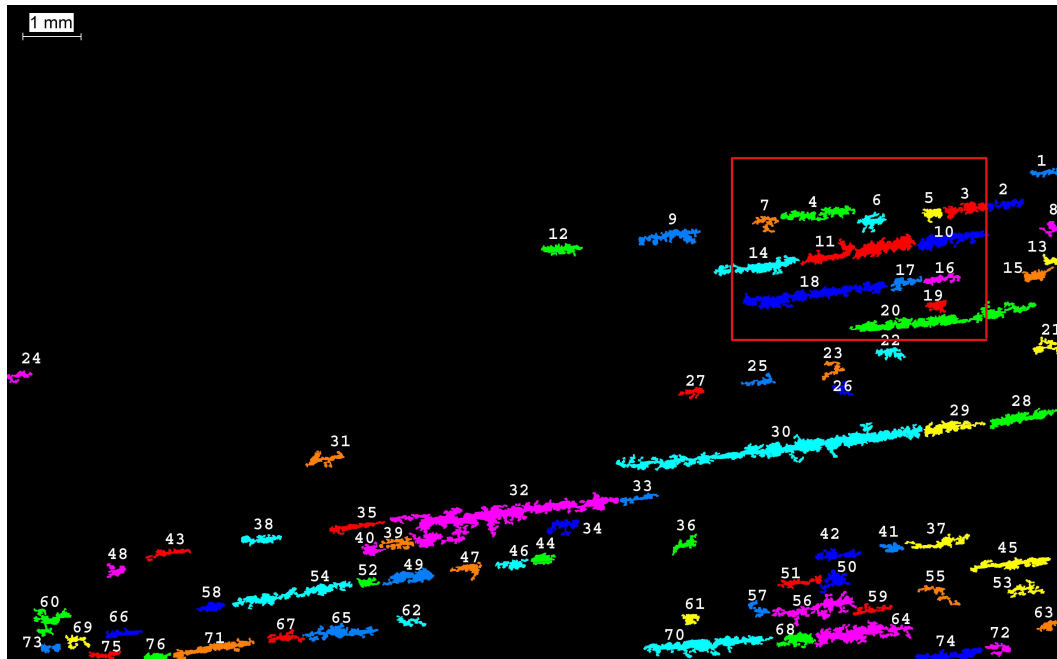


Figure VII.2 : EBSD of “plumes” [Freiherr von Thungen and Villechaise, 2011]

of cracking in transcolonies is higher than in interboundaries [Sansoz and Ghonem, 2003]. These small grains (Fig.VII.7 (a)) are arranged in two layers of BCC crystals having the same orientations corresponding to BCC orientations of the closest layer situated inside the plume and then Burger’s relationship is used for HCP crystals in every grain, around the interior plume’s part shown in Fig.VII.7 (b). Inside plumes, crystals have the same orientation in a given layer according to the data given below.

Several variants have been developed in order to study the effect of turning plumes around the axis, perpendicular to the sheet of paper, placed in the center of the main plume. Main morphological angles are chosen to study: 0° , 10° , 30° , 45° , 60° and 90° (Fig.VII.4 and Fig.VII.5). FE of reduced integration are used in our meshes with around 140000 nodes. Some mesh parameters for computations are shown in Tab.VII.2.

Morphological angle	Nb of nodes	Nb of DOF
0	143312	429936
10	142651	427953
30	146591	439773
45	140090	420270
60	128231	384693
90	116886	350658

Table VII.2 : Summary of meshes

The maximum stress, applied in direction y , is equal to $A+70$ MPa which is slightly higher than the yield level. In our case, one hundred cycles have been computed to simulate the real state as much as possible. The various fields are analysed at the maximum of the 100th

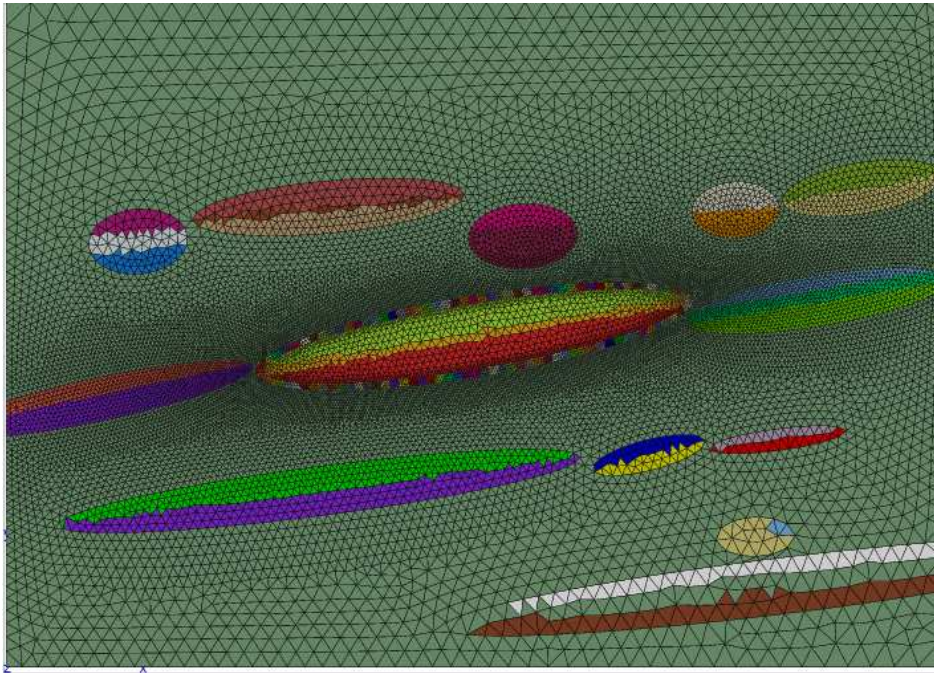


Figure VII.3 : Mesh corresponding to the red zone

cycle in fatigue tests and at the end of the hold period of time in dwell experiments. Both fatigue and dwell-fatigue (with 120 s dwell period) loadings are considered. The final values are demonstrated at the maximal stress in the 100th cycle.

VII.2.1 FE Calculations of Plumets with Real Angles

In Tab.VII.3 all calculated real variants are shown. Every morphological angle is associated to a calculation. There are 12 calculations (6 fatigue + 6 dwell). The meshes in Fig.VII.5 have been used to compute each configuration and there are four analysed domains: the outer layer around the main plume area, and layers inside the main plume, which are called top, middle, bottom according to their logical location in Fig.VII.3. All measured crystal angles

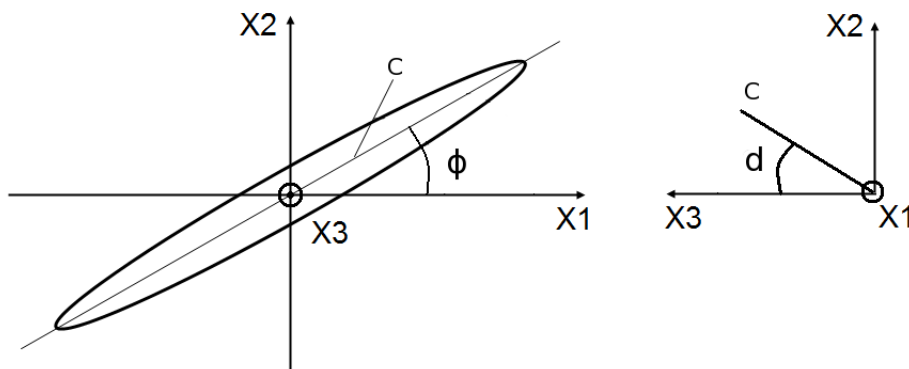


Figure VII.4 : Morphological angle ϕ attached to the global system of the plume

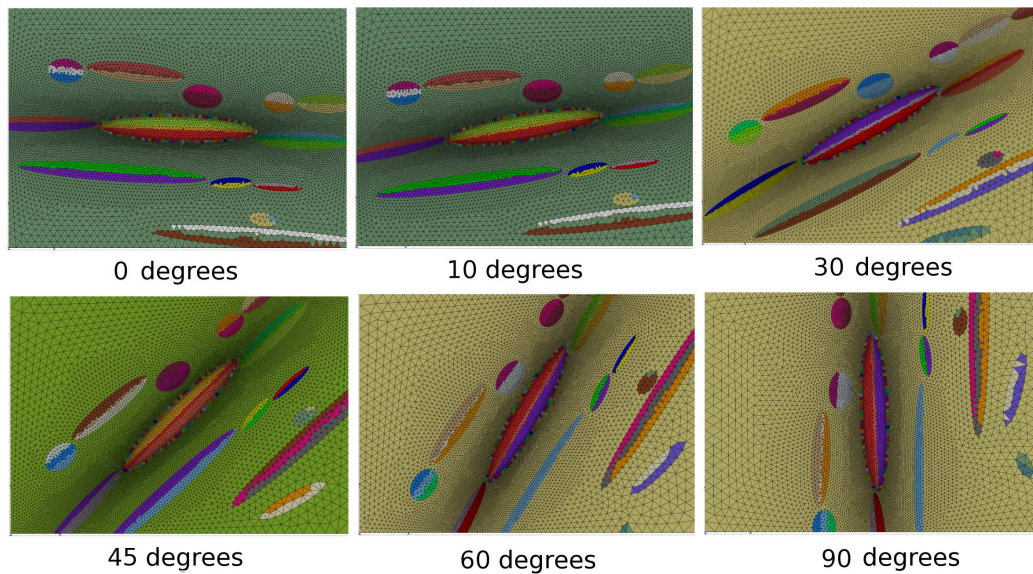


Figure VII.5 : Different variants of meshes

for every plume are summarized in Tab.VII.4.

The real configurations have been calculated properly for dwell and fatigue tests at a stress level of $A+70$ MPa. The resulting von Mises stress field obtained for the dwell test is shown in Fig.VII.8. The field is highly heterogeneous, and presents large stress concentrations around the edges of the plumes. This result may indicate that the area is critical with regard to damage, as confirmed by ENSMA's conclusions, which show probable cracks initiation along bands located on the edge and sometimes inside plumes [Freiherr von Thungen and Villechaise, 2011]. In the following, most of the post-processing will deal with strain fields, since the sum of plastic slip happens to be the most discriminant local variable. Only the α phase will be analysed, as the maximum values are much higher in α than in β phase, according to the plots shown in the previous chapter.

The graphs in Fig.VII.9 (dwell and fatigue loadings) demonstrate the distribution of the sum of the plastic slips in α phase *vs* morphological angles in the main plume's top, middle and bottom layers (indicated in the plots as t, m and b) for dwell and fatigue loadings.

One by one comparisons have been done, from the first configuration with a morphological angle equal to 0° up to the last one with a morphological angle of 90° . Components with the highest values of the sum of plastic slips have been selected. It is easily seen that the most critical morphological angle is equal to 45° for both types of tests and the safest one is equal to 90° for dwell loading and for fatigue tests in Fig.VII.9. The most critical area is always located in the outer layer of the main plume. The outer layer is a transition layer placed between the zone with the similar oriented crystals inside the plume and the matrix, with a disorganized structure. This result corresponds very well to observations done by ENSMA [Freiherr von Thungen and Villechaise, 2011]. Among all variants, the sum of plastic slips is more critical in the inner bottom layer only once at 30° , and the difference between the inner and the outer layer is quite small. Figures VII.10 and VII.11 show the ε_{22} strain fields (remember that y is the loading direction). This variable is sensitive to crystal orientation. The most dangerous configuration is in Fig.VII.10 (d) and Fig.VII.11 (d) for

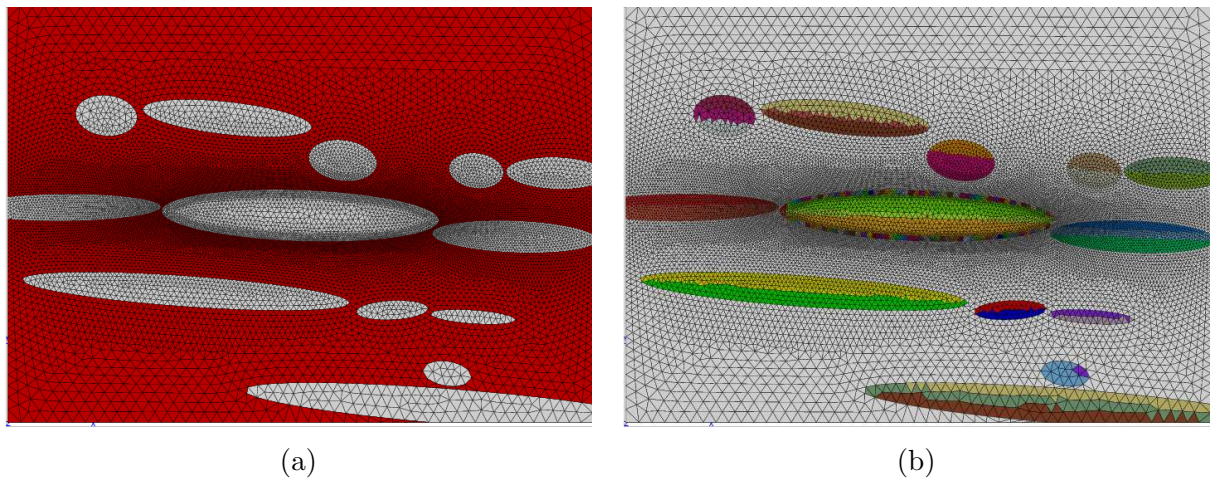


Figure VII.6 : Macroscopic model is used for the zone in red (a) and microscopic model is placed in the zones in colour (b)

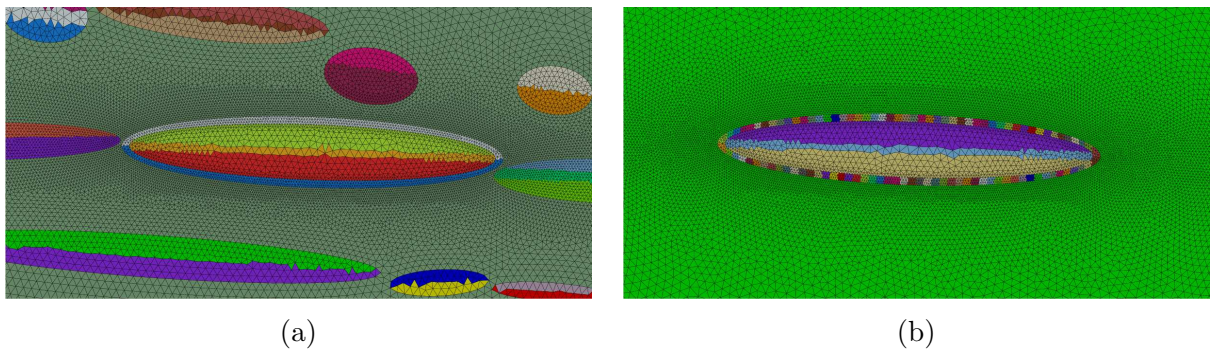


Figure VII.7 : (a) Two parts of layers for BCC crystals (β phase); (b) Main plume with one layer of small grains

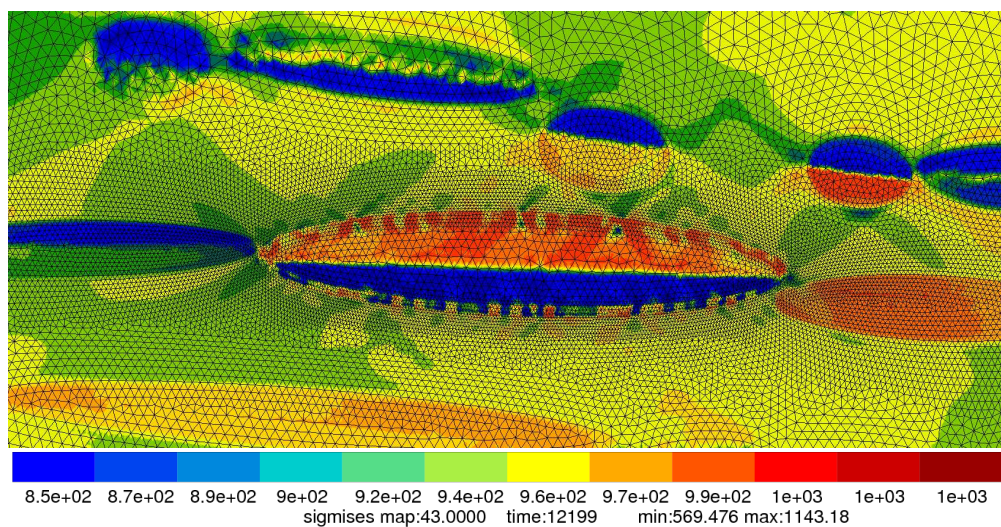


Figure VII.8 : Mises stress field in the principal and surrounding plumes

Morphological orientations ϕ (g)	Real crystal orientations
0 10 30 45 60 90	According to EBSD data (Tab.VII.4)
The number of calculations	$6 + 6 = 12$ fatigue + dwell fatigue

Table VII.3 : Morphological and real crystallographical orientations of HCP crystals (α phase) in the central three layers of the main plume

both types of tests. The strain distribution becomes quite large and the concentration is not only in the main plume's outer layer but also in its inner parts. It means that crack can initiate at the plume's edges and then expand into interior plume's layers. The morphological angles 0° and 90° are relatively safe compared to 45° , as there is less strain concentration.

The values of sum of plastic slips are around three–four times bigger in dwell tests compared to fatigue tests. This variable is then discriminant with regard to lifetime prediction, as already concluded in the previous chapter.

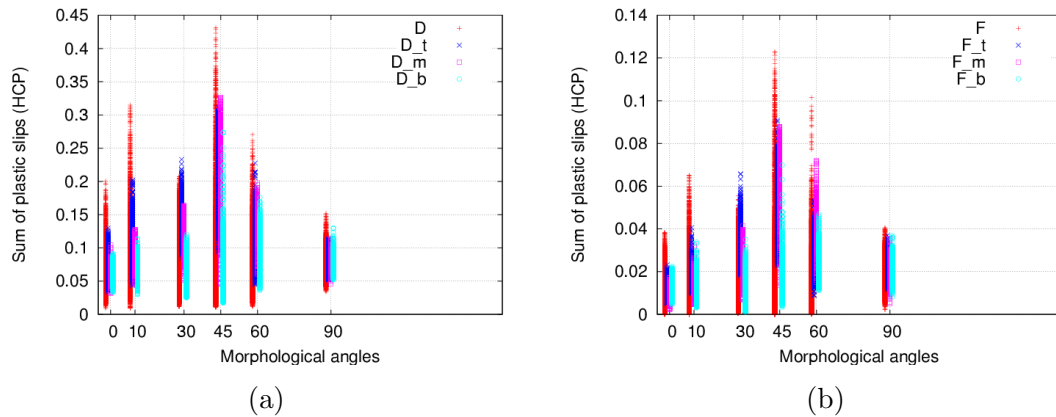


Figure VII.9 : Distribution of the sum of plastic slips in HCP crystals (α phase, dwell and fatigue loadings, real angles) in the outer layer, inside top, middle and bottom layers (denoted as t, m and b) of the main plume in the 100th cycle for different configurations (FigVII.5)

Real orientations (morphological angle = 10°)	Angles, $^\circ$ $\phi_1 \ \Phi \ \phi_2$
Plume 3 (top layer)	192. -4. 21.
Plume 3 (bottom layer)	190. 15. 20.
Plume 4 (top layer)	197. 180. 34.
Plume 4 (middle layer)	205. 160. 44.
Plume 4 (bottom layer)	197. 180. 25.
Plume 5 (top layer)	199. -3. 90.
Plume 5 (bottom layer)	192. -25. 140.
Plume 6 (top layer)	202. 8. 79.
Plume 6 (bottom layer)	199. 7. 30.
Plume 7 (top layer)	192. 175. 19.
Plume 7 (middle layer)	195. 163. 15.
Plume 7 (bottom layer)	193. 182. 70.
Plume 10 (top layer)	187. -6. 63.
Plume 10 (middle layer)	187. -6. 57.
Plume 10 (bottom layer)	187. -8. 56.
Plume 11 (top layer)	185. -10. 65.
Plume 11 (middle layer)	187. -10. 59.
Plume 11 (bottom layer)	188. -1. 16.
Plume 14 (top layer)	193. 14. 18.
Plume 14 (bottom layer)	189. 15. 29.
Plume 16 (top layer)	197. 180. 34.
Plume 16 (bottom layer)	200. 180. 50.
Plume 17 (top layer)	197. 180. 34.
Plume 17 (bottom layer)	200. 180. 50.
Plume 18 (top layer)	192. 175. 37.5
Plume 18 (bottom layer)	192. 172. 47.
Plume 19 (right layer)	190.4 315. 37.5
Plume 19 (left layer)	183. 32.7 65.5
Plume 20 (top layer)	209. 181. 172.
Plume 20 (middle layer)	212. 178. 162.
Plume 20 (bottom layer)	200. 1. 112.

Table VII.4 : Real crystal orientations in “plumes”

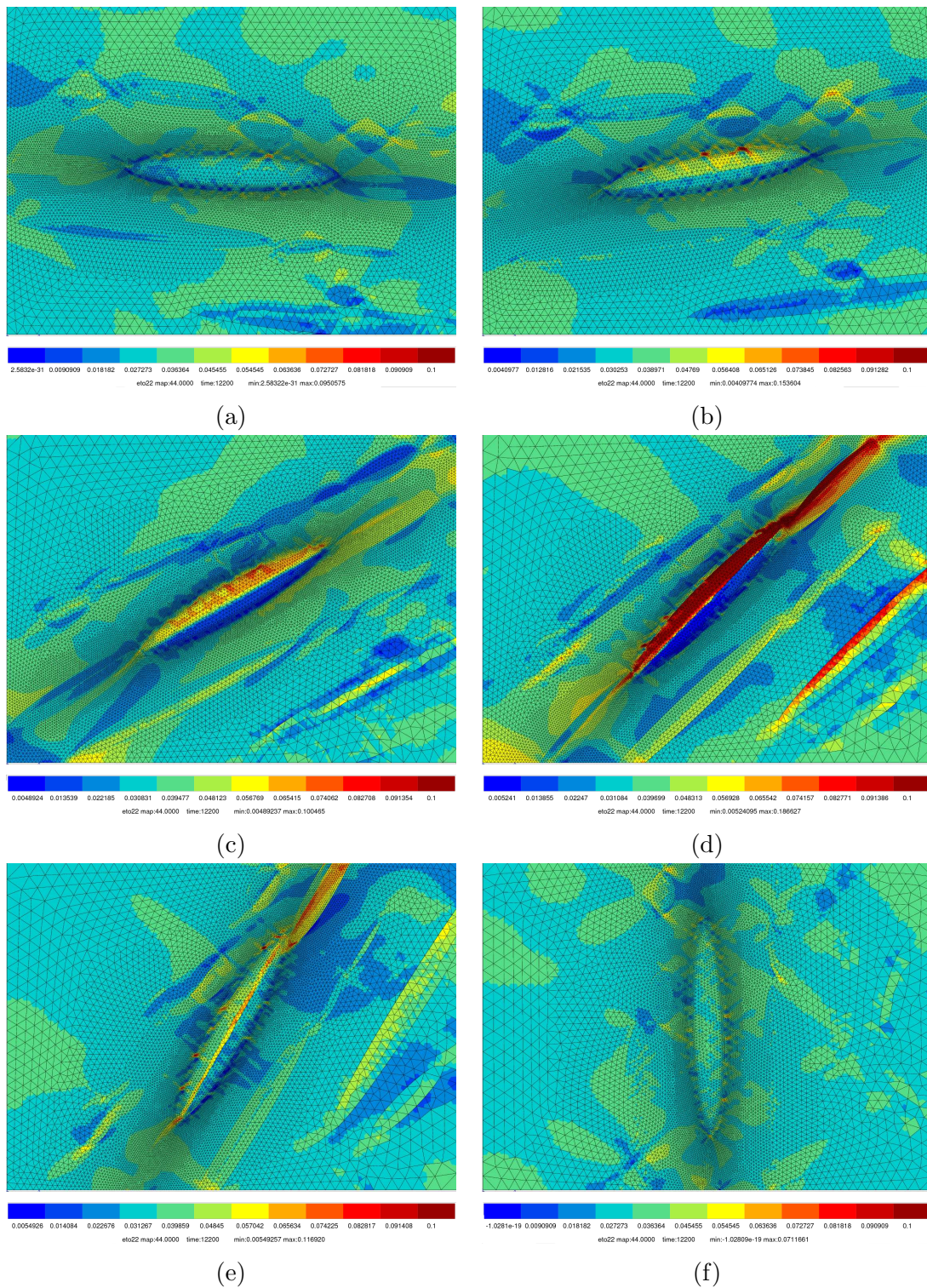


Figure VII.10 : Strain field ε_{22} in dwell tests (100th cycle) for the real microstructure with the morphological angles: (a) 0; (b) 10; (c) 30; (d) 45; (e) 60; (f) 90.

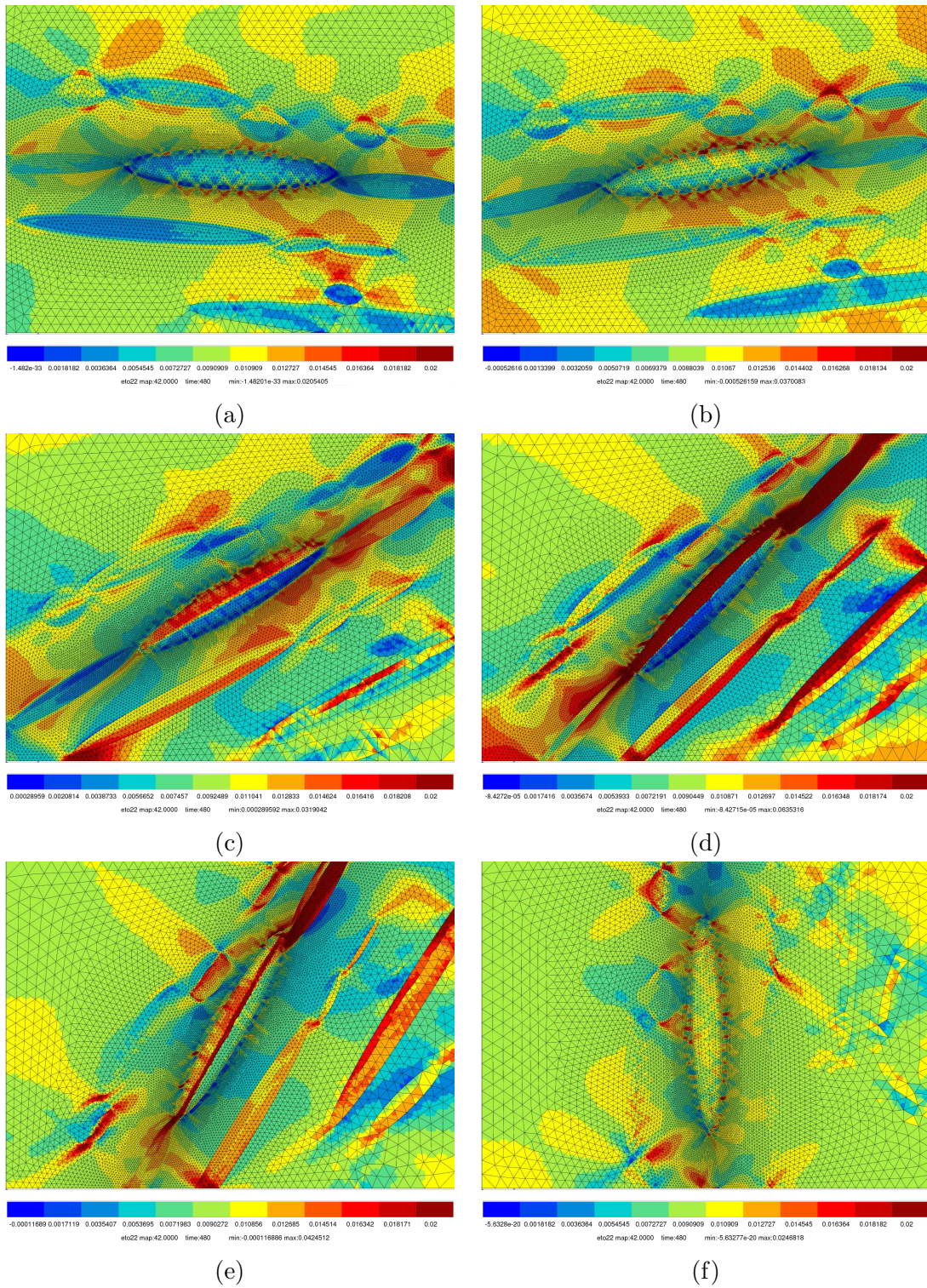


Figure VII.11 : Strain field ε_{22} in fatigue tests (100th cycle) for the real microstructure with the morphological angles: (a) 0; (b) 10; (c) 30; (d) 45; (e) 60; (f) 90.

Morphological orientations ϕ (g)	Virtual crystal orientations (d)
0 10 30 45 60 90	0, 10, 30, 45, 60, 90
Number of calculations	$36 + 36 = 72$ fatigue + dwell fatigue

Table VII.5 : Morphological and virtual crystallographical orientations of HCP crystals (α phase) in the central layer of the main plume

VII.3 FE Calculations of Plumets with Virtual Angles

The purpose of this section is to understand which crystal and morphological orientations are the most critical or the safest, as the calculations on the real microstructure carried out in the previous section are not sufficient to fully analyse these configurations. Then a systematic investigation is made in this section, with a collection of morphological and crystallographic orientations.

In Tab.VII.5, all calculated variants are shown. 72 calculations (36 fatigue + 36 dwell) are made, defined by a set of morphological and crystallographical orientations. The same meshes (Fig.VII.5) have been used to compute every configuration. Only one domain (instead of three used in the previous section) has been included in the main plume. The applied force and constraints are the same as described in the previous section.

After validating these calculations, some comparisons have been done one by one from the first configuration with a morphological angle equal to 0° up to the last one with a morphological angle equal to 90° , with a series of crystal orientations for each morphological angle.

VII.3.1 Local Stress Fields

In the previous chapter, Figure VI.8 demonstrated that there was practically no difference between local stress components in phases α and β . The computation was done on a material RVE, without any plume representation. Now, microstructure variations are considered.

The images in Fig.A.5, Fig.A.6 and Fig.VII.12 represent the local stress state for every component in the material: hcp_{sig11} , hcp_{sig22} and hcp_{sig33} in the 100th cycle, for the A+70 MPa dwell tests, at maximum loading. The images for fatigue tests are shown in Fig.A.7, Fig.A.8 and Fig.A.9. The last component hcp_{sig33} is associated with the crack initiation local stress in α phase when crystal axis c is parallel to the loading direction and basal planes are the dominant slip planes [Dunne et al., 2007]. In Fig.VII.12 (f) the stress state is quite large at 90° and even involves not only the inside parts of plumets but also

the outside layers. It seems that among all the crystal orientations it is one of the most critical one, but the highest value belongs to the crystal angle equal to 45° . However, the difference between them is negligible. If a graph is plotted for these orientations and every three local α phase components mentioned above, the evidence shows that the most critical crystal orientation depends on a configuration shown in Fig.VII.13 and Fig.VII.14 for dwell and fatigue tests respectively. In the configuration, having the crystal orientation equal to 45° , the most critical local stress is hcp_{sig22} in dwell tests. In fatigue tests, for the same configuration it can be either hcp_{sig11} or hcp_{sig33} . If the absolute values are considered, they are very similar to each other and there is no significant difference between them compared to sums of plastic slips described below. In conclusion, local stress state is not the most critical one to determine the scattering effect and lifetime of specimens. Instead of these components, the sum of plastic slips can be a candidate to the role of discriminating parameters.

VII.3.2 The Most Critical and Safest Crystal Orientations

The most critical and safest crystal orientations are characterised according to the distribution of the sum of plastic slips. In most of the configurations, the most critical crystal angles in HCP (α phase is only considered) are equal to 45° and the safest orientations are equal to 90° in Fig.VII.15 and in Fig.A.10 – Fig.A.14 (figures have been zoomed in for a better check of the difference between orientations). In most cases, the largest value is situated in the outer layer of the main plume. This result confirms the conclusions obtained with the real morphology in the previous chapter.

For the morphological angle equal to 90° in fatigue tests, the most critical orientation is equal to 0° and the safest orientation is equal to $15^\circ/60^\circ$ (they are very similar), but there is no big difference between all configurations. They are nearly the same in Fig.A.14.

For the safest crystal orientations equal to 90° (in most cases) it is easily seen that there is nearly no difference between values in the outer or inside layers of the main plume, and one can hardly define in which location of the main plume crack initiation is most likely to appear.

VII.3.3 The Most Critical and Safest Morphological Orientations

By comparing the various configurations, it can be concluded that the most critical and the safest morphological angles are both in the 0° morphological configuration, for fatigue and dwell loadings. Figure VII.16 corresponds to the most critical case, with a crystal orientation of 45° and Fig.VII.17 shows the safest configuration, with crystal orientations equal to 90° .

The maximum of the sum of plastic slips is situated in the outer layer of the main plume for the morphological angle equal to 0° , and crystal angles equal to 45° represented in Fig.VII.16 for both types of loading. However, the values of the safest sum of plastic slips can be found in the inside bottom layer of the main plume but there is no big difference between its layers, so that the safest morphological angle is equal to 90° , with crystal angles equal to 45° in Fig.VII.16 for both loading types. Surprisingly, in the case of the safest crystal angles equal to 90° in Fig.VII.17 the safest morphological angle is equal to 0° but there is a small difference between each configuration, so it is more convenient to choose the configuration with the morphological angle equal to 90° (for both types of loadings) which is also the safest one in the case with the most critical crystal orientations equal to 45° .

VII.3.4 Comparison of Configurations with Real and Virtual Crystal Orientations

The configuration with real orientations can be compared to variants with the most critical and the safest crystal orientations. It can be considered as one of the safest variants in dwell tests and relatively safe in fatigue experiments among the most dangerous cases shown in Fig.VII.16. Among the safest variants there is nothing surprising concerning the configuration with real angles, it is among the rest of other columns in Fig.VII.17.

In conclusion, the present configuration with real crystal angles is among the safest configurations.

VII.4 Influence of the Shape of the Main Plume

The shape of the main plume may influence the local response in the full field calculation. Three configurations, shown in Fig.VII.18, have been considered to investigate a possible effect. The width of the plume is preserved, and three lengths are considered (normalized by the initial length): 1 (the original one), 1/2 and 1/4. The boundary conditions and the applied loading are unchanged. Real crystallographical orientations are used.

As shown in Fig.VII.19, the sum of plastic slips presents opposite variations for dwell and fatigue tests:

- 1) The bigger plume's length, the bigger strain values in the microstructure for dwell tests;
- 2) The smaller plume's length, the bigger strain values in the microstructure for fatigue tests.

It means that the mechanisms are quite different for these types of loadings.

VII.5 Conclusions

A full field model has been developed to represent microscopic features of the alloy which can influence its behaviour and failure. Both α and β phases and size effect (thickness of laths in both types of crystals) have been included to embody the smallest nuances as much as possible. In the α phase, the following active slip systems have been modelled: 1) Basal slip systems; 2) Prismatic systems; 3) Pyramidal $\langle a \rangle$ slip systems; 4) First-order pyramidal $\langle c + a \rangle$ slip systems; 5) Second-order pyramidal $\langle c + a \rangle$ slip systems in Fig.III.8 [Venkataramani et al., 2008]. In β phase, potentially active slip systems have also been included: 1) (110); 2) (112); 3) (123) in Fig. III.8 [Venkataramani et al., 2008].

All simulations conducted by using a material RVE (tension at different strain rates, relaxation, fatigue and dwell tests at various stress levels) present a good agreement with experiments (Fig.VI.6 and Fig.VI.7).

Meshes with organised patterns called "plumes" have been proposed to elucidate local damage mechanisms, and to investigate the most critical, and the safest crystal and morphological orientations (Fig.VII.5). The fields have been analysed at maximum loading in fatigue tests and at the end of the hold period of time in dwell experiments, after 100

simulated cycles.

It seems that local stress fields in Ti-6242 forged in the domain β might not be a candidate to become a criteria in order to determine the scattering effect in the data, as there is no significant difference between stress components. The following conclusions are related to sums of plastic slips and corresponding configurations.

Concerning “real angle” configurations:

- The most critical morphological angles are equal to 45° for both tests and the safest morphological orientations are equal to 90° for dwell tests and $0^\circ/90^\circ$ for fatigue tests in Fig.VII.9.
- The most critical state is always located in the outer layer of the main plume.
- The strain distribution becomes quite large in the most critical configurations in Fig.VII.10 (d) and Fig.VII.11 (d) for dwell and fatigue loadings accordingly.

Concerning “virtual angle” configurations:

- In most configurations, the most critical crystal angles are equal to 45° and the safest crystal orientations are equal to 90° in Fig.VII.15 and in Fig.A.10 – Fig.A.14;
- In most cases, the largest values of the sum of plastic slips are found in the outer layer of the main plume.
- For the morphological angle equal to 90° in fatigue tests, the most critical crystal orientation is equal to 0° , and the safest one is equal to $15^\circ/60^\circ$ (they are very similar) but there is only a small difference between all configurations in Fig.A.14.
- In most cases, for the safest crystal orientations equal to 90° , it is easily seen that there is nearly no difference between values in the outer or inside layers of the main plume.

Concerning the most critical and safest morphological orientations in “virtual angle” configurations:

- By comparing the most critical configurations, it can be concluded that the most critical and safest morphological angles are equal to 0° in Fig.VII.16 (the most critical configurations) and Fig.VII.17 (the safest configurations) in both types of tests (dwell and fatigue loadings) but it is safer to choose the morphological angle equal to 90° , as the safest one, as it is the case for the most critical configurations in Fig.VII.16.
- The values of the most critical sum of plastic slips are found in the outer layer of the main plume.

For both real and virtual crystal orientations:

- The configuration with real angles is considered as one of the safest variants in dwell tests and relatively safe in fatigue experiments among the most dangerous cases in Fig.VII.16.
- Between the safest variants, the configuration with real angles is among the rest of other columns in Fig.VII.17.

The values of the sum of plastic slips are about three–eight times bigger in dwell tests compared to fatigue ones. It seems that cold creep plays the major role in dwell-fatigue tests and that the sum of plastic slips could be chosen as a criterion for life estimation. The same conclusion has been drawn in the previous chapter according to [Sinha et al., 2004].

The most important points to save in order to protect discs from the deleterious effects of dwell and fatigue loadings are the following:

- 0g – 45d in FigVII.20 (a) is the worst configuration.
- 90g – 90d in FigVII.20 (b) is the best one.
- Crystal orientations are more important than morphological angles. The crystallographic texture may have a critical influence on the life of Ti-6242 forged in the domain β .
- Plume sizes influence strain values. In dwell tests, the most critical plumes are the longest, although the opposite (the shortest) is true in fatigue.

Some scattering effects are a major problem in industry, as it is hardly explained by many trials and errors. This phenomenon, based on present results, can be considered and calibrated to understand why it persists in dwell and fatigue tests. The thorough analysis will be done in the next chapter.

Un modèle numérique a été développé pour représenter l'influence de la microstructure sur le comportement et la rupture de notre alliage. Les phases α , β sont représentées, et l'effet de taille (épaisseur de lattes dans les deux types de cristaux) a été inclus pour que la modélisation soit aussi précise que possible. Dans la phase α , les systèmes actifs suivants ont été introduits : 1) Systèmes basaux ; 2) Systèmes prismatiques ; 3) Systèmes pyramidaux $\langle a \rangle$; 4) Systèmes pyramidaux de premier ordre $\langle c + a \rangle$; 5) Systèmes pyramidaux de deuxième ordre $\langle c + a \rangle$ (voir Fig.III.8 et [Venkataramani et al., 2008]). Dans la phase β , les systèmes de glissement considérés sont : 1) (110) ; 2) (112) ; 3) (123) (voir Fig. III.8 et [Venkataramani et al., 2008]).

Toutes les simulations conduites en utilisant un RVE (traction à différents taux de déformation, relaxation, fatigue sans et avec temps de maintien) présentent un bon accord avec les expériences (Fig.VI.6 et Fig.VI.7).

Des calculs de structures ont été réalisés sur des “plumes” pour étudier les mécanismes d'endommagement local et examiner le caractère critique des orientations cristallographiques et morphologiques (Fig.VII.5). Les champs ont été analysés lors du chargement maximal en fatigue et à la fin du temps de maintien en fatigue avec temps de maintien (dwell) après 100 cycles simulés.

Les champs de contraintes locales ne peuvent pas être des critères pour discriminer entre les différents cas de chargement, puisqu'il n'y a pas de différence significative sans et avec temps de maintien. En revanche, l'évaluation de la somme des glissement plastique permet de statuer. On obtient les résultats suivants :

Configurations “real angle”:

- Les angles morphologiques les plus critiques sont de 45° pour les deux types de tests et les orientations morphologiques les plus sûres sont à 90° pour le dwell et $0^\circ/90^\circ$ pour la fatigue (Fig. VII.9).
- L'état le plus critique est toujours localisé dans la couche extérieure de la plume principale.
- La distribution de déformations devient très importante dans les configurations les plus critiques sur Fig. VII.10 (d) et Fig. VII.11 (d) pour la fatigue avec et sans temps de maintien.

Configurations “virtual angle”:

- Dans la plupart des configurations, les angles cristallographiques les plus critiques sont de 45° et les orientations cristallographiques les plus sûres sont à 90° (Fig. VII.15, Fig. A.10, Fig. A.14 ;
- Dans la plupart des cas, les plus grandes valeurs de la somme de glissement plastique sont observées dans la couche extérieure de la plume principale.
- Pour un angle morphologique égal à 90° dans les essais de fatigue, l'orientation cristallographique la plus critique est égale à 0° , et la plus sûre est de $15^\circ/60^\circ$ mais la différence entre toutes les configurations reste faible (Fig. A.14).
- Pour les orientations cristallographiques les plus sûres (soit 90°), il n'y a pratiquement pas de différence entre les valeurs des couches extérieures ou intérieures de la plume principale.

Orientations morphologiques les plus critiques et les plus sûres dans les configurations de type “virtual angle” :

- En comparant les configurations les plus critiques, on peut conclure que les angles morphologiques les plus critiques sont égaux à 0° (Fig. VII.16) et les plus sûrs à 90° (Fig. VII.17) dans tous les deux types de tests (avec et sans temps de maintien).
- Les valeurs de la somme la plus critique de glissement plastique sont trouvées dans la couche extérieure de la plume principale.

Pour les orientations réelles et virtuelles:

- La configuration avec les angles réels constitue en fait une des variantes les plus sûres en fatigue avec temps de maintien et relativement sûr en fatigue (Fig. VII.16).

Les valeurs de la somme de glissement plastique sont trois à huit fois plus grandes en fatigue avec temps de maintien par comparaison avec la fatigue continue. Le fluage à froid joue un rôle important dans les tests avec temps de maintien, et la somme des glissements plastiques peut être choisie comme critère pour une estimation de la durée de vie.

Les points les plus importants pour protéger des disques des effets nuisibles de la fatigue avec temps de maintien et la fatigue sont les suivants:

- $0g - 45d$ sur Fig. VII.20 (a) est la configuration la plus critique.
- $90g - 90d$ sur Fig. VII.20 (b) est la plus sûre.

- *Les orientations cristallographiques sont plus importantes que les angles morphologiques. La texture cristallographique peut avoir une influence critique sur la durée de vie.*
- *La taille des plumes influence les valeurs des déformations locales. En fatigue avec temps de maintien, les plumes les plus critiques sont les plus longues, mais c'est le contraire qui est vérifié en fatigue continue.*

La dispersion de résultats constitue un problème important dans l'industrie. Nos résultats permettent de comprendre son origine, en fatigue sans et avec temps de maintien. Une analyse approfondie sera faite dans le chapitre suivant.

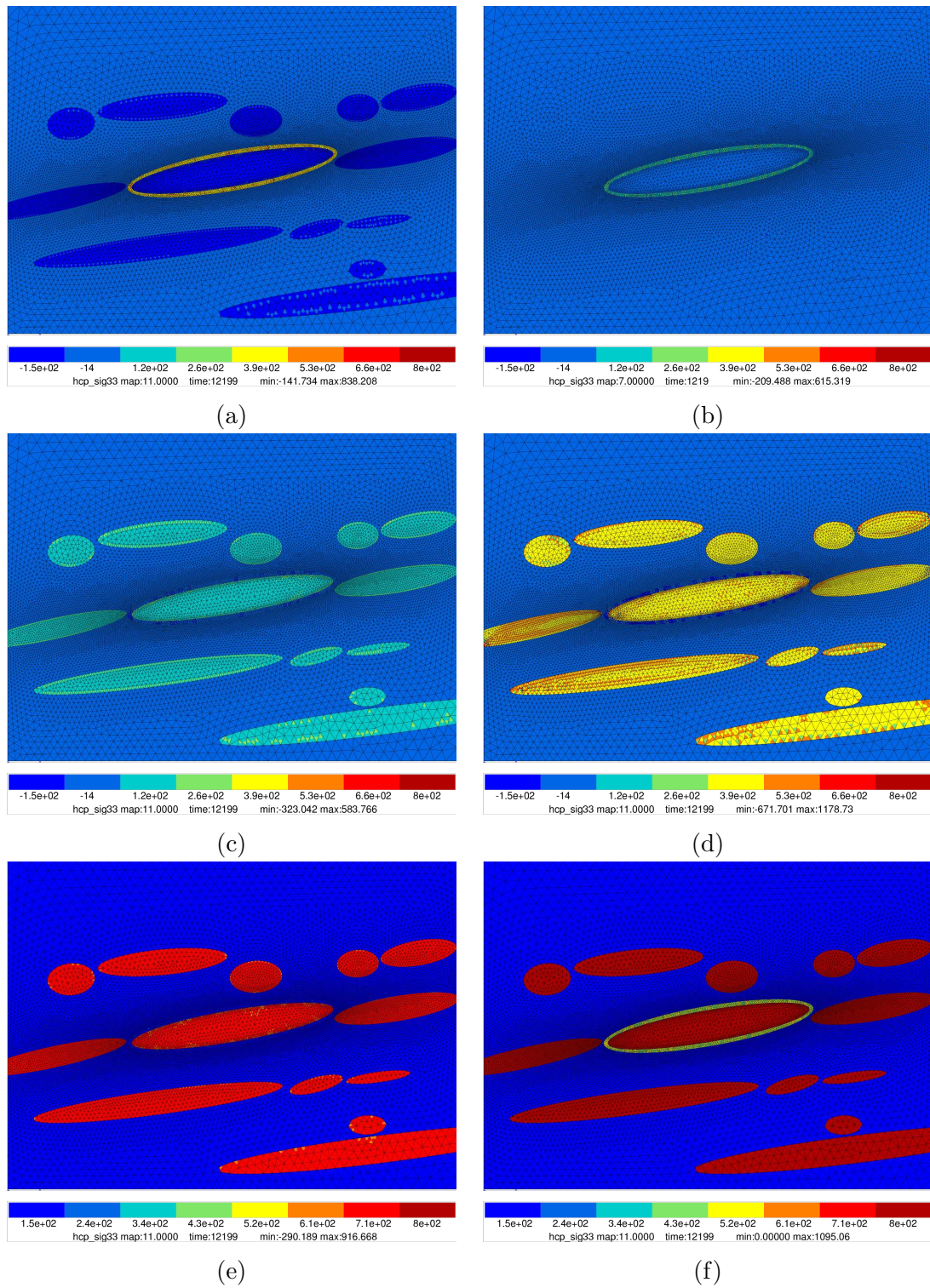


Figure VII.12 : Stress field h_{cp33} in dwell tests for the microstructure with the morphological angle 10g and crystal orientations: (a) 0d; (b) 15d; (c) 30d; (d) 45d; (e) 60d; (f) 90d;

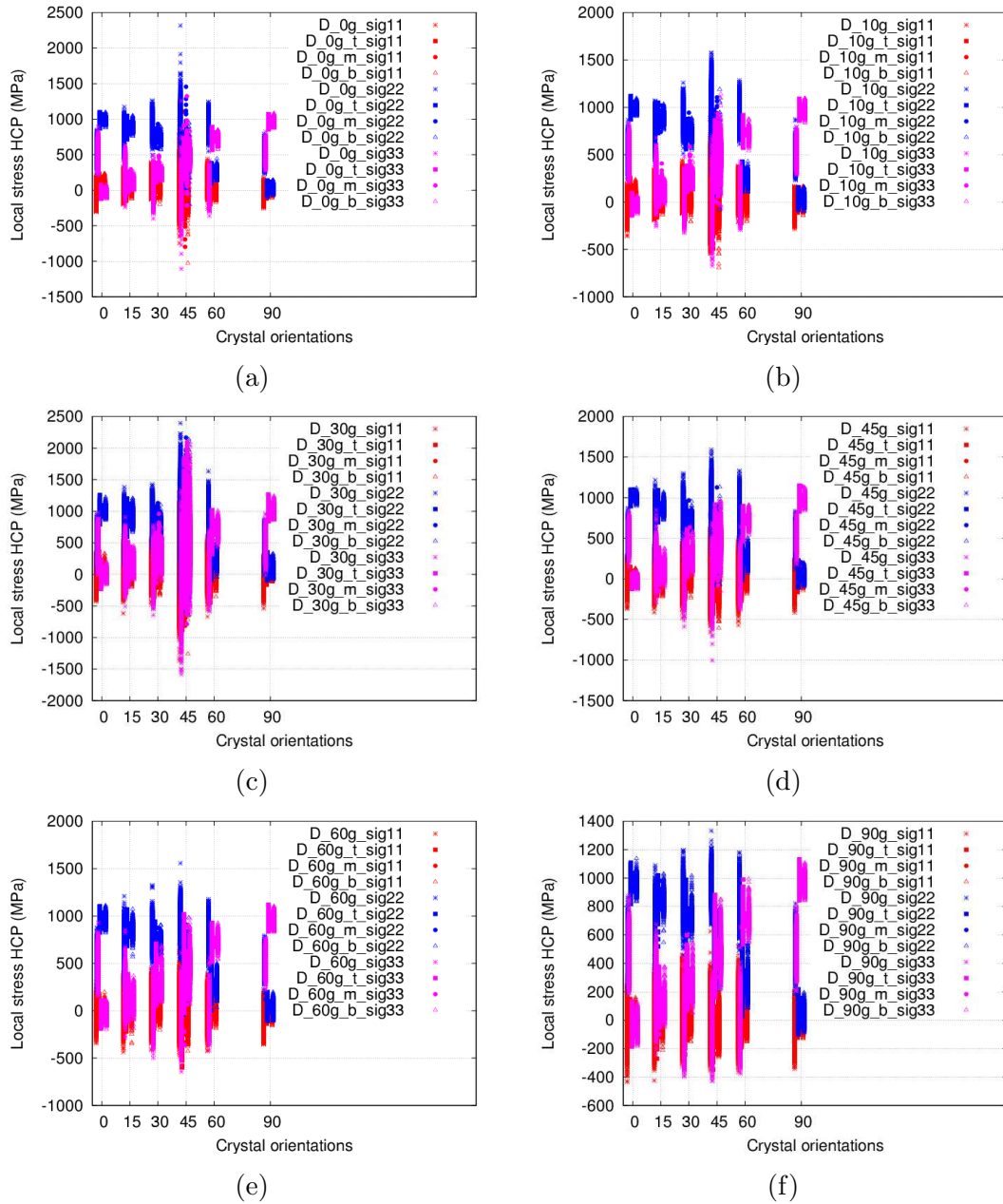


Figure VII.13 : Distribution of stress fields hcp_{11} , hcp_{22} and hcp_{33} in HCP crystals (α phase, dwell loading at A+70 MPa, virtual angles), inside top, middle and bottom layers of the principal plume in the 100th cycle for different configurations with morphological angles: (a) 0g; (b) 10g; (c) 30g; (d) 45g; (e) 60g; (f) 90g;

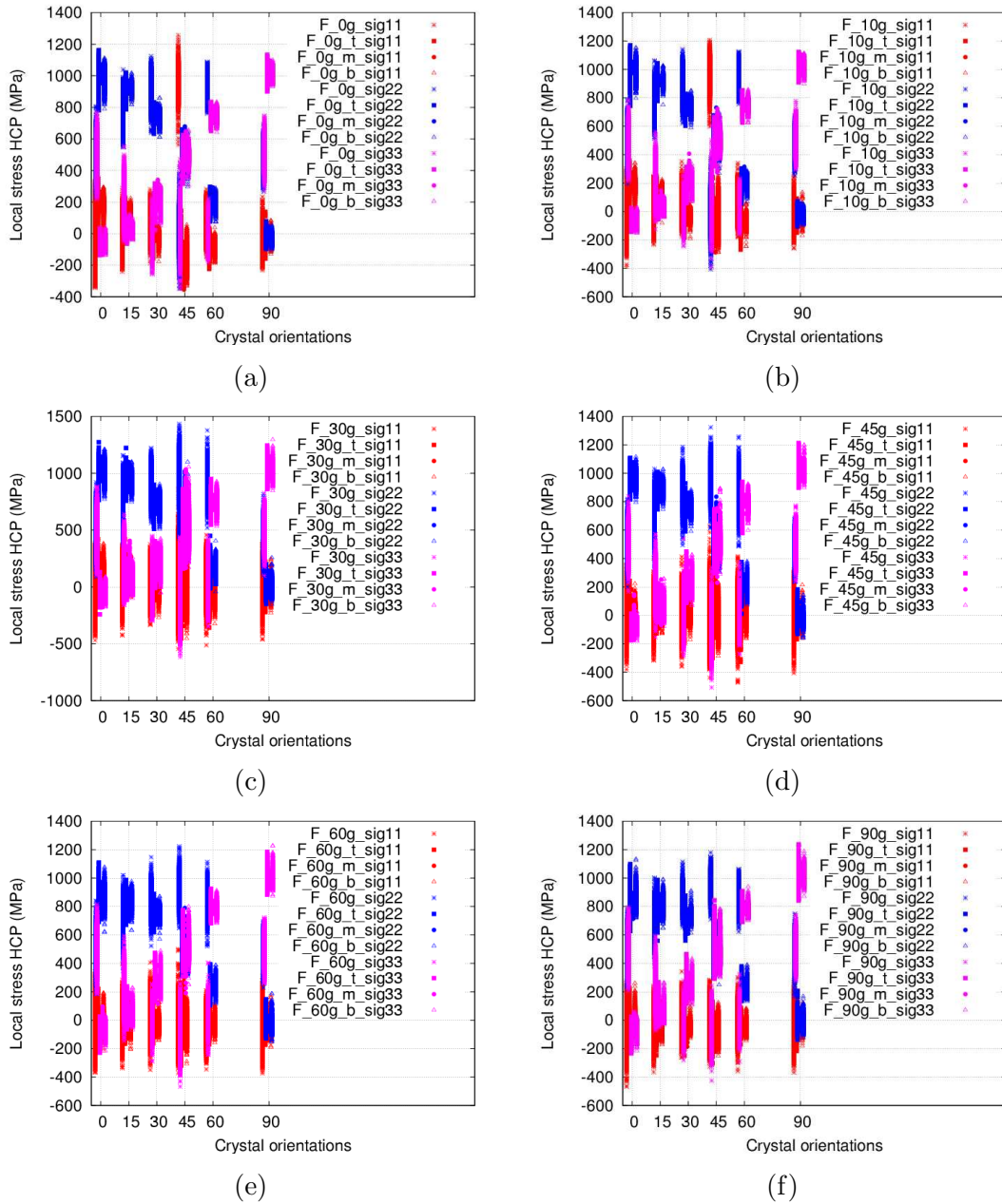


Figure VII.14 : Distribution of stress fields hcp_{11} , hcp_{22} and hcp_{33} in HCP crystals (α phase, fatigue loading at A+70 MPa, virtual angles), inside top, middle and bottom layers of the principal plume in the 100th cycle for different configurations with morphological angles: (a) 0g; (b) 10g; (c) 30g; (d) 45g; (e) 60g; (f) 90g;

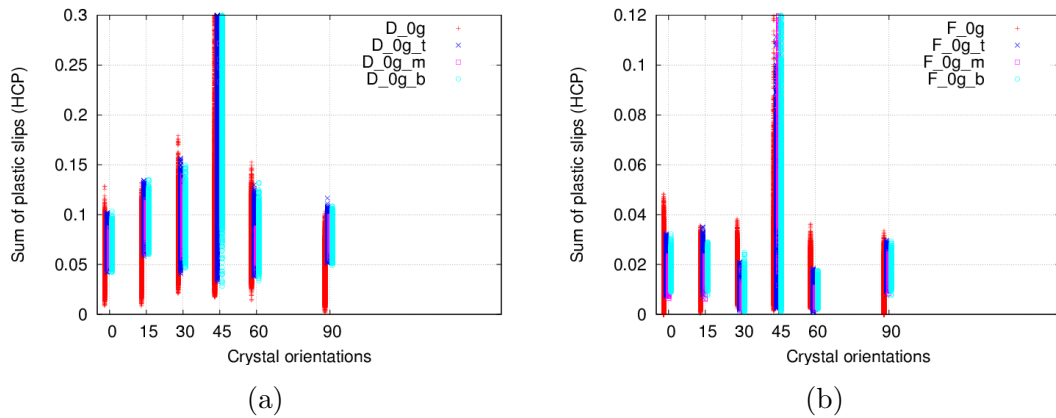


Figure VII.15 : Distribution of the sum of the plastic slips in HCP crystals (α phase, dwell (a) and fatigue (b) loadings) in the outer layer, inside top, middle and bottom layers of the main plume in the 100th cycle for different configurations (Fig.VII.5)

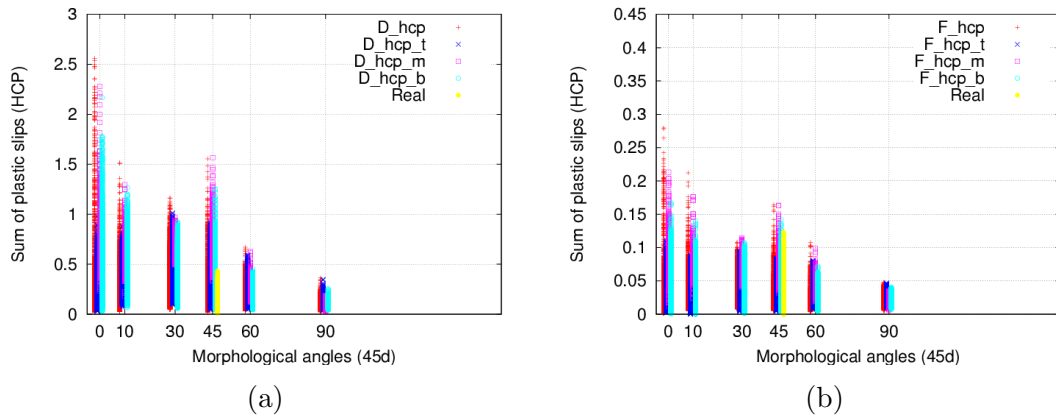


Figure VII.16 : Distribution of the most critical sum of plastic slips in HCP crystals (α phase, dwell (a) and fatigue (b) loadings, virtual angles) in the outer layer, inside top, middle and bottom layers of the main plume in the 100th cycle for various configurations (Fig.VII.5)

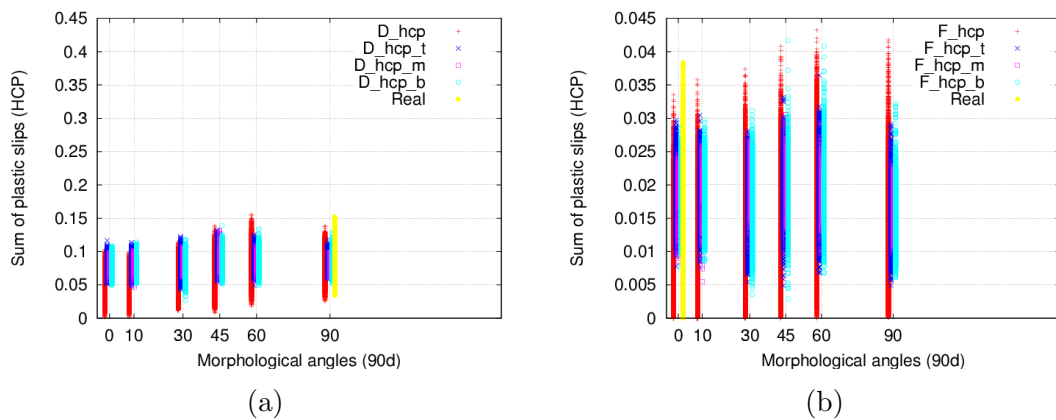


Figure VII.17 : Distribution of the safest sum of plastic slips in HCP crystals (α phase, dwell (a) and fatigue (b) loadings, virtual angles) in the outer layer, inside top, middle and bottom layers of the main plume in the 100th cycle for various configurations (Fig.VII.5)

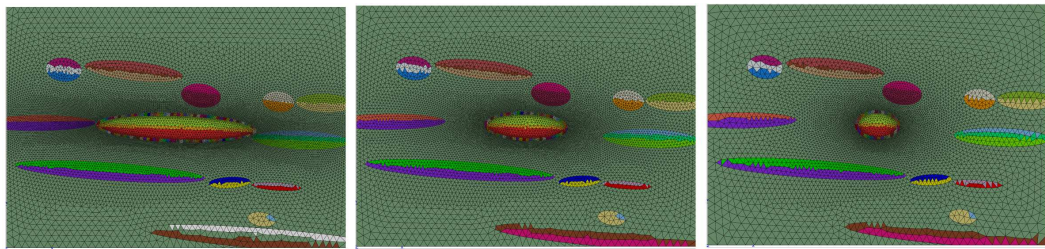


Figure VII.18 : Three different sizes having the length = 1, 1/2 and 1/4 according to the sequence of the images

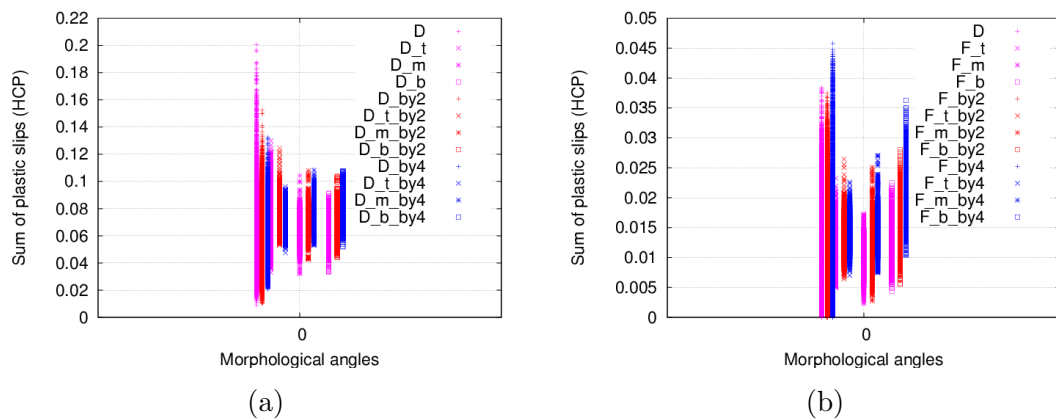


Figure VII.19 : Distribution of the sum of plastic slips in HCP crystals (α phase, dwell (a) and fatigue (b) loadings, real angles) in the outer layer, inside top, middle and bottom layers (indicated t, m and b) of the main plume at cycle 100 for three plume's sizes (FigVII.18)

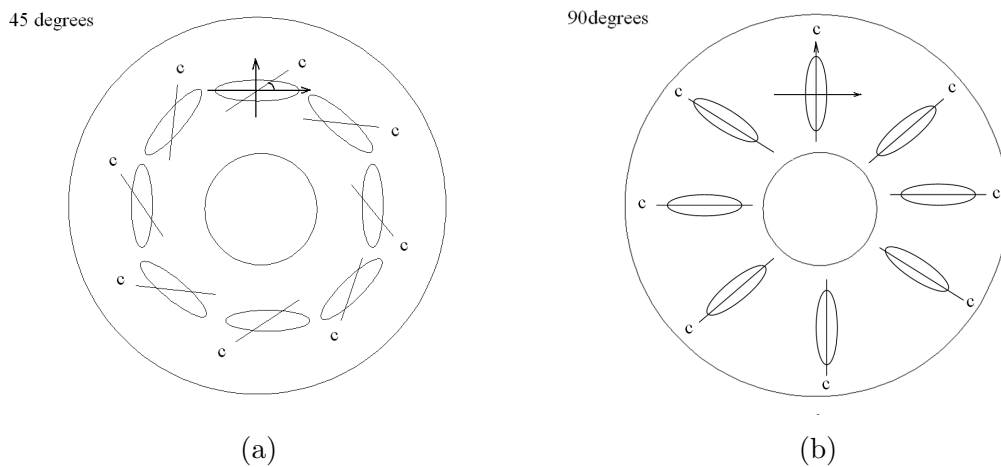


Figure VII.20 : The most critical 0g – 45d (a) and safest 90g – 90d (b) schematic configurations of forged discs

Chapter -VIII-

**Life Prediction under Fatigue and
Dwell Loadings**

Contents

VIII.1	Introduction	118
VIII.2	Macroscopic Damage Model	118
VIII.2.1	Fatigue damage model	118
VIII.2.2	Creep-Fatigue Interaction	120
VIII.2.3	Calibration results	120
VIII.3	A Microstructure Based Damage Model	122
VIII.4	Conclusions	126

VIII.1 Introduction

Having in hand the stress and strain history at the macroscale and at the microscale, the final goal of the study is the estimation of the number of cycles to crack initiation, under fatigue and dwell loadings. On the one hand, engineers need to use macroscopic models, since the time available for each new computing case is generally small in this case. On the other hand, models written at the microscale allow to introduce local variables, and provide a more reliable information on the damage mechanisms. We will consider both types of approaches in this section. The so called ONERA damage model is the selected macroscopic model, since it allows to account for cyclic and creep damages. An original model based on microstructural information will be proposed for producing a life estimation from the Crystal Plasticity Finite Element results collected in the previous chapter. This last model will allow us to evaluate the life scatter, that is classical under fatigue loading, but becomes huge for high stress dwell loadings.

The database includes first HCF tests performed at Snecma on specimens cut from a real disc (bore location). They are denoted by “HCF_Snecma_bore” in Fig.VIII.1. Low cycle fatigue tests (LCF) have also been performed, by Snecma and ENSMA [Freiherr von Thungen and Villechaise, 2011]. The fatigue tests available are all nonsymmetric load controlled fatigue tests (loading ratio $R_{sigma} = 0$ and 0.2, frequency 0.5 Hz). The dwell fatigue tests are also all nonsymmetric load controlled tests. The loading path is a trapezoidal cycle with a 120 s hold period and 1 s transients. All tests have been carried out at RT.

Figure VIII.1 (a) shows all the results in a (stress amplitude)–(number of cycles to initiation) diagram. A large scatter can be observed, when approaching the fatigue limit. This is a classical effect in fatigue, that does not require a special attention in the model. The problem related to dwell is with the scatter for high stress levels. In fact, a part of this scatter is an artefact, due to a bad value of the stress level. As shown in Fig.III.4, cyclic creep operates under unbalanced loading at prescribed stress. The section of the specimen decreases, and the stress increases during the test. This effect is specially important for dwell tests. The original points and the corrected counterparts are shown in Fig.VIII.1 (a). For all the cases, a correction has been applied by assuming that the relevant stress for a given test is the ratio of the initial stress by $(1 - \varepsilon)$, ε being the axial strain at the middle of lifetime. The corrective term is of the order of 1.015 – 1.035 for fatigue test, but can reach 1.08 for dwell tests. The plot in Fig.VIII.1 (b) shows the points that will be introduced in the simulations.

VIII.2 Macroscopic Damage Model

The pure fatigue damage model is described first. Then, we show how the mechanism of creep–fatigue interaction is taken into account, and we propose an identification procedure for the material parameters.

VIII.2.1 Fatigue damage model

The fatigue damage evolution (equation VIII.1) is written in terms of the number of cycles N . For the sake of simplicity, we restrict ourselves to the one dimensional expression. Multiaxial expression can be found for instance in [Lemaitre and Chaboche, 2002].

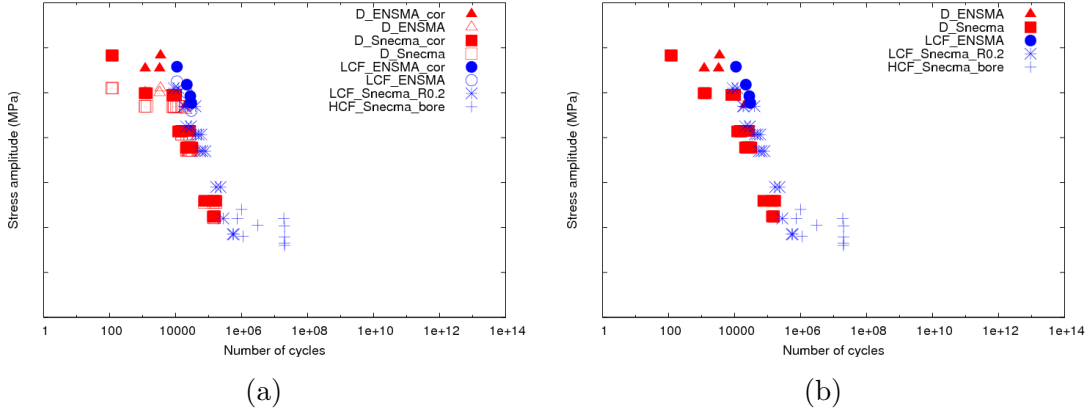


Figure VIII.1 : Experimental points in dwell and fatigue tests: (a) non-corrected and corrected; (b) non-corrected.

The essential formulas are the following:

$$\delta D = \left[1 - (1 - D)^{\beta+1}\right]^{\alpha(\Delta\sigma, \sigma_H)} \left[\frac{\Delta\sigma/2}{M(\sigma_H)(1 - D)}\right]^{\beta} \delta N \quad (\text{VIII.1})$$

where $\frac{\Delta\sigma}{2}$ is the stress amplitude, and σ_H the mean stress defining the cycle.

The α exponent depends on the loading, in order to introduce non-linear cumulation capabilities in the model:

$$\alpha(\Delta\sigma, \sigma_H) = 1 - a \left\langle \frac{\Delta\sigma/2 - \sigma_l'(\sigma_H)}{\sigma_u - \sigma_{max}} \right\rangle \quad (\text{VIII.2})$$

where $\langle \cdot \rangle$ denotes the positive part operator ($\langle f \rangle = f$ if $f > 0$, $\langle f \rangle = 0$ if $f \leq 0$), and σ_{max} is the maximum stress ($\sigma_{max} = \sigma_H + \Delta\sigma/2$ for uniaxial loadings).

The $M(\sigma_H)$ and $\sigma_l'(\sigma_H)$ coefficients depend on the mean stress σ_H in order to account for an increased fatigue damage due to positive values of the loading ratio (positive value of the mean stress). The model is then equivalent to Sines' expression for the fatigue limit.

$$\sigma_l'(\sigma_H) = \sigma_l (1 - b_1 \sigma_H) \quad (\text{VIII.3})$$

$$M(\sigma_H) = M_0 (1 - b_2 \sigma_H) \quad (\text{VIII.4})$$

The integration of the differential equation VIII.2 between 0 (virgin state) and 1 (initiation) provides the number of cycles N_f with a mechanism of pure fatigue:

$$N_F = \frac{\langle \sigma_u - \sigma_{max} \rangle}{a(\beta + 1) \langle \Delta\sigma/2 - \sigma_l'(\sigma_H) \rangle} \left[\frac{\Delta\sigma/2}{M(\sigma_H)}\right]^{-\beta} \quad (\text{VIII.5})$$

σ_u , σ_l , β , M_0 , b_1 , b_2 and a are material parameters.

- σ_u is the ultimate tensile stress, such that $N_f = 0$ when σ_{max} reaches σ_u

- σ_l is the fatigue limit for a symmetric cycle ($R = -1$), such that N_f tends to infinity when $\Delta\sigma/2$ reaches σ_l

VIII.2.2 Creep-Fatigue Interaction

The ONERA model also contains a “creep” dependent part. It was originally developed to model real creep for alloys working at high temperature. In the present approach, even if the mechanism is not fully characterized from a microscopic point of view, plastic flow is time dependent. The idea behind the present model is that dwell effect can be modelled, provided this “cold creep” is taken into account. The original model is then used here, even if the real mechanism differs from high temperature creep. Damage evolution is described by the classical Rabotnov-Kachanov model, defined by equation [VIII.6]:

$$dD_C = \left(\frac{\bar{\sigma}}{A}\right)^r \frac{1}{(1 - D_C)^k} dt \quad (\text{VIII.6})$$

where A , r and k are model coefficients that may depend on temperature, and $\bar{\sigma}$ is an equivalent stress written in the following general form:

$$\bar{\sigma} = (1 - \alpha - \beta) J(\sigma) + \alpha \sigma_I + \beta \sigma_H \quad (\text{VIII.7})$$

where $J(\sigma)$ is the von Mises invariant, σ_I the maximum principal stress and σ_H the trace of the stress tensor $\underline{\sigma}$.

In general, this model is calibrated on experimental creep tests that are not available in the experimental data base provided by Snecma. We will then determine the parameters by inverse problem simulation of the creep-fatigue tests.

The creep-fatigue interaction is determined by assuming that damages produced by each mechanism can be combined according to a simple additive rule:

The integration of the fatigue and the creep models are then integrated by replacing the fatigue damage in eq.VIII.1 and the creep damage in eq.VIII.6 by D .

$$dD = dD_F + dD_C \quad (\text{VIII.8})$$

VIII.2.3 Calibration results

The strategy to calibrate the damage model parameters uses the following procedure, in the framework of `Zopt`, the optimizer module of `Z-Set` code:

- Characterization of the full S-N curve: ultimate stress, slope in the low cycle fatigue regime ($10^2 < N_f < 10^5$), fatigue limit;
- Calibration of the fatigue parameters by using high frequency tests (50 Hz) where creep damage is absent; since no two-level tests are available in fatigue, the non linearity of the cumulation is not defined from experiment, and the material parameter a cannot be identified. As classically proposed in this case [Blétry and Cailletaud, 2011], a is taken equal to 0.1;

σ_u	σ_l	β	M_0	b_1	b_2	a	A	r	k
MPa	MPa	β	MPa	b_1	b_2	a	MPa	r	k
980.	280.	4.89	5000.	0.00052	0.00085	0.1	5440.	11.2	18.5

Table VIII.1 : The material parameters of ONERA model

- Calibration parameters accounting for mean stress effect (b_1 and b_2) by using nonsymmetric fatigue tests. Ideally, 2 tests (or, better, 3) nonsymmetric loading ratios ($R_{\sigma} \neq -1$) are needed to characterize the full Haigh diagram. Since all available experimental points correspond to nonsymmetric fatigue tests (loading factor $R = 0$), coefficients b_1 and b_2 have been calibrated automatically by means of Zopt;
- The “creep” model (namely material parameters A , r , k) are obtained by simulating the number of cycles to failure for dwell tests, seen as creep–fatigue interaction tests.

Fatigue calibration results. Calibration results of the fatigue model is presented in Fig.VIII.2. A good agreement between experimental and numerical values is noticed. The blue curve passes through the blue dots of fatigue experimental data.

Creep–fatigue interaction. Figure VIII.2 shows the result of the calibration compared to the experimental data. Given the very strong dispersion between the different tests, the calibrated model represents a satisfactory compromise. The final parameters are shown in Tab.VIII.1.

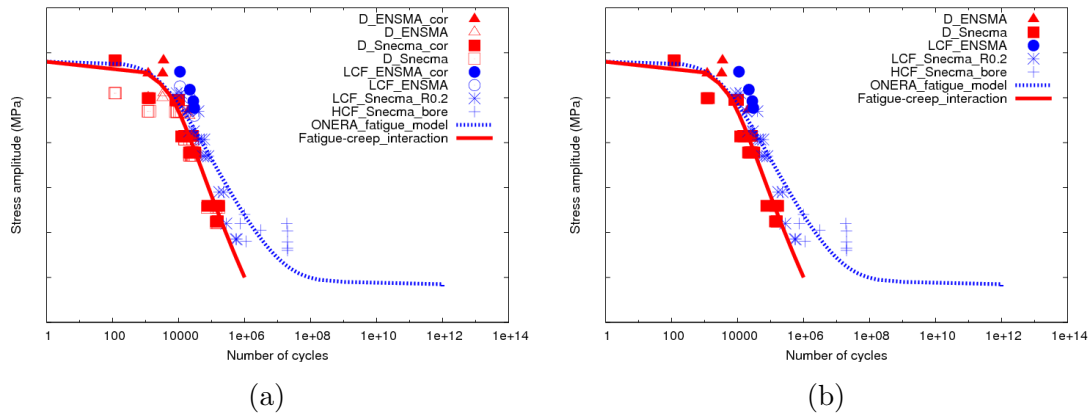


Figure VIII.2 : (a) Creep–fatigue calibration results; (b) Creep–fatigue calibration results with corrected points

VIII.3 A Microstructure Based Damage Model

The previous chapter has shown that the sum of the plastic slips is a critical parameter that allows to discriminate between fatigue and dwell tests. We will then investigate how its variations can be used for building a life estimation model involving plume effect. Since the initial information is richer than in a macroscopic approach, one can rely on a very simple expression at the microscale. Due to its input, that is a distribution instead of a simple value, this approach is able to provide an estimation of the scatter observed in the experiments. Two simple power rules are selected:

1) The inverse equation:

$$\sum_{s \in S} \gamma^s = A \cdot (N_f)^{-n}$$

where $\sum_{s \in S} \gamma^s$ is a calculated sum of plastic slips in HCP (α phase) from Tab.VIII.5, N_f - an experimental number of cycles to failure in fatigue or dwell tests. In this case for every situation, maximum and minimum dwell and fatigue curves, there must be four sets of parameters. This strategy must then be used as the first approach only;

2) The direct equation:

$$N_f = A \cdot \left(\sum_{s \in S} \gamma^s \right)^{-n}$$

where N_f stands for a number of cycles to failure in fatigue or dwell-fatigue tests, A , n are the material parameters and $\sum_{s \in S} \gamma^s$ is a sum of plastic slips. In this case for every situation, maximum and minimum dwell and fatigue curves, there can be only one set of parameters. The unique set of coefficients is an advantage of this method.

The maximum and minimum values for the sum of plastic slips were derived from six essential variants of a crystal model (Fig.VII.5) with plumes. For the same stress loading level all the six configurations have been compared to each other in fatigue and dwell tests and then the maximum and minimum values have been chosen among them. They are presented at different stress levels (A1, A2, A3, A4, A5, A6, A7) for every slip systems in Tab.VIII.2, VIII.3, VIII.4 and VIII.5 (respectively for basal, prismatic and pyramidal slip family in the α phase, the last table demonstrates the result for all the slip systems in α phase). Table VIII.6 shows the result for all the planes in β phase. All the conditions of the calculation procedure were described in the previous chapters.

The curves for the model have been obtained by simulating two types of graphs with the following axes: 1) $\sum_{s \in S} \gamma^s - N_f$ 2) $\Delta\sigma - N_f$;

1) In order to demonstrate more transparently that the model can describe the phenomenon very well, the inverse equation described above is used in this paragraph.

Straight simulated logarithmic lines are represented in Fig.VIII.3 for dwell and in Fig.VIII.4 for fatigue tests. Every point is plotted by using an experimental number of cycles to failure and associated numerical sum of plastic slips for α phase from Tab.VIII.5,

σ_{max} (MPa)	A1	A2	A3	A4	A5	A6	A7
Dwell, max	5.912e-7	1.900e-5	7.633e-4	4.233e-4	3.490e-1	1.194	1.521
Dwell, min	1.507e-12	4.904e-11	1.330e-9	6.621e-8	2.020e-2	4.436e-2	1.311e-1
Fatigue, max	1.057e-9	3.286e-8	5.640e-4	3.182e-3	2.508e-2	9.575e-2	2.936e-1
Fatigue, min	3.305e-14	9.916e-13	2.568e-11	8.395e-10	4.755e-3	1.184e-2	2.345e-2

Table VIII.2 : Total slip distribution on basal planes in α phase

σ_{max} (MPa)	A1	A2	A3	A4	A5	A6	A7
Dwell, max	5.012e-9	2.857e-4	1.742e-3	3.941e-3	9.289e-2	2.296e-1	3.057e-1
Dwell, min	1.169e-10	3.805e-09	1.686e-4	1.278e-3	2.655e-2	4.148e-2	8.353e-2
Fatigue, max	3.964e-6	8.328e-4	2.494e-3	4.376e-3	2.494e-2	8.085e-2	2.031e-1
Fatigue, min	2.579e-12	7.333e-11	3.554e-06	7.151e-4	1.443e-2	2.649e-2	4.093e-2

Table VIII.3 : Total slip distribution on prismatic planes in α phase

σ_{max} (MPa)	A1	A2	A3	A4	A5	A6	A7
Dwell, max	1.758e-7	5.714e-6	1.021e-4	1.274e-3	1.981e-1	7.166e-1	8.788e-1
Dwell, min	1.327e-09	4.319e-08	1.286e-06	3.353e-05	2.384e-2	4.725e-2	1.223e-1
Fatigue, max	3.878e-9	1.103e-7	3.271e-6	2.645e-5	1.133e-2	5.628e-2	2.231e-1
Fatigue, min	2.911e-11	8.736e-10	2.528e-08	7.240e-07	3.860e-3	7.819e-3	1.558e-2

Table VIII.4 : Total slip distribution on pyramidal planes in α phase

σ_{max} (MPa)	A1	A2	A3	A4	A5	A6	A7
Dwell, max	5.912e-07	2.858e-4	1.742e-3	4.233e-3	4.264e-1	1.470	1.847
Dwell, min	2.612e-09	5.714e-06	1.686e-4	1.280e-3	4.951e-2	8.007e-2	1.669e-1
Fatigue, max	3.964e-06	8.328e-4	2.493e-3	4.376e-3	2.637e-2	1.597e-1	5.181e-1
Fatigue, min	5.730e-11	1.103e-07	3.557e-06	7.151e-4	1.784e-2	2.649e-2	4.093e-2

Table VIII.5 : Total slip distribution for all the HCP planes in α phase

σ_{max} (MPa)	A1	A2	A3	A4	A5	A6	A7
Dwell, max	6.049e-14	1.967e-12	7.577e-11	6.630e-08	2.288e-1	9.227e-1	1.146
Dwell, min	8.672e-28	2.815e-26	2.219e-24	2.368e-19	228e-2	6.027e-2	1.443e-1
Fatigue, max	1.381e-15	4.198e-14	1.181e-12	1.381e-10	1.818e-2	9.795e-2	3.153e-1
Fatigue, min	1.369e-23	3.881e-22	2.429e-20	6.513e-18	4.165e-3	1.155e-2	2.243e-2

Table VIII.6 : Total slip distribution for all the BCC planes in β phase

then regression curves are plotted through these dots. Although there are some points which are not aligned with each model's curve, the tendency appears to be correct for maximum and minimum values in every type of test.

Instead of just one, the four sets of coefficients must be identified to represent the maximum and minimum values in dwell and fatigue tests, as there are four situations: dwell maximum, dwell minimum, fatigue maximum and fatigue minimum. They are calculated by using regression equations and their values are shown in Tab.VIII.7, so there are A and n for every associated type of test and they can reproduce the regression curves correctly enough.

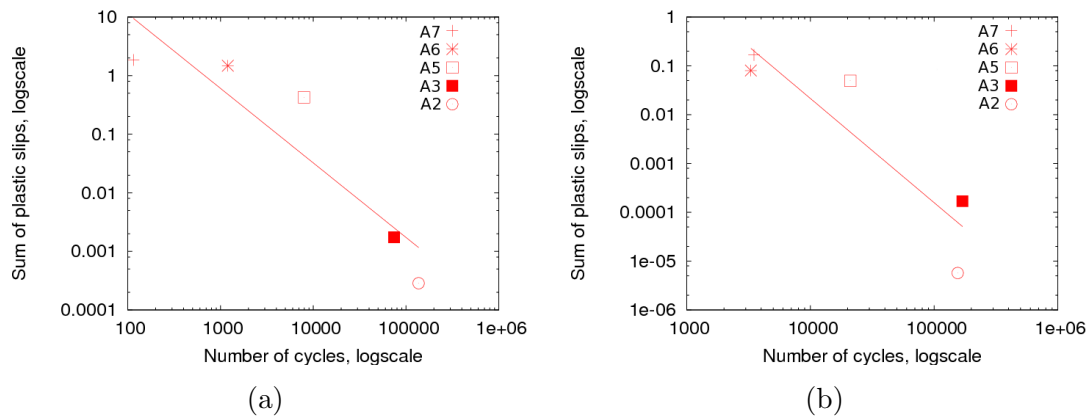


Figure VIII.3 : (a) Macroscopic curve simulating the maximum values in dwell tests; (b) Macroscopic curve simulating the minimum values in dwell tests

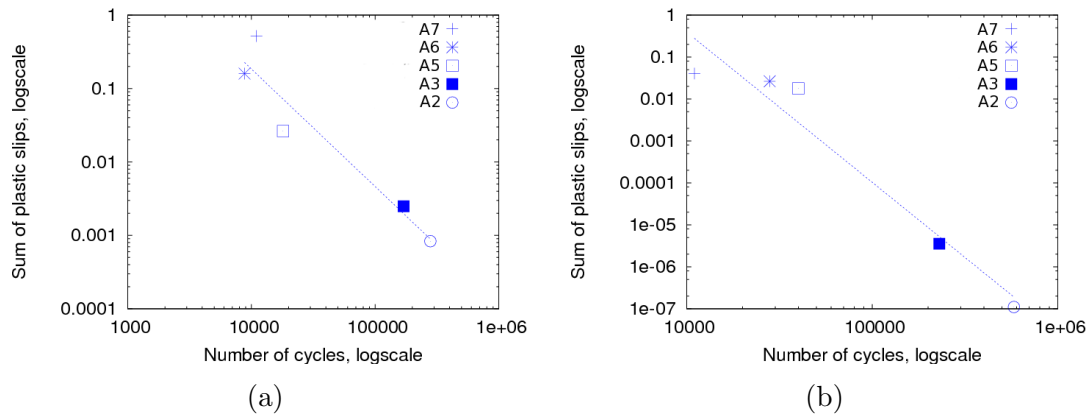


Figure VIII.4 : (a) Macroscopic curve simulating the maximum values in fatigue tests; (b) Macroscopic curve simulating the minimum values in fatigue tests

2) In this case, the normal power rule described above is used and there is a unique set of parameters. The curves are obtained by using sums of plastic slips on basal, prismatic planes from Tab.VIII.2, Tab.VIII.3 and calculated number of cycles to failure derived from the formula of the direct simple power rule described above. The simulated plots are shown in Fig.VIII.5. For this type of slip planes it is not possible to simulate dwell and fatigue scattering effect due to the fact that the curves are similar to each other for maximum and minimum values. The plots obtained by using sums of plastic slips on pyramidal and all

Type of test	A	n
Dwell, maximum	3.97e3	-1.27
Dwell, minimum	7.28e6	-2.13
Fatigue, maximum	4.64e5	-1.60
Fatigue, minimum	8.17e13	-3.58

Table VIII.7 : Coefficients A and n for the four sets of databases

planes from Tab.VIII.4, Tab.VIII.5 are shown in Fig.VIII.6. In this case there is a great difference in dwell and fatigue curves and for dwell tests the representative curves are good, but for fatigue experimental data they are not.

Finally, for the last example, where a sum of plastic slips for all the planes is used, the fitting curves are very close to the real distribution of experimental points. At the low stress level, it seems that numerically a lifetime for fatigue tests can be lower than in dwell experiments. However, the scattering is larger in fatigue than in dwell tests. If average curves are plotted, there is a significant difference at the same stress level in Fig.VIII.7 (a). On the contrary, if logarithmic average curves are plotted, they are quite similar to each other in Fig.VIII.7 (b), especially at low stress level compared to the previous example. Having this idea in the mind, both ONERA and the cumulated slip models for average curves are plotted and they are quite close to each other at high stress levels in Fig.VIII.7 (c). It means that the correlation is good enough and that both models can be used to estimate the lifetime of specimens. It is worth remarking that the latter model is more precise and can take into account the scattering effect in Ti-6242 forged in the domain β .

Possible explanation that the latter model is the best to simulate the scattering effect can be the fact that the model incorporates all the slip systems of this alloy and all of them are responsible for the crystal plastic slips. Everyone significantly contributes to that inner process.

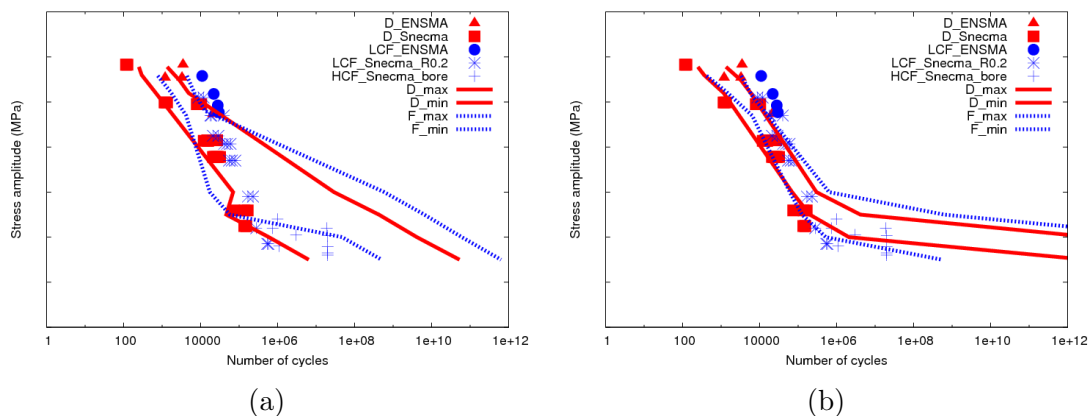


Figure VIII.5 : Macroscopic curves showing a scattering effect by using: (a) a sum of plastic slips on basal planes (b) a sum of plastic slips on prismatic planes in α phase

All calibrated coefficients for each type of sums of plastic slips in α phase are represented in Tab.VIII.8. For β phase, they are not indicated, as at the stress level lower than A6 MPa

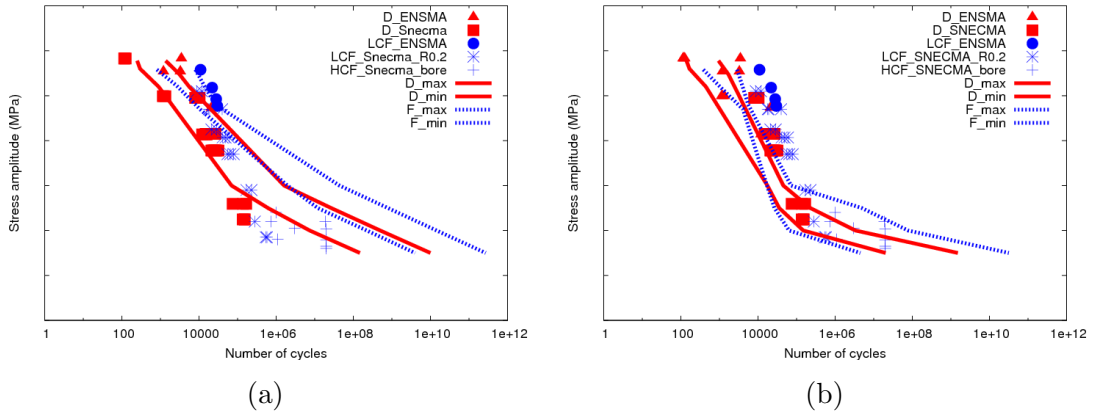


Figure VIII.6 : Macroscopic curves showing a scattering effect by using: (a) a sum of plastic slips on pyramidal planes; (b) a sum of all slips in α phase

Type of sums of plastic slips	A	n
Basal	333.67	0.69
Prismatic	53.73	1.30
Pyramidal	223.64	0.862
Total	441.45	0.93

Table VIII.8 : Coefficients A and n for each type of sums of plastic slips

(which is only a little bit higher than the elastic limit for this phase) there is no significant slip and the curves for the scattering effect cannot be plotted. This numerical results is in agreement with the fact that α phase is softer than β phase, so that β may remain in its elastic domain at relatively small applied plastic strain [Feugas and Clavel, 1997].

VIII.4 Conclusions

Ti6242 forged in the domain β mechanical behaviour is rate sensitive at RT, so that a progressive ratchetting develops in tests that introduce a hold period under prescribed loading (dwell). Due to section reduction, the effective stress applied to the specimen increases during the test. If this effect is taken into account to analyse the fatigue / fatigue-dwell database, the resulting lifetime can be easily predicted by means of a classical model (ONERA approach), provided creep-fatigue interaction is introduced. The huge reduction of the number of cycles that is experimentally observed for high level dwell tests can be explained by the fact that the ultimate stress is not far from being reached in the specimens. The moderate life reduction that is present in the intermediate level tests can be reproduced by the creep – fatigue interaction model.

The scatter can be described effectively by introducing a power function of the accumulated slip, in a FECF calculation involving plumes. A number of typical configurations have been investigated. A unique set of coefficients can be used to represent the failure of Ti-6242 in both sets of tests (fatigue and dwell). The difference between fatigue and dwell

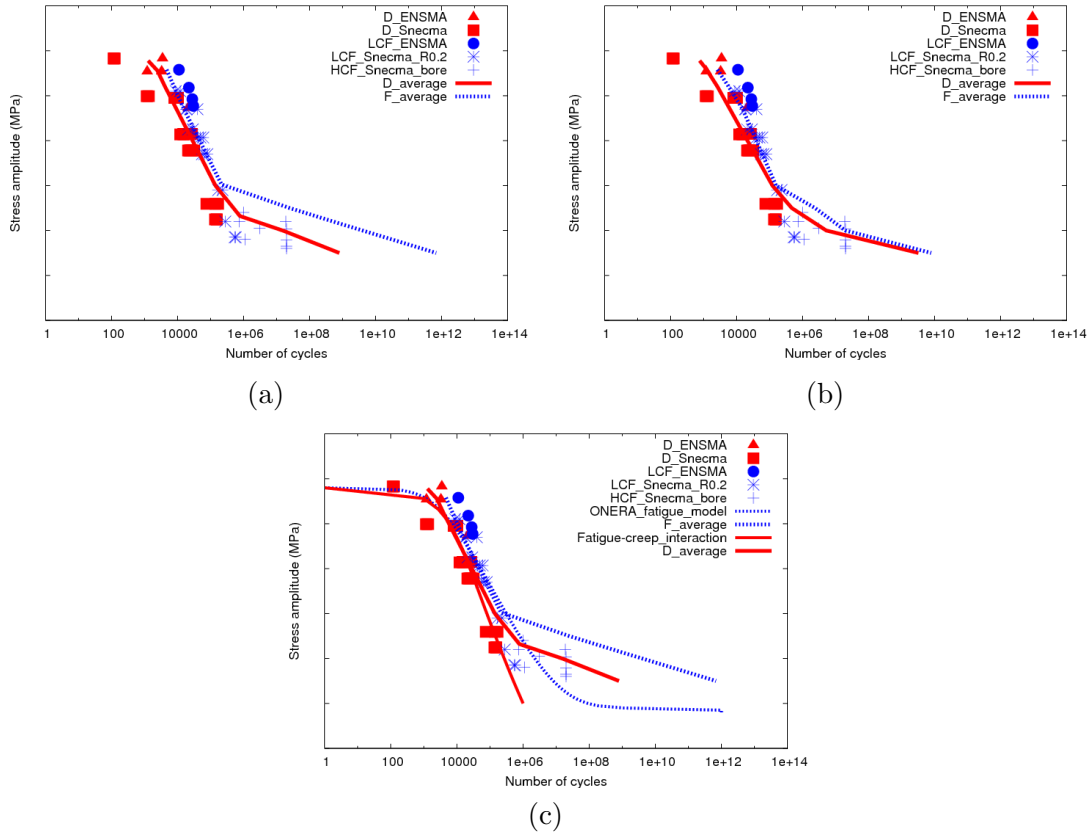


Figure VIII.7 : (a) Macroscopic average curves showing a scattering effect; (b) Macroscopic logarithmic average curves showing a scattering effect; (c) Comparison between macroscopic curves by using a microscopic and ONERA models.

tests at low stress level can be explained by means of the present model.

The difference between fatigue and dwell tests is correctly taken into account at high stress levels. The material parameters are shown in Tab.VIII.1 (ONERA model) and Tab.VIII.8 (accumulated slip model). The developed model demonstrates the capacity to simulate the scattering effect in fatigue and dwell tests.

Le comportement de l'alliage Ti6242 forgé dans le domaine β le comportement mécanique est sensible à la vitesse à la température ambiante, si bien qu'un phénomène de rochet progressif est présent dans les essais qui introduisent le temps de maintien sous le chargement imposé (dwell). En raison de la réduction de section, la contrainte efficace appliquée sur l'éprouvette augmente pendant l'essai. Si cet effet est pris en compte pour analyser la base de données obtenues en fatigue sans et avec temps de maintien la base de données, la durée de vie résultante peut être facilement prédite au moyen d'un modèle classique (l'approche d'ONERA), pourvu qu'une interaction fatigue-fluage soit introduite. L'énorme réduction du nombre de cycles qui est expérimentalement observé pour les haut niveau de contrainte peuvent être expliquées par le fait que la contrainte ultime n'est pas loin d'être atteinte dans les éprouvettes. La réduction de vie modérée qui est présente dans les essai de niveau intermédiaires peut être reproduite par le modèle avec interaction fatigue-fluage.

La dispersion peut être décrite efficacement en introduisant une fonction de glissement accumulé, dans un calcul FECF incluant des plumes. Un certain nombre de configurations typiques ont été examinées. Un ensemble unique de coefficients peut être utilisé pour représenter la rupture de Ti-6242 dans les deux types de tests (fatigue et fatigue avec temps de maintien). La différence entre la fatigue et la fatigue avec temps de maintien (dwell) au niveau de la basse contrainte bas peuvent être expliquées au moyen du présent modèle.

La différence entre les tests de fatigue et fatigue avec temps de maintien est correctement prise en compte pour les hauts niveaux de la contrainte. Les paramètres utilisés sont montrés en Tab.VIII.1 (modèle ONERA) et Tab.VIII.8 (modèle de glissement accumulé). Le modèle développé montre la capacité de simuler l'effet de la dispersion dans la fatigue et fatigue avec temps de maintien.

Chapter -IX-

General Conclusions and Outlook

IX.1 Conclusions

The main target of this thesis was to find physical laws which could improve the estimation of the lifetime of specimens and engine discs, and provide a criterion able to describe the scatter observed in dwell and fatigue tests.

The results are on two levels, macroscopic and microscopic. A macroscopic model has been specially developed to better represent cold creep. It is used to perform investigations on residual stress. The microscopic level has been involved in a multiscale model that is able to account for texture and plumes in the material. A series of possible configurations have been analysed to propose a criterion able to account for material scattering effect.

In two previous PhD theses [Robert, 2007] and [Longuet, 2010], a mechanical and a multiphase mechanical models (CC and RL) have been developed for the study of Ti6Al4V. Their nature are different, nevertheless, their comparison shows that the fields of residual stress in the forged discs calculated on the basis of the two models are similar. This allows to validate the simplest model for performing disc calculations.

In the part dealing with the macroscopic approach, a whole set of experiments has been simulated, including tensile, relaxation, creep, cyclic fatigue and dwell tests at different temperatures from 20°C up to 600°C (Snecma and ENSMA databases). A mechanical model, called CN, consisting of three potentials (parts) has been calibrated to produce high temperature viscoplastic flow and to account for cold creep which persists at RT. This model has represented a first step, facilitating the subsequent creation of the microscopic model.

By utilising the CB model [Baroumes, 1998] (there is just a little difference between this model and CN), a 3D disc has been calculated. The results illustrate that specimens cut in the disc are not the seat of big residual von Mises stress (maximum 49.4 MPa, that is less than 10% of a classically applied loading during the conduction of fatigue/dwell tests. Nevertheless, the maximum value of cumulated strain reaches 7.4×10^{-3} , and significant distortions do not play a role during the machining of the specimens. It is worth mentioning that these values are overestimations, as only quenching treatment process was modelled in order to find an upper bound of the effect and the final shape of cut specimens were not modelled either.

In the second part of the thesis, a multiscale size-dependent crystal plasticity model has been developed to represent Ti-6242 forged in the domain β . The relevant slip system families have been incorporated, for HCP and BCC phases. Two modes, soft and hard, have been taken into account. The values, corresponding to these types of modes in the Hall-Patch equation, have been calculated.

All simulations and experimental curves have been compared and the agreement obtained with the multiscale model is very satisfactory. It provides an information at a microscale that can be compared for dwell and fatigue tests. The analysis demonstrates that there is just a little difference between local stress components for each phase, but a large difference in the sum of plastic slips where the values for pyramidal slips systems of HCP crystals (α phase) and 123 slip systems of BCC crystals (β phase) are the highest in the tests (after 1000 cycles). The ratio between dwell and fatigue tests is between 3 and 7, that is in agreement with experiments that find a 7.6 ratio [Sinha et al., 2004].

To model “plumes” in the material, a complex structure has been created. It takes into account both phases and the size effect (thickness of laths in crystals), and represents correctly all the tests in our experimental data base (tension at different strain rates, relaxation, fatigue and dwell tests at various stress levels). Meshes with organised patterns have been proposed in order to investigate the effect of crystal and morphological orientations in the material. The fields have been analysed at the maximum of the 100th cycle in fatigue tests and at the end of the hold period of time in dwell. Both fatigue and dwell-fatigue (with 120 s dwell period) loadings were considered. The most critical configurations are mentioned. They should be avoided in engine discs. An important conclusion is that crystal orientations are more critical than the morphology of the plumes.

By using ONERA classical model, the fatigue-creep interaction has been modelled and the resulting lifetime is well predicted. The huge reduction of the number of cycles that is experimentally observed for high level dwell tests can be explained by the fact that the ultimate stress is approached in the specimens due to section reduction.

By introducing a model based on accumulated slip, the scattering effect has been successfully described. The sum of plastic slips involves basal, prismatic and pyramidal families in α phase. Both types of tests, fatigue and dwell-fatigue experimental points have been modelled properly.

IX.2 Outlook

In the model involving plumes a matrix has been created by using a macroscopic constitutive equations to simplify calculations, otherwise in the present it would not be possible to compute all variations for a given period of time. It is recommended to incorporate a real texture for the material matrix to consider other effects which might happen in Ti-6242 forged in the domain β .

A database of variants could be enlarged to analyse other possible configurations with not only one domain in the main plume, but also with two and three, as they can exist in the real situation.

Thanks to the rapid development of computers, it will be possible in the future to simulate the real microstructure with an explicit geometrical representation of lamellae, without introducing scale transition laws. This would give an improved view toward the microscopic scale.

From the recent observations in ENSMA, it is evident that plumes have very complex shapes in the depth of the material [Freiherr von Thungen and Villechaise, 2011]. They can provoke the early microcrack in a critical spot. It could be quite useful to model all such nuances of the alloy.

Calculations of crack propagation are being developed to find a criterion of lifetime of discs or specimens. This approach may contribute to a better understanding of the scattering phenomenon.

The proposed models in the thesis are not ideal and have some positive and negative points. Despite of all their drawbacks, they represent an original approach of the studied effects. In Sciences, all approaches are reviewed, revised and improved eventually. The thesis is not an exception. It can be ameliorated, specially by going further in the research and development of numerical approaches.

Conclusions *Le but principal de cette thèse était de trouver des lois physiques qui pourraient améliorer l'estimation de la durée de vie des éprouvettes et des disques de moteur aéronautique et de fournir un critère capable de décrire la dispersion observée dans les essais de fatigue et de fatigue avec temps de maintien.*

Les résultats sont à deux niveaux, macroscopique et microscopiques. Un modèle macroscopique a été spécialement développé pour mieux représenter le fluage à froid. Il est utilisé pour l'estimation des contraintes résiduelles. Le niveau microscopique a été impliqué dans un modèle multiéchelle qui est capable de représenter la texture et les plumes dans la matière. Une série de configurations possibles a été analysée pour proposer un critère capable de représenter la dispersion dans l'alliage.

Dans les deux thèses de doctorat précédentes [Robert, 2007] and [Longuet, 2010], des modèles mécaniques phénoménologiques mono- et polyphasés (CC et RL) ont été développés pour simuler le comportement du Ti6Al4V. Leur nature est différente, néanmoins, leur comparaison montre que les champs de contrainte résiduelle dans les disques forgés calculés sur la base des deux modèles sont similaires. Cela permet de valider le modèle le plus simple pour exécuter les calculs sur le disque.

Dans la partie s'occupant de l'approche macroscopique, un ensemble d'expériences a été simulé : il comporte des essais de traction, relaxation, fluage, fatigue sans et avec temps de maintien à différentes températures, de 20° C jusqu'à 600° C (bases de données de Snecma et ENSMA). Un modèle mécanique, appelé CN, composé de trois potentiels, a été calibré pour produire un comportement dominé par la viscosité à haute température et pour autoriser un fluage limité à température ambiante. Ce modèle a représenté un premier pas, en facilitant la création ultérieure du modèle microscopique.

En utilisant le modèle CB [Baroumes, 1998] (très voisin du modèle CN), on a calculé un disque en 3D. Les résultats illustrent le fait que les échantillons coupés du disque ne sont pas le siège d'une contrainte résiduelle de von Mises importante (49,4 MPa maximum, ce qui représente moins de 10% d'un chargement classiquement appliqué pendant la conduction des tests de la fatigue/dwell. La valeur maximale de déformation accumulée atteint $7,4 \times 10^{-3}$, cependant les distorsions obtenues ne jouent pas un rôle significatif après la phase d'usinage des échantillons. Il faut noter que ces valeurs sont des surestimations, puisque seule la trempe a été modélisée.

Dans la deuxième partie de la thèse, un modèle multiéchelle cristallographique plastique dépendant de la taille a été développé pour représenter le Ti-6242 forgé dans le domaine β . Les familles de systèmes de glissement ont été incorporées pour les phases de HCP et BCC. Les deux types de systèmes de glissement, "mous" et "durs", ont été pris en compte, les valeurs correspondantes des cissions critiques étant calculés au moyen de l'équation de Hall.

Toutes les simulations et les courbes expérimentales ont été comparées, et l'accord obtenu avec le modèle multiéchelle est très satisfaisant. Il fournit des renseignements au niveau de la microstructure qui peuvent être comparés pour la fatigue et la fatigue avec temps de maintien. L'analyse montre qu'il y a une grande différence entre les deux types de chargement pour ce qui concerne la somme des glissements plastiques : les valeurs pour les systèmes de glissement pyramidaux de HCP (α) et systèmes de glissement 123 de BCC (β) sont les plus élevées dans les tests (après 1000 cycles). Le rapport entre la fatigue et la fatigue avec temps de maintien est entre 3 et 7, qui est en accord avec les expériences qui trouvent un rapport de 7,6 [Sinha et al., 2004].

Pour modéliser les "plumes" dans l'alliage, une structure complexe a été créée. Elle tient compte des deux phases et de l'effet de taille (l'épaisseur de lattes dans les cristaux) et représente correctement tous les tests dans notre base de données expérimentales (la traction à différents taux de déformation, la relaxation, la fatigue et la fatigue avec temps de maintien à des niveaux de contrainte différents). On a étudié l'effet de différentes orientations cristallographiques et morphologiques dans l'alliage. Les champs ont été analysés au maximum du 100e cycle dans les tests de fatigue et à la fin du temps du maintien dans les tests de type "dwell". Les configurations les plus critiques sont mentionnées. Une conclusion importante est que l'orientation cristallographique est un paramètre plus important que la morphologie des plumes.

En utilisant le modèle classique de l'ONERA, l'interaction fatigue-fluage a été modélisée et la vie résultante est bien prédite. L'énorme réduction du nombre de cycles qui est observé expérimentalement peut être expliquée par le fait que la contrainte appliquée se rapproche de la contrainte ultime pour les échantillons les plus chargés, en raison de la réduction de section qui résulte du fluage cyclique à froid.

En introduisant un modèle basé sur le glissement accumulé, l'effet de la dispersion a été décrit avec succès. La somme des glissements plastiques inclut les familles basales, prismatiques et pyramidales dans la phase α . Les deux types de tests, les points expérimentaux de fatigue et de fatigue avec temps de maintien ont été modélisés correctement.

Perspectives Dans le modèle impliquant des plumes, la matrice a été modélisée en utilisant des équations de comportement macroscopiques pour des raisons de temps de calcul. Il serait souhaitable dans le futur d'utiliser une texture réelle, qui pourra orienter différemment l'écoulement plastique au voisinage des plumes.

La base de données des variants devrait également être élargie afin d'analyser de nouvelles configurations, qui n'aient pas un seul domaine dans la plume principale, mais deux ou trois, comme on le rencontre dans les observations.

Grâce au développement rapide d'ordinateurs, il sera possible dans l'avenir de simuler la microstructure réelle avec une représentation géométrique explicite des lamelles, sans introduire de lois de transition d'échelles. Cela donnerait une vue améliorée vers une échelle microscopique.

D'après des observations récentes de l'ENSMA, il apparaît que les plumes ont des formes très complexes dans la profondeur de la matière [Freiherr von Thungen and Villechaise, 2011]. Cette forme peut être la cause de la première fissure, et varier selon la nuance de l'alliage. Sa bonne description est donc fondamentale pour développer une ingénierie des microstructures.

La détermination de la durée de vie des composants ne se réduit pas à la détermination de l'amorçage. Il faut donc mettre en place des simulations de propagation de fissure. Cette approche pourrait contribuer à une meilleure compréhension de la dispersion.

Les modèles proposés représentent une approche originale des effets étudiés en considérant une modélisation multiéchelles. En Science, toutes les approches sont destinées à être reconsidérées, révisées et améliorées. Cette thèse n'est pas une exception. Elle peut être améliorée, spécialement en allant plus loin dans la recherche et le développement des approches numériques.

Chapter -X-

Abbreviation

BOR - burgers orientation relation;

CB - "Classical Chaboche" with coefficients identified by Baroumes, L.;

CC - "Classical Chaboche";

CN - new identification with several combined strain (CdM);

CRSS - crytical resolved shear stress;

FEA - finite element approach;

RL - model of Robert, Y. and Longuet, A. (CdM);

RT - room temperature;

Appendix -A-

Appendix

Contents

A.1	Crystallographic Slip Systems	137
A.2	CC model	141
A.3	RL model (alternative model)	142
A.4	Relationship between Eigenstrain Influence Operators	145
	References	155

A.1 Crystallographic Slip Systems

HCP structure:

1) Basal 3 HCP basal slip systems

$$\begin{aligned} & (0\ 0\ 0\ 1)[1\ -2\ 1\ 0] \\ & (0\ 0\ 0\ 1)[2\ -1\ -1\ 0] \\ & (0\ 0\ 0\ 1)[1\ 1\ -2\ 0] \end{aligned}$$

2) Prismatic 3 HCP second-order prismatic systems

$$\begin{aligned} & (1\ 0\ -1\ 0)[1\ -2\ 1\ 0] \\ & (0\ 1\ -1\ 0)[2\ -1\ -1\ 0] \\ & (-1\ 1\ 0\ 0)[1\ 1\ -2\ 0] \end{aligned}$$

3) Pyramidal $\langle a \rangle$ 12 pyramidal systems:

$$\begin{aligned} & (1\ 0\ -1\ 1)[2\ -1\ -1\ -3] \\ & (1\ 0\ -1\ 1)[1\ 1\ -2\ -3] \\ & (0\ 1\ -1\ 1)[1\ 1\ -2\ -3] \\ & (0\ 1\ -1\ 1)[-1\ 2\ -1\ -3] \\ & (-1\ 1\ 0\ 1)[-1\ 2\ -1\ -3] \\ & (-1\ 1\ 0\ 1)[-2\ 1\ 1\ -3] \end{aligned}$$

$$\begin{aligned}
 &(-1\ 0\ 1\ 1)\ [-2\ 1\ 1\ -3] \\
 &(-1\ 0\ 1\ 1)\ [-1\ -1\ 2\ -3] \\
 &(0\ -1\ 1\ 1)\ [-1\ -1\ 2\ -3] \\
 &(0\ -1\ 1\ 1)\ [1\ -2\ 1\ -3] \\
 &(1\ -1\ 0\ 1)\ [1\ -2\ 1\ -3] \\
 &(1\ -1\ 0\ 1)\ [2\ -1\ -1\ -3]
 \end{aligned}$$

4) Pyramidal 6 Π_1 pyramidal systems:

$$\begin{aligned}
 &(1\ 0\ -1\ 1)\ [1\ -2\ 1\ 0] \\
 &(0\ 1\ -1\ 1)\ [2\ -1\ -1\ 0] \\
 &(-1\ 1\ 0\ 1)\ [1\ 1\ -2\ 0] \\
 &(-1\ 0\ 1\ 1)\ [1\ -2\ 1\ 0] \\
 &(0\ -1\ 1\ 1)\ [2\ -1\ -1\ 0] \\
 &(1\ -1\ 0\ 1)\ [1\ 1\ -2\ 0]
 \end{aligned}$$

5) Pyramidal 6 Π_2 pyramidal systems:

$$\begin{aligned}
 &(-1\ 2\ -1\ 2)\ [-1\ 2\ -1\ -3] \\
 &(2\ -1\ -1\ 2)\ [2\ -1\ -1\ -3] \\
 &(1\ 1\ -2\ 2)\ [1\ 1\ -2\ -3] \\
 &(1\ -2\ 1\ 2)\ [1\ -2\ 1\ -3] \\
 &(-2\ 1\ 1\ 2)\ [-2\ 1\ 1\ -3] \\
 &(-1\ -1\ 2\ 2)\ [-1\ -1\ 2\ -3]
 \end{aligned}$$

BCC structure:

1) (110) 12 system:

$$\begin{aligned}
 &(1\ 0\ 1)\ [-1\ 1\ 1] \\
 &(1\ 0\ 1)\ [1\ 1\ -1] \\
 &(1\ 1\ 0)\ [-1\ 1\ 1] \\
 &(1\ 1\ 0)\ [1\ -1\ 1] \\
 &(0\ 1\ 1)\ [1\ -1\ 1] \\
 &(0\ 1\ 1)\ [1\ 1\ -1] \\
 &(-1\ 0\ 1)\ [1\ 1\ 1] \\
 &(-1\ 0\ 1)\ [-1\ 1\ -1] \\
 &(-1\ 1\ 0)\ [1\ 1\ 1] \\
 &(-1\ 1\ 0)\ [-1\ -1\ 1] \\
 &(0\ -1\ 1)\ [1\ 1\ 1] \\
 &(0\ -1\ 1)\ [1\ -1\ -1]
 \end{aligned}$$

2) (112) 12 system:

$$\begin{aligned}
 &(1\ 1\ 2)\ [1\ 1\ -1] \\
 &(-1\ 1\ 2)\ [1\ -1\ 1] \\
 &(1\ -1\ 2)\ [-1\ 1\ 1] \\
 &(1\ 1\ -2)\ [1\ 1\ 1] \\
 &(1\ 2\ 1)\ [1\ -1\ 1] \\
 &(-1\ 2\ 1)\ [1\ 1\ -1] \\
 &(1\ -2\ 1)\ [1\ 1\ 1]
 \end{aligned}$$

(1 2 -1)[-1 1 1]
(2 1 1)[-1 1 1]
(-2 1 1)[1 1 1]
(2 -1 1)[1 1 -1]
(2 1 -1)[1 -1 1]

3) (123) 24 system:

(1 2 3) [1 1 -1]
(-1 2 3) [1 -1 1]
(1 -2 3) [-1 1 1]
(1 2 -3) [1 1 1]
(1 3 2) [1 -1 1]
(-1 3 2) [1 1 -1]
(1 -3 2) [1 1 1]
(1 3 -2) [-1 1 1]
(2 3 1) [1 -1 1]
(-2 3 1) [1 1 -1]
(2 -3 1) [1 1 1]
(2 3 -1) [-1 1 1]
(2 1 3) [1 1 -1]
(-2 1 3) [1 -1 1]
(2 -1 3) [-1 1 1]
(2 1 -3) [1 1 1]
(3 1 2) [-1 1 1]
(-3 1 2) [1 1 1]
(3 -1 2) [1 1 -1]
(3 1 -2) [1 -1 1]
(3 2 1) [-1 1 1]
(-3 2 1) [1 1 1]
(3 -2 1) [1 1 -1]
(3 2 -1) [1 -1 1]

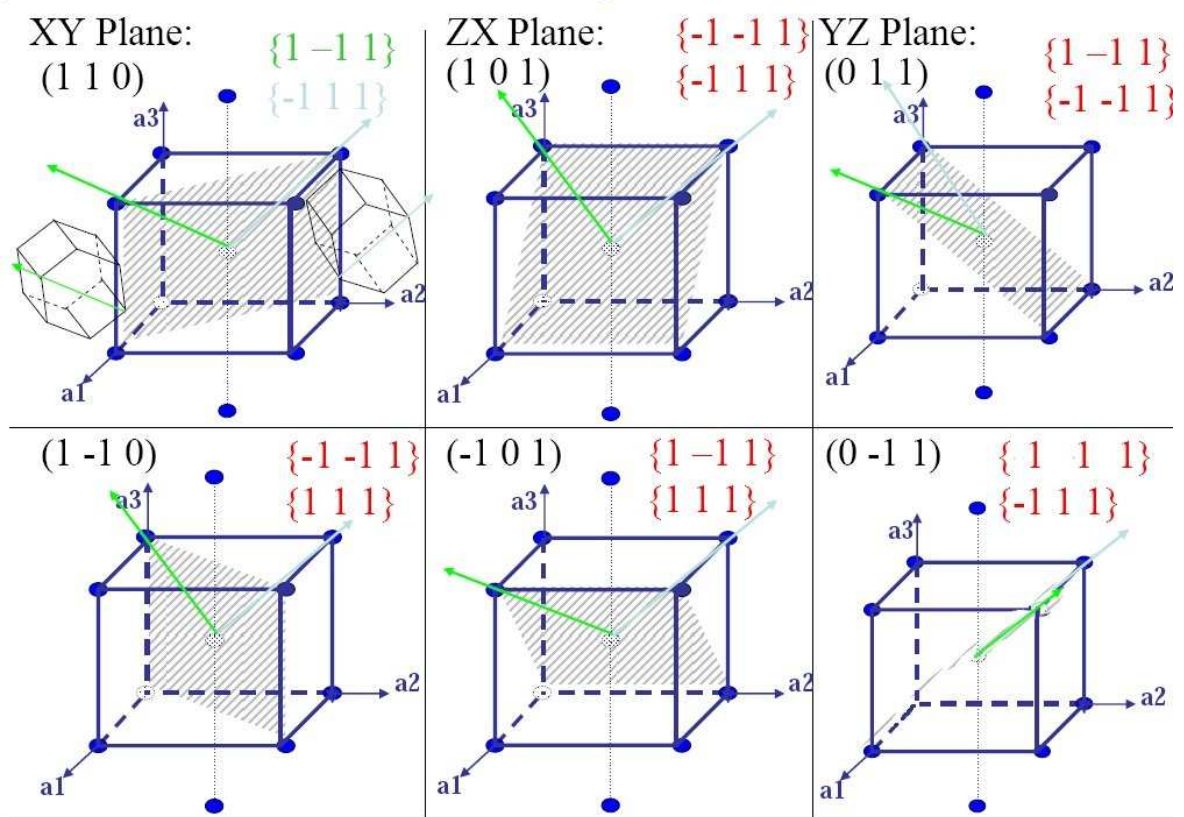


Figure A.1 : The slip systems 110 in BCC crystals [Karthikeyan et al., 2006]

A.2 CC model

Constitutive equations:

Strain partitions:

$$\underline{\underline{\varepsilon}} = \underline{\underline{\varepsilon}}^{el} + \underline{\underline{\varepsilon}}^v + \underline{\underline{\varepsilon}}^{th} \quad (\text{A.1})$$

Viscoplastic flow:

$$\dot{v} = \left\langle \frac{J(\underline{\underline{\sigma}} - \underline{\underline{\mathbf{X}}}) - R}{K} \right\rangle^n \quad (\text{A.2})$$

Kinematic hardening with time recovery:

$$\underline{\underline{\mathbf{X}}} = \frac{2}{3} C \underline{\underline{\alpha}} - \lambda(X) \underline{\underline{\mathbf{X}}} \quad \text{with} \quad \dot{\underline{\underline{\alpha}}} = \dot{v} \left(\underline{\underline{\mathbf{n}}} - \frac{D}{C} \underline{\underline{\mathbf{X}}} \right) \quad \text{and} \quad \lambda(X) = \left(\frac{\underline{\underline{\mathbf{X}}} : \underline{\underline{\mathbf{X}}}}{M} \right)^m \quad (\text{A.3})$$

Isotropic hardening with time recovery:

$$R = R0 + Q (1 - e^{-bv}) - g(R) \quad (\text{A.4})$$

A.3 RL model (alternative model)

Essential constitutive equations [Longuet et al., 2009] and [Longuet, 2010]:

$$\underline{\sigma} = \underline{\mathbf{E}} \underline{\varepsilon}_e \quad (\text{A.5})$$

The inelastic strain is composed of several parts, where the last one represents the strain due to phase change:

$$\underline{\varepsilon}_{in} = z_\alpha \underline{\xi}_\alpha^p + (1 - z_\alpha - z_{\alpha'}) \underline{\xi}_\beta^p + z_{\alpha'} \underline{\xi}_{\alpha'}^p - \delta_{\alpha \rightarrow \beta} (z_{\alpha'} + z_\alpha) \underline{\mathbf{I}} \quad (\text{A.6})$$

For each current phase the residual stress is defined by an intergranular accommodation variable:

$$\underline{\beta} = z_\beta \underline{\beta}_\beta + z_\alpha \underline{\beta}_\alpha + z_{\alpha'} \underline{\beta}_{\alpha'} \quad (\text{A.7})$$

The components of residual stress are shown here:

$$\underline{\sigma}_\alpha = \underline{\sigma} + \mu(\underline{\beta} - \underline{\beta}_\alpha) \quad (\text{A.8})$$

$$\underline{\sigma}_{\alpha'} = \underline{\sigma} + \mu(\underline{\beta} - \underline{\beta}_{\alpha'}) \quad (\text{A.9})$$

$$\underline{\sigma}_\beta = \underline{\sigma} + \mu(\underline{\beta} - \underline{\beta}_\beta) \quad (\text{A.10})$$

The second von Mises invariants and yield functions:

$$J_\alpha = \sqrt{\frac{3}{2}(\underline{\mathbf{s}}_\alpha - \underline{\mathbf{X}}_\alpha) : (\underline{\mathbf{s}}_\alpha - \underline{\mathbf{X}}_\alpha)} \quad \text{with} \quad f_\alpha = J_\alpha - R_\alpha \quad (\text{A.11})$$

$$J_\beta = \sqrt{\frac{3}{2}(\underline{\mathbf{s}}_\beta - \underline{\mathbf{X}}_\beta) : (\underline{\mathbf{s}}_\beta - \underline{\mathbf{X}}_\beta)} \quad \text{with} \quad f_\beta = J_\beta - R_\beta \quad (\text{A.12})$$

$$J_{\alpha'} = \sqrt{\frac{3}{2}(\underline{\mathbf{s}}_{\alpha'} - \underline{\mathbf{X}}_{\alpha'}) : (\underline{\mathbf{s}}_{\alpha'} - \underline{\mathbf{X}}_{\alpha'})} \quad \text{with} \quad f_{\alpha'} = J_{\alpha'} - R_{\alpha'} \quad (\text{A.13})$$

$$\underline{\mathbf{X}}_\alpha = \frac{2}{3} C_\alpha \underline{\alpha}_\alpha \quad \text{and} \quad \underline{\mathbf{X}}_\beta = \frac{2}{3} C_\beta \underline{\alpha}_\beta \quad \text{and} \quad \underline{\mathbf{X}}_{\alpha'} = \frac{2}{3} C_{\alpha'} \underline{\alpha}_{\alpha'} \quad (\text{A.14})$$

If $f_\alpha > 0$ and $z_\alpha > 0$ then :

$$\underline{\dot{\xi}}_\alpha^p = \dot{v}_\alpha \underline{\mathbf{n}}_\alpha \quad \text{with} \quad \dot{v}_\alpha = \left(\frac{J_\alpha - R_\alpha}{K_\alpha} \right)^{n_\alpha} \quad \text{and} \quad \underline{\mathbf{n}}_\alpha = \frac{3 \underline{\mathbf{s}}_\alpha - \underline{\mathbf{X}}_\alpha}{2 J_\alpha} \quad (\text{A.15})$$

$$\dot{\underline{\alpha}}_\alpha = \underline{\dot{\xi}}_\alpha^p - d_\alpha \underline{\alpha}_\alpha \dot{v}_\alpha - \left(\frac{J(\underline{\alpha}_\alpha)}{M_{b\alpha}} \right)^{m_{b\alpha}} \frac{\underline{\alpha}_\alpha}{J(\underline{\alpha}_\alpha)} \quad \text{with} \quad J(\underline{\alpha}_\alpha) = \sqrt{\frac{3}{2} \underline{\alpha}_\alpha : \underline{\alpha}_\alpha} \quad (\text{A.16})$$

$$\underline{\dot{\beta}}_\alpha = \underline{\dot{\xi}}_\alpha^p - D_\alpha \underline{\beta}_\alpha \dot{v}_\alpha \quad (\text{A.17})$$

If $f_\beta > 0$ and $z_\beta > 0$ then :

$$\dot{\xi}_\beta^p = \dot{v}_\beta \underline{n}_\beta \quad \text{with} \quad \dot{v}_\beta = \left(\frac{J_\beta - R_\beta}{K_\beta} \right)^{n_\beta} \quad \text{and} \quad \underline{n}_\beta = \frac{3 \underline{s}_\beta - \underline{X}_\beta}{2 J_\beta} \quad (\text{A.18})$$

The evolution rule of the kinematic hardening variable involves a dynamic recovery term and a static recovery term:

$$\dot{\alpha}_\beta = \dot{\xi}_\beta^p - d_\beta \alpha_\beta \dot{v}_\beta - \left(\frac{J(\alpha_\beta)}{M_{b\beta}} \right)^{m_{b\beta}} \frac{\alpha_\beta}{J(\alpha_\beta)} \quad \text{with} \quad J(\alpha_\beta) = \sqrt{\frac{3}{2} \alpha_\beta : \alpha_\beta} \quad (\text{A.19})$$

$$\dot{\tilde{\beta}}_\beta = \dot{\xi}_\beta^p - D_\beta \tilde{\beta}_\beta \dot{v}_\beta \quad (\text{A.20})$$

If $f_{\alpha'} > 0$ and $z_{\alpha'} > 0$ then :

$$\dot{\xi}_{\alpha'}^p = \dot{v}_{\alpha'} \underline{n}_{\alpha'} \quad \text{with} \quad \dot{v}_{\alpha'} = \left(\frac{J_{\alpha'} - R_{\alpha'}}{K_{\alpha'}} \right)^{n_{\alpha'}} \quad \text{and} \quad \underline{n}_{\alpha'} = \frac{3 \underline{s}_{\alpha'} - \underline{X}_{\alpha'}}{2 J_{\alpha'}} \quad (\text{A.21})$$

$$\dot{\alpha}_{\alpha'} = \dot{\xi}_{\alpha'}^p - d_{\alpha'} \alpha_{\alpha'} \dot{v}_{\alpha'} - \left(\frac{J(\alpha_{\alpha'})}{M_{b\alpha'}} \right)^{m_{b\alpha'}} \frac{\alpha_{\alpha'}}{J(\alpha_{\alpha'})} \quad \text{with} \quad J(\alpha_{\alpha'}) = \sqrt{\frac{3}{2} \alpha_{\alpha'} : \alpha_{\alpha'}} \quad (\text{A.22})$$

$$\dot{\tilde{\beta}}_{\alpha'} = \dot{\xi}_{\alpha'}^p - D_{\alpha'} \tilde{\beta}_{\alpha'} \dot{v}_{\alpha'} \quad (\text{A.23})$$

Another part of the study concerns kinetics of phases:

If $\dot{T} \geq 0$ then the volume fraction of β phase is:

$$z_\beta = 1 - z_{\alpha'} - z_\alpha \quad (\text{A.24})$$

If $T < T_\beta = 1040^\circ\text{C}$ then $\Delta z_{\alpha_2} = 0$

$$\Delta z_\alpha = z_{\alpha_{max}} - z_\alpha - z_{\alpha'} \quad (\text{A.25})$$

If $\Delta z_\alpha < 0$ then :

$$\Delta z_{\alpha_2} = z_{\alpha_{max_2}} - z_\alpha - z_{\alpha'} \quad (\text{A.26})$$

• If $z_\alpha > 0$ then :

$$\dot{z}_\alpha = z_\alpha \left(\frac{\Delta z_\alpha}{\tau_\alpha} + \frac{\Delta z_{\alpha_2}}{\tau_\alpha} \right) \quad (\text{A.27})$$

• If $z_{\alpha'} > 0$ then :

$$\dot{z}_{\alpha'} = z_{\alpha'} \frac{\Delta z_\alpha}{\tau_{\alpha'}} \quad (\text{A.28})$$

If not and if $T < M_s$ then :

$$\dot{z}_{\alpha'} = -z_{\beta_{trans}} \frac{\dot{T}}{\tau_{\beta}} \quad (\text{A.29})$$

If $(\dot{z}_{\alpha} + \dot{z}_{f\alpha'}) \leq 0$ and $(z_{\beta_{trans}} - z_{\beta}) \leq 0$ then :

$$\dot{z}_{\beta_{trans}} = z_{\beta} \frac{z_{\beta} - z_{\beta_{trans}}}{\tau_{trans}} \quad (\text{A.30})$$

If not

$$\dot{z}_{\beta_{trans}} = -\dot{z}_{\alpha} - \dot{z}_{\alpha'} \quad (\text{A.31})$$

A.4 Relationship between Eigenstrain Influence Operators

Starting with the fundamental law

$$\sigma_s + L_s \gamma_s = L_s \varepsilon_s$$

Strain Localization Law

$$B_s \Sigma - \sum_r F_{sr} L_r \beta_r - \tau_s + L_s \gamma_s = L_s (A_s E + \sum_r D_{sr} \beta_r)$$

where the value of τ_s is to be determined later. Substituting the macroscopic law

$$B_s L (E - \Gamma) - \sum_r F_{sr} L_r \beta_r - \tau_s + L_s \gamma_s = L_s (A_s E + \sum_r D_{sr} \beta_r)$$

or

$$-B_s L \Gamma - \sum_r F_{sr} L_r \beta_r - \tau_s + L_s \gamma_s = L_s \sum_r D_{sr} \beta_r$$

Replacing the expression of the macroscopic inelastic strain for the strain localization law gives

$$-B_s L \left(\sum_r c_r B_r^T \beta_r + L^{-1} \sum_r c_r L_r (\gamma_r - \beta_r) \right) - \sum_r F_{sr} L_r \beta_r - \tau_s + L_s \gamma_s = L_s \sum_r D_{sr} \beta_r$$

$$-B_s L \left(\sum_r c_r B_r^T \beta_r - B^s \sum_r c_r L_r (\gamma_r - \beta_r) \right) - \sum_r F_{sr} L_r \beta_r - \tau_s + L_s \gamma_s = L_s \sum_r D_{sr} \beta_r$$

or

$$-B_s \sum_r c_r L_r (\gamma_r - \beta_r) - \tau_s + L_s (\gamma_s - \beta_s) = \sum_r (L_s D_{sr} + c_r B_s L B_r^T \beta_r + F_{sr} L_r - L_s \delta_{sr}) \beta_r$$

if we define

$$\tau_s = L_s (\gamma_s - \beta_s) - B_s \sum_r c_r L_r (\gamma_r - \beta_r)$$

That is we assume the strain localization dual law

$$\varepsilon_s = A_s E + \sum_r D_{sr} \beta_r$$

$$\sigma_s = B_s \Sigma - \sum_r F_{sr} L_r \beta_r - L_s (\gamma_s - \beta_s) + B_s \sum_r c_r L_r (\gamma_r - \beta_r)$$

then

$$\sum_r (L_s D_{sr} + c_r B_s L B_r^T + F_{sr} L_r - L_s \delta_{sr}) \beta_r$$

This must be true for any eigenstrain

$$L_s D_{sr} + c_r B_s L B_r^T + F_{sr} L_r - L_s \delta_{sr} = 0$$

or

$$L_s D_{sr} L_r^{-1} + c_r B_s L B_r^T L_r^{-1} + F_{sr} - \delta_{sr} I = 0$$

$$F_{sr} = \delta_{sr} I - L_s D_{sr} L_r^{-1} - c_r B_s A_r^T L_r L_r^{-1}$$

$$F_{sr} = \delta_{sr} I - L_s D_{sr} L_r^{-1} - c_r B_s A_r^T$$

this may also be expressed as

$$F_{sr} = \delta_{sr} I - L_s (D_{sr} + c_r A_s B_r^T) L_r^{-1}$$

$$D_{sr} = \delta_{sr} I - L_s^{-1} F_{sr} L_r - c_r A_s B_r^T$$

$$D_{sr} = \delta_{sr} I - L_s^{-1} (F_{sr} + c_r B_s A_r^T) L_r$$

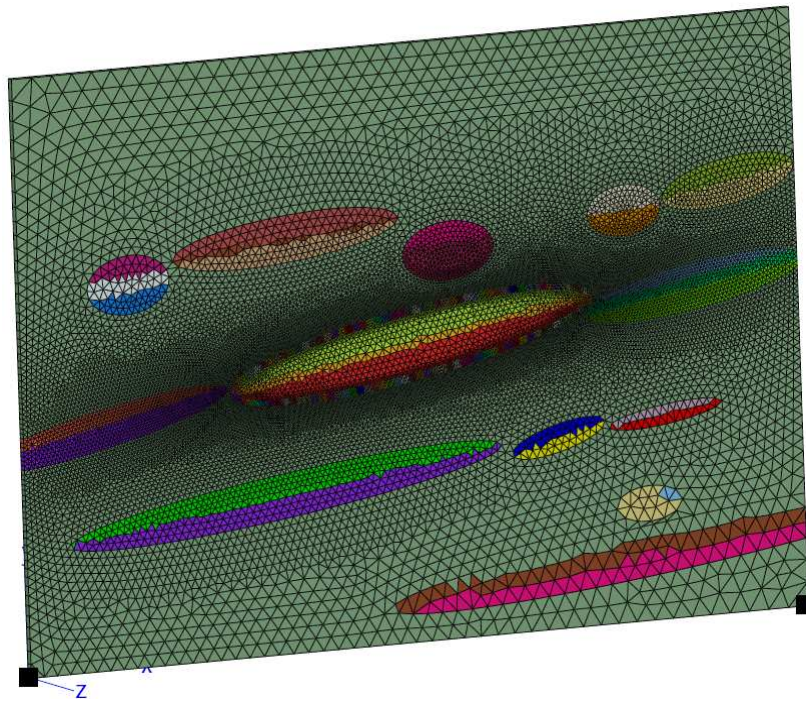


Figure A.2 : Boundary conditions in two nodes

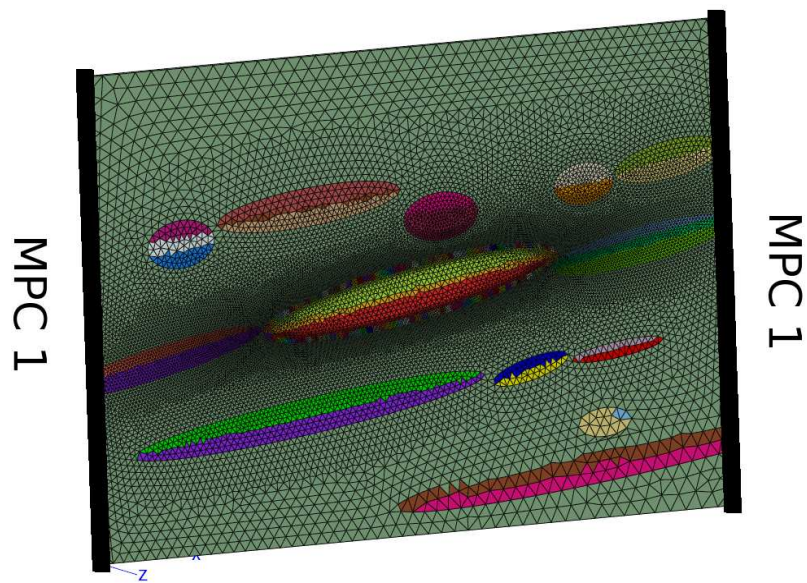


Figure A.3 : Boundary conditions on two sides

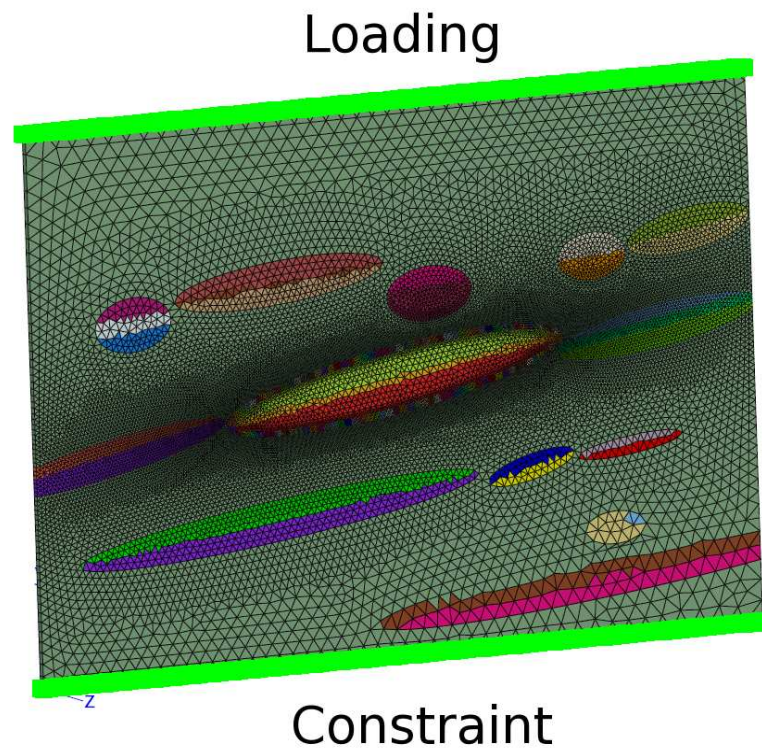


Figure A.4 : Boundary conditions on the bottom side and loading on the top one

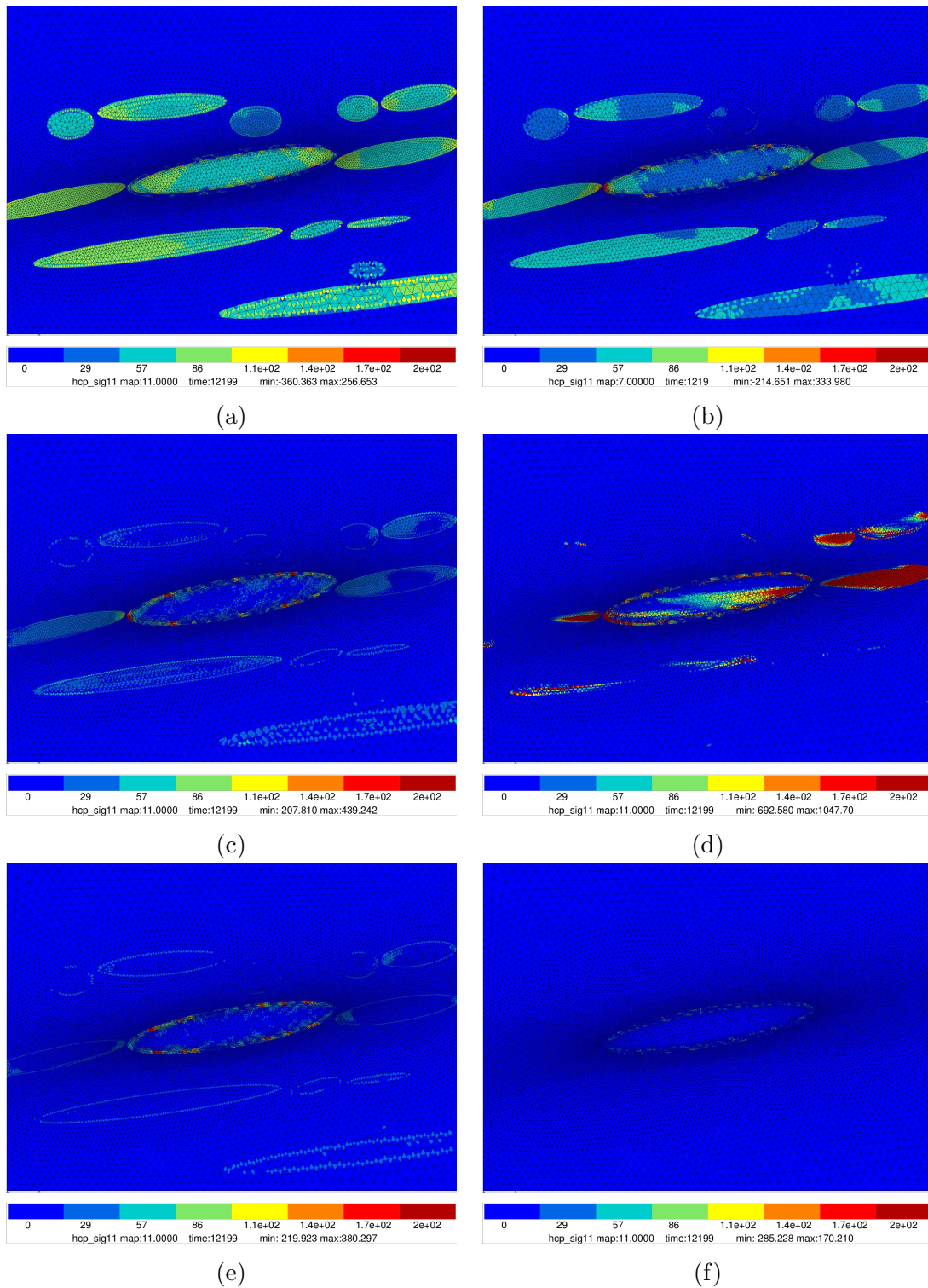


Figure A.5 : Stress field hcp_{11} in dwell tests for the microstructure with the morphological angle $10g$ and crystal orientations: (a) 0d; (b) 15d; (c) 30d; (d) 45d; (e) 60d; (f) 90d;

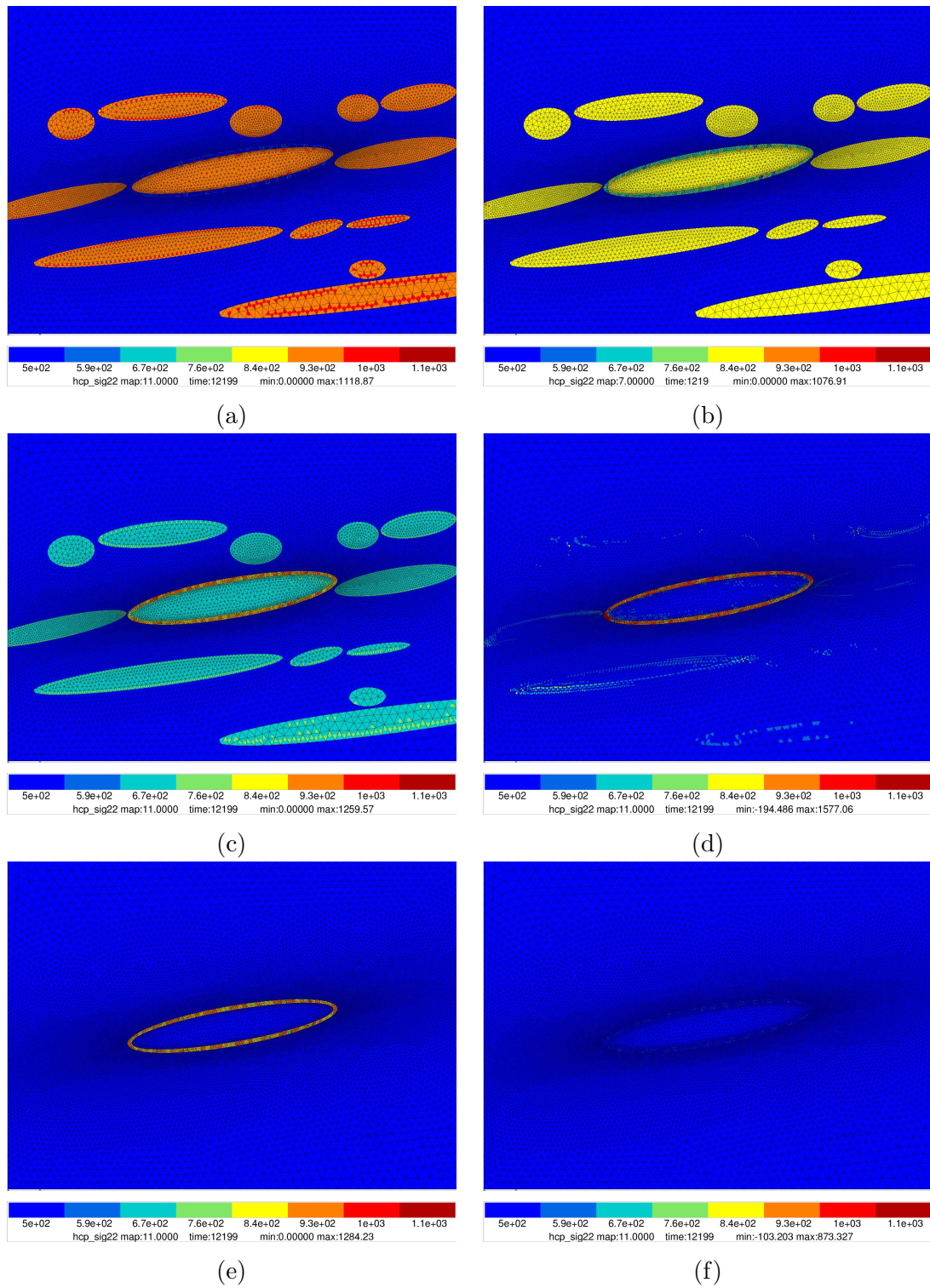


Figure A.6 : Stress field hcp_{22} in dwell tests for the microstructure with the morphological angle 10g and crystal orientations: (a) 0d; (b) 15d; (c) 30d; (d) 45d; (e) 60d; (f) 90d;

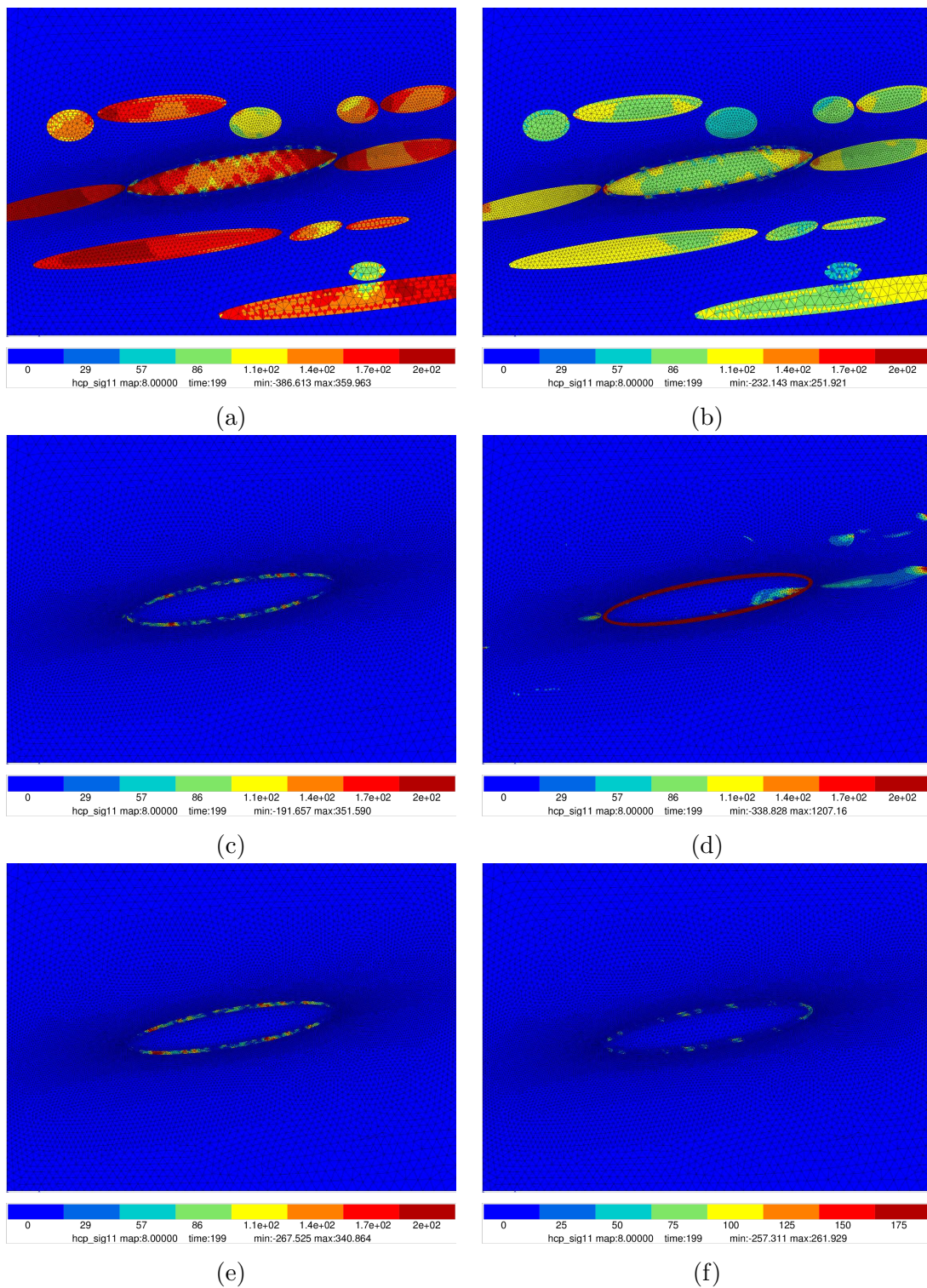


Figure A.7 : Stress field h_{cp11} in fatigue tests for the microstructure with the morphological angle 10g and crystal orientations: (a) 0d; (b) 15d; (c) 30d; (d) 45d; (e) 60d; (f) 90d;

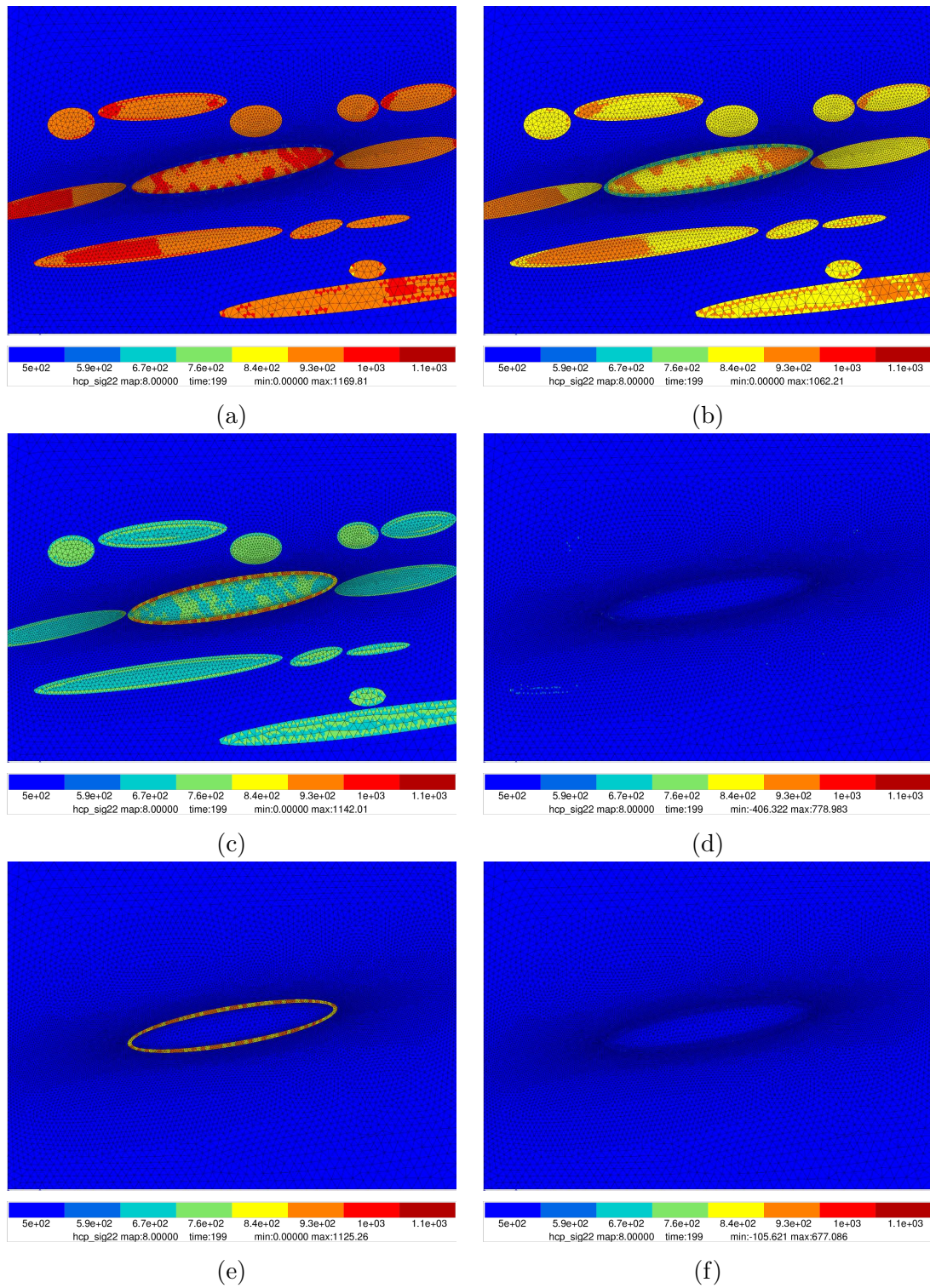


Figure A.8 : Stress field hcp_{22} in fatigue tests for the microstructure with the morphological angle 10g and crystal orientations: (a) 0d; (b) 15d; (c) 30d; (d) 45d; (e) 60d; (f) 90d;

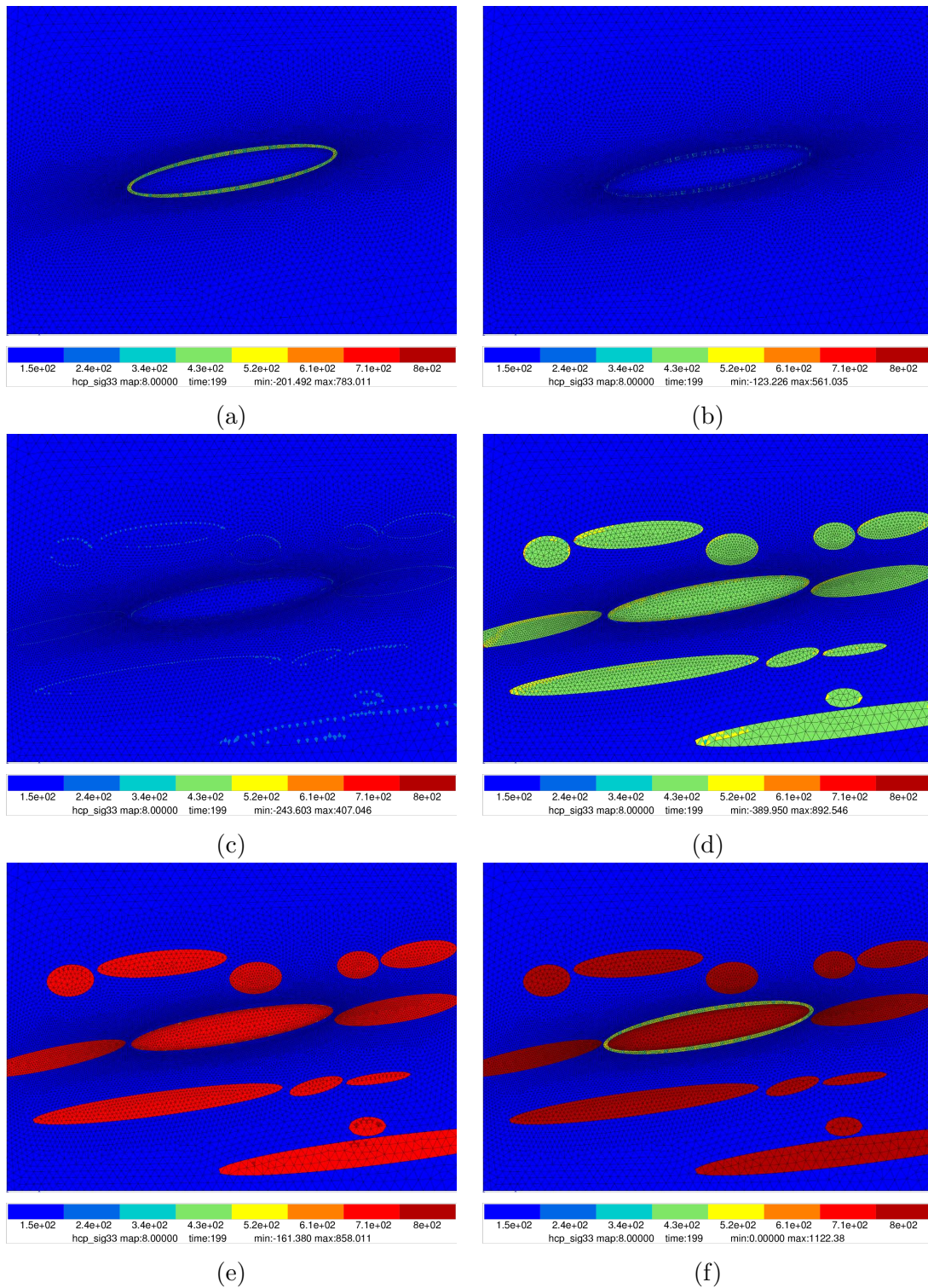


Figure A.9 : Stress field hcp_{33} in fatigue tests for the microstructure with the morphological angle 10g and crystal orientations: (a) 0d; (b) 15d; (c) 30d; (d) 45d; (e) 60d; (f) 90d;

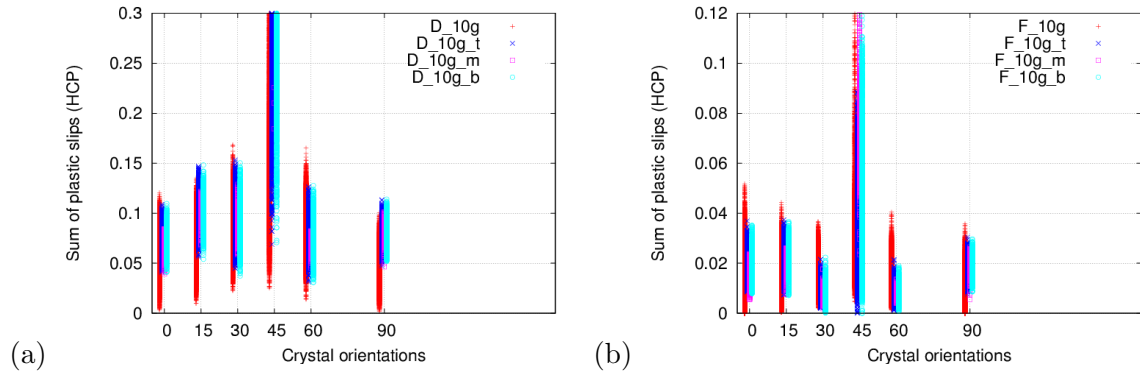


Figure A.10 : Distribution of sum of plastic slips in HCP crystals (α phase, dwell (a) and fatigue (b) loadings, virtual angles) in the outer layer, inside top, middle and bottom layers of the principal plume in the 100th cycle for different configurations (FigVII.5)

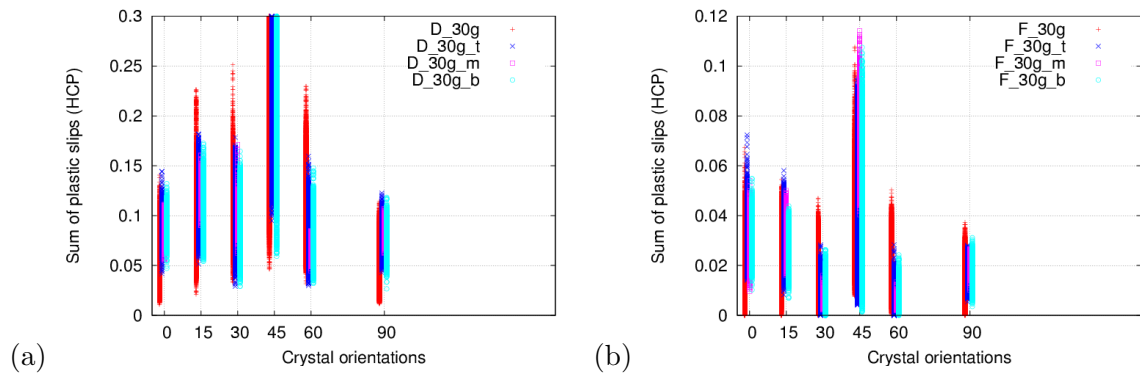


Figure A.11 : Distribution of sum of plastic slips in HCP crystals (α phase, dwell (a) and fatigue (b) loadings, virtual angles) in the outer layer, inside top, middle and bottom layers of the principal plume in the 100th cycle for different configurations (FigVII.5)

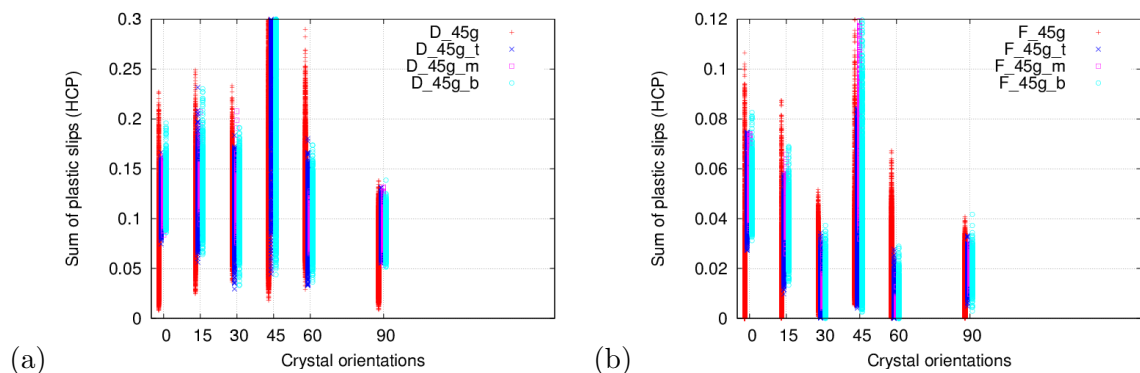


Figure A.12 : Distribution of sum of plastic slips in HCP crystals (α phase, dwell (a) and fatigue (b) loadings, virtual angles) in the outer layer, inside top, middle and bottom layers of the principal plume in the 100th cycle for different configurations (FigVII.5)

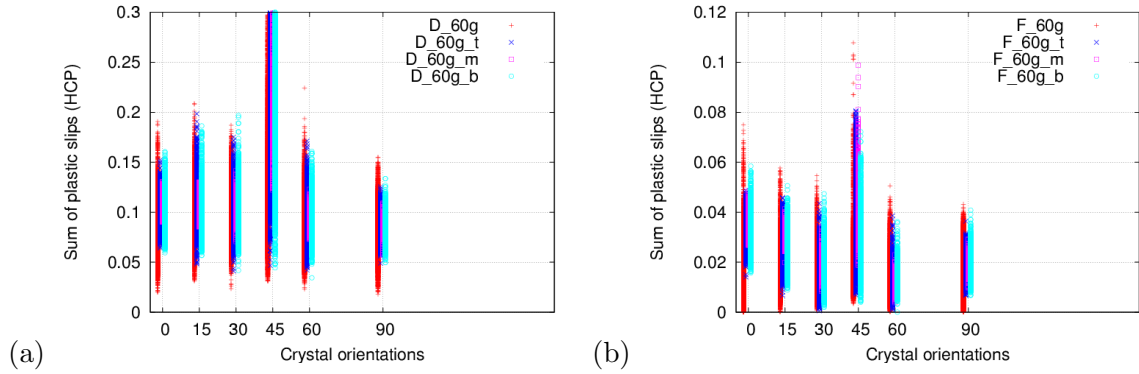


Figure A.13 : Distribution of sum of plastic slips in HCP crystals (α phase, dwell (a) and fatigue (b) loadings, virtual angles) in the outer layer, inside top, middle and bottom layers of the principal plume in the 100th cycle for different configurations (FigVII.5)

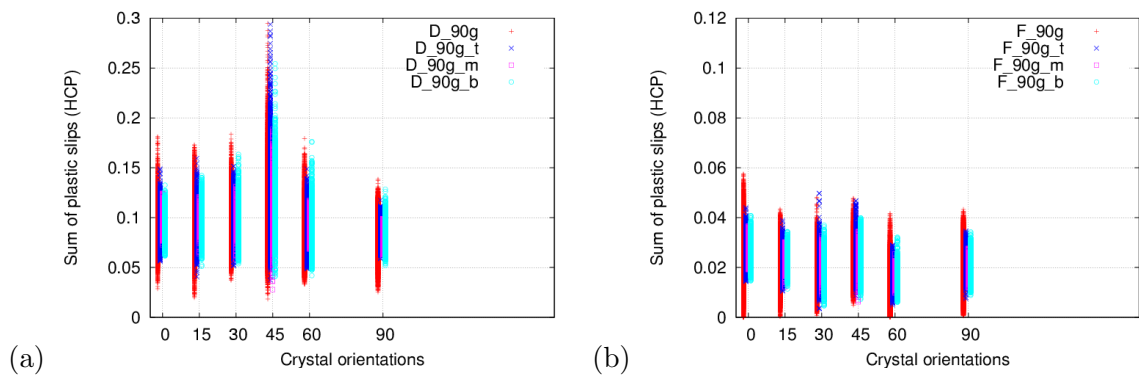


Figure A.14 : Distribution of sum of plastic slips in HCP crystals (α phase, dwell (a) and fatigue (b) loadings, virtual angles) in the outer layer, inside top, middle and bottom layers of the principal plume in the 100th cycle for different configurations (FigVII.5)

Bibliography

- [Han, 1990] (1990). *Metals Handbook TENTH EDITION Voume 2 Properties and Selection: Nonferrous Alloys and Special-Purpose Materials (First printing, October 1990)*. ASM International The Materials Information Society.
- [saf, 2010] (2010). <http://safran.cn>.
- [sta, 2010] (2010). <http://stanford.edu>.
- [Ankem and Greene, 1999] Ankem, S. and Greene, C. (1999). Recent developments in microstructure/property relationships of beta titanium alloys. *Materials Science and Engineering*, pages 127–131.
- [Ankem et al., 2006] Ankem, S., Margolin, H., Green, C., Neuberger, B., and Oberson, P. (2006). Mechanical properties of alloys consisting of two ductile phases. *Progress in Materials Science*, pages 632–709.
- [Bache, 1999] Bache, M. (1999). Processing titanium alloys for optimum fatigue performance. *International Journal of Fatigue*, pages 105–111.
- [Bache, 2003] Bache, M. (2003). A review of dwell sensitive fatigue in titanium alloys: the role of microstructure, texture and operating conditions. *International Journal of Plasticity*, 25:1079–1087.
- [Bache et al., 1997] Bache, M., Cope, M., Davies, H., Evans, W., and Harrison, G. (1997). Dwell sensitive fatigue in a near alpha titanium alloy at ambient temperature. *International Journal of Fatigue*, 19:S83–S88.
- [Bache et al., 1998] Bache, M., Evans, W., Randle, V., and Wilson, R. (1998). Characterization of mechanical anisotropy in titanium alloys. *Materials Science and Engineering*, pages 139–144.
- [Barbe et al., 2001] Barbe, F., Decker, L., Jeulin, D., and Cailletaud, G. (2001). Intergranular and intragranular behavior of polycrystalline aggregates. part 1: F.e. model. *International Journal of Plasticity*, pages 513–536.
- [Baroumes, 1998] Baroumes, L. (1998). *Comportement des composites à matrice métallique: Du processus de fabrication à la tenue en service*. PhD thesis, "L'université Paris VI".
- [Bathias and Pineau, 2010] Bathias, C. and Pineau, A. (2010). *Fatigue of Materials and Structures*. ISTE Ltd and John Wiley & Sons, Inc.
- [Besson and Foerch, 1997] Besson, J. and Foerch, R. (1997). Large Scale Object–Oriented Finite Element Code Design. *Comp. Meth. Appl. Mech. Engng*, 142:165–187.

- [Blétry and Cailletaud, 2011] Blétry, M. and Cailletaud, G. (2011). *Fatigue of Materials and Structures: Application to Design and Damage*, volume 4, chapter Multiaxial Fatigue, pages 19–58. Wiley.
- [Boyer, 1996] Boyer, R. R. (1996). An overview on the use of titanium in aerospace industry. *Material Science and Engineering*, pages 103–104.
- [Bridier et al., 2005] Bridier, F., Villechaise, P., and Mendez, J. (2005). Analysis of the different slip systems activated by tension in a $\alpha+\beta$ titanium alloy in relation with local crystallographic orientation. *Acta Materialia*, 53:555–567.
- [Cabocel, 2004] Cabocel, N. (2004). *Étude du dwell dans le Ti-6242 beta*. Master's thesis. PhD thesis, "Ecole Nationale Supérieure de Mécanique et d'Aérotechnique".
- [Cailletaud and Sai, 1995] Cailletaud, G. and Sai, K. (1995). Study of plastic/viscoplastic models with various inelastic mechanisms. *International Journal of Plasticity*, pages 991–1005.
- [Cao et al., 2000] Cao, G., Fu, L., Lin, J., Zhang, Y., and Chen, C. (2000). The relationships of microstructure and properties of a fully lamellar tial alloy. *I*, pages 647–653.
- [Chaboche, 1989] Chaboche, J. (1989). Constitutive equations for cyclic plasticity and cyclic viscoplasticity. *International Journal of Plasticity*, pages 247–302.
- [Chun et al., 2005] Chun, Y., Yu, S., Semiatin, S., and Hwang, S. (2005). Effect of deformation twinning on microstructure and texture evolution during cold rolling of cp-titanium. *Materials Science and Engineering*, pages 209–219.
- [Davidson and Eylon, 1980] Davidson, D. and Eylon, D. (1980). Titanium alloy fatigue fracture facet investigation by selected area electron channeling. *Metallurgical Transactions A*, pages 837–843.
- [Deka et al., 2006] Deka, D., Joseph, D., Ghosh, S., and Mills, M. (2006). Crystal plasticity modeling of deformation and creep in polycrystalline ti-6242. *Metallurgical and materials transactions*, 37A:1371–1388.
- [Delfosse, 2005] Delfosse, J. (2005). *Forgeage beta du Ti17 Propriétés en fatigue*. PhD thesis, "École Centrale Paris".
- [Dick, 2006] Dick, T. (2006). *Modélisation multiéchelle du phénomène de fretting dans le contact aube-disque*. PhD thesis, "Ecole Nationale Supérieure de Mécanique et d'Aérotechnique".
- [Dimiduk et al., 1998] Dimiduk, D. M., Hazzledine, P. M., Parthasarathy, T. A., Seshagiri, S., and Mendiratta, M. G. (1998). The role of grain size and selected microstructural parameters in strengthening fully lamellar tial alloys. *Metallurgical and Materials Transactions*, pages 37–47.
- [Dunne et al., 2007] Dunne, F., Rugg, D., and Walker, A. (2007). Lengthscale-dependent, elastically anisotropic, physically-based hcp crystal plasticity: Application to cold-dwell fatigue in ti alloys. *International Journal of Plasticity*, 23:1061–1083.
- [Dvorak, 1993] Dvorak, G. (1993). Micromechanics of inelastic composite materials: Theory and experiment. *Journal of Engineering Materials and Technology*, pages 332–338.

- [Eshelby, 1963] Eshelby, J. (1963). The distribution of dislocations in an elliptical glide zone. *Physica status solidi*, pages 2057–2060.
- [Evans, 1998] Evans, W. (1998). Optimising mechanical properties in alpha+beta titanium alloys. *Material Science and Engineering*, A243:89–96.
- [Evans and Gostelow, 1979] Evans, W. and Gostelow, C. (1979). The effect of hold time on the fatigue properties of a beta-processed titanium alloy. *Metallurgical transactions A*, pages 1837–1846.
- [Evans et al., 2005] Evans, W., Jones, J., and Whittaker, M. (2005). Texture effects under tension and torsion loading conditions in titanium alloys. *International Journal of Fatigue*, 27:1244–1250.
- [Evans and Bache, 1994] Evans, W. J. and Bache, M. (1994). Dwell-sensitive fatigue under biaxial loads in the near-alpha titanium alloy imi685. *Fatigue*, pages 443–452.
- [Feaugas, 1994] Feaugas, X. (1994). *Microstructure et modelisation du comportement en fatigue uniaxiale et multiaxiale d'un alliage de titane biphasé*. PhD thesis, "Université de Technologie de Compiègne".
- [Feaugas and Clavel, 1997] Feaugas, X. and Clavel, M. (1997). Cyclic deformation behaviour of an alpha/beta titanium alloy - 1. micromechanisms of plasticity under various loading paths. *Acta Materialia*, pages 2685–2701.
- [Freiherr von Thungen and Villechaise, 2011] Freiherr von Thungen, I. and Villechaise, P. (2011). Personal communication.
- [Freiherr von Thungen et al., 2011] Freiherr von Thungen, I., Villechaise, P., and Dalloz, A. (2011). Deformation modes of a beta-ti6242 alloy submitted to dwell loading at 20c. *The 12th World Conference on Titanium. Program and Abstracts*, page 92.
- [Furuhara and Maki, 2001] Furuhrara, T. and Maki, T. (2001). Variant selection in heterogeneous nucleation on defects in diffusional phase transformation and precipitation. *Materials Science and Engineering*, pages 145–154.
- [Gautier et al.,] Gautier, E., Bonina, D., Khélifa, M., Lazaro, S., Lamendin, A., Bruneseaux, F., and Appolaire, B. Etude du comportement en fatigue fluage (dwell) à 20 c de l'alliage ti6242.
- [Hall, 1951] Hall, E. (1951). *Proc. Phys. Soc. London*.
- [Hasija et al., 2003] Hasija, V., Mills, M., and Joseph, D. (2003). Deformation and creep modeling in polycrystalline ti-6al alloys. *Acta Materialia*, 51:4533–4549.
- [Hsiung et al., 2002] Hsiung, L., Nieh, T., Choi, B., and Wadsworth (2002). Interfacial dislocations and deformation twinning in fully lamellar tial. *Materials Science and Engineering*, pages 637–643.
- [James and Gaines, 1967] James, C. L. and Gaines, C. L. (1967). Circular dislocation pile-ups 1. strength of ultra-fine polycrystalline aggregates. *Philosophical Magazine*, pages 1059–1063.
- [Jaoul, 2008] Jaoul, B. (2008). *Étude de la plasticité et application aux métaux*. École des Mines de Paris.

- [Jousset, 2008] Jousset, H. (2008). *Viscoplasticité et microstructures d'un alliage de titane: effets de la température et de la vitesse de sollicitation*. PhD thesis, "Ecole des Mines de Paris".
- [Karthikeyan et al., 2006] Karthikeyan, T., Saroja, S., and Vijayalakshmi, M. (2006). Evaluation of misorientation angle-axis set between variants during transformation of bcc to hcp phase obeying burgers orientation relation. *Scripta Materialia*, pages 771–774.
- [Kassner et al., 1999] Kassner, M., Kosaka, Y., and Hall, J. (1999). Low-cycle dwell-time fatigue in ti-6242. *Metallurgical and Materials Transactions*, pages 2383–2389.
- [Kocks and Brown, 1966] Kocks, U. and Brown, T. (1966). Latent hardening in aluminum. *Philosophical Magazine*, pages 87–98.
- [Lapczuk et al., 2000] Lapczuk, I., Rajagopal, K., and Srinivasa, A. (2000). Deformation twinning during impact of a titanium cylinder-numerical calculations using a constitutive theory based on multiple natural configurations. *Computational methods in applied mechanics and engineering*, pages 527–541.
- [Lebensohn and Canova, 1997] Lebensohn, R. and Canova, G. (1997). A self-consistent approach for modelling texture development of two-phase polycrystals: application to titanium alloys. *Acta Materialia*, pages 3687–3694.
- [Lefranc, 2007] Lefranc, P. (2007). *Endommagement sous chargement cyclique avec temps de maintien de l'alliage de titane Ti-6242. Role de l'hydrogène interne*. PhD thesis, "Ecole Nationale Supérieure de Mécanique et d'Aérotechnique".
- [Lemaitre and Chaboche, 2002] Lemaitre, J. and Chaboche, J.-L. (2002). *Mechanics of solid materials, 558 p.* Cambridge University Press, The Edinburgh Building, Cambridge.
- [Li and Chou, 1970] Li, J. and Chou, Y. (1970). The role of dislocations in the flow stress grain size relationships. *Metallurgical Transactions*, pages 1145–1159.
- [Li et al., 2008] Li, S., Xiong, B., Hui, S., Ye, W., and Yu, Y. (2008). Effects of microstructure on fatigue crack growth behavior of ti-6al-2zr-1mo-1v eli alloy. *Materials characterization*, pages 397–401.
- [Longuet, 2010] Longuet, A. (2010). *Modélisation du procédé de projection laser: application au Ti-6Al-4V*. PhD thesis, "Ecole des Mines de Paris".
- [Longuet et al., 2009] Longuet, A., Robert, Y., Aeby-Gautier, E., Appolaire, B., Mariage, J. F., Colin, C., and Cailletaud, G. (2009). A multiphase mechanical model for ti-6al-4v: application to laser assisted process modeling. *Computational Materials Science*, 46:761–766.
- [Lutjering and Williams, 2003] Lutjering, G. and Williams, J. (2003). *Titanium*. Springer, New York.
- [Maruyama et al., 2001] Maruyama, K., Yamada, N., and Sato, H. (2001). Effects of lamellar spacing on mechanical properties of fully lamellar ti-39.4mol%al alloy. *Materials Science and Engineering*, pages 360–363.
- [McBagonluri et al., 2005] McBagonluri, F., Akpan, E., Mercer, C., Shen, W., and Soboyejo, W. (2005). An investigation of the effects of microstructure on dwell fatigue crack growth in ti-6242. *Material Science and Engineering*, A405:111–134.

- [Medina Perilla and Gil Sevillano, 1995] Medina Perilla, J. and Gil Sevillano, J. (1995). Two-dimensional sections of the yield locus of a ti-6%al-4%v alloy with a strong transverse-type crystallographic alpha-texture. *Materials Science and Engineering*, pages 103–110.
- [Méric et al., 1991] Méric, L., Poubanne, P., and Cailletaud, G. (1991). Single crystal modeling for structural calculations part1: Model presentation. *JEMT 113*, A405:62–170.
- [Mills et al., 1998] Mills, M. J., Hou, D. H., Suri, S., and Viswanathan, G. (1998). Orientation relationship and structure of alpha/beta interfaces in conventional titanium alloys. *Boundaries and Interfaces in Materials: The David A. Smith Symposium*, pages 295–301.
- [Mueller, 2000] Mueller, A. (November 29, 2000). Report to onera, northwest numerics, inc.
- [Naka et al., 1988] Naka, S., Lasalmonie, A., Costa, P., and Kubin, L. P. (1988). The low-temperature plastic deformation of alpha-titanium and the core structure of a-type screw dislocations. *Philosophical Magazine*, pages 717–740.
- [Oberson and Ankem, 2009] Oberson, P. and Ankem, S. (2009). The effect of time-dependent twinning on low temperature (<0.25 tm) creep of an alpha-titanium alloy. *International Journal of Plasticity*, pages 881–900.
- [Paton et al., 1973] Paton, N., Williams, J., and G.P., R. (1973). The deformation of alpha-phase titanium. *Titanium Science and Technology*, pages 1049–1069.
- [Petch, 1953] Petch, J. (1953). *Iron Steel Inst.*
- [Rao and Hazzledine, 1999] Rao, S. and Hazzledine, P. (1999). Simulation of an edge source in the cu-ni multilayer system. *Scripta Materialia*, pages 1085–1090.
- [Robert, 2007] Robert, Y. (2007). *Simulation numérique du soudage du TA6V par laser yag impulsif: caractérisation expérimentale et modélisation des aspects thermomécanique associées à ce procédé*. PhD thesis, "Ecole Nationale Supérieure de Mécanique et d'Aérotechnique".
- [Saleh and Margolin, 1979] Saleh, Y. and Margolin, H. (1979). Bauschinger effect during cyclic straining of two ductile phase alloys. *Acta Metallurgica*, pages 533–544.
- [Salem and Semiatin, 2009] Salem, A. and Semiatin, S. (2009). Anisotropy of the hot plastic deformation of ti-6al-4v single-colony samples. *Materials Science and Engineering*, pages 114–120.
- [Salem et al., 2003] Salem, A. A., Kalidindi, S. R., and Doherty, R. D. (2003). Strain hardening of titanium: role of deformation twinning. *Acta Materialia*, pages 4225–4237.
- [Sansoz and Ghonem, 2003] Sansoz, F. and Ghonem, H. (2003). Effects of loading frequency on fatigue crack growth mechanisms in alpha/beta ti microstructure with large colony size. *Material Science and Engineering*, A356:81–92.
- [Savage et al., 2004] Savage, M., Tatalovich, J., and Mills, M. (2004). Anisotropy in the room-temperature deformation of alpha-beta colonies in titanium alloys: role of the alpha-beta interface. *Philosophical Magazine*, pages 1127–1154.
- [Savage et al., 2001] Savage, M., Tatalovich, J., Zupan, M., Hemker, K., and Mills, M. (2001). Deformation mechanisms and microtensile behavior of single colony ti-6242si. *Material Science and Engineering*, A319–321:398–403.

- [Semiatin and Bieler, 2001] Semiatin, S. and Bieler, T. (2001). The effect of alpha platelet thickness on plastic flow during hot working of ti-6al-4v with a transformed microstructure. *Acta Materialia*, pages 3565–3573.
- [Shen et al., 2004] Shen, W., Soboyejo, W., and Soboyejo, A. (2004). An investigation on fatigue and dwell-fatigue crack growth in ti-6al-2sn-4zr-2mo-0.1si. *Journal of Engineering Materials and Technology*, 36:117–140.
- [Simmons and Wang, 1971] Simmons, G. and Wang, H. (1971). *Single Crystal Elastic Constants and Calculated Aggregate Properties: A HANDBOOK*. THE M.I.T PRESS, Cambridge, Massachusetts, and London, England.
- [Sinha et al., 2004] Sinha, V., Mills, M., and Williams, J. (2004). Understanding the contributions of normal-fatigue and static loading to the dwell fatigue in a near-alpha titanium alloy. *Metallurgical and Materials Transactions*, pages 3141–3148.
- [Stapleton et al., 2008] Stapleton, A., Raghunathan, S., Bantounas, I., Stone, H., Lindley, T., and Dye, D. (2008). Evolution of lattice strain in ti-6al-4v during tensile loading at room temperature. *Acta Materialia*.
- [Stubbington and Pearson, 1978] Stubbington, C. and Pearson, S. (1978). Effect of dwell on the growth of fatigue cracks in ti-6al-4v alloy bar. *Engineering Fracture Mechanics*, pages 723–756.
- [Suri et al., 1997] Suri, S., Neeraj, T., Daehn, G., Hou, D.-H., Scott, J., Hayes, R., and Mills, M. (1997). Mechanisms of primary creep in alpha/beta titanium alloys at lower temperatures. *Materials Science and Engineering*, pages 996–999.
- [Suri et al., 1999] Suri, S., Viswanathan, G., Neeraj, T., Hou, D.-H., and Mills, M. (1999). Room temperature deformation and mechanisms of slip transmission in oriented single-colony crystals of an alpha/beta titanium alloy. *Acta Materialia*, 47(3):1019–1034.
- [Toubal et al., 2009] Toubal, L., Bocher, P., and Moreau, A. (2009). Dwell-fatigue life dispersion of a near alpha titanium alloy. *International Journal of Fatigue*, pages 601–605.
- [Venkataramani et al., 2008] Venkataramani, G., Kirane, K., and Ghosh, S. (2008). Microstructural parameters affecting creep induced load shedding in ti-6242 by a size dependent crystal plasticity fe model. *International Journal of Plasticity*, 24:428–454.
- [Venkataramani et al., 2007] Venkataramani, G., Ghosh, S., and Mills, M. (2007). A size-dependent crystal plasticity finite-element model for creep and load shedding in polycrystalline titanium alloys. *Acta Materialia*, 55:3971–3986.
- [Wang et al., 2009] Wang, J., Hirth, J., and Tomé (2009). (-1012) twinning nucleation mechanisms in hexagonal-close-packed crystals. *Acta Materialia*, pages 5521–5530.
- [Xianping et al., 2007] Xianping, W., Kalidindi, S. R., Necker, C., and Salem, A. A. (2007). Prediction of crystallographic texture evolution and anisotropic stress-strain curves during large plastic strains in high purity alpha-titanium using a taylor-type crystal plasticity model. *Acta Materialia*, pages 423–432.
- [Xiaoli et al., 1995] Xiaoli, T., Haicheng, G., and Zhongguang, W. (1995). Cyclic deformation features in high purity titanium bicrystals. *Materials Science and Engineering*, pages 45–52.

-
- [Zaefferer, 2003] Zaefferer, S. (2003). A study of active deformation systems in titanium alloys: dependence on alloy composition and correlation with deformation texture. *Material Science and Engineering*, pages 20–30.
- [Zhang et al., 2007] Zhang, M., Zhang, J., and McDowell, D. (2007). Microstructure-based crystal plasticity modeling of cyclic deformation of ti-6al-4v. *International Journal of Plasticity*, 23:1328–1348.

Etude de l'effet du temps de maintien sur le comportement et la rupture de l'alliage Ti-6242

Résumé : L'application d'un temps de maintien, même de faible durée, lors d'un chargement cyclique, modifie de façon très sensible à la fois le comportement contrainte-déformation et le nombre de cycles à amorçage dans l'alliage base titane TI-6242. Ceci est lié à un régime de fluage cyclique, conduisant à de la déformation progressive d'une part, et à une forte interaction fatigue-temps de maintien pour ce qui concerne le nombre de cycles à amorçage. Les différents phénomènes sont pour le moment assez mal analysés, si bien qu'il n'est pas possible d'effectuer une conception optimale des pièces, de larges marges de sécurité étant nécessaires.

Le but du travail est de mieux comprendre les mécanismes locaux qui régissent le comportement et l'amorçage des fissures, dans le but de suggérer des microstructures optimales, et de calibrer des modèles macroscopiques utilisables en bureau d'études.

En s'appuyant sur une base expérimentale fournie par Snecma et l'ENSMA, une approche multi-échelles a été mise en place pour représenter les hétérogénéités locales qui ont un rôle significatif sur les comportements observés. Dans les calculs des microstructures, faisant intervenir une étape d'évaluation statistique, on se focalise sur la représentation explicite des "plumes", grains de taille exceptionnelle, qui sont à l'origine des premières microfissures en raison du contraste cristallin qu'ils introduisent avec l'environnement.

Une revue des différentes configurations de plumes, afin de retenir celles qui sont le plus critique, a été établie. Cette analyse a permis de mettre en évidence la présence de plumes simples, doubles ou triples, les domaines se présentant sous formes de bandes. Les configurations à étudier comportent comme paramètres critiques l'orientation géométrique de la bande par rapport à la direction du chargement macroscopique, mais surtout l'orientation cristallographique au sein de cette (ces) bande(s).

Des calculs systématiques ont été effectués afin de mener une étude statistique et de déterminer les configurations les plus sensibles.

Mots clés : Alliage de titane, rupture en fatigue, effet de maintien, plasticité cristalline, hcp, bcc

Study of dwell-effect on behaviour and fracture of the alloy Ti-6242

Abstract: The application of a dwell period, even of short length, during a cyclic loading, simultaneously changes the stress-strain behaviour and the number of cycles to failure in a very sensitive way. This phenomenon is connected to a cyclic creep regime, generating progressive deformation, and to a strong interaction between the fatigue process and dwell periods for the number of cycles to failure. All these phenomena are poorly analysed nowadays, so that engineers hardly perform optimal design of the components, since large security margins are necessary.

The aim of the work is to better understand the local mechanisms which govern both behaviour and crack initiation, having in view optimal microstructures, and to calibrate manageable macroscopic models for the design department.

Using an experimental data set given by Snecma and ENSMA, a multiscale approach has been developed to represent the local heterogeneities that play a significant role on observed behaviour. In the calculations of microstructures that are performed for a statistical evaluation, the focus is made on the explicit representation of the so called "plumes", that are grains of exceptional size, which are at the origin of the first microcracks due to crystal contrast they introduce with the environment.

A review of various "plume" configurations is made, in order to investigate the most critical ones. This analysis allowed to shed the light on the presence of simple, double or triple "plumes", the domains being in band shapes. The critical parameters are the geometric arrangement of the band with respect to the direction of the macroscopic loading, but essentially the crystal orientation within this (these) band(s).

Systematic calculations were carried out in order to do a statistical study and to determine the most critical configurations.

Keywords: Ti alloys, fatigue, dwell-effect, crystal plasticity, hcp, bcc

